

https://dspace.org/

Mapping acidic mine water using geophysics

De Villiers, Daniel Petrus de Wet

2018

https://hdl.handle.net/10539/24849

De Villiers, Daniel Petrus De Wet (2018) Mapping acidic mine water using geophysics, University of the Witwatersrand, Johannesburg, https://hdl.handle.net/10539/24849

Downloaded from a DSpace repository. https://dspace.org/

MAPPING ACIDIC MINE WATER USING GEOPHYSICS

Daniël Petrus de Wet de Villiers
396761

A Dissertation submitted to the Faculty of Science, University of the Witwatersrand, Johannesburg, in fulfilment of the requirements for the degree of Master of Science

Supervised by Prof Susan Webb and Dr Mike Jones

Johannesburg, 2018



Table of Contents

Contents		**Page**
Declaration		i
Abstract		ii
Acknowledgements		iv
List of Figures		v
List of Tables		xviii
Chapter 1 – Introduction		1
1.1	Background	1
1.2	Acid generation	4
1.3	Remediation strategies	5
1.4	Geology and hydrogeology	7
1.5	Hydrogeophysics	11
1.6	Objectives	12
1.7	Prospectus	12
Chapter 2 – Geophysics for Investigating Acid Mine Drainage (AMD)		14
2.1	Introduction	14
2.2	Resistivity	15
2.3	Induced polarization (IP)	22
	2.3.1 Chargeability	23
2.4	Equipment	26
2.5	Modelling of electrical geophysical data	28
	2.5.1 Inversion	30
2.6	Other geophysical methods	32
2.7	Summary	32
Chapter 3 – Data Acquisition		34

3.1 Electrical methods along the tree roots 34
3.1.1 Resistivity data 36
3.1.2 IP data 37
3.1.3 SO_4 concentration data 38
3.2 Electrical resistivity profile in the direction of the groundwater flow in the lavas 39
3.2.1 Resistivity data 40
3.2.2 SO_4 concentration data 41
3.3 Electrical resistivity profile in the direction of the groundwater flow in the dolomites 41
3.3.1 Resistivity data 42
3.3.2 SO_4 concentration data 43
3.4 GPR data 43
3.5 Summary 44

Chapter 4 – Interpretation 46

4.1 Electrical methods along the tree roots 48
4.1.1 Line 1: ER data near a *Eucalyptus* tree with deep roots 49
4.1.1.1 Resistivity for line 1 49
4.1.1.2 Final model for line 1 51
4.1.2 Line 2: ER and IP data near a *Eucalyptus* tree with shallow roots 54
4.1.2.1 Wenner alpha ER data for line 2 54
4.1.2.2 Dipole-dipole ER data for line 2 58
4.1.2.3 Wenner alpha IP data for line 2 62
4.1.2.4 Dipole-dipole IP data for line 2 63
4.1.2.5 Final models for line 2 64
4.1.3 Line 3: ER and IP data near a *Searsia lancea* tree with deep roots 66
4.1.3.1 Wenner alpha ER data for line 3 66
4.1.3.2 Dipole-dipole ER data for line 3 69

4.1.3.3 Wenner alpha IP data for line 3 71
4.1.3.4 Final models for line 3 71
4.1.4 Line 4: ER and IP data near a *Searsia lancea* tree with shallow roots 73
4.1.4.1 Wenner alpha ER data for line 4 73
4.1.4.2 Wenner beta ER data for line 4 76
4.1.4.3 Wenner alpha IP data for line 4 78
4.1.4.4 Final models for line 4 79
4.2 Electrical resistivity profile in the direction of the groundwater flow in the lavas 81
4.2.1 ER data along line 9 81
4.2.1.1 Wenner Schlumberger ER data along line 9 81
4.2.1.2 Dipole-dipole ER data along line 9 84
4.2.1.3 Final model for line 9 86
4.2.2 ER data along line 12 87
4.2.2.1 Wenner Schlumberger ER data along line 12 88
4.2.2.2 Dipole-dipole ER data along line 12 91
4.2.2.3 Final model for line 12 93
4.2.3 ER data along line 5 94
4.2.3.1 Wenner Schlumberger ER data along line 5 95
4.2.3.2 Dipole-dipole ER data along line 5 97
4.2.3.3 Final model for line 5 100
4.2.4 ER data along line 6 102
4.2.4.1 Wenner alpha ER data along line 6 102
4.2.4.2 Wenner Schlumberger ER data along line 6 105
4.2.4.3 Dipole-dipole ER data along line 6 107
4.2.4.4 Final model for line 6 110
4.3 Electrical resistivity profile in the direction of the groundwater flow in the dolomites 111
4.3.1 ER data along line 11 112
4.3.1.1 Wenner Schlumberger ER data along line 11 112
4.3.1.2 Dipole-dipole ER data along line 11 115
4.3.1.3 Final model for line 11 117

4.3.2 ER data along line 8 118
4.3.2.1 Wenner Schlumberger ER data along line 8 118
4.3.2.2 Dipole-dipole ER data along line 8 121
4.3.2.3 Final model for line 8 123
4.3.3 ER data along line 10 124
4.3.3.1 Wenner Schlumberger ER data along line 10 125
4.3.3.2 Dipole-dipole ER data along line 10 127
4.3.3.3 Final model for line 10 129
4.4 Summary 130

Chapter 5 – Archie's law and hydraulic conductivity 131

Chapter 6 – Summary of results 136

6.1 Discussion of electrical resistivity results 139
6.2 Discussion of induced polarization results 146
6.3 Interpretation 148

Chapter 7 – Conclusions and further studies 150

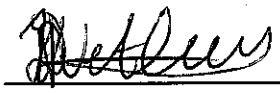
7 **References** 152

8 **Appendices** 159

A Setting used for smoothness constrained inversion in Res2DInv 159
B Select convergence curves for resistivity inversion 161
C Matlab code used for resistivity processing 172
D Acquired data 175

DECLARATION

I declare that this Dissertation is my own, unaided work. It is being submitted for the Degree of Master of Science at the University of the Witwatersrand, Johannesburg. It has not been submitted before for any degree or examination at any other University.



Daniel Petrus de Wet de Villiers

Signed on the 22nd of January 2018 in Johannesburg

Abstract

The oxidation of pyrite in water produces sulphuric acid that can decrease the pH of groundwater to the point where it is acidic itself. Furthermore, such an increase in acidity causes an increase in water conductivity. The water is referred to as acid mine drainage (AMD). It degrades the environment by enabling groundwater to carry high amounts of heavy metals. Efforts to remediate AMD effects in the Witwatersrand Basin include phytoremediation, specifically the use of *Searsia lancea*, *Eucalyptus* and *Tamarix* trees; these efforts are monitored by water periodically sampled from boreholes. This study investigates the potential of geophysical methods for identifying and monitoring the propagation of an AMD plume and the effects of phytoremediation associated with an old tailings dump in the Orkney area. The electrical resistivity method mapped the water table at a depth of 2-4 m and the maximum depth to bedrock at 18 m. Error analysis of the electrical resistivity data suggests that data can be interpreted down to a depth of only 10 m for profiles where the water is highly conductive due to its high level of contamination. The electrical resistivity results show a decrease in conductivity with distance from the contaminant source. In addition, a clear decrease in conductivity is observed downstream from a *Tamarix* woodland established for remediation. In the absence of metallic conductors in sediments the resistivity of the pore water governs the resistivity of the sediment medium. However, in this study the relationship determined between the conductivity of pore water and the geological unit is not linear and Archie's law is not applicable at this site, suggesting that either the resistivity of the surficial aquifer is poorly determined or the aquifer matrix is in itself conductive. The Induced Polarization (IP) method produces a chargeability response, which coincides with the *Eucalyptus* and *Searsia lancea* tree roots, suggesting that metallic contaminants are stored in and around the tree roots and are polarizable. Although ground penetrating radar has very little penetration in conductive media, GPR data were collected in an effort to image the plume geometry. However, the source waves did not penetrate through the topsoil due to the topsoil being conductive. This study demonstrates that the electrical resistivity method can effectively map the water table depth, can aid in groundwater conductivity mapping between boreholes and possibly tracking AMD. The data coverage of the electrical resistivity method was not sufficient to map the plume as a whole but does provide evidence for the effect of an established woodland in remediating groundwater. The IP method provides preliminary evidence for

the removal of AMD pollutants from the groundwater by *Searsia lancea* and *Eucalyptus* tree roots.

Acknowledgements

I would like to acknowledge and thank the following organisations, institutions and individuals for their technical and financial assistance and support in and out of the field:

- Prof Susan Webb and Dr Mike Jones for supervising the project, my work and my writing;
- This study was assisted by Isabel Weiersbye, with data from the Ecological Engineering and Phytotechnology Programme (EEPP), School of Animal, Plant and Environmental Sciences and AngloGold Ashanti Ltd Vaal River Operations. I am grateful to THRIP (Department of Trade and Industry of S.A.) and AGA S.A. Region Environmental Management Department for support;
- The South African Geophysical Association which helped me when I really needed it most and without whose support I could not have completed this study;
- Terry Odgers from Red Dog Scientific for being an all-round great guy and letting me use his equipment;
- De Beers for use of FDEM equipment;
- Stephanie Scheiber-Enslin for being a very good friend and editor;
- Bruce Mcgleorth, Peter Dye and Suzie Grindley for discussing the site and the remediation with me;
- The staff in the School of Geosciences, for helping me with my admin, teaching me about geology, answering my questions and running a ship from where we can do our work;
- My wife, for I cannot do a thing if I am not supported as much as I am. You really offered up a lot and your editing, patience and humour made this.

List of Figures

Figure	Caption	Page
Figure 1-1	The position of Orkney and an outline of the Witwatersrand Basin in Southern Africa (a) and the field site with the surveyed lines with respect to Orkney with stratigraphic units underlying the field site (SACS, 1980) (b). Latitude and longitude are shown for the WGS84 datum.	2
Figure 1-2	Conceptual model showing where acid mine water is generated and interacts with ground and surface water in TSFs. Some of the processes are shown in more detail in the magnified inserts, the processes on top of the TSF (A), the processes at the base of the TSF (B), the processes in cross section of a stream (C) and the processes at places on or near the TSF which floods each year (D, from Tutu *et al*., 2008).	4
Figure 1-3	Conceptual model of the study site showing the geological stratigraphy (from De Sousa *et al*., 2006).	8
Figure 1-4	Hydrogeological model used in this study. Green symbols indicate lava, yellow cross lines indicate quartzites and the red lined area indicates dolomite. Blue lines indicate contours of equal water table level with the contours shown for the water table in mamsl. Black arrows show the direction of water flow based on head measurements in the boreholes. Coordinates are for the LO27 projection on the WGS84 datum (in metres, from De Sousa *et al.*, 2006).	10
Figure 2-1	Four points where the ammeter and voltmeter will be placed on a surface. c1 and c2 show the positions of the current electrodes and P1 and P2 the positions of the potential electrodes. *r* is the distance between the different electrodes (one example shown).	16
Figure 2-2	The three most common array types for acquiring electrical resistivity data. For the dipole-dipole array the current and potential electrodes are separated by a distance *a* and two dipoles are separated by *na* (a). For the Wenner Schlumberger array the potential electrodes are separated by a distance *a* and the current electrodes are separated by a distance *na* (b). The Wenner alpha array is a special case of the Wenner Schlumberger array with *n=1* (c).	17
Figure 2-3	Schematic diagram showing how electrical conductivity (in log S/m) and pH of acidic water change when they are subject to different processes. Point A represents acid mine water (from Tutu *et al*., 2008).	19

Figure	Caption	Page
Figure 2-4	Theoretical IP response showing the secondary voltage (φ_s), the primary or instantaneous voltage (φ_σ) and the sum of these two (φ_η) (from Oldenburg and Li, 1994).	24
Figure 2-5	Phase response (in milliradian) of laboratory prepared samples to frequency domain IP measurements for four different samples prepared and tested in a laboratory environment. The filled symbols are showing the phase (primary vertical axis) and the unfilled symbols the resistivity. The three samples contained 0%, 5% and 10% pyrite respectively and the remainder of each sample being sand and water (from Gudjurgis *et al*., 1997).	25
Figure 2-6	Additive noise from stacking when not enough time has been allowed for chargeability to decay fully. The difference in the expected to actual responses (a) and the percentage difference for each increasing stack (b, from Fiandaca *et al*., 2012).	27
Figure 3-1	Location map of the first set of ER lines. Water flow is from east to west. Latitude and longitude are shown for the WGS84 datum.	35
Figure 3-2	Location map of the first set of ER lines with the SO_4 readings taken in some select boreholes in 2010 contoured in colour. The legend is shown in the bottom right and the colour bar shows SO_4 concentration values in ppm. The line names have been omitted for clarity but are shown in Figure 3-1. Latitude and longitude are shown for the WGS84 datum.	36
Figure 3-3	Location map of the second set of ERT lines with the SO_4 readings taken in some select boreholes in 2010 contoured in colour. The legend is shown in the bottom right and the colour bar shows SO_4 concentration values in ppm. Latitude and longitude are shown for the WGS84 datum. Line names have been omitted for clarity but are shown in Figure 1-1.	40
Figure 3-4	Location map of the third set of ERT lines with the SO_4 readings taken in some select boreholes in 2010 contoured. The legend is shown in the bottom right and the colour bar shows SO_4 values in ppm concentration values in ppm. Latitude and longitude are shown for the WGS84 datum. Line names have been omitted for clarity but are shown in Figure 1-1.	42
Figure 3-5	Positions of low frequency (40 MHz) GPR scans with the stratigraphy underlying the field site (SACS, 1980).	44

Figure	Caption	Page
Figure 4-1	A model of resistivity (a) and the misfit in the apparent resistivity space (b) for the third iteration for Wenner Schlumberger data acquired along line 1 (Res2dInv).	50
Figure 4-2	Alternative models for the data acquired along line 1 using different initial models. Homogenous half-spaces are used with initial resistivities of 53 ohm.m (a) and 1000 ohm.m (b) and 53 ohm.m (c). The model in (c) uses the Ekblom norm. The models are faded out using a DOI value of 0.1 (DCIP2D).	52
Figure 4-3	Final resistivity model for line 1.	53
Figure 4-4	Final resistivity model with surface features for line 1.	54
Figure 4-5	A model of resistivity (a) and the misfit in the apparent resistivity space (b) for the second iteration for Wenner alpha data acquired along line 2 (Res2dInv).	55
Figure 4-6	Model of resistivity (a) and misfit (b) for the fourth iteration, using a robust inversion scheme for Wenner alpha data acquired along line 2 (Res2dInv).	56
Figure 4-7	Different starting models produced similar model resistivities for the Wenner alpha data acquired on line 2 for depths up to 10 m. The calculated DOI index values are shown.	57
Figure 4-8	Different starting models produced similar model resistivities for the Wenner alpha data acquired on line 2 for depths up to 10 m.	58
Figure 4-9	A model of resistivity (a) and the misfit in the apparent resistivity space (b) for the second iteration for the dipole-dipole data acquired on line 2 (Res2dInv).	59
Figure 4-10	Model of resistivity (a) and misfit (b) for the sixth iteration using a robust inversion scheme on the dipole-dipole data acquired along line 2 (Res2dInv).	60
Figure 4-11	Different starting models produced similar model resistivities for the dipole-dipole data acquired on line 2 and the DOI indices are shown.	61
Figure 4-12	Models produced using a slightly different algorithm minimising the L_1 norm (a) and the L_2 norm (b). No DOI have been calculated for these two models (DCIP2D).	62
Figure 4-13	Model of chargeability from IP data collected using the Wenner	63

Figure	Caption	Page
	alpha array on line 2. See text for window and pulse length (Res2dInv).	
Figure 4-14	Model of chargeability from IP data collected using the dipole-dipole array on line 2. See text for window and pulse length (Res2dInv).	63
Figure 4-15	Final resistivity model for line 2.	64
Figure 4-16	Final chargeability model for line 2.	65
Figure 4-17	Final resistivity model for line 2 with surface features.	65
Figure 4-18	Final chargeability model for line 2 with surface features.	66
Figure 4-19	A model of resistivity (a) and the misfit in the apparent resistivity space (b) for the second iteration modelling the Wenner alpha data acquired on line 3 (Res2dInv).	67
Figure 4-20	Model of resistivity (a) and misfit (b) for the fourth iteration using a robust inversion scheme on the Wenner alpha data acquired along line 3 (Res2dInv).	68
Figure 4-21	Different starting models produced similar model resistivities for the Wenner alpha data acquired on line 3 for depths up to 10 m with the DOI index shown.	69
Figure 4-22	A model of resistivity (a) and the misfit in the apparent resistivity space (b) for the second iteration of the smoothness constrained inversion of the dipole-dipole data acquired on line 3 (Res2dInv).	70
Figure 4-23	Model of chargeability from IP data collected using the Wenner alpha array on line 3. See text for window and pulse length (Res2dInv).	71
Figure 4-24	Final resistivity model for line 3.	72
Figure 4-25	Final chargeability model for line 3.	72
Figure 4-26	Final resistivity model for line 3 with surface features.	72
Figure 4-27	Final chargeability model for line 3 with surface features.	73
Figure 4-28	The model obtained after three iterations of running the inversion scheme on the Wenner alpha data acquired on line 4. A calculated model (a) and the difference between the observed and calculated	74

Figure	Caption	Page
	apparent resisitiivity values (b, Res2dInv).	
Figure 4-29	The model from Figure 4-28b in (a) with a different histogram for the misfit data (b) (Res2dInv).	75
Figure 4-30	Depth of investigation index for the Wenner alpha data acquired along line 4.	76
Figure 4-31	A model of resistivity (a) and a misfit in the apparent resistivity space (b) for the third iteration of inversion of the Wenner beta data on line 4 (Res2dInv).	77
Figure 4-32	Different starting models produced similar model resistivities for the Wenner beta data acquired on line 4 for depths up to 15 m. The DOI index is shown.	78
Figure 4-33	Different starting models produced similar model resistivities for the Wenner beta data acquired on line 4 for depths up to circa 15 m deep. Both models started as homogenous half-spaces with a reference resistivity of 25 ohm.m (a) and 100 ohm.m (b), respectively.	78
Figure 4-34	Model of chargeability from IP data collected using the Wenner alpha array on line 4. See text for window and pulse length (Res2dInv).	79
Figure 4-35	Final resistivity model for line 4.	80
Figure 4-36	Final chargeability model for Line 4.	80
Figure 4-37	Final resistivity model for line 4 with surface features.	80
Figure 4-38	Final chargeability model for line 4 with surface features.	81
Figure 4-39	A model of resistivity (a) and a misfit in the apparent resistivity space (b) for the third iteration of the Wenner Schlumberger data acquired on line 9 (Res2dInv).	82
Figure 4-40	A model of the Wenner Schlumberger data from line 9, obtained using a different inversion algorithm (DCIP2D).	84
Figure 4-41	A model of resistivity (a) and a misfit in the apparent resistivity space (b) for the second iteration of the dipole-dipole data acquired along line 9 (Res2dInv).	85

Figure	Caption	Page
Figure 4-42	Different starting models produced similar model resistivities for the dipole-dipole data on line 9. The DOI index is shown.	86
Figure 4-43	A model of the Wenner Schlumberger data (line 9) from line obtained using a different inversion algorithm (DCIP2D).	87
Figure 4-44	A model of resistivity (a) and the misfit in the apparent resistivity (b) for the third iteration of the Wenner Schlumberger data acquired along line 12 (Res2dInv).	89
Figure 4-45	Alternative model for the Wenner Schlumberger data acquired on line 12 (Res2dInv).	90
Figure 4-46	A model of the Wenner Schlumberger data from line 12 obtained using a different inversion algorithm (DCIP2D).	91
Figure 4-47	A model of resistivity (a) and the misfit in the apparent resistivity space (b) for the third iteration of the smoothness-constrained inversion of the dipole-dipole data on line 12 (Res2dInv).	92
Figure 4-48	DOI indices for the resistivity data acquired with the dipole-dipole array on line 12.	93
Figure 4-49	Final resistivity model for line 12, the Wenner Schlumberger model from Figure 4-46.	94
Figure 4-50	DOI indices for the resistivity data acquired with the Wenner Schlumberger array on line 5.	95
Figure 4-51	A model of resistivity (a) and the misfit in the apparent resistivity space (b) for the third iteration for the Wenner Schlumberger data from line 5 (Res2dInv).	96
Figure 4-52	A model of the Wenner Schlumberger data from line 5 obtained using a different inversion algorithm (DCIP2D).	97
Figure 4-53	A model of resistivity (a), and a misfit in the apparent resistivity space (b) for the second iteration of the inversion of the dipole-dipole data along line 5 (Res2dInv).	98
Figure 4-54	DOI indices for the resistivity data acquired with the dipole-dipole array on line 5.	99
Figure 4-55	A model of the dipole-dipole data from line 5 obtained using a different inversion algorithm (DCIP2D).	100

Figure	Caption	Page
Figure 4-56	Final resistivity model for line 5, the Wenner Schlumberger model from Figure 4-52 (DCIP2D).	101
Figure 4-57	A model of resistivity (a) and the misfit in the apparent resistivity space (b) for the second iteration of the Wenner alpha data acquired on line 6 (Res2dInv).	103
Figure 4-58	A model of resistivity (a) and the misfit in the apparent resistivity space (b) for the fourth iteration of Wenner alpha data acquired on line 6 (Res2dInv).	104
Figure 4-59	A model of the Wenner alpha data from line 6 obtained using a different inversion algorithm (DCIP2D).	105
Figure 4-60	A model of resistivity (a) and the misfit in the apparent resistivity space (b) for the third iteration of the Wenner Schlumberger data of line 6 (Res2dInv).	106
Figure 4-61	A model of the Wenner Schlumberger data from line 6, obtained using a different inversion algorithm (DCIP2D).	107
Figure 4-62	A model of resistivity (a) and the misfit in the apparent resistivity space (b) for the fourth iteration of the dipole-dipole data acquired on line 6 (Res2dInv).	109
Figure 4-63	Different starting models produced similar model resistivities for the dipole-dipole data acquired on line 6 for depths up to 10 m with the DOI indices plotted.	110
Figure 4-64	A model of the Wenner Schlumberger data from line 6 (DCIP2D).	111
Figure 4-65	A model of resistivity (a) and the misfit in the apparent resistivity space (b) after the third iteration of the Wenner Schlumberger data acquired on line 11 (Res2dInv).	113
Figure 4-66	Alternative model for the Wenner Schlumberger data acquired on line 11 (a) with the misfit in apparent resistivity space (b) (Res2dInv).	114
Figure 4-67	DOI indices for the resistivity data acquired with the dipole-dipole array on line 11.	115
Figure 4-68	A model of resistivity (a) and the misfit in the apparent resistivity space (b) for the fourth iteration of the dipole-dipole data acquired along line 11 (Res2dInv).	116

Figure	Caption	Page
Figure 4-69	Final resistivity model for line 11.	117
Figure 4-70	Final resistivity model for line 11 with the position and throw of the fault (the vertical scale has been increased).	117
Figure 4-71	The model obtained after four iterations of running the inversion scheme on the Wenner Schlumberger data acquired on line 8. The figure shows a calculated model (a) and the difference between the observed and calucated apparent resisitiivity values (b).	119
Figure 4-72	An alternative model for the Wenner Schlumberger data acquired in line 8 (a) with the resulting misfit pseudo section (b).	120
Figure 4-73	DOI for the Wenner Schlumberger data acquired along line 8.	121
Figure 4-74	The model obtained after four iterations of running the inversion scheme on the dipole-dipole data acquired on line 8. The figure a calculated model (a) and the difference between the observed and calucated apparent resisitiivity values (b).	122
Figure 4-75	Alternative models for the dipole-dipole data collected on line 8 using smoothness constrained inversion with initial models of homogenous half-spaces with resistivities of 300 ohm.m (a) and 1200 ohm.m (b).	123
Figure 4-76	DOI indices for the dipole-dipole data acquired on line 8 for depths up to 100 m (a) and the scaled values (b).	123
Figure 4-77	Final resistivity model for line 8.	124
Figure 4-78	Final resistivity model for line 8 (the vertical scale has been increased).	124
Figure 4-79	The DOI index for the Wenner Schlumberger data acquired on line 10.	125
Figure 4-80	A model of resistivity (a) and the misfit in the apparent resistivity space (b) obtained after the third iteration of the smoothness-constrained inversion process for the Wenner Schlumberger data acquired on line 10 (Res2dInv).	126
Figure 4-81	DOI for dipole-dipole data acquired on line 10 (a), and the scaled DOI indices for the same line (b).	127

Figure	Caption	Page
Figure 4-82	A model of resistivity (a) and the misfit in the apparent resistivity space (b) for the fourth iteration of the inversion of the dipole-dipole data acquired on line 10 (Res2dInv).	128
Figure 4-83	Final resistivity model for line 10.	129
Figure 4-84	Final resistivity model for line 10 vertical scale has been exaggerated.	130
Figure 5-1	Logarithmic correlation between ER of the layer and SO_4 content in boreholes surrounding the resistivity sections for data in areas underlain by lava (a) and dolomite (b).	134
Figure 5-2	Correlation between ER of the water and SO_4 content in boreholes surrounding the resistivity sections for data in areas underlain by lava (a) and dolomite (b).	135
Figure 6-1	Final resistivity model with tree locations for Wenner Schlumberger data acquired line 1 (reproduced from Figure 4-6).	140
Figure 6-2	Final ER resistivity model of the dipole-dipole data for line 4 with tree (reproduced from Figure 4-39).	140
Figure 6-3	Schematic diagram showing how electrical conductivity (in log S/m) and pH of acidic water change when they are subject to different processes. Point A represents acid mine water (from Tutu *et al*., 2008).	141
Figure 6-4	Parallel line ER models from the Wenner Schlumberger in the direction of the groundwater flow in the lavas. The final resistivity model for line 9 (reproduced from Figure 4-44a), final resistivity model for line 5 (reproduced from Figure 4-56b), the final resistivity model for line 6 (reproduced from Figure 4-62c) the final model for line 12 (DCIP2D).	143
Figure 6-5	Parallel line ER models from the Wenner Schlumberger in the direction of the groundwater flow in the dolomites. The final resistivity model for line 11 (reproduced from Figure 4-68a), the final resistivity model for line 8 (reproduced from Figure 4-76b) and the final resistivity model for line 10 (reproduced from Figure 4-82c. The vertical scale has been exaggerated for this figure).	145
Figure 6-6	Parallel line ER models from the Wenner Schlumberger in the	146

Figure	Caption	Page
	direction of the groundwater flow in the dolomites (Google Earth, 26°56'43.74" S 26°41'42.89" E, 2017).	
Figure 6-7	Final chargeability model for line 2 with surface features (reproduced from Figure 4-20).	146
Figure 6-8	Final chargeability model for line 3 with surface features (reproduced from Figure 4-29).	147
Figure 6-9	Final chargeability model for line 4 with surface features (reproduced from Figure 4-40).	147
Figure A-1	Data misfit in percent root mean squared versus number of iterations (Wenner Schlumberger data line 1).	161
Figure A-2	Data misfit in percent root mean squared versus number of iterations (Wenner alpha data line 2).	161
Figure A-3	Data misfit in percent root mean squared versus number of iterations (dipole-dipole data line 2).	162
Figure A-4	Data misfit in percent root mean squared versus number of iterations (Wenner alpha data line 3).	162
Figure A-5	Data misfit in percent root mean squared versus number of iterations (dipole-dipole data line 3).	163
Figure A-6	Data misfit in percent root mean squared versus number of iterations (Wenner alpha data line 4).	163
Figure A-7	Data misfit in percent root mean squared versus number of iterations (Wenner beta data line 4).	164
Figure A-8	Data misfit in percent root mean squared versus number of iterations (Wenner Schlumberger data line 9).	164
Figure A-9	Data misfit in percent root mean squared versus number of iterations (dipole-dipole data line 9).	165
Figure A-10	Data misfit in percent root mean squared versus number of iterations (Wenner Schlumberger data line 12).	165
Figure A-11	Data misfit in percent root mean squared versus number of iterations (dipole-dipole data line 12).	166

Figure	Caption	Page
Figure A-12	Data misfit in percent root mean squared versus number of iterations (Wenner Schlumberger data line 5).	166
Figure A-13	Data misfit in percent root mean squared versus number of iterations (dipole-dipole data line 5).	167
Figure A-14	Data misfit in percent root mean squared versus number of iterations (Wenner alpha data line 6).	167
Figure A-15	Data misfit in percent root mean squared versus number of iterations (Wenner Schlumberger data line 6).	168
Figure A-16	Data misfit in percent root mean squared versus number of iterations (dipole-dipole data line 6).	168
Figure A-17	Data misfit in percent root mean squared versus number of iterations (Wenner Schlumberger data line 11).	169
Figure A-18	Data misfit in percent root mean squared versus number of iterations (dipole-dipole data line 11).	169
Figure A-19	Data misfit in percent root mean squared versus number of iterations (Wenner Schlumberger line 8).	170
Figure A-20	Data misfit in percent root mean squared versus number of iterations (dipole-dipole data line 8).	170
Figure A-21	Data misfit in percent root mean squared versus number of iterations (Wenner Schlumberger line 10).	171
Figure A-22	Data misfit in percent root mean squared versus number of iterations (dipole-dipole data line 10).	171
Figure D-1	Wenner Schlumberger apparent resistivity data for line 1. See Figure 3-1 for line position.	176
Figure D-2	Wenner alpha apparent resistivity data for line 2. See Figure 3-1 for line position.	177
Figure D-3	Dipole-dipole apparent resistivity data for line 2. See Figure 3-1 for line position.	177
Figure D-4	Wenner alpha apparent resistivity data for line 3. See Figure 3-1 for line position.	178

Figure	Caption	Page
Figure D-5	Dipole-dipole apparent resistivity data for line 3. See Figure 3-1 for line position.	178
Figure D-6	Wenner alpha apparent resistivity data for line 4. See Figure 3-1 for line position.	179
Figure D-7	Wenner beta apparent resistivity data for line 4. See Figure 3-1 for line position.	179
Figure D-8	Wenner Schlumberger IP data for line 1. Windows 5 to 8 are shown. See Figure 3-1 for line position (Res2dInv).	180
Figure D-9	Wenner alpha IP data for line 2. Integral windows 2 to 6 are summed and the delay after the pulse is 0.04 s for only 0.26 s. See Figure 3-1 for line position (Res2dInv).	181
Figure D-10	Dipole-dipole IP data for line 2. Integral windows 6 to 10 are summed and the delay after the pulse is 0.22 s for 1.04 s. See Figure 3-1 for line position (Res2dInv).	181
Figure D-11	Wenner alpha IP data for line 3. Integral windows 6 to 10 are summed and the delay after the pulse is 0.22 s for 1.04 s. See Figure 3-1 for line position (Res2dInv).	181
Figure D-12	Dipole-dipole IP data for line 3. Integral windows 6 to 10 are summed and the delay after the pulse is 0.1 s for 0.52 s. See Figure 3-1 for line position (Res2dInv).	182
Figure D-13	Wenner beta IP data for line 4. Integral windows 6 to 10 are summed and the delay after the pulse is 0.1 s for 0.52 s. See Figure 3-1 for line position (Res2dInv).	182
Figure D-14	Wenner alpha IP data for line 4. Integral windows 6 to 10 are summed and the delay after the pulse is 0.06 s for 0.4 s. See Figure 3-1 for line position (Res2dInv).	183
Figure D-15	Wenner Schlumberger apparent resistivity data for line 9. See Figure 1-1 for line position.	184
Figure D-16	Dipole-dipole apparent resistivity data for line 9. See Figure 1-1 for line position.	184
Figure D-17	Wenner Schlumberger apparent resistivity data for line 12. See Figure 1-1 for line position.	185
Figure D-18	Dipole-dipole apparent resistivity data for line 12. See Figure 1-1	185

Figure	Caption	Page
	for line position.	
Figure D-19	Wenner Schlumberger apparent resistivity data for line 5. See Figure 1-1 for line position.	186
Figure D-20	Dipole-dipole apparent resistivity data for line 5. See Figure 1-1 for line position.	186
Figure D-21	Wenner Schlumberger apparent resistivity data for line 6. See Figure 1-1 for line position.	187
Figure D-22	Dipole-dipole apparent resistivity data for line 6. See Figure 1-1 for line position.	187
Figure D-23	Wenner alpha apparent resistivity data for line 6. See Figure 1-1 for line position.	188
Figure D-24	Wenner Schlumberger apparent resistivity data for line 11. See Figure 1-1 for line position.	189
Figure D-25	Dipole-dipole apparent resistivity data for line 11. See Figure 1-1 for line position.	189
Figure D-26	Wenner Schlumberger apparent resistivity data for line 8. See Figure 1-1 for line position.	190
Figure D-27	Dipole-dipole apparent resistivity data for line 8. See Figure 1-1 for line position.	190
Figure D-28	Wenner Schlumberger apparent resistivity data for line 10. See Figure 1-1 for line position.	191
Figure D-29	Dipole-dipole apparent resistivity data for line 10. See Figure 1-1 for line position.	191
Figure D-30	Representative sample of distance normalised raw GPR data.	191

List of Tables

Table	Caption	Page
Table 2-1:	Geometric factors and proportionality of geometric factor on a and n spacing of some simple and common arrays.	17
Table 5-1:	Borehole data showing the name, description and date measured for pH, electrical conductivity, SO_4 concentration, water level from the collar and coordinates in LO27 (WGS84 datum) for some boreholes installed in the dolomite (data provided by AGA without unit of measure).	131
Table 5-2:	Borehole data showing the name, description and date measured for pH, electrical conductivity, SO_4 concentration, water level from the collar and coordinates in LO27 (WGS84 datum) for some boreholes installed in the lava (data provided by AGA without unit of measure).	132
Table 5-3:	The high and low values of the SO_4 concentration (in ppn) distribution extracted from the SO_4 contour maps and the *in situ* ER (in ohm.m) read from the final models.	132

Chapter 1 - Introduction

1.1 Background

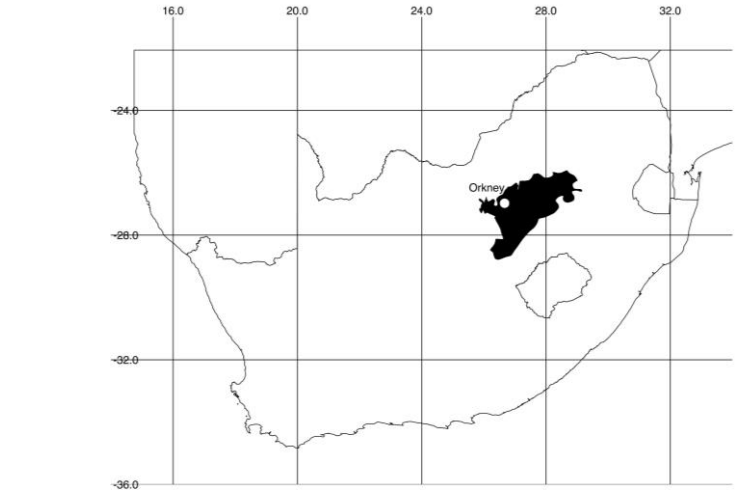
The Witwatersrand Basin covers a large geographical area in north-eastern South Africa (Figure 1-1a). The Witwatersrand Supergroup (WSG, the rock that fills the paleobasin) is the host of the largest gold deposits on Earth (Ewart, 2011) and has been extensively mined for over a century, mainly for gold (McCarthy, 2006). Sulphides are found in high concentrations in the ore and they produce acid when they react with oxygen. Not all the sulphide minerals are removed by mining (Akcil and Koldas, 2006) and heavy metals, which can be dissolved in acidic water, make for a significant environmental hazard (Rosner and Van Schalkwyk, 2000).

Pyrite is an acid producing mineral and it is the most abundant accessory mineral in the WSG ore (and with gold and uraninite the most important economically, Robb and Robb, 1998). There are seventy accessory minerals that have been identified in the WSG lithologies (Robb and Robb, 1998). These minerals are often concentrated in the ore but are not specifically mined and may be discarded in dumps (gold poor dust referred to locally as tailings).

Tailings dumps are sometimes referred to as tailings storage facilities or TSFs (Naicker *et al.*, 2003). Durand (2012) put the number of tailings dumps in the areas where the WSG gold deposits are exploited at more than 270. While the design of tailing dumps has improved and the risk posed to groundwater has been reduced with modern technologies (see for example Johnson and Hallberg, 2005), many of the older dumps continue to contribute to environmental degradation as large amounts of pyrite is available in the TSFs on or near the surface of the Earth (see for example Camden-Smith *et al*., 2013). In total TSFs emanating from gold mining activities in Gauteng alone, cover more than 180 km^2 of land (Rösner, 1999). The size of the TSF including the emergency dam in the area of study is approximately 40 hectares and is comprised of 0.7% pyrite (Grindley, 2014) and is shown in Figure 1-1b.

a)

b)



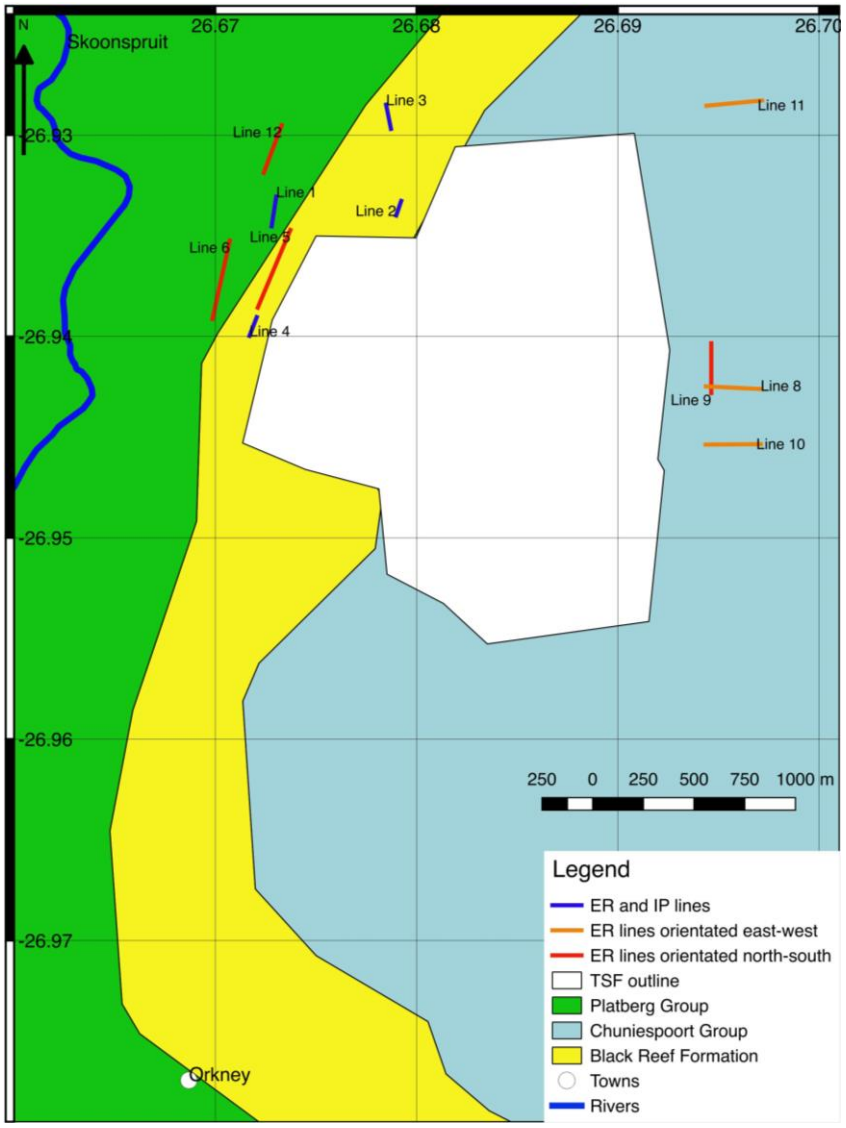


Figure 1-1: The position of Orkney and an outline of the Witwatersrand Basin in Southern Africa (a) and the field site with the surveyed lines with respect to Orkney with stratigraphic units underlying the field site (SACS, 1980) (b). Latitude and longitude are shown for the WGS84 datum.

In this study the pyrite is of specific importance as it is the cause of an environmental hazard: acid mine drainage (AMD), which is water that is affected by mining activities that also has a pH lower than 6. AMD is formed both above and below surface. Below surface it forms in old abandoned gold mine tunnels that are today flooded with groundwater when coming into contact with pyrite. Above surface AMD is formed after gold is removed from host rock large amounts of pyrite remain in the discarded material and TSFs increase the opportunity for pyrite to come into contact with oxidising agents and run into ground water, causing AMD. AMD is the single greatest threat to the environment caused by gold mining and will continue to be, long after mining has ceased (Naidoo, 2009), as AMD is generated through oxidisation of pyrite exposed to oxygen and water at dumps which are not intended to be processed ever again after their construction.

Three hazardous consequences of AMD are:

1) it reduces the pH of groundwater, which increases the water's ability to carry heavy metals that can be toxic to animals and humans (Akcil and Koldas, 2006).

2) The formation of iron oxide can be a product of AMD and can cause water to be deoxygenated (Hustwit *et al.*, 1992) which makes the water less usable for plants and other species.

3) If the acidic water is exposed to dolomite, it can cause dissolution of the calcium carbonate minerals and the formation of dissolution cavities. The overlying material may fall into these cavities and this can cause structural damage to buildings. The world famous Cradle of Humankind is also threatened due to the dissolution of dolomite as this is the lithology that hosts the area's fossils.

To prevent continuous and indefinite AMD formation the acid producing minerals must be removed from the natural system (Akcil and Koldas, 2006). Presently there is no cost effective way of doing this and the polluted water percolates into the ground where it contaminates groundwater over large areas (Naicker *et al*., 2003).

1.2 Acid generation

The generation of acid in and around a TSF is best described by Tutu et al. (2008). Figure 1-2 shows a model of how pyrite and other sulphuric minerals interact with oxygen and water to cause the environmental problem of AMD.

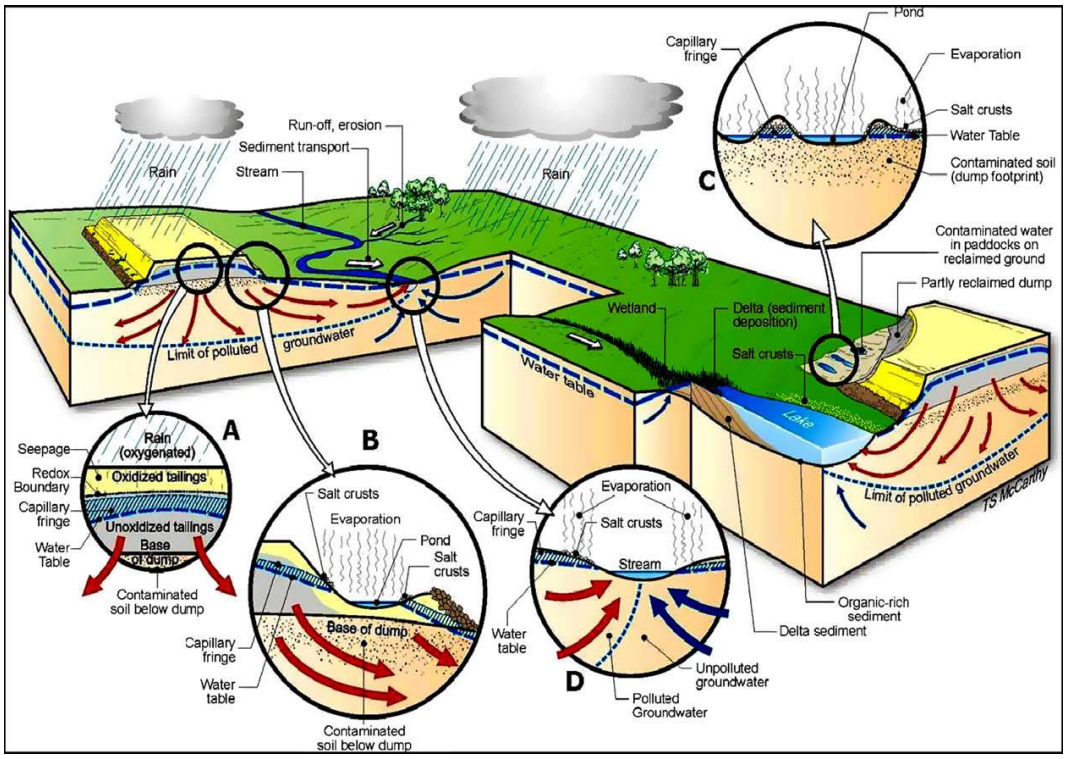


Figure 1-2: Conceptual model showing where acid mine water is generated and interacts with ground and surface water in TSFs. Some of the processes are shown in more detail in the magnified inserts, the processes on top of the TSF (A), the processes at the base of the TSF (B), the processes in cross section of a stream (C) and the processes at places on or near the TSF which floods each year (D, from Tutu *et al.*, 2008).

Sulphuric acid is generated by the oxidation of pyrite (a sulphide mineral) (e.g. Sherlock *et al.*, 1995). The chemical process of producing acid from pyrite is one of the most acid forming in nature (Nordstrom, 1979). Rainwater reacts with the pyrite in the TSF and forms sulphuric acid that percolates into the groundwater. For this reason the amount of acid produced is a function of the amount of rain that falls on the TSF. The average annual rainfall in the area of study is 650 mm (Grindley, 2014) and the climate is classified as semi-arid in the Köppen climate classification scheme.

Rainwater is contaminated with sulphuric acid and then slowly migrates through the TSF (McCarthy, 2011). In the TSF, it dissolves heavy metals as water's ability to dissolve metals is increased with decreased pH (Sherlock *et al.*, 1995). The water that permeates all the way through the TSF flows into the groundwater where it flows through the weathered aquifer through the pore spaces (Abiye *et al.*, 2011) and into the fractures in the crystalline rocks where it propagates through fractures and micro fractures in the rock (McCarthy, 2011).

Some of the rainwater does not infiltrate the aquifer and flows on the surface of the Earth as surface runoff. The groundwater that contains acid water is diluted by water that has not been exposed to the TSF material and flows into the aquifer from the surface. The dilution of the acidic water increases the pH and decreases the total dissolved solids in the water not only by mixing but also by precipitating salts as the decreased pH changes the solubility potential of the water.

Groundwater with a pH higher than the AMD facilitates the precipitation of some metals out of the groundwater, as they are only soluble in water at certain pH levels. Other metals (e.g. U) do not precipitate out in this way. The acidic water is neutralized by reactions with silicate minerals as naturally happen with AMD (Sherlock *et al.*, 1995). This is dependent on the presence of silicate minerals that readily dissolve in water and thus weather easily.

1.3 Remediation strategies

Remediation strategies are varied and the approaches usually involve some of the following: keeping the sulphur-bearing minerals unoxidised (e.g. Fraser and Robertson, 1994), keeping the acidified water away from ground and surface water (e.g. Johnson and Halberg, 2005), neutralising the already acidified water (e.g. Hedlin and Watzlaf, 1994; Fripp et al., 2000), removing the sulphur bearing minerals (e.g. Hawkins, 1994), controlling the pH of the water that interacts with the sulphur (e.g. Akcil and Koldas, 2006), controlling the amount of bacteria that can act as a catalyst for acid generation (e.g. Egiebor and Oni, 2007) or removing the contaminants (e.g. Gazea *et al*. 1996; Garcia *et al*., 2001). This can be done using plants.

According to the American EPA (Environmental Protection Agency) phytoremediation is the process by which plants are used (usually green plants), and micro fauna and flora associated with plants, to try and remove contamination, or stabilize contamination from water and soils. The soils include the sediments underlying them and the water they refer to is both surface water and groundwater. In phytoremediation, sulphur is removed from the water in the aquifer using plants.

Removing the acid-causing agent from the system is the most sustainable way of resolving the problem. Re-mining is a viable solution but economically viable grades of gold and uranium need to be recoverable. Costly processing of the ore and developing a new TSF are also required. Modern TSF plants can be constructed in such a way as to minimise the generation of AMD. An alternative way of removing (or at least immobilising) the sulphur is the use of aerobic or anaerobic wetlands. Both still require management many years after establishment, which is costly and unsustainable. Phytoremediation is an alternative, which has the advantage over some of the methods mentioned here in that it is comparatively cost effective (Weiersbye, 2007).

In phytoremediation programs plants with the ability to remove or immobilise contaminants carried in water are established in forests, woodlands or lanes. The root, stem, bark or leaf systems of the plants stabilise or extract the contaminants and impede their spread. The Mine Woodlands Project (MWP) focuses on phytoremediation techniques applicable to inorganic pollutants, such as those found in the water systems of the WSG as a result of gold mining.

The MWP is in the process of establishing woodlands made up of trees that have deep roots and large leaf areas, as well as being able to live in highly saline environments, to replace the natural grasslands in the areas around the TSF in the study area. The three most important objectives are:

a. Limiting pollution of air (dust) and water (acid mine drainage) by vegetating the surface areas of TSFs;
b. Protecting the areas surrounding TSFs by delivering a remedy to the contamination problem that is sustainable;
c. Fixing the areas surrounding the TSFs by ridding the soil and groundwater of any impurities.

To do this, four types of phytoremediation are used:

A. Phytoextraction:

The process of removing heavy metals from soils and groundwater by plants (Kumar *et al*., 1995; Huang *et al*., 1997; Blaylock and Huang, 2000 etc.). These are stored in the plant system or excreted and this can cause recontamination.

B. Phytohydraulics:

The process of drastically increasing the evapotranspiration in an area by using plants that use high amounts of water which decreases the mobility of contaminants (Hong *et al*., 2001; Sridhar *et al*., 2002; Anjum *et al*., p.79, 2012). This can be problematic in low rainfall areas.

C. Phytodesalination:

This is a process whereby plants remove salt from the area surrounding the roots and move it to their shoots (Rabhi *et al*., 2010a). This is distinct from phytoextraction as it focuses on the salts and not the metals.

D. Phytostabilisation:

The process by which plants accumulate contaminants around their roots (Mendez and Maier, 2008).

The plants that are preferred are hyperaccumulator plants that can absorb high concentrations of metals through their roots. Accumulator species (plants that store a variety and large amount of contaminants in their plant structure) are used because they can immobilise a variety of pollutants and remove more contaminants from the soil and groundwater than other species (Grindley, 2014).

1.4 Geology and hydrogeology

An understanding of the geology of the field study area is required to explain the ground water flow.

Underlying the western side of the field area are lithologies of the Ventersdorp Supergroup (2.70 to 2.75 Ga, Crow and Condie, 1988) and pieces of these lavas (float debris) can be seen in the area of study. The Ventersdorp Supergroup is up to 8 km thick and comprises three different groups that overlie the metasedimentary WSG at an angular discordance in the Klerksdorp area (Burke *et al.*, 1985). The continental flood basalts of the Klipriviersberg Group at the base are overlain unconformably by the Platberg Group of metamorphosed bimodal volcanics and immature clastic sediments with minor chemical sediments (Van der Westhuizen *et al.*, 1991). The Pniel Group conformably overlies this (Van der Westhuizen *et al*., 2006). The two members of the Pniel Group are the lower mature clastic sediment of the Bothaville Formation and the upper continental flood basalts of the Allanridge Formation (Burke *et al.*, 1985). The Ventersdorp Supergroup is unconformably overlain by the sediments of the Transvaal Supergroup (Van der Westhuizen *et al.*, 2006, Figure 1-3).

The basal formation of the Transvaal Supergroup, the Black Reef Formation (BRF), is present in the central part of the study area and underlies parts of the TSF. The BRF has metaconglomerates at its base and quartzites in the younger units. It is overlain by the Chuniespoort Group sediments (Eriksson *et al.*, 1998). These sediments are mostly chemical sediments (banded iron formation, dolomite and chert) with some quartzite and shale also preserved (Eriksson *et al.*, 2006). These are the rocks that occur in the field site and host the ground water.

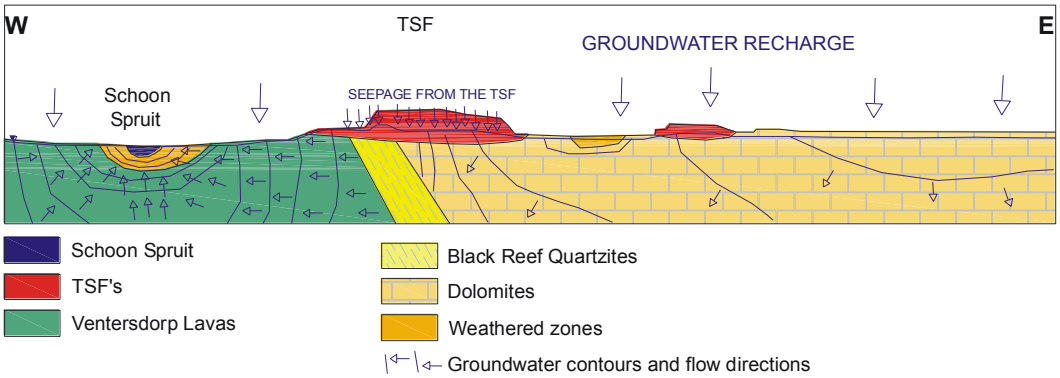


Figure 1-3: Conceptual model of the study site showing the geological stratigraphy (from De Sousa *et al.*, 2006).

The discussion of the hydrogeology that follows is based on the hydrogeology of Johannesburg that is documented in the 1:500 000 "Geological map of Johannesburg" (and its accompanying explanation, Barnard, 1999 and 2000) and the subsequent work

of Abiye *et al.* (2011). Abiye *et al.* (2011) propose that groundwater occurs in three different zones in the Johannesburg area, which has the same geology as the study area. These are: i) the weathered soil profile near the surface, ii) within the dolomites where cavities have been formed by dissolution, and iii) zones where the crystalline rock has been altered by shearing, fracturing or igneous intrusion. The geology that underlies the study area near Orkney is broadly the same as the geology underlying Johannesburg. Dolomite occurs to the east of the study area and partially underlies the TSF (see Figures 1-1 and 1-3).

The Chuniespoort Group with extensive dolomites are the most important host for groundwater in the area (Abiye *et al.*, 2011). Dissolution of carbonate minerals from acidic water results in the formation of underground cavities in dolomite. The acidic water percolates into the rocks from the surface or from another aquifer, using fractures and joints as the conduit. These caves are often filled with ground water and this type of aquifer is known as a karstic aquifer (Franke *et al.*, 1990). Ground water flow in the east and the west of the study site is different as these two areas are cut off from each other by the BRF.

The BRF does not allow water to flow through it and acts as an aquitard as can be seen in Figure 1-4 where the water flow direction is different to the east and to the west of this unit. De Sousa *et al.* (2006) used borehole data and found that the ground water in the east of the study site (dolomite and the dolomite derived soil) flows southwards. In the west the ground water (in the lava and lava derived soils) flows west towards the Schoonspruit. To the north of the TSF a water flow path exists where the water flows in a WSW direction and this is attributed (by De Sousa *et al.*, 2006) to a fracture zone that exists in the lava.

The hard crystalline lavas of the Ventersdorp Supergroup underlying the weathered profile in the west of the field area could have fractured aquifers. These aquifers can be filled with a combination of water from the overlying weathered and soil profile and water from the surface. Rain that falls on the surface that does not percolate into the weathered profile will move towards the Schoonspruit as surface runoff. This study focuses on ground water rather than surface water.



Figure 1-4: Hydrogeological model used in this study. Green symbols indicate lava, yellow cross lines indicate quartzites and the red lined area indicates dolomite. Blue lines indicate contours of equal water table level with the contours shown for the water table in mamsl. Black arrows show the direction of water flow based on head measurements in the boreholes. Coordinates are for the LO27 projection on the WGS84 datum (in metres, from De Sousa *et al.*, 2006).

Ground water may be found perched on the crystalline basement in the weathered zone or in the deeper fractured or karstic aquifers. The site geology is dominated by dolomite, lavas and quartzites, all of which have been metamorphosed (Alexandre *et al*., 2006) to the green schist facies (Frimmel, 1994), which mean these rocks form a crystalline basement. Crystalline rocks are either metamorphic rocks or igneous rocks of hypabyssal or plutonic origin (Wright and Burgess eds., 1992) and may contain fractured aquifers.

The specific storage of the crystalline basement aquifers is low and they are therefore sensitive to surface changes brought about by drought or by changing use of the surface

(Wright and Burgess eds., 1992). The amount of the water and quality of the water in crystalline basement aquifers are also dependant on the topography (on surface and the rock profile at depth), surface water flow and the soils and vegetation present (Wright and Burgess eds., 1992). A TSF, as in the study area, introduces pollutants to the environment, and changes surface topography. *Eucalyptus* trees planted for use in mines, as found in the study site, also impact the water flow. Proximity of fractured aquifers to the surface makes them more susceptible to pollutants from the surface (Wright and Burgess eds., 1992) or from the aquifer in the overburden.

The overburden in the area of study is the weathered rock of the geology immediately beneath it as is evident from the low level of relief in the area. In hot areas such as South Africa chemical weathering is dominant over physical weathering. Sediment is slowly removed to the Schoonspruit and/or the Vaal River depending on the topographic gradient. The interface between this weathered profile and solid unweathered rock is referred to as the rockhead or the weathering front and can be sharp or gradational. Water can occur interstitially in this weathered profile and this type of aquifer (intergranular aquifer) and its storage and spread of contaminated water will be the main target of this project.

1.5 Hydrogeophysics

Traditionally, boreholes are used to monitor the spread of contaminated water, such as water that has been acidified. Boreholes serve as sampling points but laterally continuous data are not obtained. Geophysics can aid in filling in the gaps between boreholes. Specifically, as Naicker *et al.* (2003) pointed out, shallow aquifers are not well understood and geophysics will help shed light on some of an aquifer's physical properties to assist in understanding the flow of AMD. This is one of the aims of this study.

There is a directly proportional relationship between total dissolved solids in water as occurs in AMD and its electrical conductivity. The use of plants to decrease the amount of dissolved solids (including sulphides) in the water will therefore increase the water's electrical resistivity.

Due to the difference in resistivity (a physical property of matter) values between contaminated and uncontaminated water, methods that measure the resistivity (such as the Electrical Resistivity method) are suitable for mapping the extent and occurrence of AMD in the aquifer (Merkel, 1972).

In this study, electrical resistivity, time-domain induced polarisation, and low frequency ground probing radar will be used. These geophysical methods should enable cheap, effective and non-invasive mapping of AMD flow through an aquifer to aid in the monitoring of the success of remediation.

In order to test the usefulness of the resistivity method for mapping AMD pollution and monitoring remediation, a representative site has been located at the west Complex of the Vaal Reefs mine in the Northwest Province (Figure 1-1). This site hosts a TSF, which is not isolated from the subsurface and acid is generated which forms a plume around the TSF.

1.6 Objectives

The objectives of this project are to establish some of the hydrogeological parameters (hydraulic conductivity) of the surficial aquifer underlying the study site to enable better information on AMD plume propagation and on phytoremediation. Geophysical methods will be applied to investigate the water table depths, the effect of the trees and their root systems on contaminants, the depth of bedrock, the distribution of the contaminant plume, and the relationship between physical parameters and the contaminant plume. Parallel profile lines, each one further away from the TSF than the previous line, will be used to show how the electrical resistivity of the aquifer changes with distance in the two distinct flow directions in the site. Parallel profile lines will also be used to measure electrical resistivity upstream and downstream in the groundwater flow from one of the *Tamarix* woodlands established by the MWP on the site.

1.7 Prospectus

This chapter has provided a background and motivation for this study and set out its objectives.

Chapter 2 sets out the theoretical and methodological context for the study. It examines the background of the use of geophysical data for solving AMD problems and explains the choice of methods employed for research, data acquisition and modelling in this project.

The processes of acquiring electrical resistivity, IP and GPR data for this project are described in Chapter 3.

Chapter 4 contains a detailed exposition on data modelling and interpretation and relates these findings to the objectives for this project. Electrical resistivity and IP data are discussed separately.

Chapter 5 is a short chapter wherein I try and use Archie's law to learn about the surficial aquifer

In Chapter 6 the work is summarised and the data are discussed in terms of Archie's Law.

Chapter 7 recommends a way forward and discusses the conclusions.

Chapter Two - Geophysics for Investigating Acid Mine Drainage (AMD)

2.1 Introduction

This chapter describes geophysical methods and their effectiveness for mapping AMD and the effects of phytoremediation. To understand AMD and to monitor phytoremediation, data on the chemical and physical properties of groundwater must be acquired. Boreholes offer a mechanism for acquiring these data.

In groundwater studies boreholes are used to study the geology, measure the total dissolved solids, electrical conductivity, chemical composition of the water, and the depth of the water table in boreholes. The greatest limitation is that the data gathered can be heavily influenced by conditions in the immediate vicinity of the borehole. The boreholes provide point data and may not be representative of the entire aquifer.

Geophysical methods can be used to acquire more continuous data on groundwater than boreholes. These data are useful qualitatively and can be used to empirically determine physical properties, which under controlled conditions allow inference of subsurface geology. In this study data gathered through borehole sampling have been correlated with data collected using geophysical methods. The methods that may be applicable to measure the electrical resistivity (the ability of material to impede the flow of current) or conductivity and chargeability in sites where AMD occurs are electrical and electromagnetic (EM) methods. Such methods can be used to determine subsurface geology and delineate the groundwater distribution and the chemical composition of groundwater (Unsworth *et al.*, 2007).

Geological properties, required resolution, depth of investigation and logistical considerations provide factors in selecting the best applicable method for a study. According to Unsworth *et al.* (2007) electrical resistivity and frequency-domain EM are best used for shallow studies. The depth penetration of these methods is, amongst others, a function of the receiver – source separation of the equipment.

In this study the factors in favour of electrical resistivity are: (1) the bedrock is expected to be found at a shallow depth of between 2 m and 11 m below the surface (De Sousa *et al.*, 2006); (2) the earth materials are expected to have electrical resistivities between 10 ohm.m and 10 000 ohm.m and would be measurable by the resisitivty equipment; (3)

the resolution of the electrical resistivity method is higher at shallow depths than the frequency-domain EM method; and (4) induced polarisation data can also be obtained at the same time using the same equipment.

2.2 Resistivity

The electrical resistivity method was developed in 1909 by the Schlumberger brothers as a prospecting tool. In the 1930s and again in the 1970s the method was refined. The refinements included development of different arrays, conversion of data to true resistivity using computer modelling (or earlier methods of curve fitting), automatic data acquisition and smart cables.

In the electrical resistivity method four electrodes are used in configurations determined by the geometry of the area under study, to inject current into the ground between two points (current electrodes) and measure the potential difference between two more electrodes (potential electrodes). The position of the four electrodes used, the measured current and the potential drop, give the *apparent* resistivity for a volume of Earth beneath the electrodes by (from Loke, 2004):

$$V = \frac{\rho I}{2\pi}\left(\frac{1}{r_{C_1P_1}} - \frac{1}{r_{C_2P_1}} - \frac{1}{r_{C_1P_2}} + \frac{1}{r_{C_2P_2}}\right) \quad (2.1)$$

where V is the electrical potential, ρ is the electrical resistivity, I is the electrical current and r is the positon of the electrodes (Figure 2-1). Apparent resistivity is the resistivity of the volume if it was electrically homogenous and these data can be modelled to obtain the actual distribution of electrical resistivity. The data obtained in this way are the apparent electrical resistivity, at an apparent depth, at an apparent location in the survey area. The apparent depth is where half the current density is beneath the data point and half above it in a homogenous half space (Edwards, 1977). This can be plotted as a section referred to as a pseudo section, which is a hypothetical section in the hypothetical homogenous half space.

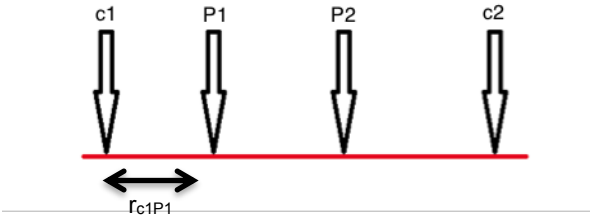


Figure 2-1: Four points where the ammeter and voltmeter will be placed on a surface. c1 and c2 show the positions of the current electrodes and P1 and P2 the positions of the potential electrodes. *r* is the distance between the different electrodes (one example shown).

The four electrode system is used because if the same electrodes are used for current and potential at the same time, there is high electrode polarisation potential. This is also true when an electrode is used as a potential electrode shortly after it was used as a current electrode. Modern electrical resistivity data acquisition systems acquire their data in such a sequence as to give an electrode time to lose the polarisation before being used as a potential electrode.

Different arrays (geometric combinations of potential and current electrodes) are used to measure apparent electrical resistivity (Figure 2-2). A geometric factor can be defined (Table 2.1) where *a* is the potential electrode spacing and *n*, in meters, the current electrode spacing as a multiplier of *a*. The signal to noise ratio is related to this geometric factor and for large *n* values Wenner-Schlumberger data suffer from high noise content. This is even more pronounced for dipole-dipole data. The physical premise on which the geometric factor is based appears from Equation 2.1 above, where the potential for the positions of the current and potential electrodes was defined.

The use of different arrays for different targets is an area of on-going research. Some of the approaches that have been used are: (i) the use of combined inversion, (ii) the use of non-standard arrays, and (iii) combined acquisition of standard arrays to try to get the maximum data for a given (sometimes unknown) geology. The Wenner alpha array is most sensitive to horizontal resistivity variations and it has high noise tolerance. It also has low spatial resolution due to the small amount of data acquired and is not the most sensitive to mapping vertical resistivity variations. The dipole-dipole array acquires the most data points but has the limitations from noise discussed above.

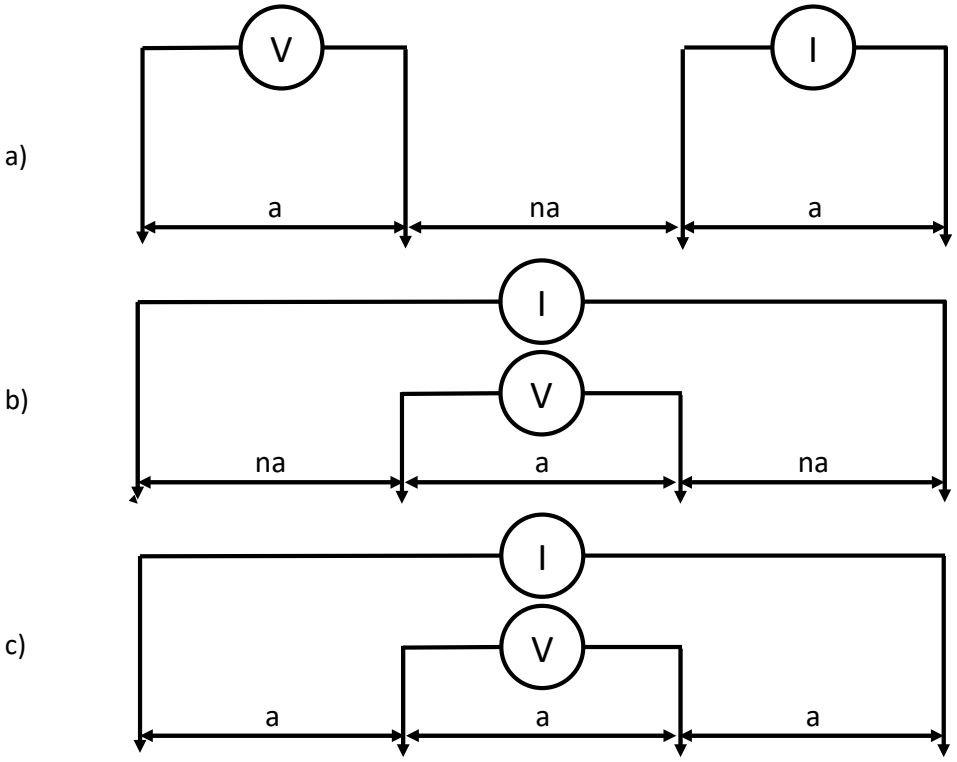


Figure 2-2: The three most common array types for acquiring electrical resistivity data. For the dipole-dipole array the current and potential electrodes are separated by a distance *a* and two dipoles are separated by *na* (a). For the Wenner Schlumberger array the potential electrodes are separated by a distance *a* and the current electrodes are separated by a distance *na* (b). The Wenner alpha array is a special case of the Wenner Schlumberger array with *n=1* (c).

Table 2.1: Geometric factors and proportionality of geometric factor on *a* and *n* spacing of some simple and common arrays.

Array	Geometric factor	Geometric factor proportional to:
Wenner Alpha	$2\pi a$	a
Wenner Schlumberger	$\pi n(n+1)a$	a and n^2
Dipole-dipole	$\pi n(n+1)(n+2)a$	a and n^3

Perren (2005) modelled simplified geology and tested and ranked different arrays for how well they would resolve an ideal model. She ranked the dipole-dipole array the highest of the standard arrays for mapping vertical boundaries, undulating boundaries, and for a model dry soil overlying bedrock with the water table in either the soil or the rock. The good performance of the dipole-dipole array in all these different settings was attributed to the high number of data points. Perren did not, however, add synthetic noise to any of her models. When noise is present it is best to use a simple comparison of the three most common arrays (Table 2.1) as a guide. In this study the Wenner

Schlumberger and dipole-dipole arrays are used as combined they give the maximum number of data points or a large number of data points with high noise tolerance.

Certain types of geological materials are electrically very noisy and measurements on such materials are hard to interpret. There is also a difference in apparent resistivities measured along strike and across strike of a geological body. Across strike is called Transverse Resistance (T) and along strike Longitudinal Conductance (S) and the differences in values constitute the electrical anisotropy of the medium. As the T and S directions are not always known a mixture of the two is frequently encountered which can also lead to confusing results especially when the anisotropy is profound. In the case of profiling in this study, the data are assumed to only vary along the directions in which the measurements are made, although earth is three-dimensional and anisotropic. A further two assumptions are made with the electrical resistivity method. Firstly, it is assumed that the Earth is a linear system. This is only correct when electrical resistivity is constant for the frequencies of injected current used in the experiment and when dielectric polarisation does not occur in the same material. These are polarisable materials, which will lead to a decreased apparent electrical resistivity (Revil and Glover, 1998). The second assumption is that the magnetic field induced by the electric field (Faraday's law of induction) is negligible. This assumption is only correct when the material in which the field lines exist has low magnetic susceptibility as expected on the study site.

The physical property contrast the electrical resistivity method is measuring is the conductivity (or its inverse, resistivity) and this is influenced by the presence of AMD in the way shown schematically in Figure 2-3. Typical acid mine water is plotted at point A and the diagram shows how the pH and the conductivity of this water will change when the water is subjected to various processes (e.g. evaporation, dissolution etc.). The diagram was drawn to explain the effects of processes as shown by lines (vectors) named for the processes on the diagram.

Electrical conductivity and pH will change along the line AB as acidic water is diluted by adding fresh water to it, while evaporation (removing fresh water) will change the properties along AC or AE depending on the saturation of the fluid with an electrolyte (Tutu *et al.*, 2008). Rainwater can percolate into the aquifer without encountering the

TSF in a field area. Dissolving salts into the water will result in the properties changing along either the AD or AF vector depending on whether the salts are acid producing (Tutu *et al.*, 2008). If the fluid is oxidised by being exposed to atmospheric oxygen the properties will change along vector AG (Tutu *et al.*, 2008). This can happen where plant roots increase the amount of oxygen that infiltrates the ground. Finally, neutralisation of the acidic water can occur by either precipitating metals out in a wetland or treating the water with lime (Tutu *et al.*, 2008). The properties will change along AH or AI for these two processes. Acid can also be neutralized by encountering naturally occurring materials such as silica and carbonates (Sherlock *et al.*, 1995), not shown but is expected to change the relationship along the vector AI.

Typically fresh groundwater in the area of the study has a conductivity of 0.05 S/m or 2000 ohm.m and AMD contaminated water a conductivity of more than 1 S/m or 1 ohm.m (Tutu *et al.*, 2008).

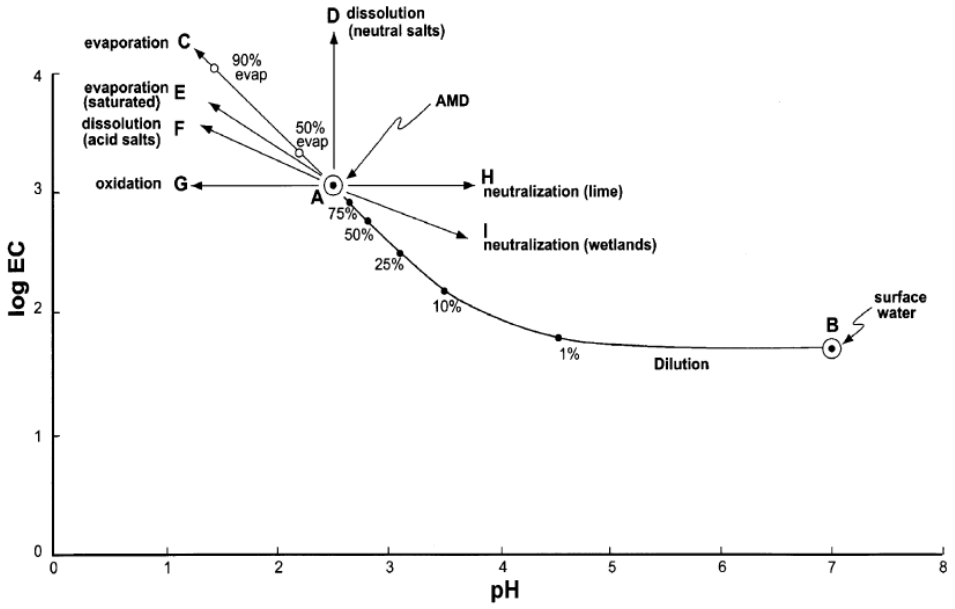


Figure 2-3: Schematic diagram showing how electrical conductivity (in log S/m) and pH of acidic water change when they are subject to different processes. Point A represents acid mine water (from Tutu *et al.*, 2008).

For EM to be useful for generating data for studying AMD, the chemical composition of the matrix material and the physical condition (porosity and permeability) must be consistent over the aquifer. In a homogenous water-bearing material, changes in electrical conductivity of the geology can be a measure of either the change in quantity

of pore water or the conductivity of pore water or a combination of both (Telford *et al*., 1990, p. 286). The relationship between the electrical resistivity of pore water and the measured apparent resistivity of the aquifer in which the pore water is contained is not well understood. An empirical relationship exists where these two values are concerned. This is known as Archie's law.

$$R_{rock} = \tau p^{-c} Sat^{Sat_{exp}} R_{water} \quad (2.2)$$

where R_{rock} and R_{water} are the electrical resistivities of the rock and the pore fluid, p is the porosity, Sat is the saturation of the aquifer, Sat_{exp} is an exponent related to the infiltration of fluid throughout the rock, c and τ are factors that describe the geometry of the pore spaces in the aquifer (Rucker, 2010).

Archie's law is different for each aquifer and some of the factors can change over time. Changing the porosity, fluid content, resistivity of the contained fluid, cementation of the grains or the sorting of the grains will influence the resistivity of the Earth material (Campbell and Fitterman, 2000). Resistivity of the pore water changes with the temperature of the water and the type and concentrations of cations and anions that are in the water (McCleskey *et al.*, 2012).

For two geological settings that have the same moisture content, porosity and cementation but different pore water resistivities, the difference between the resistivities of the two materials can be the same order as the differences between the resistivities of the fluids, unless the porosity of the unit is really low. The resistivity of groundwater that has not been polluted by acidic mine water could be an order of magnitude different from water that has been polluted (Merkel, 1972). Other parameters that influence the Earth material resistivity could also change over the interface between polluted and unpolluted water. For example, acidic water can dissolve salts precipitated between grains. This can make it difficult to delineate the difference between normal and acidic groundwater accurately as the relationship between electrical conductivity and pH is complex (e.g. Merkel, 1972).

Merkel (1972) used the electrical resistivity method to delineate aquifers contaminated with AMD in Pennsylvania near coal mines. The difference between the resistivity of water contaminated by AMD and uncontaminated groundwater allowed for this. In that

study, due to large resistivity differences, an array was used with the current source for the resistivity method, placed down boreholes. The relationship between formation and water resistivity was assumed linear but not measured.

By the mid 1980s electrical resistivity acquisition systems were capable of surveying multiple electrodes and the computer power to process these data was available. This gave rise to the development of tomography imaging, or, in the case of 3D and time lapse measurements, imaging. The simplicity of measuring equipment and computers in the 1970s and 80s only allowed for profiling and sounding methods.

Ebraheem *et al.* (1990) used the resistivity method to obtain a model of TDS distribution at a site contaminated with acid producing waste by using the technique as a profiling and sounding tool at an inactive coal mine in Indiana. They used empirical relationships between TDS and formation resistivity to obtain the model. The relationship between formation and water resistivity was obtained by correlating both to a calculated total dissolved solid, and was found to be linear.

Yuval and Oldenburg (1996) used the electrical resistivity method (along with induced polarisation) on the TSF itself to determine a model of the TDS distribution beneath the dump in their study. The site was located in Northern Ontario at a layered igneous intrusion mineral deposit. The relationships in Ebraheem *et al*. (1990) and Merkel (1972) were used to correlate formation (or geologic) resistivity with TDS.

According to Paterson *et al.* (1994) mining companies often use the resistivity method for AMD preferential flow path or TDS distribution mapping but these results are not published and it is not clear how the data are used. Modern multi-channel systems acquire data for many profiles at virtually the same time and automatic and semiautomatic inversion schemes improve data modelling processes.

A good example of an extensive 3D survey was completed at a disused goldmine in Montana and was reported by Rucker *et al.* (2009). The survey had a huge amount of data points and a combination of surface and down hole electrodes were used. The modelled resistivity and TDS had a linear relationship.

Combining electrical resistivity data acquired in profiles (2D) and in grids (3D) as Bridge

et al. (2015) did near Melrose Mining District, Ottawa County, Oklahoma, allows for mapping of the entire plume emanating from a TSF. The size of the area affected by AMD in that study is small and is easily mapped using a couple of lines of geophysical data. The study, much like the one in this paper, shows that geophysics is useful as a first look tool into an area to obtain a stronger map of AMD plume propagation. It was shown that AMD affected groundwater is replied by an aquitard at about 10 m depth.

Olenchenko *et al*. (2016) combined two-dimensional electrical resistivity readings into a three-dimensional mesh and inverted the data to obtain a three-dimensional model of electrical resistivity next to a TSF in Ursk village, Kemerovo region, Russia. They used this model to show that acid mine water mixes with groundwater at 20 m depth. This study is pertinent to what is described in this paper as the combination of geochemical and geophysical data are used. It differs in two important ways. Firstly, more data were acquired and only one plume emanating from the TSF were studied. Secondly, the data was inverted using only the most basic inversion workflow. It does, however, show clearly the advantages of mapping acid mine drainage *in situ* using geophysical methods.

The relationship between resistivity and environmental parameters cannot always be described using simple laws because of the complex interaction of various factors (ion concentration of pore water, temperature, pore size and pore interconnectedness). This study aims to demonstrate how well modern electrical resistivity methods and technology fare in establishing plume geometry and remediation success from the geophysical data correlated with borehole data near a TSF from a Witwatersrand gold mine.

2.3 Induced polarisation (IP)

Resistivity data are acquired ideally when Earth is a linear system, as discussed in the previous section. Ions flowing in rock and weathered material do so uninhibited by interaction with the rock or the porous medium in which they occur. In certain geological conditions this is not the case and ions will not start moving or stop moving immediately when an electromotive force is applied to or removed from the geological unit in which they occur. This phenomenon can give valuable geological information and the study of this is termed the induced polarisation (IP) method. IP data should always

be considered when doing resistivity surveying in that the apparent resistivity will be undervalued if a non-polarisable subsurface is incorrectly assumed.

2.3.1 Chargeability

The physical property measured and solved for is chargeability. Seigel (1959) states that chargeability is an intrinsic property of a geophysical body. Practically, ascertaining chargeability of a bulk unit depends on the experiment's ability to measure the entire decay curve and remove certain noise effects from the data. This is not always possible and the time windows after current switch off are studied together to establish a response that can be linked to the geology. Two different mechanisms are proposed for IP effects. They are:

i. Membrane polarisation, which occurs where clay minerals are present; and
ii. Electrode polarisation, which occurs where conductive minerals are present.

Both mechanisms are sometimes present but electrode polarisation has a much larger IP effect than membrane polarisation. Rocks that are not considered chargeable also show some small IP effects. If electrode polarisation is present the measured IP effect is a combination of the natural IP effects on all materials, the IP effect of membrane polarisation and the IP effect of electrode polarisation. The whole Earth IP effect also affects each discreet measurement (Soininen, 1984).

Measurements of the IP effect are taken between two electrodes as a fraction of the maximum potential reached in the unit that was charged. Current is injected into the ground (using two other electrodes) and is maintained for a defined period, before it is switched off. The time of the injected current is important as the mathematics assumes that the medium has been charged for an infinite amount of time. Physically this can mean that all the dielectric effects have been made to move ions and electrons as far as they will go. Sumner (1976, p.5) proposed a diagram (Figure 2-4) to demonstrate the macroscopic effects of chargeable earth materials. After a current has been applied the instantaneous measurable potential is known as the instantaneous voltage. After applying this current for some time the material is charged and has an electrical potential of the sum of the instantaneous potential and the stored up potential. When the current is switched off the potential drops to the secondary potential, which is the

potential stored in the chargeable material. This is the quantity sought in the IP method, but in general it is not possible to measure this.

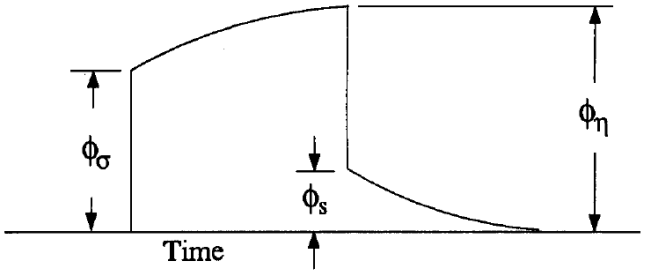


Figure 2-4: Theoretical IP response showing the secondary voltage (φ_s), the primary or instantaneous voltage (φ_σ) and the sum of these two (φ_η) (from Oldenburg and Li, 1994).

Firstly, the current is switched on and the potential difference over an element is instantly measurable as the primary voltage. This is the potential used in electrical resistivity. For chargeable media the total potential reached after an infinite (or sufficient) amount of time is the potential drop due to the electrical resistivity and the chargeability of the medium. The material is charged at this point. When the current is switched off, the potential falls to the secondary potential, the potential due to the chargeable nature of the subsurface. The theoretical IP response (Figure 2-4) is an idealisation and does not consider noise; especially electromagnetic induction effects (eddy currents) that are present in time just after current switch off has occurred.

The potential after switch off can be measured as integrals over time windows and is normalised by the potential used for the resistivity method. The exact length of time-windows are not standardised which leads to different surveys not being comparable. There exists a standard in the literature called the Newmont-standard (after the Newmont company) that measures this integral between 0.15 and 1.1 seconds after switch off. In Telford *et al.* (1990, p. 584) three tables with chargeabilities are given, two of which used an input current time of 3 s and integrated the potential in the off time over a full second.

For this study, three sources of IP signal could potentially be present. Firstly clays in the soil layers could give an IP response and because the presence of these minerals will influence the resistivity measurements it is important to measure the IP response. For the phytoremediation project it is envisaged that some of the trees remove

contaminants from the groundwater and store these in their plant mass or in and around their roots. This could also potentially give an IP response. Finally AMD affected groundwater itself could potentially show an IP response. High frequency data in laboratory measurements (Figure 2-5) show a meaningful response can be seen at frequencies from approximately 100 to 100 000 Hz. The time-domain and frequency-domain methods are not equivalent (Van Schoor *et al.*, 2009) but time-domain measurements are more common and it would be useful to see if an aquifer containing AMD contaminated water can be mapped with IP.

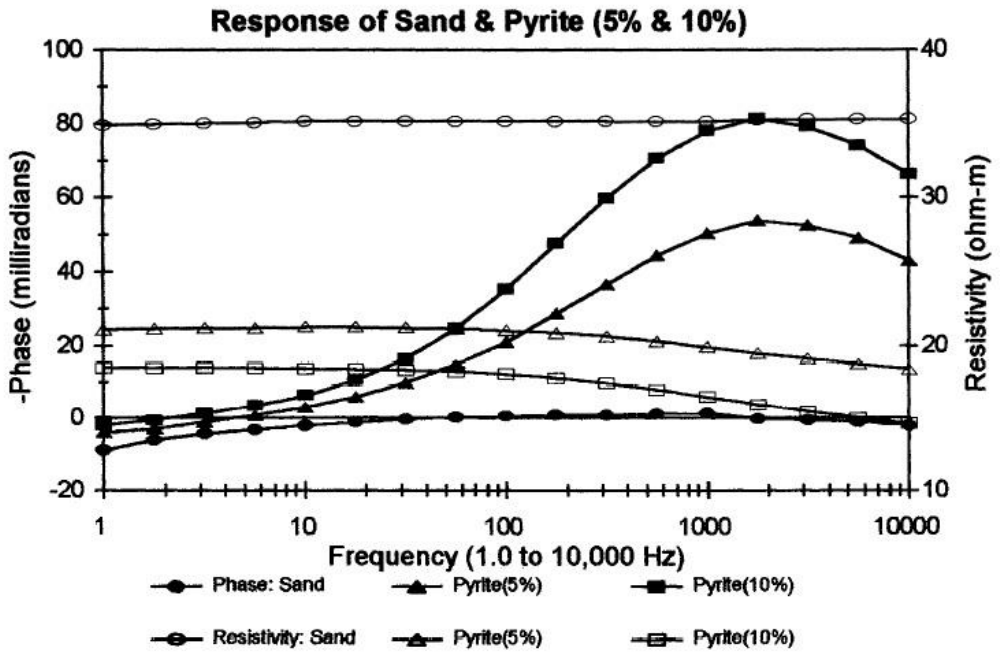


Figure 2-5: Phase response (in milliradian) of laboratory prepared samples to frequency-domain IP measurements for four different samples prepared and tested in a laboratory environment. The filled symbols are showing the phase (primary vertical axis) and the unfilled symbols the resistivity. The three samples contained 0%, 5% and 10% pyrite respectively and the remainder of each sample being sand and water (from Gudjurgis *et al.*, 1997).

Anderson and Keller (1964), Wardlaw and Wagner (1994) and Yuval and Oldenburg (1996) mapped sulphide concentrations in tailings dumps. The IP data for this study are acquired in between the TSF and surface water bodies and no examples of this exist in the literature.

IP data can be acquired in the shallow subsurface for soil mapping. In the next chapter the data acquired for this survey will be presented. The data quality is extremely poor

assessed on the data precision. Loke (2004) states that the greatest problem with using low power electrical resistivity equipment (such as the ARES system) is that the injected current is extremely low and that natural telluric currents are possibly impact-measured values. Loke (2004) states that two ways of assessing whether the data are usable is if either the resistivity or the chargeability pseudo sections are noisy. Furthermore, values of 1000 mV/V are reported by him as indicative of a (then) new trend to use multi-channel battery operated equipment incorrectly as IP instruments in engineering, environmental and hydrogeological applications and should not be modelled. Some of the manufacturers (e.g. American Geosciences Institute) present examples of clay, pollution and water table mapping, where the resistivity data alone could not solve the problem and the IP data have helped to solve the geophysical question.

2.4 Equipment

The School of Geosciences, University of the Witwatersrand, has an ARES electrical surveying system that injects current and measures potential drops between electrodes. The system utilises a line or a grid of electrodes. Two electrodes are positioned as poles for the applied electrical field and two others as poles for measuring voltage from which the resistance is determined. The geometry allows the system to calculate the apparent resistivity of each reading on the profile. Repeating the measurements allows for a measurement of the standard deviation of the apparent resistivity.

Fiandaca *et al*. (2012) note that modern data acquisition equipment repeats and sums the data and reverses the injected current direction. This is done to minimise the electrode potential build up at the interface between electrodes and the Earth, to remove random variation and to sum out telluric current, but this is not always helpful in IP studies.

The accumulated charge does not have the opportunity to decay fully when the process of reversal and stacking is used and the differences are accumulated (Figure 2-6). Fiandaca *et al*. (2012) propose that the decays might take “tens of seconds” to fully disappear and the more pulses are used (Figure 2-6b) the larger the problem becomes. This is not possible to mitigate with commercially available battery-powered data acquisition equipment but ideally the current should be switched off and allowed to decay completely before measurements are taken in the opposite direction.

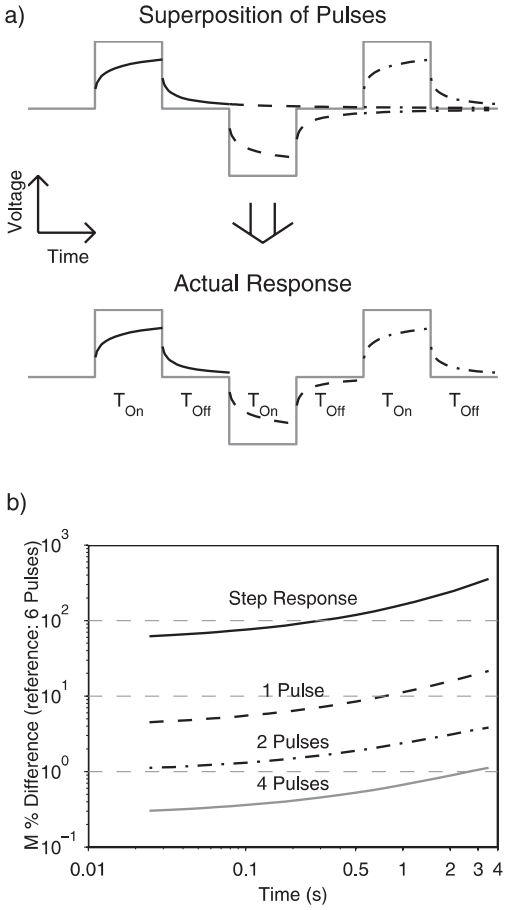


Figure 2-6: Additive noise from stacking when not enough time has been allowed for chargeability to decay fully. The difference in the expected to actual responses (a) and the percentage difference for each increasing stack (b, from Fiandaca *et al.*, 2012).

The precision of the measured data is recorded by logging the standard deviation of the measurements for IP and resistivity data. The most common way of establishing the accuracy of the data (and the required fit and misfit between observed and calculated datum points) is an assumption of the accuracy made from the precision. The standard deviation is given in percentage of the apparent resistivity by:

$$SD_{\%} = \sqrt{\frac{\sum_{i=1}^{N}(o_i - \hat{o})^2}{N}} \tag{2.3}$$

where $\hat{o}$ is the mean of the readings. If another reading is taken it would be within the SD defined bound of the mean 65% of the time, if the data are normally distributed.

Apparent electrical resistivity data are two steps removed from the geological reality. The apparent resistivity data must be converted to the actual electrical resistivity distribution in the Earth. Then the electrical resistivity distribution in the Earth must be

converted to geology. In the case of ERT and IP an electrical field and its propagation through the Earth are studied. How the Earth responds to electrical fields is determined by electrical properties that materials of the Earth exhibit. The first step is achieved through modelling. The second step requires interpretation of the model generated in the first step.

Unique models, in general, cannot be obtained and the possible variations need to be considered. After a realistic physical property model is obtained different geological materials are assigned to different parts of the model through interpretation.

2.5 Modelling of electrical geophysical data

To obtain the true resistivity distribution of the Earth from the measured apparent resistivity happens by modelling. Models of electrical resistivity distributions are created and the response of such a model is calculated and compared to the measured values of apparent resistivity. In this way realistic models can be generated. By taking this information and combining it with surface geological, borehole, or other geophysical data, models of the subsurface geology can be constrained and a geological interpretation can be made.

The resistivity in the Earth can vary abruptly or smoothly and any model must be allowed to take on any shape to reflect this. For this reason more model parameters are usually chosen than there are data points available. It is thus impossible to predict the observations uniquely as the problem is over determined and modelling must be done using optimisation.

Inversion algorithms are used to minimise the difference between calculated and measured apparent electrical resistivities. The model space can be built into:

i. Rectangular blocks (cells). The electrical resistivity for each cell is then solved; or
ii. Different layers that are continuous in their electrical resistivity and depth. The electrical resistivity for each layer is then solved; or
iii. Different layers that are fixed. The depth to layer boundaries are then solved.

All these methods require some input or prior knowledge. The software used in this study splits the model space into different rectangles and assigns resistivity values to each rectangle.

The model parameters (model resistivity values and positions of rectangles) are converted to apparent electrical resistivity values so that these can be compared to the measured apparent electrical resistivity values. The forward model can be written as:

$$\nabla.[\sigma(x,y,z)\nabla\phi(x,y,z)] = \frac{\partial j_c}{\partial t}\delta(x',y',z') \tag{2.4}$$

where σ is the conductivity, Φ the electrical potential at x,y,z and, j_c is the current density. The source of the field is a point source located at x',y' and z'. Appropriate boundary conditions need to be adhered to for the model.

A measure of the difference between the observed and predicted measurements are required and can be defined. Either the L_1 norm or the L_2 norm is typically used. The L_1 norm is:

$$L_1^{Norm} = \sum_{i=1}^{N} o_i - c_i \tag{2.5}$$

where N is the number of data points and o and c are the observed and calculated data points at each rectangle in the model space. This formulation of the data misfit is used when outliers are present in the data. The L_2 norm is:

$$L_2^{Norm} = \sum_{i=1}^{N}(o_i - c_i)^2 \tag{2.6}$$

with o, c and N as before. This is the most commonly used formulation of the misfit and allows for a smoother model than the L_1 norm.

It has been stated here that the data as measured are not perfectly accurate. The objective function can be modified to allow for this inaccuracy:

$$L_2^{Norm} = \sum_{i=1}^{N}\frac{(o_i-c_i)^2}{\sigma_i} \tag{2.7}$$

where σ is a measure of the accuracy of the measured point. Models should predict the observed data to the same accuracy as the original measurement. The measured data are under or over utilised by predicting the data to a more or less accurate degree than

the measured data. Over utilising the data by allowing the misfit to become smaller than the accuracy of the data will produce a model less smooth than the data permit (Constable *et al*., 1987).

2.5.1 Inversion

Most inversion schemes used for electrical resistivity data are linearized and then optimised (e.g. Occam's inversion, Gauss-Newton etc.). Linear inversions are strongly influenced by the choice of starting model (Oristaglio and Spies, p.581, 1999). A series of different parameters (including different starting models) should be used in order to obtain reliable models. The algorithm used for modelling in this study (discussed below) allows the user to choose between initial models that are the apparent resistivity section, or a homogenous half space. The default setting is to use a half space with an apparent resistivity equal to the average apparent resistivity of the measured data, but a half space with any resistivity can be used. Through experimentation it was determined in this study that the differences obtained from the two default starting models are negligible.

Many different models can explain the data equally well. A quantitative way is needed to distinguish between these models to overcome the challenge of non-uniqueness. The model objective function (the function the inversion is trying to minimise) must be set in such a way that it allows for specific models to be generated. The algorithms used in this study allow for a choice of (1) the misfit between the measured and calculated resistivities to be set; (2) the smoothness of the properties in the horizontal and vertical directions to be set independently; (3) the norm of the entire resulting model to be compared to a reference model; and (4) a choice between using a L_1 and L_2 norm for the misfit calculation. These models then need to be generated.

The model obtained from the inversion needs to be assessed so that the models obtained (and interpreted) only contain features that are necessary to explain the measured data. As the initial model can influence the models that the inversion results in, Oldenburg and Li (1999) propose using two vastly different starting models, and only interpret the parts of the resulting models that are the same. The justification for this is that features obtained in both models by both sets of initial settings are caused by the

measured data, while features that are different are caused by the choice of reference model.

Oldenburg and Li (1999) recommend the use of two different initial models where the electrical resistivity is varied by a factor of 10 to 100 for the two starting models. The difference between the two models are subtracted from each other and divided by the difference of the starting models and a value termed the depth of investigation (DOI) index is obtained in this way. The models used need to fit the data and should be realistic in terms of their model norms (Li and Oldenburg, 1994). The models must also be either smooth or change rapidly depending on the geology and the range of resistivity values in the model must reflect the range in the Earth.

The range of the apparent resistivity values measured when doing tomography can reasonably be expected to change by some orders of magnitude for most experiments and almost all survey sites. Therefore, if the actual value is used in inversion, the way the objective function is defined will bias the inversion scheme to the low resistivity values. This is because differences between low apparent electrical resistivity values and model points will be much larger in percentage terms than points with large apparent electrical resistivities. To remedy this the logarithm of the apparent resistivity is usually used in the inversion and this bias in the inversion process will be mitigated.

The steps to be followed for inversion are:

i. Choose an initial model *m*;

ii. The program calculates *c* (the model response, or the forward model);

iii. A misfit function is defined using a norm;

iv. The software calculates *J* (the sensitivity matrix); and

v. The software solves for Δm_i.

This model is added to the original model and is used in the next step as though it is the original model. The inversion ceases when Δm_i becomes sufficiently small (i.e. the inversion process converges) or when the chosen norm reaches a specified value

(usually related to the expected error in the data) or when a maximum number of iterations are completed.

2.6 Other geophysical methods

Ground penetrating radar (GPR) is a high resolution, fast and easy to deploy geophysical technique that is sensitive to changes in dielectric properties of the subsurface. Campbell et al. (1999) state that GPR has enormous potential for mapping AMD plumes. In *Groundwater Geophysics* (Kirsch, ed., 2009) mapping of pollution is made possible by the increase in conductivity and consequent decrease in depth of penetration of radar waves caused by the pollutant. This was not observed in the study site.

GPR is a high-resolution method and if the ground conditions are favourable it may be possible to obtain the permittivity of the surficial aquifer from the GPR data. If the depth of penetration is favourable in areas where the groundwater is uncontaminated, deeper depth penetration is expected from the GPR method than in areas where the water is contaminated. This is because of the change in conductivity and the resultant change in skin depth.

Frequency-domain EM equipment was taken to the field but the days scheduled for field work rained out and no experimenting was possible.

2.7 Summary

Geophysical methods are likely to be useful to map AMD and the effectiveness of phytoremediation. This is because both the contamination and remediation of water are expected to change the pore water chemistry, which results in changes in pore water conductivity.

The methods employed in this study, ER and IP, are well established hydrogeophysical tools but care must be taken with the preparation of the data for modelling and with modelling the data to mitigate against risks of over or under interpreting the data. Incorrect models will lead to invalid interpretations.

ER data are expected to be useful to map resistivity changes in the subsurface attributable to changes in pore water chemistry. In addition, if a correlation between

the resistivity of the geology and the physical parameters measured in the boreholes can be obtained, information about the aquifer can be obtained from surface by using the geophysical method instead of point data available at the boreholes, in future. Phytoremediation is expected to render water more resistive after being successfully remediated. This process will be mapped in this study using parallel surveyed lines.

IP data are not expected to be able to map the interface between contaminated and uncontaminated (or remediated) water directly. It is possible that the AMD affected groundwater shows some response measurable by the IP method. Areas where sulphides have been stored in the subsurface should also give an IP response, but the presence of clay may distort the interpretation of these IP data.

Chapter 3 - Data Acquisition

This chapter will describe the process of acquisition of electrical resistivity (ER), induced polarisation (IP) and ground penetrating radar (GPR) data for this study. In total three site visits were made to acquire data: the first for ER and IP, the second for ER and the third for ground penetrating radar (GPR) data which were very poor and which are briefly discussed in Section 3.4.

The data acquired using the methods discussed above are presented as pseudo sections or pseudo plots with the depth scale in pseudo depth in the appendix. It is not possible to interpret pseudo sections and for this reason the data are modelled (see Chapter Four).

3.1 Electrical methods along the tree roots

During the first trip in September 2013 four lines (lines 1 to 4) were surveyed using ER and IP in the time-domain. The primary aim of the first set of lines was to test what could be found in the IP data and to map the depth to water tables with the ER data. The lines were centred over trees chosen for their species type. Two profile lines (lines 1 and 2) were placed with a *Eucalyptus* tree at or near the centre of the profile and a further two with a *Searsia lancea* tree at or near the middle of the profile. Four were studied because the *Eucalyptus* trees were expected to have deep roots and the *Searsia lanceas* were expected to have shallow roots. These trees have already been the subjects of studies as part of research programmes for the Mine Woodlands Project (MWP). The positions of the four lines are shown in Figure 3-1.

In Figure 3-1 the four trees are marked by their type (*Eucalyptus* or *Searsia lancea*) and by stating if the tree roots are expected to be deep or shallow (as pointed out in the field by Suzie Grindley (personal communication, 2013) with respect to the other tree of the same species.

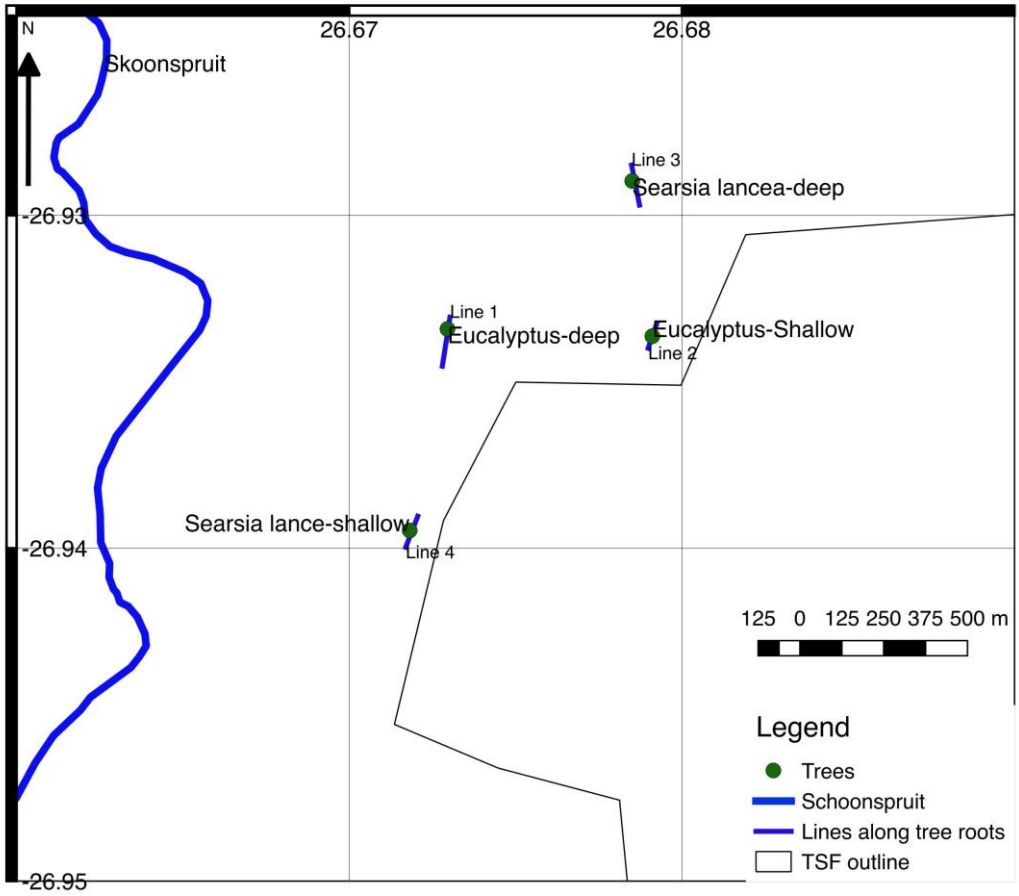


Figure 3-1: Location map of the first set of ER lines. Water flow is from east to west. Latitude and longitude are shown for the WGS84 datum.

To correlate the ER data with the borehole data, a separate map (Figure 3-2) is shown with the positions of the boreholes. SO_4 concentration (in ppm) measured in the boreholes in 2010 (see Section 5.4) is shown at the borehole positions. A surface has been fitted to borehole the data and the SO_4 concentrations at the location of the ER line are read from the contour map.

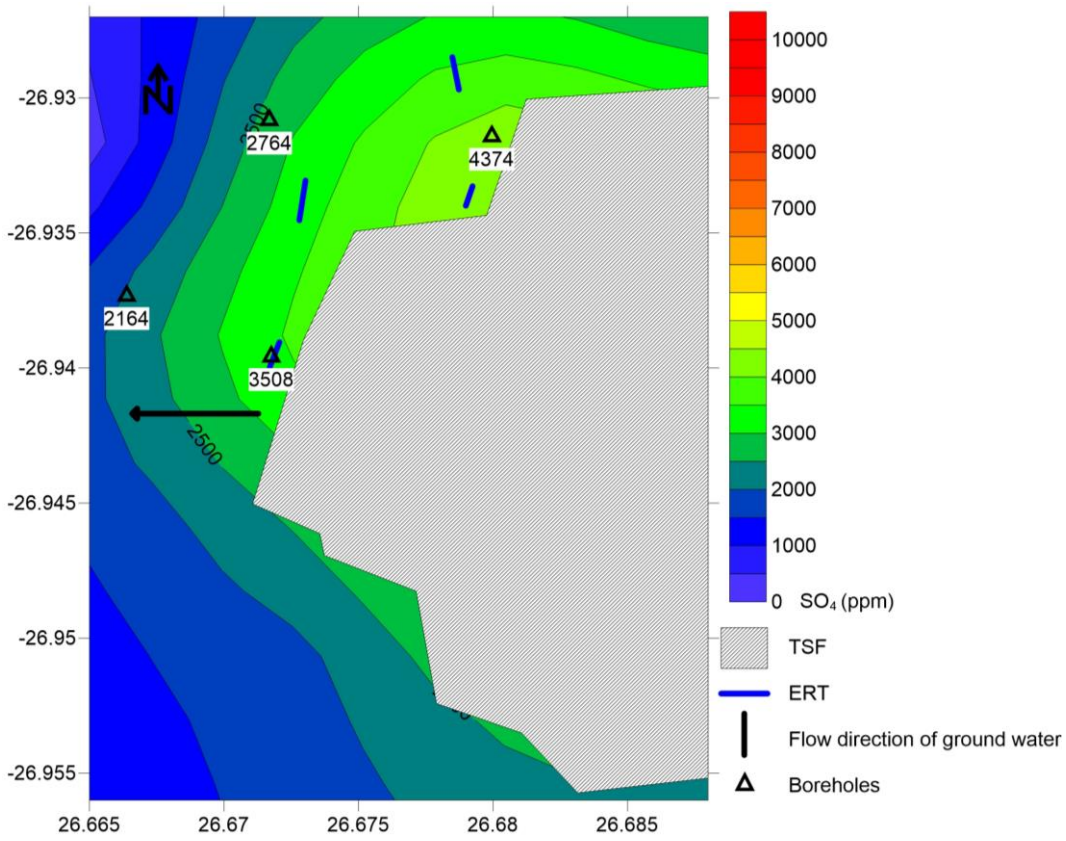


Figure 3-2: Location map of the first set of ER lines with the SO_4 readings taken in some select boreholes in 2010 contoured in colour. The legend is shown in the bottom right and the colour bar shows SO_4 concentration values in ppm. The line names have been omitted for clarity but are shown in Figure 3-1. Latitude and longitude are shown for the WGS84 datum.

3.1.1 Resistivity data

The apparent resistivity data for line 1 (Figure 3-1) were acquired using the Wenner Schlumberger array. The pulse length for the least shallow data (a= 3 m, 6 m, 9 m and n= 5) was decreased to 1 s (from 2.5 s) for the shallow data (a=3 m and n=1, 2, 3, 4 and 5) as the site had to be vacated in the middle of the afternoon.

Line 1 (Figure 3-1) was centred on a *Eucalyptus* tree. It is 165 m long and used an electrode spacing of 3 m. A total of 571 data points were collected and the average apparent resistivity for line 1 is 91.3 ohm.m. The highest apparent resistivity is 249.9 (±17.8) ohm.m with a minimum of 17.9 (±0.51) ohm.m. The average error of these readings is 6.0% (maximum 22.6% and minimum 0.3%).

Line 2 (Figure 3-1) was centred on a *Eucalyptus* tree that is expected to have a shallower root system than the tree in line 1, as it is a much smaller tree. The apparent resistivity data for line 2 were acquired using the Wenner alpha and dipole-dipole arrays. The line is 82.5 m long and an electrode spacing of 1.5 m is used to measure more data at shallow depths for the less deep tree roots. For the Wenner alpha dataset 455 data points were collected, the average apparent resistivity is 15.7 ohm.m and the average error of these readings is 1.6%. For the dipole-dipole dataset 1286 data points were collected, the average apparent resistivity is 16.9 ohm.m and the average error of these readings is 21.3%. This high error average is due to the constraint that was built into the data that the potential readings are inaccurate to 0.001 V and shows the sensitivity of dipole-dipole data to noise.

Line 3 (Figure 3-1) was done along a path that runs near a *Searsia lancea* tree. The apparent resistivity data for line 3 were acquired using the Wenner alpha and the dipole-dipole arrays. The line is 136.5 m long and an electrode spacing of 3.5 m was used because the tree roots for this tree are expected to be deeper than for the trees on line 1 and line 2. For the Wenner alpha array 246 data points were collected, the average apparent resistivity is 23.17 ohm.m and the average error of these readings is 3.6%. For the dipole-dipole array 539 data points were collected, the average apparent resistivity is 18.98 ohm.m and the average error of these readings is 81.2%. The dipole-dipole array data have large errors due to very low potentials measured in the field.

Line 4 (Figure 3-1) used the Wenner alpha and Wenner beta arrays. The Wenner beta array was used because it is faster than the dipole-dipole array. It is a special case of the dipole-dipole array, with *n=1* for all measurements. The line is 110 m long and an electrode spacing of 2 m is used because the tree roots are expected to be much shallower than for the tree on line 3. For the Wenner alpha array 488 data points were collected, the average apparent resistivity is 46.8 ohm.m and the average error of these readings is 1.8%. For the Wenner beta array 495 data points were collected, the average apparent resistivity is 46.5 ohm.m and the average error of these readings is 9.6%.

3.1.2 IP data

The SD errors are large for all the IP data in this study. The voltages recorded in the off time are low and the reason for this is the low output current (battery powered system).

The IP data are still presented here for two reasons. One is that the inverted data (presented in Chapter Four) show anomalous chargeability zones in and around the root systems of the *Searsia lancea* tree in the study site. Some plants are expected to store sulphuric minerals in and around their roots (Dye and Weiersbye, 2010) and the anomaly confirms this expectation spatially. Secondly, the data used are limited to chargeability readings that decrease for each set of four electrodes. All the decay curves for each electrode pair that do not decay for each of the measured windows have been removed to limit the amount of noisy points used for the inversion. The measure windows and the pulse lengths of the IP data are not the same for each line. This means that the data and subsequent models cannot be compared directly.

The IP data were acquired over the root systems of the trees that were expected to accumulate contaminants in and around their roots. The positioning of the IP lines is presented in Figure 3-1.

On line 2 IP data were acquired using the dipole-dipole and the Wenner alpha arrays. The Wenner alpha array data were acquired using a 1 s pulse with eight measurements over windows of 0.02 s, 0.02 s, 0.04 s, 0.04 s, 0.08 s, 0.08 s, 0.16 s and 0.16 s. The dipole-dipole array data were acquired using a 1.5 s pulse with 8 measuremnts over windows of 0.02 s, 0.02 s, 0.04 s, 0.04 s, 0.08 s, 0.08 s, 0.16 s, 0.16 s, 0.32 s and 0.32 s. The windows and the pulse length were increased, as the time in the field allowed for this to be done.

On line 3 Wenner alpha and dipole-dipole arrays were used to acquire the IP data. The data were acquired using a 1 s pulse and eight measurements over windows of 0.02 s, 0.02 s, 0.04 s, 0.04 s, 0.08 s, 0.08 s, 0.16 s and 0.16 s.

On line 4 data were acquired using the Wenner alpha and Wenner beta arrays. The data were acquired using a 1 s pulse and eight measurements over windows of 0.02 s, 0.02 s, 0.04 s, 0.04 s, 0.08 s, 0.08 s, 0.16 s and 0.16 s.

3.1.3 SO_4 concentration data

Extracting the SO_4 concentration from the coloured contour map in Figure 3-2, along the profile line for line 1 the SO_4 content should be between 3173 and 3251 ppm.

Extracting the SO_4 concentration from the coloured contour map in Figure 3-2, along the profile line for line 2 the SO_4 content should be between 4420 and 4431 ppm.

Extracting the SO_4 concentration from the coloured contour map in Figure 3-2, along the profile line for line 4 the SO_4 content should be between 3482 and 3486 ppm.

3.2 Electrical resistivity profile in the direction of the groundwater flow in the lavas

The second trip was undertaken in February 2014 with three objectives. The first was to map the depth to bedrock from between the two dumps towards the Schoonspruit (see Chapter One) as well as any changes in resistivity resulting from acid mine water. This was conducted along the direction of the groundwater flow over the lava (see Figure 1-4 for groundwater flow model). Resistivity sections were also collected (Figure 1-1) showing the variation from affected dolomite to the east of the main TSF (line 9), down to the Schoonspruit through the aquifer overlying the lava (line 5 and line 6). An additional line (line 12) was acquired to try and establish what kind of resistivities can be expected in the lava-derived soil if the pollution plume has less of an effect on the groundwater.

For the ER data and the borehole data correlation, a separate map (Figure 3-3) is shown with the positions of the boreholes. SO_4 concentration (in ppm) measured in the boreholes in 2010 (see Section 5.4) is shown at the borehole positions. A planar surface has been fitted to the data and the SO_4 concentration at the location of the ER line is read from the contour map. This is presented with the results in Chapter Four.

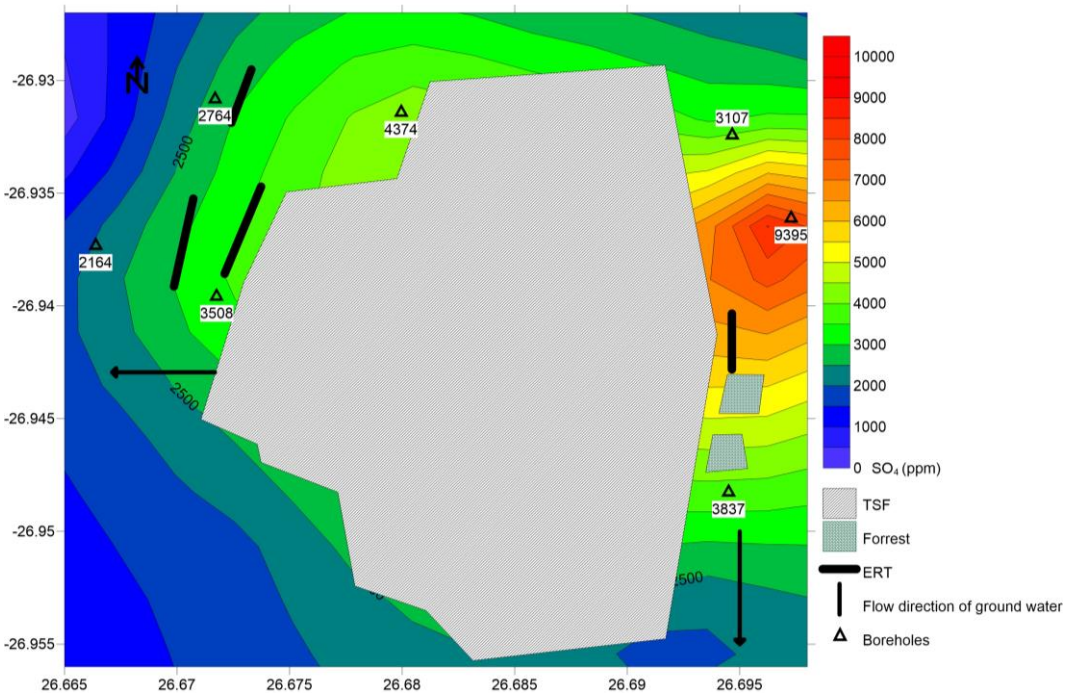


Figure 3-3: Location map of the second set of ERT lines with the SO_4 readings taken in some select boreholes in 2010 contoured in colour. The legend is shown in the bottom right and the colour bar shows SO_4 concentration values in ppm. Latitude and longitude are shown for the WGS84 datum. Line names have been omitted for clarity but are shown in Figure 1-1.

3.2.1 Resistivity data

In line 9 (Figure 1-1) the Wenner Schlumberger and the dipole-dipole arrays were employed. The line is 275 m long and an electrode spacing of 5 m is used. For the Wenner Schulmberger array 667 data points were collected, the average apparent resistivity is 324.35 ohm.m and the average error of these readings is 1.1%. For the dipole-dipole array 1309 data points were collected, the average apparent resistivity is 325.04 ohm.m, and the average error of these readings is 1.6%.

On line 12 (Figure 1-1) the Wenner Schlumberger and dipole-dipole arrays were used. The line is 275 m long and an electrode spacing of 5 m is used. For the Wenner Schlumberger array 729 data points were collected, the average apparent resistivity is 57.2 ohm.m and the average error of these readings is 6%. For the dipole-dipole array 1429 data points were collected, the average apparent resistivity is 44.2 ohm.m and the average error of these readings is 40%.

In line 5 (Figure 1-1) the Wenner Schlumberger and dipole-dipole arrays were employed. The line is 470 m long and an electrode spacing of 5 m is used. For the Wenner Schlumberger array 1569 data points were collected, the average apparent resistivity is 127.3 ohm.m and the average error for these readings is 2.6%. For the dipole-dipole array 1429 data points were collected, the average apparent resistivity is 94.5 ohm.m and the average error of these readings is 16.4%.

On line 6 (Figure 1-1) the Wenner Schlumberger, dipole-dipole and Wenner alpha arrays were used. The line is 435 m long and an electrode spacing of 5 m is used. For the Wenner Schlumberger array 1199 data points were collected, the average apparent resistivity is 318.4 ohm.m and the average error for these readings is 1.6%. For the dipole-dipole array 2331 data points were collected, the average apparent resistivity is 294.2 ohm.m and the average error for these readings is 9.1%. For the Wenner alpha array 451 data points were collected, the average apparent resistivity is 282.5 ohm.m and the average error for these readings is 1.2%.

3.2.2 SO_4 concentration data

Extracting the SO_4 concentration from the coloured contour map in Figure 3-3, along the profile line for line 9 the SO_4 content should be between 3847 and 3944 ppm.

Extracting the SO_4 concentration from the coloured contour map in Figure 3-3, along the profile line for line 12 the SO_4 content should be between 2941 and 2951 ppm.

Extracting the SO_4 concentration from the coloured contour map in Figure 3-3, along the profile line for line 5 the SO_4 content should be between 3450 and 3452 ppm.

Extracting the SO_4 concentration from the coloured contour map in Figure 3-3, along the profile line for line 6 the SO_4 content should be between 2898 and 3054 ppm.

3.3 Electrical resistivity profile in the direction of the groundwater flow in the dolomites

The second objective of the project was to map the change in groundwater resistivity from groundwater unaffected by acid water (line 11) to groundwater affected by pollutants from the TSF (line 8) to groundwater that should have undergone

remediation by flowing underneath the *Tamarix* forest (see Figure 1-1 for positions of these lines). The SO_4 concentration data from select boreholes are shown in Figure 3-4 and a coloured contour map of these (obtained from fitting a plane through the data) are also shown.

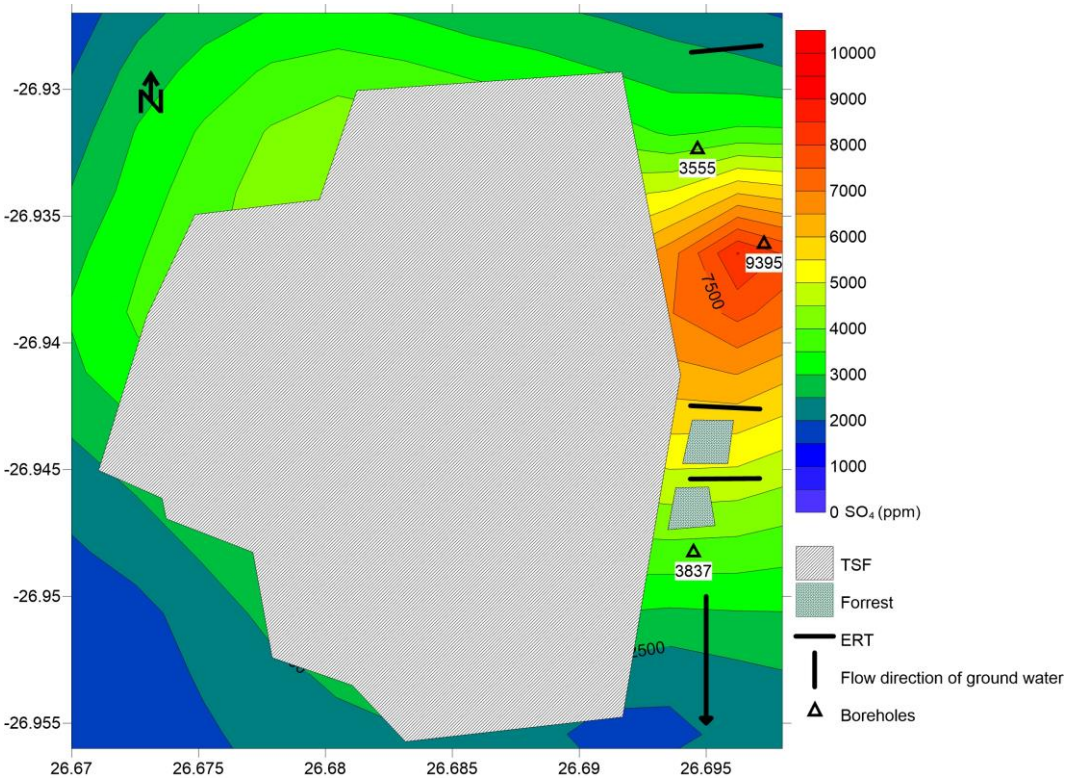


Figure 3-4: Location map of the third set of ERT lines with the SO_4 readings taken in some select boreholes in 2010 contoured. The legend is shown in the bottom right and the colour bar shows SO_4 values in ppm concentration values in ppm. Latitude and longitude are shown for the WGS84 datum. Line names have been omitted for clarity but are shown in Figure 1-1.

3.3.1 Resistivity data

For line 11 (Figure 1-1) the Wenner Schlumberger and dipole-dipole arrays were used. The line is 275 m long and an electrode spacing of 5 m is used. For the Wenner Schlumberger array 729 data points were collected, the average apparent resistivity is 1749.34 ohm.m and the average error of these readings is 1.3%. For the dipole-dipole array 1378 data points were collected, the average apparent resistivity is 1780.07 ohm.m and the average error of these readings is 1.6%.

For line 8 (Figure 1-1) the Wenner Schlumberger and dipole-dipole arrays were used. The line is 275 m long and an electrode spacing of 5 m is used. For the Wenner

Schlumberger array 729 data points were collected, the average apparent resistivity is 490.34 ohm.m and the average error of these readings is 1.2%. For the dipole-dipole array 1408 data points were collected, the average apparent resistivity is 630.09 ohm.m and the average error of these readings is 1.5%.

For line 10 (Figure 1-1) the Wenner Schlumberger and dipole-dipole arrays were used. The line is 275 m long and an electrode spacing of 5 m is used. For the Wenner Schlumberger array 672 data points were collected, the average apparent resistivity is 770.0 ohm.m and the average error of these readings is 1.2%. For the dipole-dipole array 1310 data points were collected, the average apparent resistivity is 746.0 ohm.m and the average error of these readings is 2.4%.

A third objective of the project was to map and outline the Black Reef Formation as an aquitard between the dolomite and the lava. The data acquisition of this line was interrupted due to industrial activities very near the site and the data collection could not be completed.

3.3.2 SO_4 concentration data

Extracting the SO_4 concentration from the coloured contour map in Figure 3-3, along the profile line for line 8 the SO_4 content should be between 4041 and 9294 ppm.

Extracting the SO_4 concentration from the coloured contour map in Figure 3-3, along the profile line for line 10 the SO_4 content should be between 4137 and 9380 ppm.

3.4 GPR data

GPR was acquired all around the TSF. The aim was to map more detail where the resistivity was higher and the depth of penetration subsequently increased. The positions of the scans are shown in Figure 3-5.

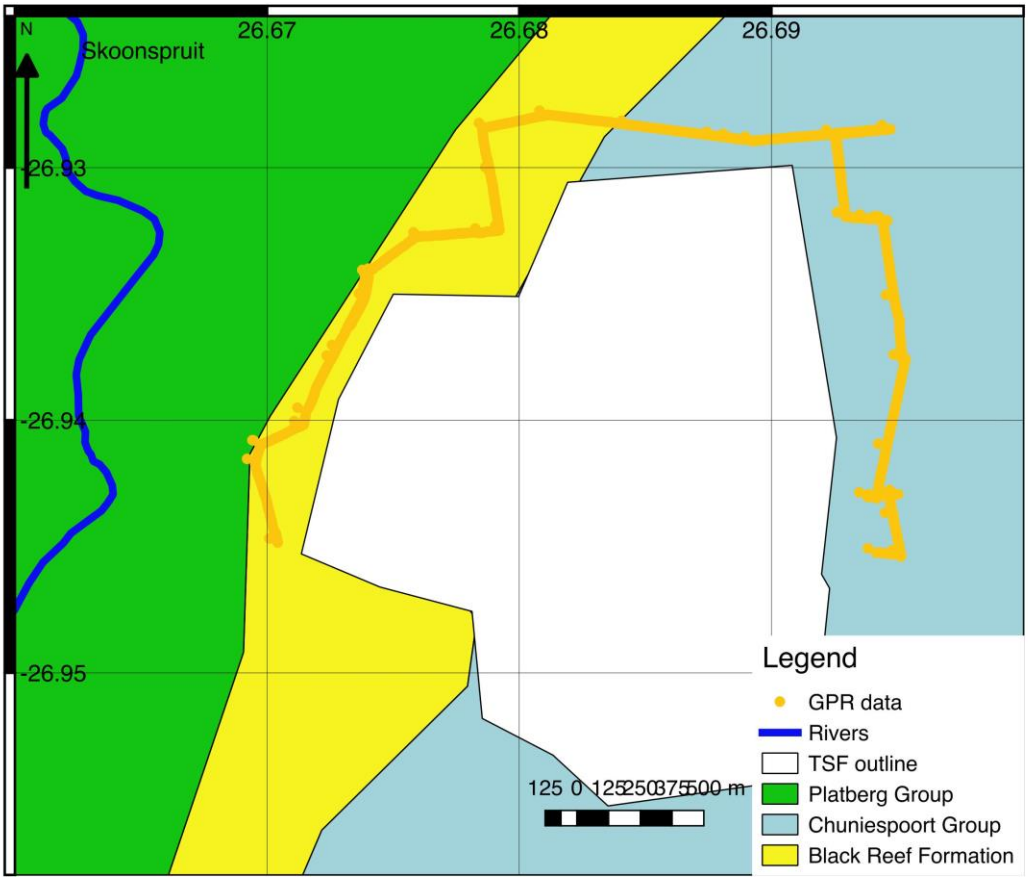


Figure 3-5: Positions of low frequency (40 MHz) GPR scans with the stratigraphy underlying the field site (SACS, 1980).

The GPR data were acquired using the GSSI data logger using a Mala 40 MHz unshielded antenna. The acquisition settings were as follows: sixty-four scans were recorded each second consisting of one thousand and twenty-four samples over 250 ns. The radar data are acquired using a function to increase each sampled waveform by a gain function. The GSSI standard gain was used with five points with a decibel of -20, -13, -5, 0 and 5 respectively. Four scans were stacked for each recorded scan to remove random fluctuations.

3.5 Summary

This chapter details the acquisition of the geophysical data. The subsections relate to the objectives of each field site visit. Positions of the acquired lines, the position of the trees (in Section 3.1) and the SO_4 concentration data from some select boreholes are presented.

The ER data are acquired as paralel profiles, and the data have been affected by noise in the manner expected of each array used. The IP data are not of good quality due to the low power source used. This has been mitigated (somewhat) by using only the data from electrode pairs where each consecutive measurement window has a decreased reading with respect to the previous window (i.e. the noise has been removed from the decay curve). The GPR data were acquired around the TSF on the three sides that are accessible on foot. The GPR data have been presented by a single radargram in the appendix, wiche demonstrates that the skin depth does not change on the site and the depth penetration of the method is insufficient to offer valuable insight into plume propagation and the effects of phytoremediation. These data will not be used any further.

Chapter 4 - Interpretation

In this chapter the two steps to solve the geological problem using the measured geophysical data will be discussed: modelling and interpretation. Measured data are firstly connected to the actual physical parameter distribution in the Earth by modelling the physical parameters and matching the theoretical response of the model to the measured data. The second step is to link the model of the physical parameters to the geology. The aim of modelling resistivity data is to explain which electrical resistivity variations in the Earth will cause the measured apparent resistivities on the surface of the Earth.

In this study the modelling is done by inversion. To mitigate the problem of non-uniqueness models (it is not possible to overcome non-uniqueness) can be infinitely complex. One approach is not to use over complex models that have more detail in them than is absolutely required by the data. Extraneous detail could be due to either artefacts of the inversion routine, or artefacts created by noise. The initial and reference models influences the convergence of the iterative optimisation problem in which the measured data should be replicated. Further, the way the models are optimised allows the modeller to give different weightings to smoothness, sharpness and size of the norms of the data in both direction and with respect to a reference model. If all reference models and all weighting functions are considered and the function that links the measured (apparent) data and model parameters (forward problem) is correct, the different solutions allow us to determine which features in the subsurface are needed to explain the measured resistivities. The manner of splitting the subsurface into model blocks is important for this work because there is a sharp resistivity boundary in most data sets where the overburden reaches crystalline bedrock. There is also an expected smooth variation of the resistivities within the material overlying the bedrock. The sharp and smooth variations are both accounted for by using both the blocky and smooth inversions. The results of this process are presented here. Many models were created for each set of measured data and the models presented here are representative of the subset of models that show features in the subsurface that are consistent through many of the models.

Each set of data (mostly two per line) needs to be inverted to obtain a model that predicts the data within the bounds of the estimated data error. The model space is generated in such a way that there are more rectangles in the model space than measurements that are available. Different inversion parameters need to be chosen (as done in this study) and the question: "What features in the model space are absolutely necessary to predict the data?" should be answered. One of the most important concepts, is that the models produced are partially a function of the inversion and specifically the reference model used. A different reference model will lead to two models that show to which depths the data mostly influence the obtained models and which features are mostly due to the choice of reference model. A second parameter that is chosen by the modeller is the type and sizes of norms to use. The model can be made to be (1) as close to a reference model as possible, (2) as smooth in the x or z directions as possible or (3) a combination of the first two. The misfit should often also be varied. In the algorithm used by Res2dInv, this is chosen directly as a percentage, while the size of the objective function for the algorithm used by DCIP2D is influenced by the choice of the chi-fact value. One way to choose the correct value for the misfit is by varying this chi fact value between two values less than one, one and two values greater than one. This allows for the construction of a Tikhonov Curve where the value of the misfit is plotted against the value of the model norm. The L-bend in the curve should be used, as this is the optimal compromise between the size of the norm and the size of the misfit

A measure of the depth to which the resistivity method is sensitive can be obtained from modelling. The depth of investigation of each line is calculated using the method proposed by Oldenburg and Li (1999). For all the models used in these depth of investigation methods, the misfit between the measured data and the modelled data (apparent resistivities) must be as small and no smaller than the average error of the measured data. This will ensure that the two models that are compared to obtain the depth of investigation do not themselves over or under interpret the data.

The misfit discussed in Chapter Two can be defined in various ways. Both equations 2-4 and 2-5 from Chapter Two have been used here. The smooth inversion (L_2 norm minimisation) in Res2dInv uses the L_2 norm for calculating the objective function, and it minimizes the model change vector squared (Loke, 2004). The blocky inversion in

Res2dInv uses the L_1 norm and optimises for the smallest size, the size of the model change vector i.e. the smooth inversion's handling of the change vector square rooted. The choice of norm is read in to the software as inversion settings.

As was discussed and motivated for in in earlier chpaters, the data accuracy is assumed to be 5%. When the inversion process calculates the misfit between the measured and calculated apparent resistivities to be less than this threshold, the inversion is ceased. Practically, this means that the number of iterations used are low (less than four in most cases), and the data dare not over interpreted.

The settings for the smoothness constrained inversion (the first model shown for each of the sections in this chapter) form a long list. These are presented in Appendix A. Variations from this is described in the text here. The IP data were modelled using the same settings.

The induced polarisation (IP) data are modelled by Res2DInv as though it is resistivity data. The model parameters and the measured data are set exactly as discussed for the resistivity data in Chapter Two. This is a common way of obtaining chargeability models.

The models are presented along with the measured apparent resistivity data that, in some cases, are different from the measured data presented in Appendix D. This is because "bad-points" have been removed. This is done by using the initial inversion settings and eliminating points where the measured and calculated apparent resistivities are different to the point where the misfit histogram does not show a decaying shape. The inversion is then run with the same inversion parameters but without the measured points. This, in the authors opinion, is a less subjective way of removing the unwanted points than the graphical method Loke (2004) proposes.

4.1 Electrical methods along the tree roots

In this section the modelling and interpretation of the four lines for which electrical resistivity (ER) and induced polarisation (IP) data are available are discussed. These lines were positioned near *Eucalyptus* or *Searsia lancea* trees, with deep or shallow roots with respect to the other. The positioning of the four lines is shown in Figure 1-1 and Figure 3-1. Borehole data are plotted in a coloured contour map in Figure 3-2. The lines are presented consecutively as they were collected.

4.1.1 Line 1: ER data near a *Eucalyptus* tree with deep roots

4.1.1.1 Resistivity data for line 1

The model obtained from the smoothness-constrained inversion (see Appendix A for the Res2DInv settings) of the Wenner Schlumberger data acquired on line 1 (see Appendix D: Figure D-2 in Appendix D with bad points removed) has a misfit of 4.5% after three iterations (see Appendix B: Figure A-1), shown in Figure 4-1a. The estimated data error is 6.0%. The model fits the data better than the average error and the percentage difference between the expected and measured apparent resistivity models is qualitatively random as shown in Figure 4-1b.

Many models can explain the measured data so different models are generated to test which subsurface features appear repeatedly and are therefore essential to explaining the measured data. Comparing models obtained from vastly different starting models also studies the maximum depth of investigation. Three *a posteriori* models with different *a priori* models are used to explain the data measured along line 1 (Figure 4-2). The first model (Figure 4-2a) is very similar to the model shown in Figure 4.1a using a slightly different algorithm. The depths of the resistors are the same and the value of the second layer's resistivity is the same. The difference in the algorithm is the use of a more flexible objective function (for the models in Figure 4-2) that allow for incorporating the standard deviation of each datum and for the minimisation of the model norm, after the target misfit has been reached. The first two models in this section (Figure 4-1a and Figure 4-2a) used the same reference model (a homogenous half space with the average resistivity of the measurements as the reference model). The next model (Figure 4-2b) uses the same algorithm as the model shown in Figure 4-2a with a reference model of 1000 ohm.m. The last model shown here uses a reference model with the same resistivity as the average resistivity of the measured pseudo section, but differs from the model in Figure 4.2a in that a norm for the objective function is used that creates models that are more blocky than the previous models.

The depth of investigation using the method proposed by Oldenburg and Li (1999) is shown in Figure 4-2 and gives an indication of the depth to which the models can be reliably interpreted. Two reference models, homogenous half-spaces that are different to each other by a factor of 10 to 100, are used in the inversion algorithm and the

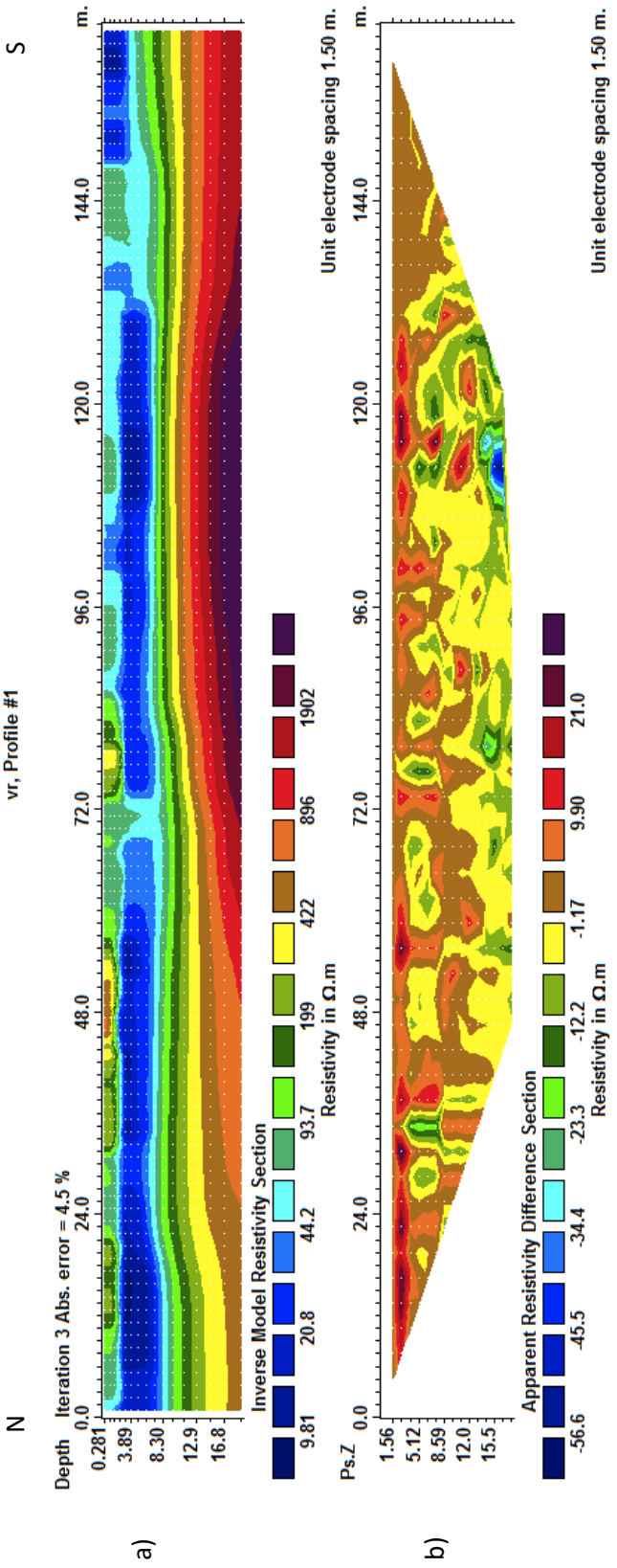


Figure 4-1: A model of resistivity (a) and the misfit in the apparent resistivity space (b) for the third iteration for Wenner Sclumberger data acquired along line 1 (Res2dInv).

resulting model resistivity of the two models are compared by subtracting the models' resistivity of the two models from each other. This result is divided by the difference of the reference model and the result for each model block is the DOI index.

Oldenburg and Li (1999) propose using a depth of investigation index of zero point one (0.1) as the cut-off data to be interpreted. No justification is given for this cut-off and the zero point two (0.2) DOI index can also be used. Alternatively, the steepest gradient of the DOI index should be used. All three options demonstrate that resistivity data become unreliable at depths greater than approximately 18 m for the experimental setup used and the geology specific to this line.

4.1.1.2 Final model for line 1

From the DOI indexes (Figure 4-2) the model should only be interpreted to about 18 m depth. The models shown in Figure 4-2 are qualitatively at all depths and quantitatively at shallow depths very similar to the model shown in Figure 4-1a. At shallow depths the the resistivity is about 20 ohm.m and at larger depth it ranges from approximately 750 ohm.m to 4000 ohm.m. For these two reason the model in Figure 4-1a is the one interpreted and is the model presented in Figure 4-3.

The model goes to a depth of 12 m. The resistivity at the greatest depth is 1000 ohm.m and higher and this is interpreted as bedrock. The rock has not been mapped extensively, because the bedrock is mostly deeper than the depth to which the method is sensitive. The rock type is lava. A zone of possibly weathered material (resistivities of 56 ohm.m to 1000 ohm.m) overlies the bedrock. The contact between the conductive material (2-7 m in depth) and the highly resistive material (c. 10 m deep) is smoothed out, because a smoothness-constrained inversion process was used to obtain the model. The smoothness constrained least square method limits the possibility of the inversion obtaining very high or very low electrical resistivities. This is directly constrained by the input parameters for this inversion process by limiting the range of the resistivity values (see Appendix A for all the inversion settings). The bedrock is well constrained in the model shown in Figure 4-2c. This model (using the conjugate gradient method to solve for the L_1 norm) is obtained by a method that obtains models where the data changes abruptly such as at a change to bedrock. From the models presented in Figure 4-2 it is

clear that the bedrock depth is approximately 10 m deep for most of the profile. At the southern end of the profile line, the bedrock is shallower.

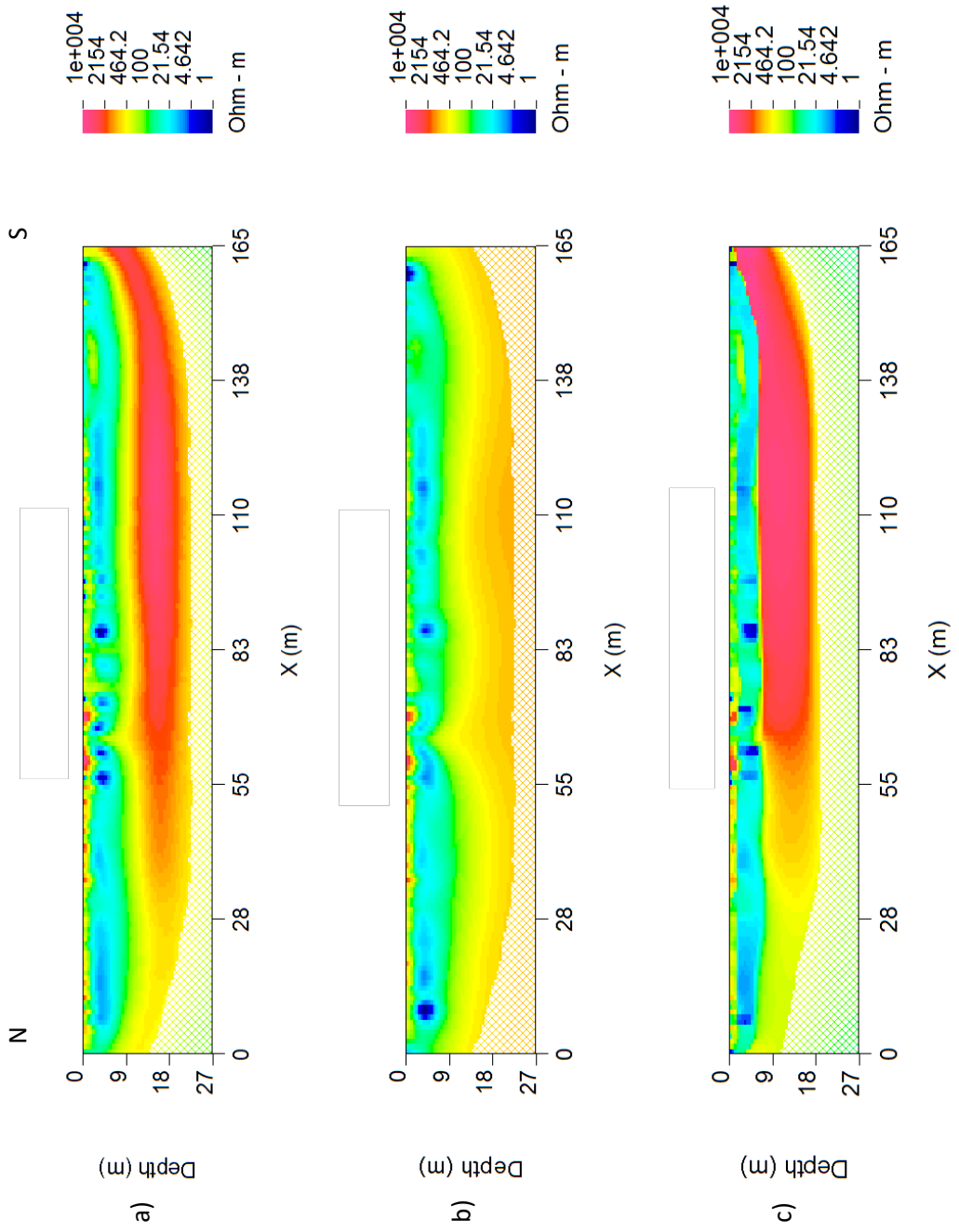


Figure 4-2: Alternative models for the data acquired along line 1 using different initial models. Homogenous half-spaces are used with initial resistivities of 53 ohm.m (a) and 1000 ohm.m (b) and 53 ohm.m (c). The model in (c) uses the Ekblom norm. The models are faded out using a DOI value of 0.1 (DCIP2D).

The zone between 2 and 7.5 m deep is interpreted as moist weathered bedrock and sediment with resistivity between 10 ohm.m and 56 ohm.m. Two zones of increased resistivity are present in the model at about 69 to 73 m along the profile and at about 138 m to 148 m along the profile. The southernmost anomaly is most likely due to the line of Eucalyptus trees running perpendicular to the profile line in the south. A 2 m layer of more resistive material overlies the moist sediment and weathered bedrock and this may be interpreted as dry soil.

An alternative possibility is that the contact between two soil units (as mapped by a soil survey conducted by Bruce Mcgleorth, personal communication, February 2014) could be associated with faster drainage and this may explain the two vertical resistive structures. This cannot explain the northernmost anomaly (from 69 to 73 m along the profile), as this is not where the soil contact is expected to occur. The northernmost anomalies could be from a small clump of trees that were planted near this area which were noted in the field.

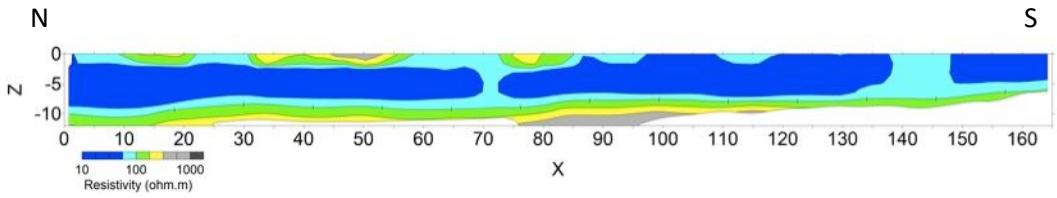


Figure 4-3: Final resistivity model for line 1.

The tree named “Eucalyptus Deep” (Figure 3-1, the tree is labelled as such as it formed part of a different study in the same field area) does not show any effects on the aquifer in the resistivity models. There is, however, at 35 m in Figure 4-1a (the raw data), a more resistive zone. Modelling the data using inversion routines with sharp (or robust) data constraints (as per the method proposed by Wolke and Schwetlick, 1988) that allow the inversion to calculate values for the model that are not smooth (“blocky”) does show this anomaly in the model subsection but only if the inversion is allowed to fit the data more tightly than the estimated error and this result was discarded as spurious.

The interpretation and some of the surface features are shown in Figure 4-4 with the final model.

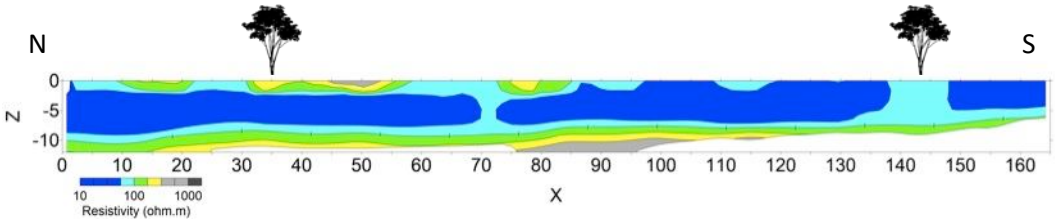


Figure 4-4: Final resistivity model with surface features for line 1.

4.1.2 Line 2: ER and IP data near a *Eucalyptus* tree with shallow roots

4.1.2.1 Wenner alpha ER data for line 2

The model obtained from the smoothness-constrained inversion (see Appendix A for the Res2DInv settings) of the Wenner alpha data acquired on line 2 in has a misfit of 3.2% after two iterations (see Appendix B: Figure A-2), shown in Figure 4-5a. The average data precision is 1.6 % is lower than the misfit for this line of data but it is expected that the accuracy of the data will be less than this precision. The raw data are shown in Figure D-2 (in Appendix D) with the model obtained from the inversion shown in Figure 4-5a.

The misfit pseudo section (Figure 4-5b) shows a trend. The data acquired with small electrode separations (shallow with pseudo depths of less than 8 m) show a small difference between calculated and measured values (between -1 and 1 %). The data from larger dipoles (deeper with pseudo depths greater than 8 m) show a larger misfit (-10 to -20%). It will be shown below that this is not problematic for this study as the data with large dipole sizes are mostly influenced by resistivity variations at depths greater than those investigated here (these have a small misfit, shown in Figure 4-5b).

An alternative model is presented in Figure 4-6 where two actions have been used to improve the model: using additional iterations, four in this case; and using the L_1 norm and minimising the model change vector as opposed to the size of the vector. Loke (1996) states that this is only an advantage if low noise content is expected in the data, as is the case for the Wenner alpha data on line 2 (Figure D-2 in Appendix D).

The advantages of this model (as opposed to the previous one) are: the data misfit is 1.5%, which is closer to the estimated precision in the measured data (1.6%) than for the model shown in Figure 4-5b; and the misfit pseudo section is random (Figure 4-6b). The

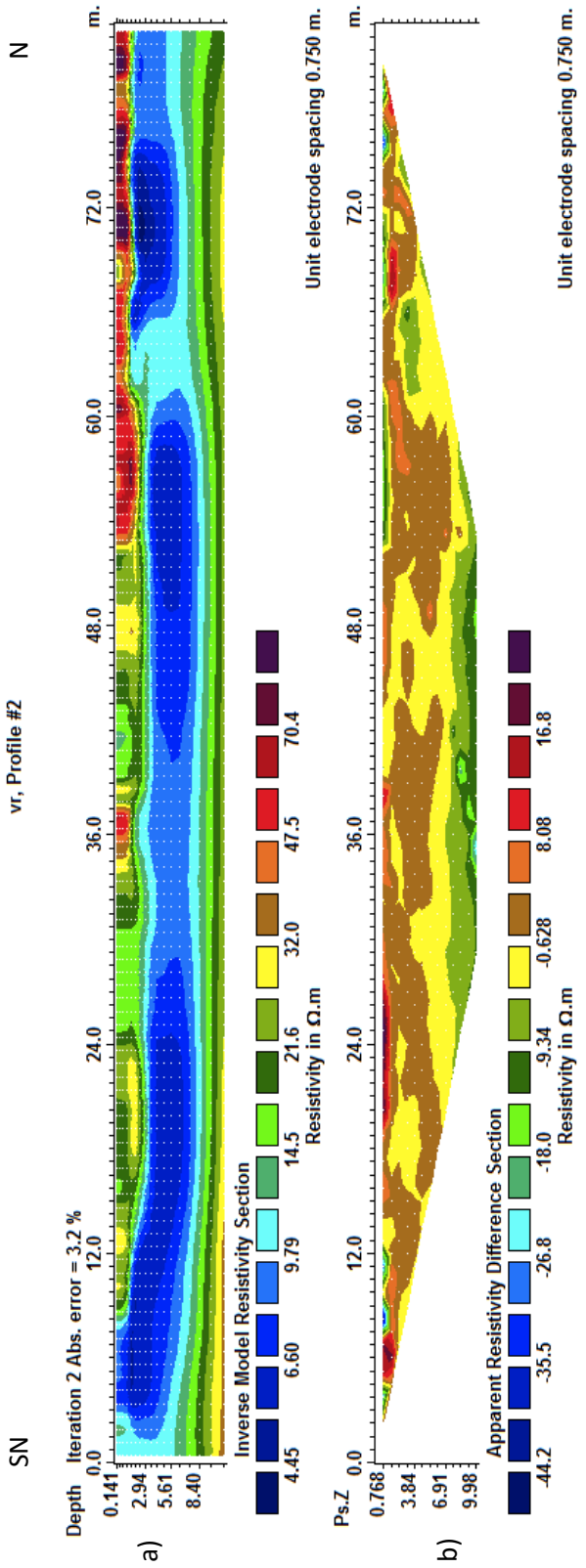


Figure 4-5: A model of resistivity (a) and the misfit in the apparent resistivity space (b) for the second iteration for Wenner alpha data acquired along line 2 (Res2dInv).

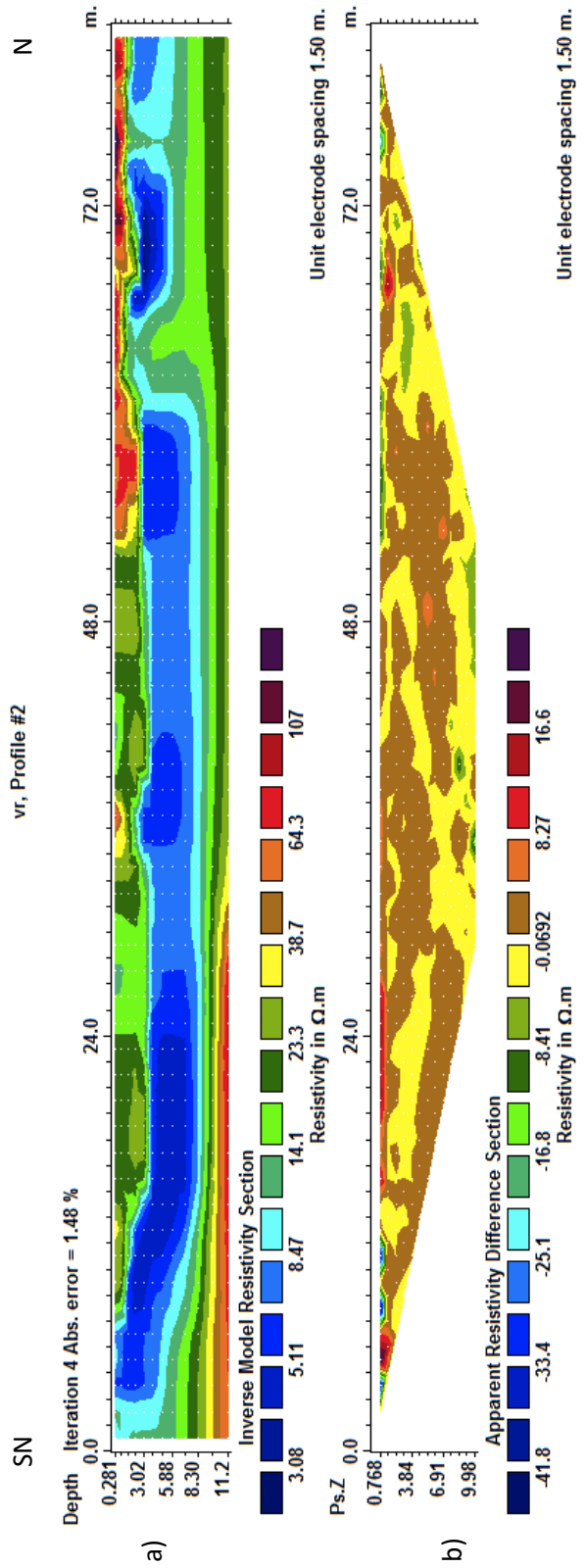


Figure 4-6: Model of resistivity (a) and misfit (b) for the fourth iteration, using a robust inversion scheme for Wenner alpha data acquired along line 2 (Res2dInv).

models in Figure 4-5a and Figure 4-6a are similar in that a resistive (c. 100 ohm.m) overlies a layer with low resistivity (<10 ohm.m) which in turn overlies a layer with resistivity of approximately 20 ohm.m. It is interesting to note, that using a slightly different algorithm (as programmed into the UBC inversion codes) the inversion did not converge to the expected misfit (amount of data points) even after 100 iterations for the L_2 inversion.

Using large changes in initial models to investigate the depth of investigation did not yield areas that had DOI indices above 0.1 for the uppermost 10 m of the model space. Using different initial models shows the changes in model resistivity as shown in Figure 4-7. This implies that at shallow depths the models are very similar. The density of contour lines in these shallower depths (less than 10 m) also corroborates the model.

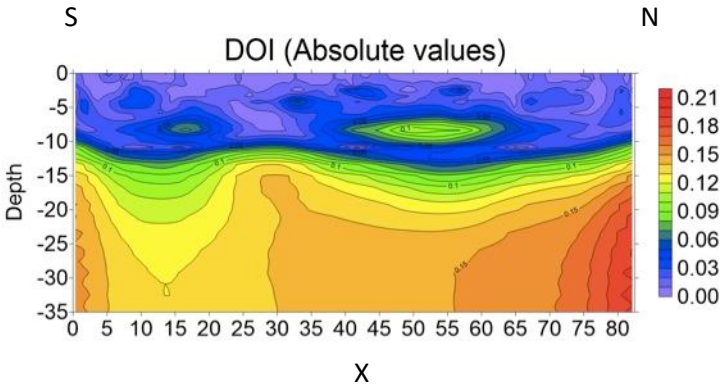


Figure 4-7: Different starting models produced similar model resistivities for the Wenner alpha data acquired on line 2 for depths up to 10 m. The calculated DOI index values are shown.

Figure 4-8 shows two *a posteriori* models with different *a priori* models using the same inversion parameters (smoothness constrained inversion) as before but different starting models (an homogenous half space of 10 ohm.m for Figure 4-9a and of 30 ohm.m in Figure 4-8b).

The models are all quite similar at depths below 5 m but at greater depths the similarity is less as it is (for example) not possible map the depth of the resistor (of c. 10 ohm.m and higher) with any degree of certainty. Dipole-dipole data are available and this allows for comparison with the Wenner alpha models for this line. By using the dipole-dipole models in conjunction with the Wenner alpha models and limiting the depth it is possible to obtain a good model of the subsurface resistivity distribution.

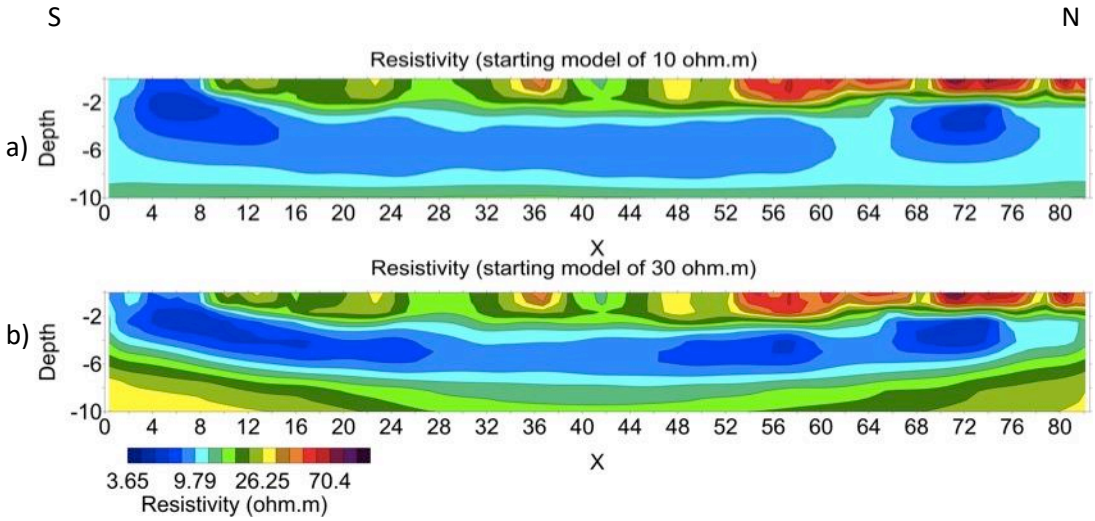


Figure 4-8: Different starting models produced similar model resistivities for the Wenner alpha data acquired on line 2 for depths up to 10 m.

4.1.2.2 Dipole-dipole ER data for line 2

The model obtained from the smoothness-constrained inversion (see Appendix A for the Res2DInv settings) of the dipole-dipole data acquired on line 2 in (Figure D-3 in Appendix D) has a misfit of 3.9% after two iterations (see Appendix B: Figure A-3), shown in Figure 4-9a. The estimated data precision of 1.4% is lower than the misfit for this line of data. The misfit pseudo section in Figure 4-9b shows a trend as with the Wenner alpha models have shown before. The data acquired with small electrode separations (shallow data) show a small difference (approximately 4%) between calculated and measured values while the data from larger dipoles show larger misfit. There are also many points included in the misfit pseudo section that warps the picture and nothing meaningful can be said about how random the misfit is from this.

An alternative model is presented in Figure 4-10a where the same improvement was made as for alternative models for the Wenner alpha data (improvements shown in Figure 4-6). This model shows a much lower misfit (approximately 2.0%) and is closer to being random with smaller variations seen at lower depths. The expectation is that the deeper data are influenced by noise more than the shallow data because of the separation between dipoles. The colour scale for the misfit pseudo section (Figure 4-10b) has been altered from the default as some outliers heavily influence the display.

The model is quite different from the model presented in Figure 4-9b. The features appear much less smooth in Figure 4-10b. The resistivities of the larger features are

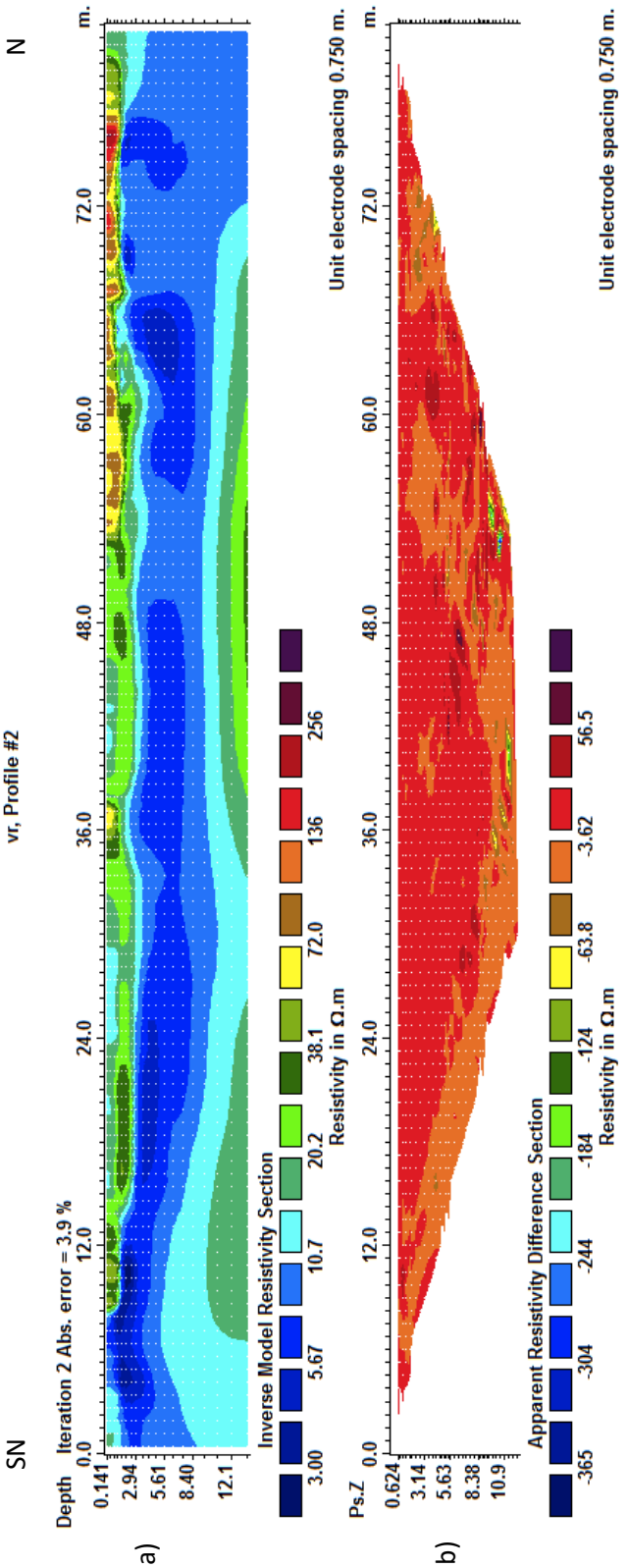


Figure 4-9: A model of resistivity (a) and the misfit in the apparent resistivity space (b) for the second iteration for the dipole-dipole data acquired on line 2 (Res2dInv).

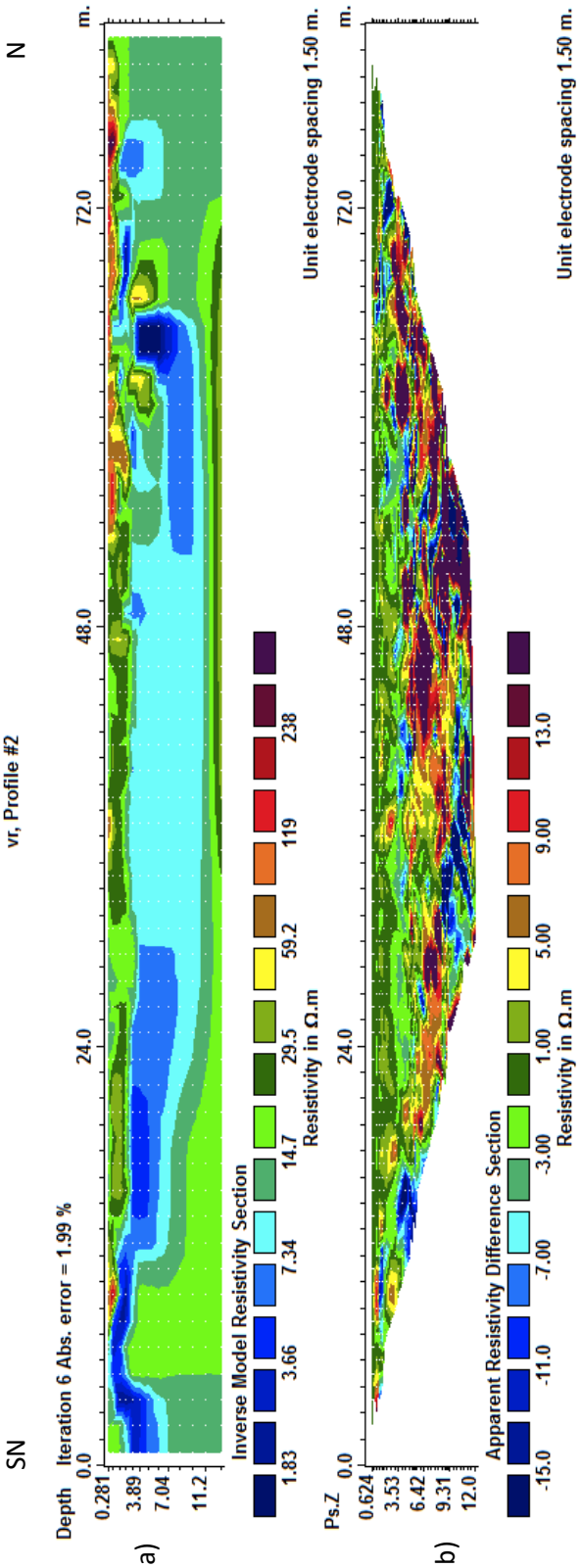


Figure 4-10: Model of resistivity (a) and misfit (b) for the sixth iteration using a robust inversion scheme on the dipole-dipole data acquired along line 2 (Res2dInv).

similar in both models. In Figure 4-11 the DOI profile is shown and it demonstrates that at less than 10 m the models are very similar, as can be seen by the DOI indices (which are less than 0.1) and the density of contour lines.

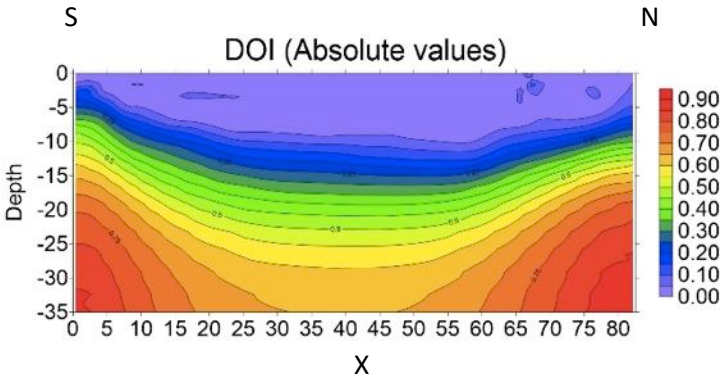


Figure 4-11: Different starting models produced similar model resistivities for the dipole-dipole data acquired on line 2 and the DOI indices are shown.

Figure 4-12 shows two *a posteriori* models with different *a priori* models used to corroborate the models produced for the Wenner alpha data (the models in this figure are from the dipole-dipole data). Using the default settings for a slightly different algorithm than used for the models above produces the first model. The inversion for this model (Figure 4-12a) minimises the L_2 norm and was achieved after 47 iterations with the misfit being larger than the amount of data points. The L_1 norm is minimised for the second model (Figure 4-12b) and the target misfit is achieved after 70 iterations.

Three things are worth mentioning in these models. Firstly, highly resistive material occur from approximately 55 m along the profile towards the north in the near subsurface. Secondly, a first relatively resistive layer overlies a more conductive layer with a undulating base into a third more resistive layer. Thirdly, the third layer has resistivities not nearly comparable to bedrock and reading at a depth that can be considered depth does not influence the data.

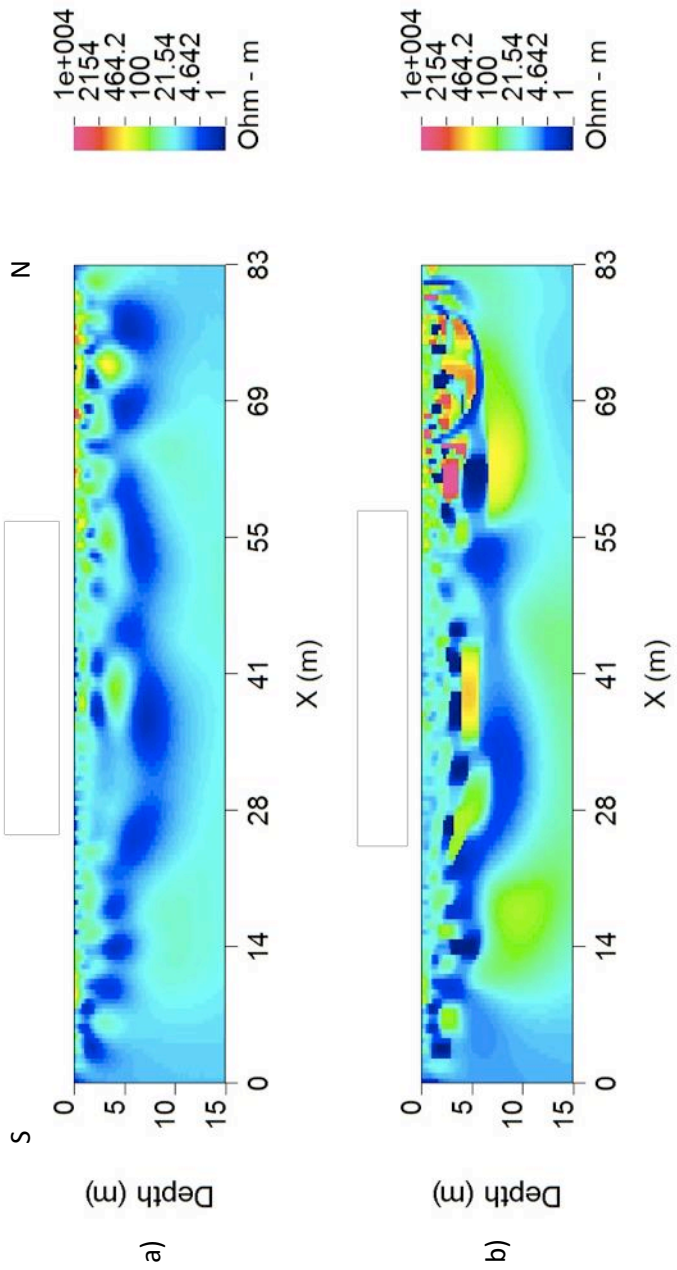


Figure 4-12: Models produced using a slightly different algorithm minimising the L_1 norm (a) and the L_2 norm (b). No DOI have been calculated for these two models (DCIP2D).

The final resistivity model is shown in Section 4.1.2.5.

4.1.2.3 Wenner alpha IP data for line 2

The models obtained from smoothness-constrained inversion (see Appendix A for the Res2DInv settings) of the IP acquired on line 2 with the Wenner Alpha array show three

anomalous zones (Figure 4-13). Two slightly elevated zones are present on the north and south sides of the centre of the profile. The cause of this is unclear. The third anomaly is the low reading in the centre of the profile, which, as mentioned below, should show a positive anomaly. The data are measured as integrals over time-windows and the first six windows duration are as follows (measured after a 1 second pulse) with a 0.04 s delay before measuring 0.26 s.

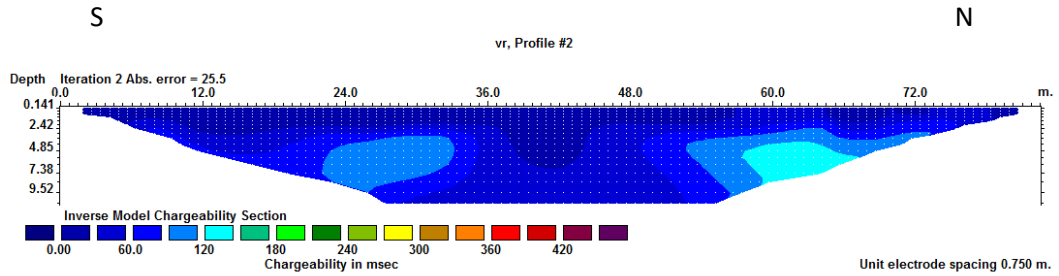


Figure 4-13: Model of chargeability from IP data collected using the Wenner alpha array on line 2. See text for window and pulse length (Res2dInv).

4.1.2.4 Dipole-dipole IP data for line 2

A second data set (dipole-dipole data) is available for line 2 and the models obtained from smoothness-constrained inversion (see Appendix A for the Res2DInv settings) of these IP show five distinct anomalies (Figure 4-14). The slightly elevated chargeability to in the centre of the profile that coincides with the root system of the *Eucalyptus* tree. The reason for this is not clear but it may be that the response is from contaminants stored around the root system of the tree. It may also be entirely caused by noisy data. The data for this data set are measured as integrals over time-windows and the last five windows are summed, inverted ad shown (measured after a 1.5 second pulse, after a delay of 0.22 seconds for 1.04 seconds).

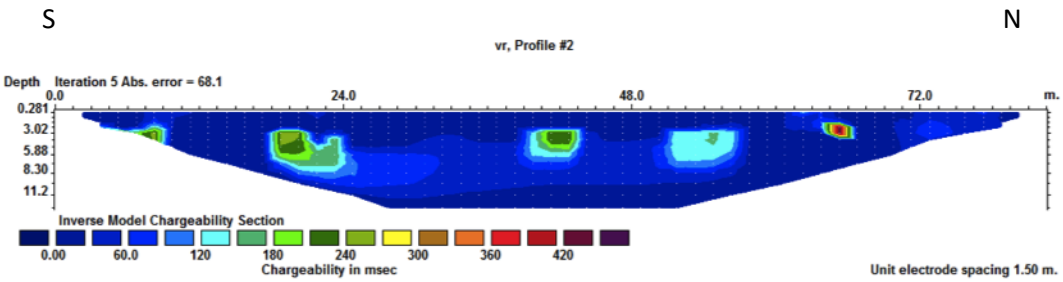


Figure 4-14: Model of chargeability from IP data collected using the dipole-dipole array on line 2. See text for window and pulse length (Res2dInv).

4.1.2.5 Final models for line 2

In Figure 4-15 the final resistivity model is shown for line 2. It is the model obtained from the smooth inversion of the dipole-dipole data presented in Figure 4-12a. This model is chosen to represent the resistivity for both arrays, as they are similar. The model goes to a depth of 12 m and bedrock cannot be defined from the data set. A conductive zone is interpreted as highly conductive groundwater. The groundwater level is between 3 and 4 m deep and has an *in situ* electrical resistivity of 3 to 56 ohm.m.

The first layer is interpreted as dry soil with more electrically resistive material between 52 and 78 m along the profile in approximately the first meter below surface, which may be soil that is even drier.

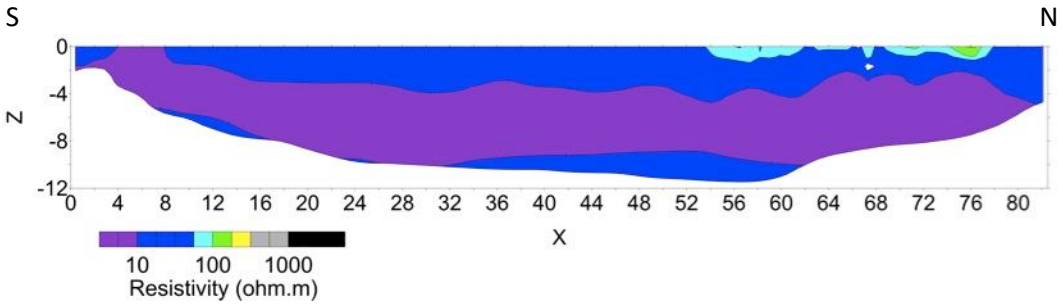


Figure 4-15: Final resistivity model for line 2.

In Figure 4-16 the interpreted chargeability section is shown. This model is obtained by combing the centre anomaly from the dipole-dipole models with the anomalies found in both sets of data. Two anomalous zones are seen in this model. A slightly polarisable section exists at about 2–3 m deep and runs all along the profile except where it is interrupted by the expected location of the root system of the tree. A deeper anomaly is also visible in the dipole-dipole model at this location. It is possible that the increased interchange between surface water and oxygen near the stems of plants such as trees has allowed for a higher influx of water to the root system. The resultant slightly more conductive polarisable section could be from excess pollutant remaining in and around the root system around the tree as it pumps water to the surface (and beyond) and leaves contaminants behind.

The reason for having confidence in the final chargeability model is that the time-domain IP contains all the spectral information found in the frequency-domain IP method. The frequency-domain data show a positive response for laboratory samples

contaminated with AMD as can be seen in Figure 2-2 and Figure 2-7. Moreover, the spatial relationship between the anomalies and the root system of the trees, at the very least, warrants further investigation.

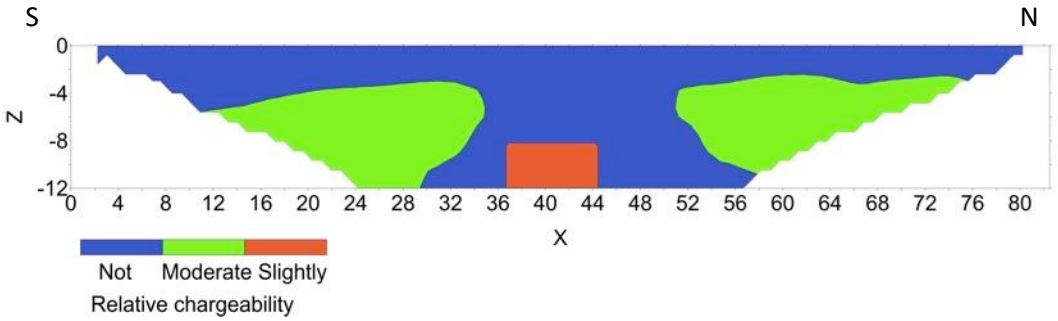


Figure 4-16: Final chargeability model for line 2.

In the final resistivity and IP models model the water table coincides with the depths shown in the model in Figure 4-19 (Grindley, 2014). Peter Dye, who accompanied Grindley for the fieldwork, said there was some clay present when an excavator opened the section (personal communication, September 2014). A combination of clay and noise can explain the IP response of the Earth here and further work should be done to achieve certainty.

The interpretation and some of the surface features are shown in Figure 4-17 with the final resistivity model for line 2.

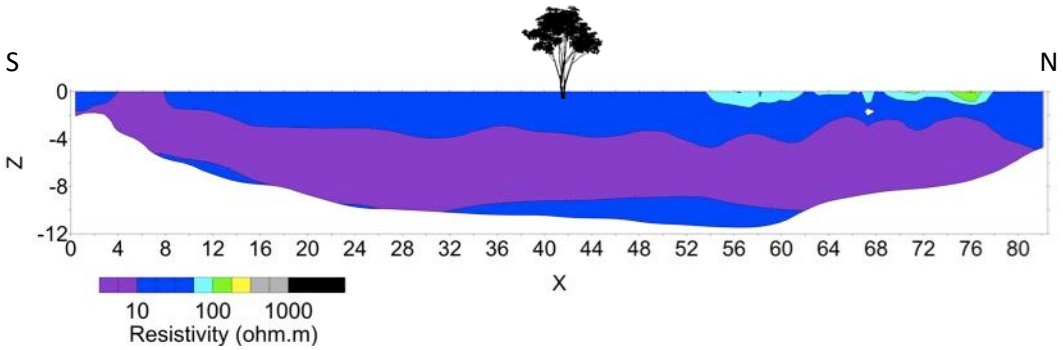


Figure 4-17: Final resistivity model for line 2 with surface features.

The interpretation and some of the surface features are shown in Figure 4-18 with the final chargeability model for line 2.

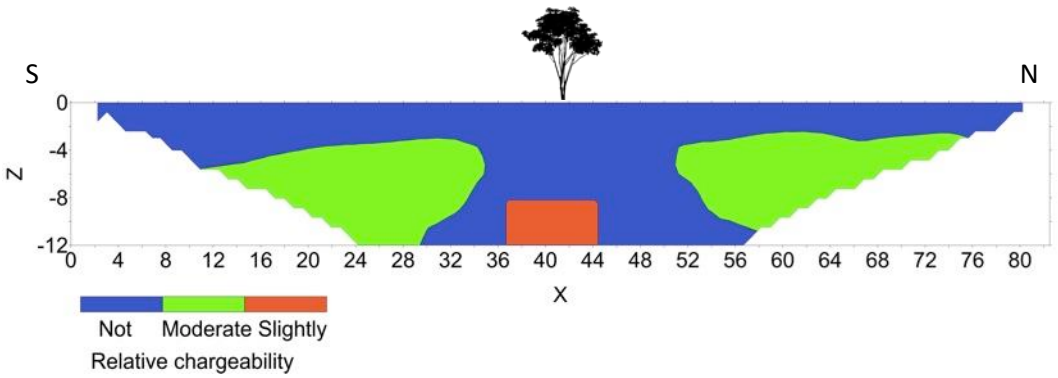


Figure 4-18: Final chargeability model for line 2 with surface features.

4.1.3 Line 3: ER and IP data near a *Searsia lancea* tree with deep roots

4.1.3.1 Wenner alpha ER data for line 3

The model obtained from smoothness-constrained inversion (see Appendix A for the Res2DInv settings) of the Wenner alpha data acquired on line 3 has a misfit of 4.7% after three iterations (see Appendix B: Figure A-4, model shown in Figure 4-19b). The estimated data error of 3.6 % is lower than the misfit for this line of data and the data are therefore underinterpreted. The raw data are shown in Figure D-4 in Appendix D and the model obtained from the inversion (Figure 4-19a) is clearly not valid as the misfit pseudo section is layered (Figure 4-19b).

An alternative model where different inversion parameters are used i.e. sharp models, or models created using the robust inversion scheme, which fit the data better (Figure 4-20). The model produced after the fourth iteration (Figure 4-20a) has a misfit of 2.0% (model over interprets the data) and the misfit pseudo section (Figure 4-20b) is random for this model.

The DOI is presented in Figure 4-21. At shallow depths the models are very similar as can be seen at the DOI indices and density of contour lines in the depths shallower than 10 m. The lower values of the DOI index at 20 m are due to the models not differing in this zone. The model should not be interpreted at this depth; the density of contour lines should be used instead of a low DOI index.

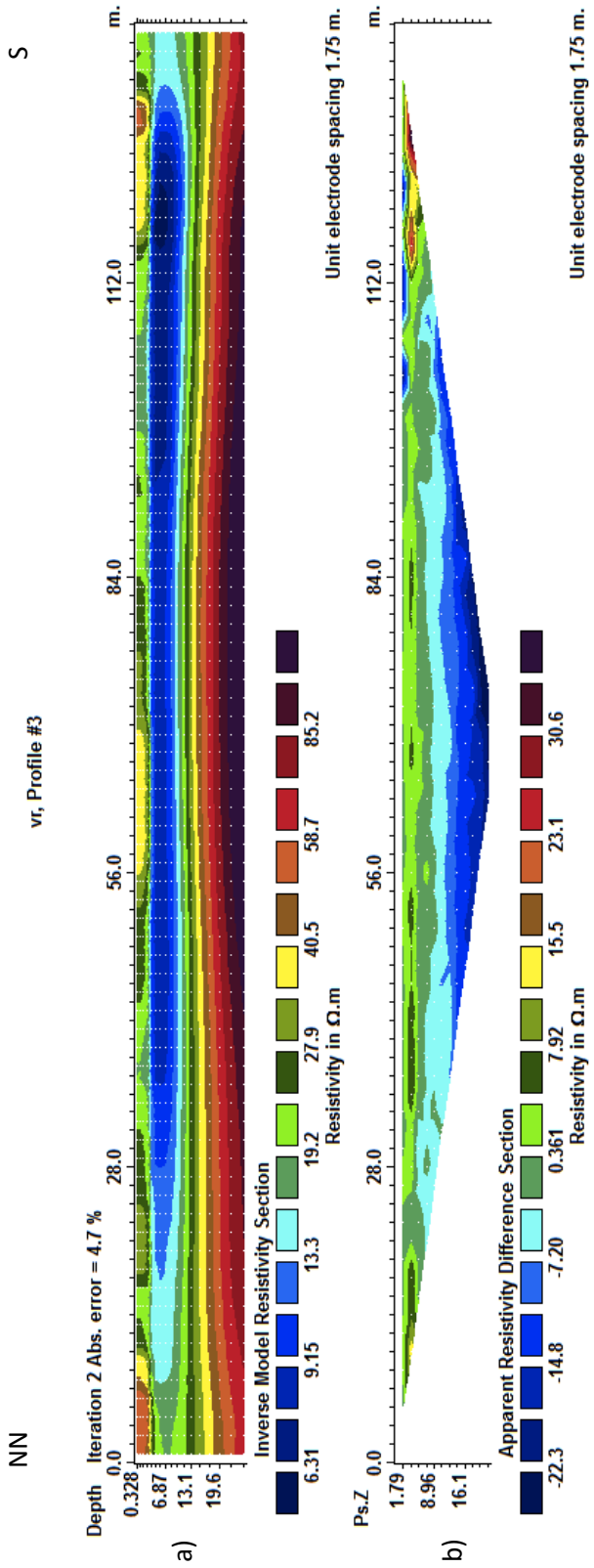


Figure 4-19: A model of resistivity (a) and the misfit in the apparent resistivity space (b) for the second iteration modelling the Wenner alpha data acquired on line 3 (Res2dInv).

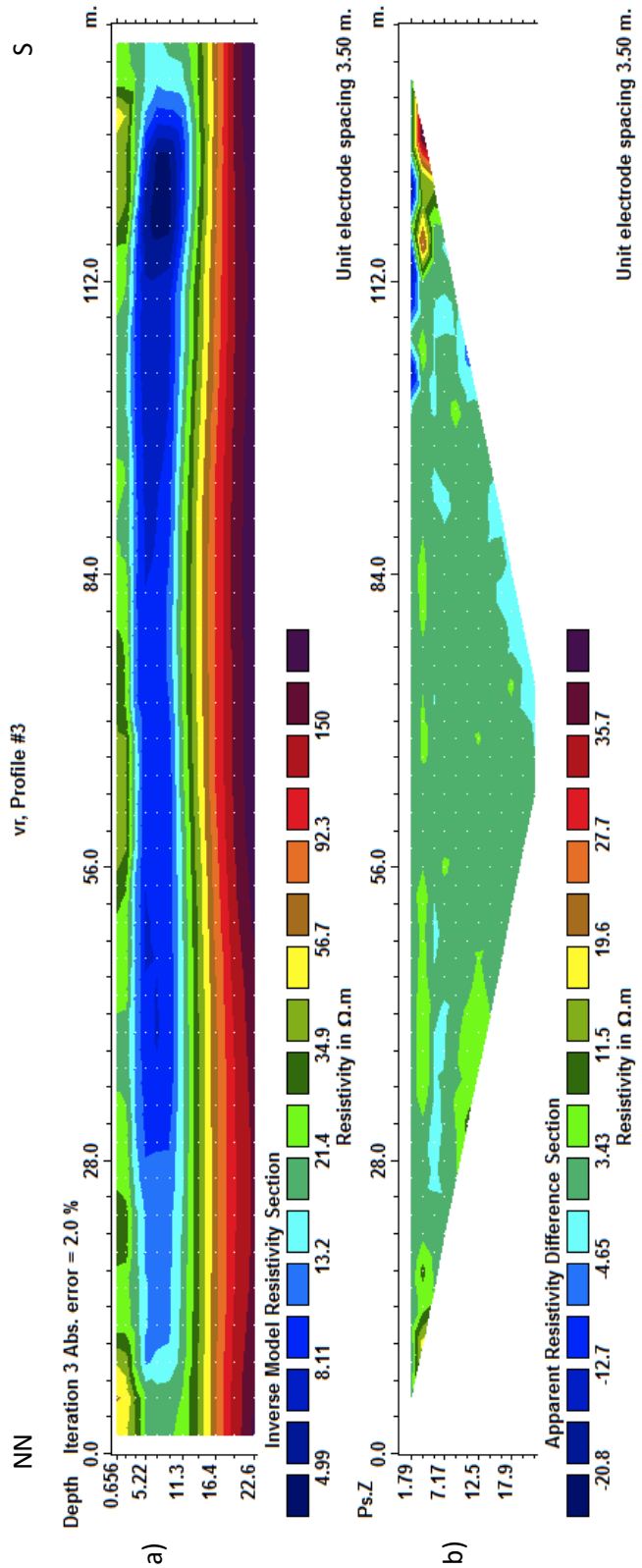


Figure 4-20: Model of resistivity (a) and misfit (b) for the fourth iteration using a robust inversion scheme on the Wenner alpha data acquired along line 3 (Res2dInv).

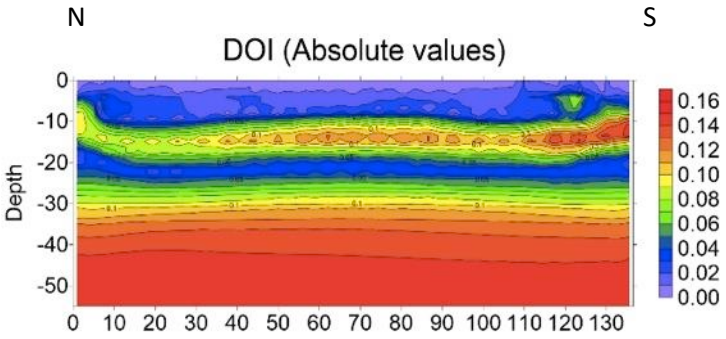


Figure 4-21: Different starting models produced similar model resistivities for the Wenner alpha data acquired on line 3 for depths up to 10 m with the DOI index shown.

No other alternative models will be shown for this array on line 3 as dipole-dipole data are available and the model in Figure 4-20a match the data satisfactory.

4.1.3.2 Dipole-dipole ER data for line 3

The model obtained from smoothness-constrained inversion (see Appendix A for the Res2DInv settings) of the dipole-dipole data acquired on line 4 has a misfit of 3.6% after two iterations (see Appendix B: Figure A-5, model shown in Figure 4-22a). Assuming an accuracy of 0.001 mV for the potential reading gives unreasonably high errors (81.2%) for the data set. The average standard deviation (SD) of the readings is 2.8% and the SD can be used to better estimate the error because of the unreasonably high error caused by low injection currents. The data are therefore underinterpreted. The raw data are very noisy (Figure D-5 in Appendix D). The model obtained from the inversion are obtained using an extended subsurface and the areas where data are not present (north of 20 m and south of 109 m) should not be interpreted. The difference between the calculated and observed apparent resistivities in line 3 must also be random but the pseudo section (Figure 4-22b) shows a trend.

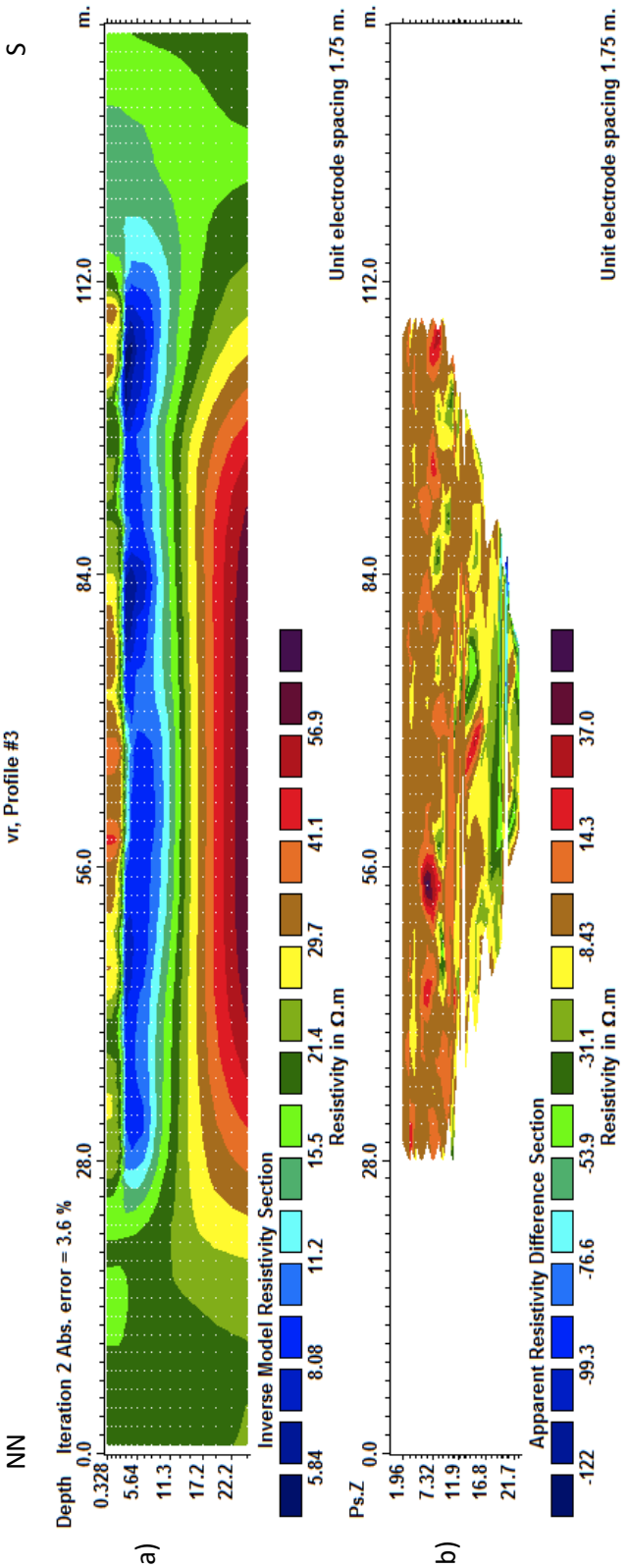


Figure 4-22: A model of resistivity (a) and the misfit in the apparent resistivity space (b) for the second iteration of the smoothness constrained inversion of the dipole-dipole data acquired on line 3 (Res2dInv).

4.1.3.3 Wenner alpha IP data for line 3

The inversion models from the Wenner alpha IP data acquired on line 3 (Figure 4-23, see Appendix A for inversion parameters) has a large misfit. A smoothness-constrained inversion was used to obtain the model and this might be why the anomaly is larger than expected. It still correlates exactly with where the roots system of the *Searsia lancea* is expected to be.

These models are of data (Figure D-11 in Appendix D) recorded over line 3 using the Wenner alpha array. The data are measured as integrals over time-windows added together with the signal used here recorded from 0.1 s after current switch off for 0.52 s (measured after a 1 second pulse).

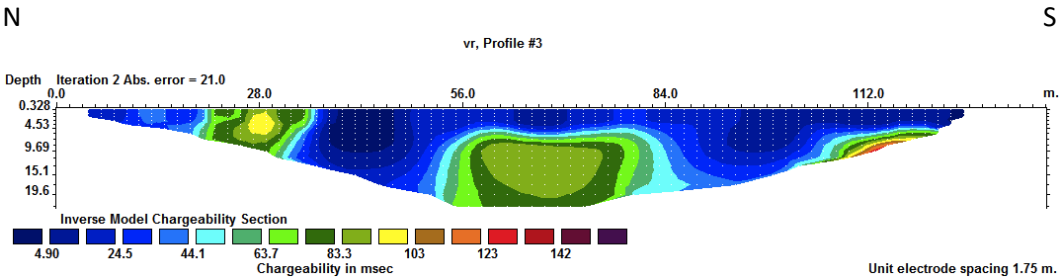


Figure 4-23: Model of chargeability from IP data collected using the Wenner alpha array on line 3. See text for window and pulse length (Res2dInv).

4.1.3.4 Final models for line 3

The final model for the resistivity data acquired on line 3 is shown in Figure 4-24. It is Wenner alpha model presented in Figure 4-20a. The area around line 3 is the most conductive of the data measured in September 2013. The shallowest 2.5 m is interpreted as dry soil overlying the water in the ground. This layer is conductive relative to the other lines. The *Searsia lancea* trees are known as salt trees as they draw salt from the underground and deposit it on surface. This could have had an influence on the soil resistivity. It is unlikely that the whole profile can be affected in this way and either the soil mineral content is more conductive (possibly as a result of higher iron content) or the soil is comparatively moist. The interval from 3 to 13 m depth is interpreted as groundwater with a resistivity of 3 ohm.m to 17 ohm.m that is extremely low and this water is interpreted as highly contaminated.

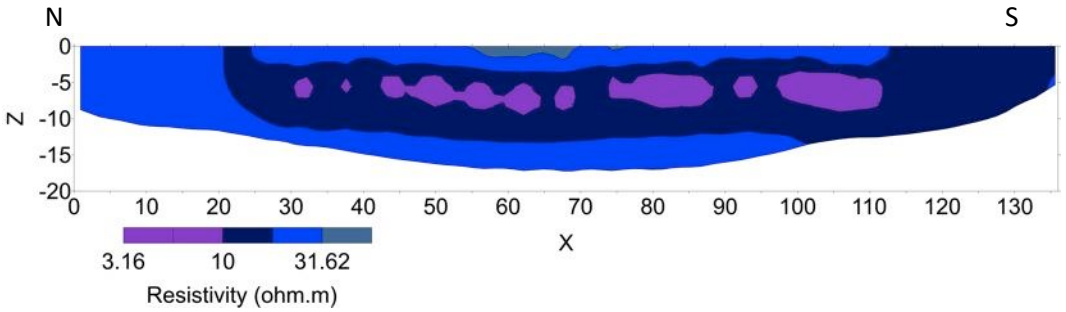


Figure 4-24: Final resistivity model for line 3.

In Figure 4-25 the interpreted chargeability section is shown. A strong IP anomaly is seen in the models for the IP data acquired on line 3, coinciding spatially with the expected location of the tree roots. This anomaly can be caused by the presence of clay in the subsurface or noise in the data as the deepest readings with both arrays have the highest susceptibility to noise contamination.

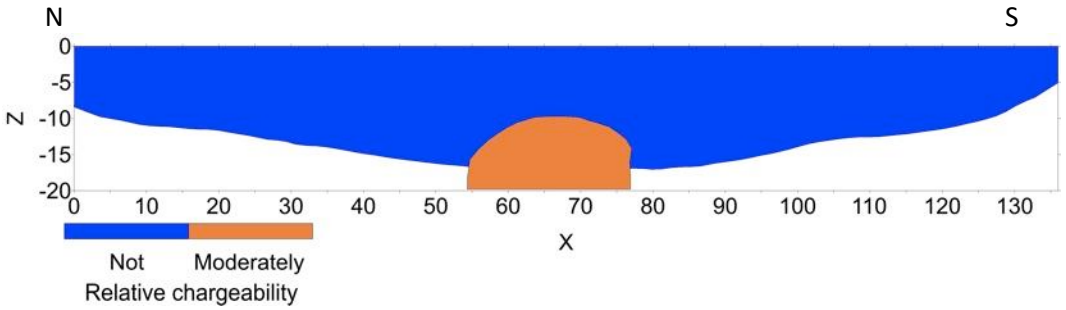


Figure 4-25: Final chargeability model for line 3.

The interpretation and some of the surface features are shown in Figure 4-26 with the final resistivity model for line 3.

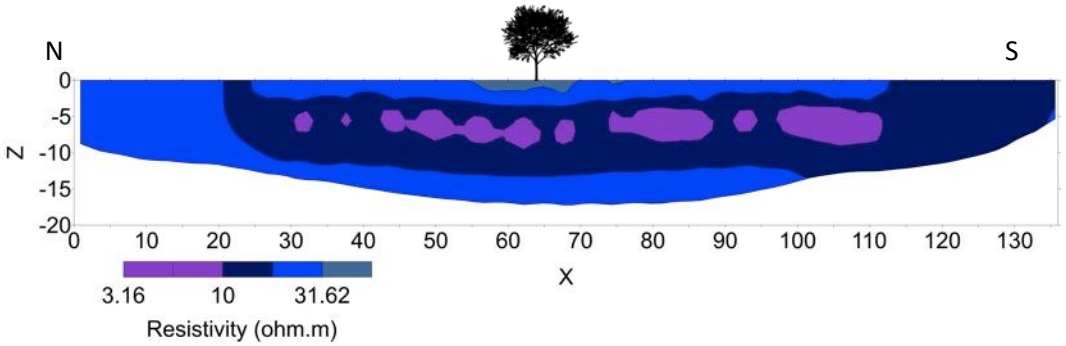


Figure 4-26: Final resistivity model for line 3 with surface features.

The interpretation and some of the surface features are shown in Figure 4-27 with the final chargeability model for line 3.

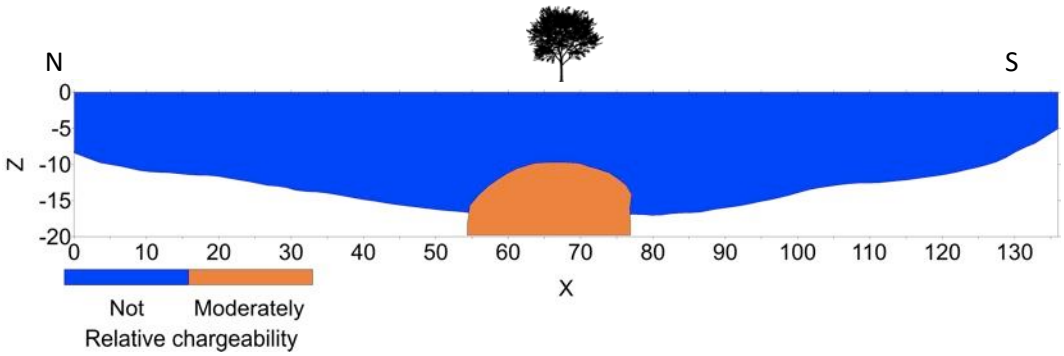


Figure 4-27: Final chargeability model for line 3 with surface features.

4.1.4 Line 4: ER and IP data near a *Searsia lancea* tree with shallow roots

4.1.4.1 Wenner alpha ER data for line 4

The model obtained from smoothness-constrained inversion (see Appendix A for the Res2DInv settings) of the Wenner alpha data acquired on line 4 has a misfit of 3.8% after three iterations (see Appendix B: Figure A-6, shown in Figure 4-28a). The estimated data error of 1.8 % is lower than the misfit for this line of data and the data are therefore underinterpreted. It is hard to tell from the misfit pseudo section (Figure 4-28b) if the misfit is random as many misfit values fall close to 0% but the outliers in the data set obscure the colour scale.

The same pseudo section and model (Figure 4-28) are repeated below with a different colour bar for the misfit data (Figure 4-29). The model (Figure 4-29a) fits the data well and the difference between the expected and measured apparent resistivity models are random (Figure 4-29b).

The DOI for the Wenner alpha data is shown in Figure 4-30. The linear average was used again instead of the average of the logarithm. In the DOI images the variations in model resistivity are small at shallow depths and large at deeper depths, as is to be expected, because the ER method is more sensitive to near surface resistivity variations. The depth to which this data are sensitive is approximately 10 m.

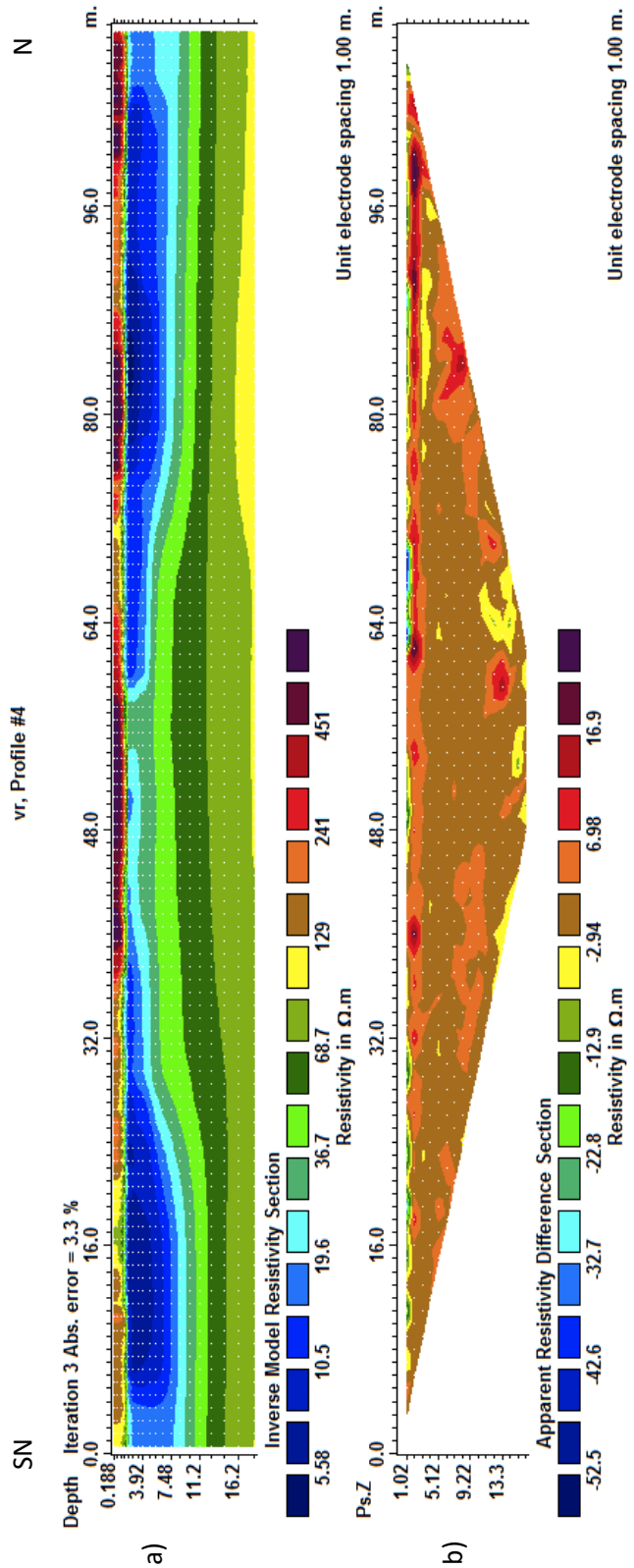


Figure 4-28: The model obtained after three iterations of running the inversion scheme on the Wenner alpha data acquired on line 4. A calculated model (a) and the difference between the observed and calucated apparent resisitiivity values (b, Res2dInv).

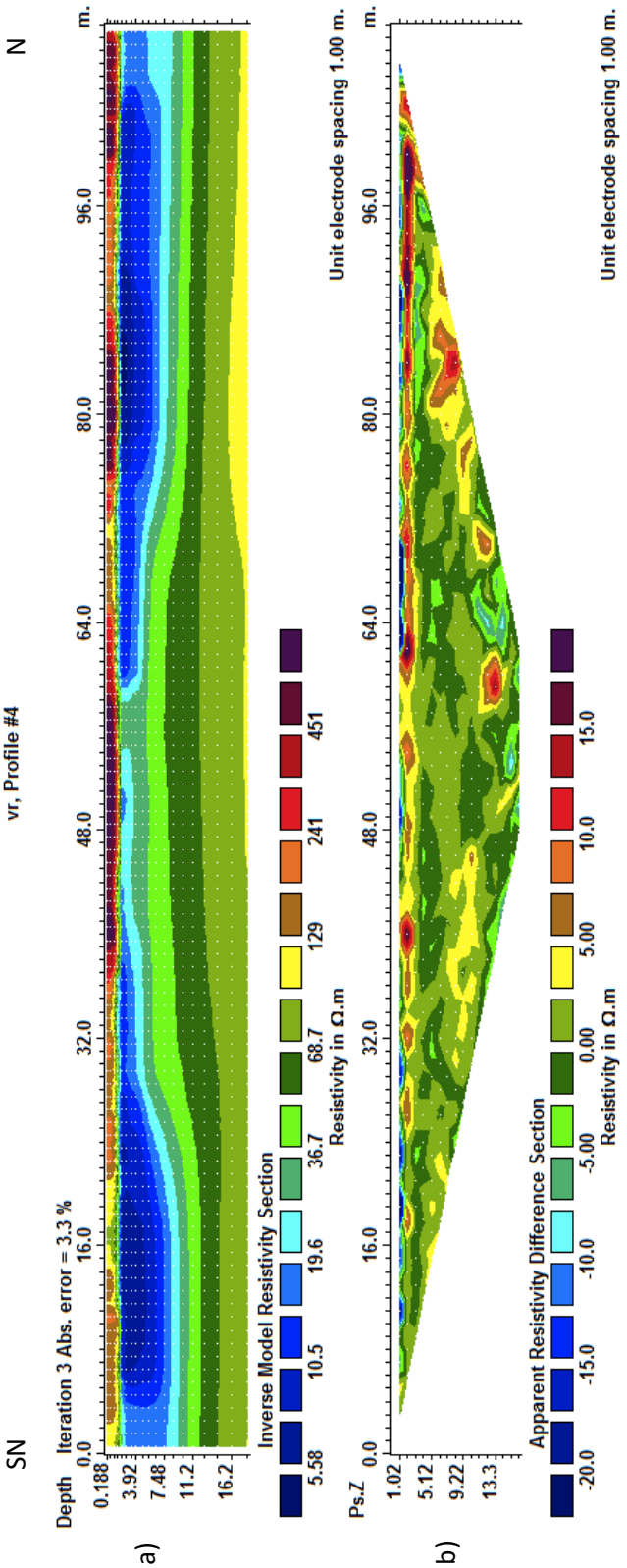


Figure 4-29: The model from Figure 4-28b in (a) with a differnet histogram for the misfit data (b) (Res2dInv).

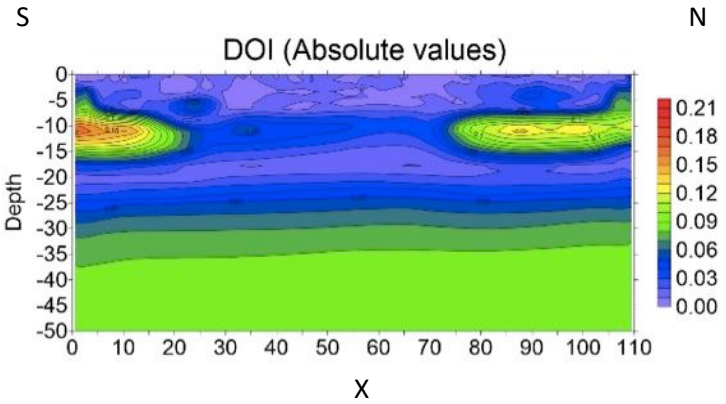


Figure 4-30: Depth of investigation index for the Wenner alpha data acquired along line 4.

4.1.4.2 Wenner beta ER data for line 4

The model obtained from smoothness-constrained inversion (see Appendix A for the Res2DInv settings) of the Wenner beta data acquired on line 4 has a misfit of 3.8% after three iterations (see Appendix B: Figure A-7, model shown in Figure 4-31a). The estimated data error of 9.6 % is much higher than the misfit for this line of data and the data are therefore over interpreted. The Wenner beta array is a special case of the dipole-dipole array with *n=1*. This was used because of time constraints in the field. The difference between the measured and apparent resistivity, presented as a misfit pseudo section is random (Figure 4-31b).

Initial models testing large variations in resistivity were used to obtain the DOI index section shown in Figure 4-32. Near the centre of the profile the Wenner beta data for line 4 is sensitive to resistivity changes at larger depths than line 1, 2 and 3. If a DOI index of 0.2 is used, the model is interpretable at even 20 m depth.

It is likely incorrect to interpret the models to these depths. The models used to obtain the DOI index were similar in the region but this may be by chance rather than the resistivity being well defined at this depth by the method used and for the geology present.

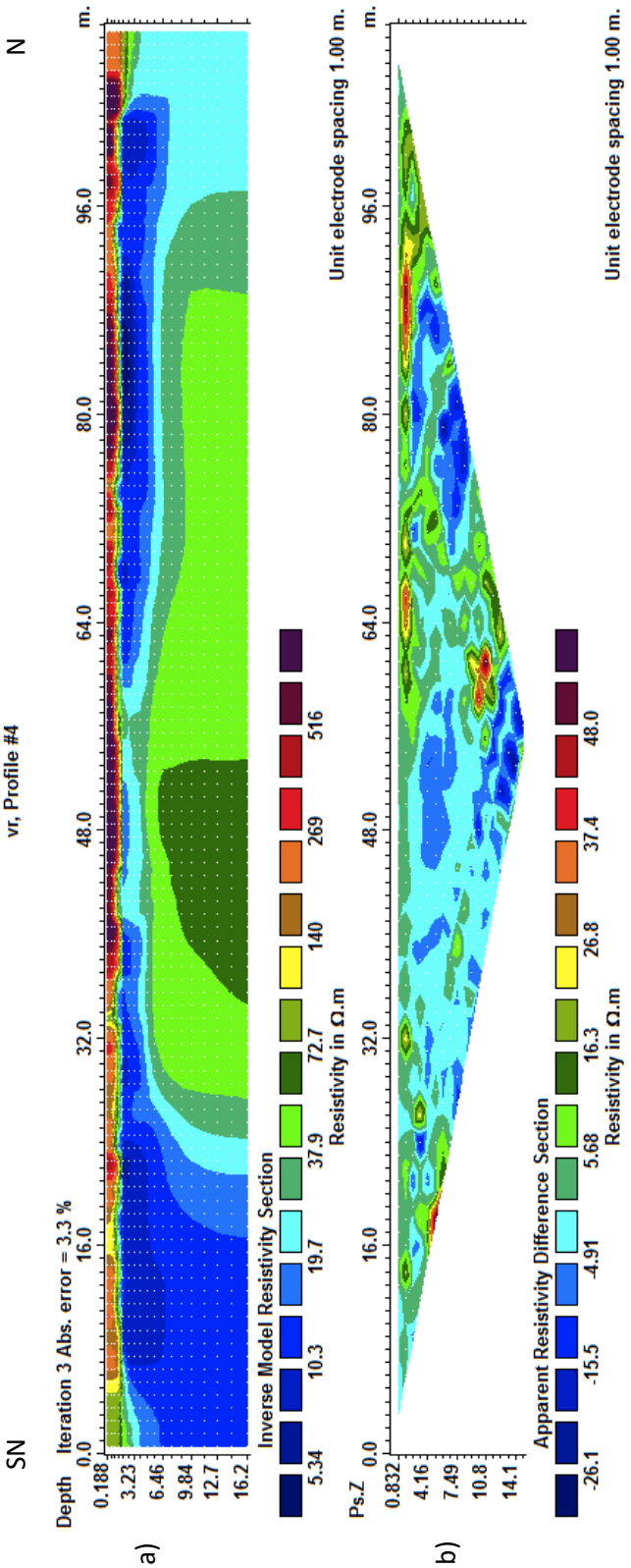


Figure 4-31: A model of resistivity (a) and a misfit in the apparent resistivity space (b) for the third iteration of inversion of the Wenner beta data on line 4 (Res2dInv).

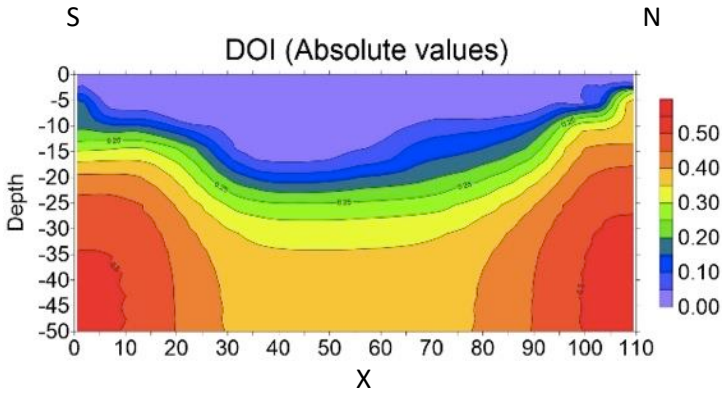


Figure 4-32: Different starting models produced similar model resistivities for the Wenner beta data acquired on line 4 for depths up to 15 m. The DOI index is shown.

Alternative models for the Wenner beta data are shown in Figure 4-33. A model obtained by using a reference resistivity for a homogenous half-space of 25 ohm.m is shown in Figure 4-33a. The model in Figure 4-33b is obtained by using a reference resistivity of 100 ohm.m for the homogenous half-space (the other inversion parameter that was changed is the damping of the initial model). These models show that large variations in electrical resistivity at an intermediate depth (10 to 20 m) are not present.

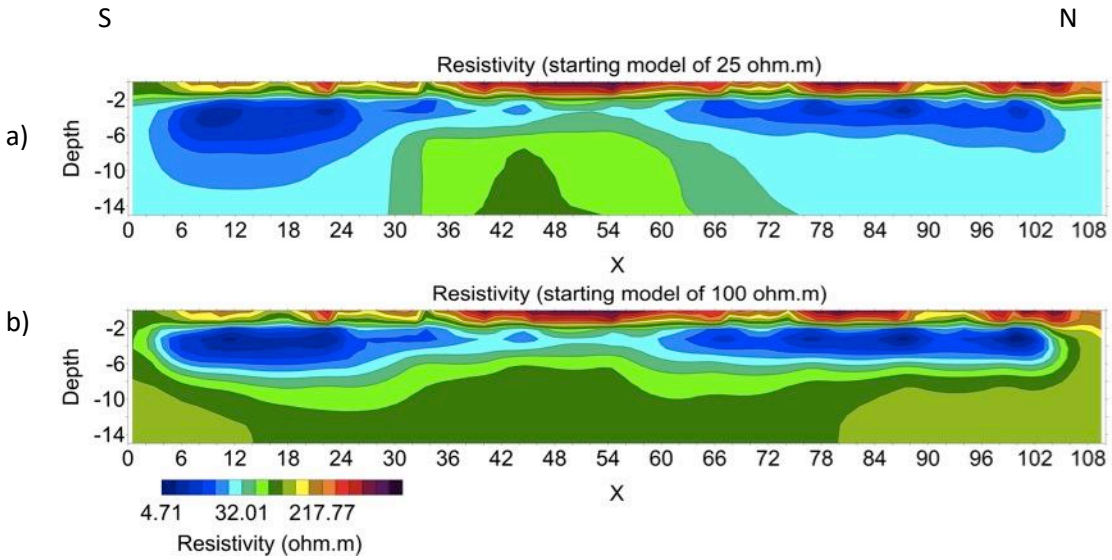


Figure 4-33: Different starting models produced similar model resistivities for the Wenner beta data acquired on line 4 for depths up to circa 15 m deep. Both models started as homogenous half-spaces with a reference resistivity of 25 ohm.m (a) and 100 ohm.m (b), respectively.

4.1.4.3 Wenner alpha IP data for line 4

For the IP data the misfit between the measured data and the calculated data is large. The error in precision or a calculated accuracy (by assuming a minimum error on the

voltmeter readings of 1 mV) is large and the data is of not good quality. There is, however, a correlation between the expected location of the roots of the *Searsia lancea* tree and the IP anomalies shown in the inversion model (Figure 4-34). The anomaly in the shallow part in the middle of the section and the largest anomaly are elongated at depth and dips towards the north. The absolute errors of the original data are so imprecise (and probably inaccurate) it is not possible to say at what kind of misfit the inversion process should halt.

Figure 4-34 shows eight inverted models for the Wenner alpha data. These models are the first to eighth windows of the data presented in Figure D-14 (in Appendix D). The data are measured as integrals over time-windows and summed and the data used here were measured after 0.06 s of switching of the current for 0.4 s (after a 1 second pulse).

The anomaly coincides with the *Searsia lancea* tree was observed in the field. Line 4 was positioned near the TSF and cultural features might be present although these weren't noted in the field either. It cannot be definitively stated that the anomaly is "real" except that one of the position of the anomaly coincided with the position of the roots of a tree that is known to accumulate contaminants from the subsurface. Data acquired on a line positioned near a similar tree along line 3 can be presented as a comparison to test if the anomaly is "real", but this will require a high power source, and an auger to sample the data again.

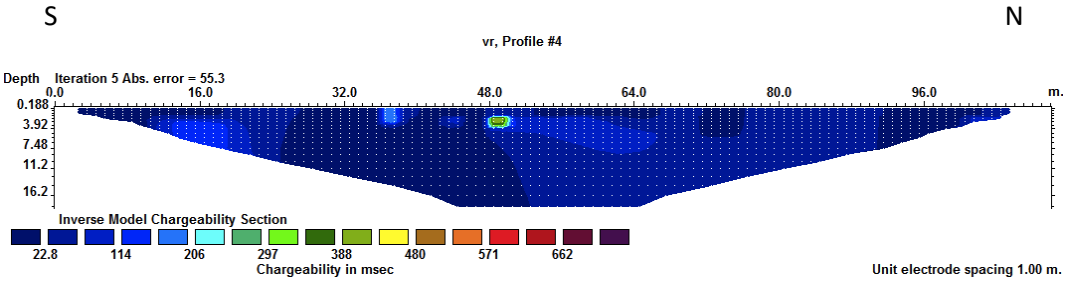


Figure 4-34: Model of chargeability from IP data collected using the Wenner alpha array on line 4. See text for window and pulse length (Res2dInv).

4.1.4.4 Final models for line 4

In Figure 4-35 the final resistivity model is shown for the data acquired on line 4. This model shows very simple geology and is interpreted as dry soil overlying more conductive groundwater-saturated soil. Some variation is present in the resistivity under the water table (4 to 25 m and 76 to 92 m along the profile at 2 to 8 m depth) and it is

not possible to definitely determine the source of this variation. The groundwater-saturated soil has *in situ* electrical resistivity of 6 to 56 ohm.m.

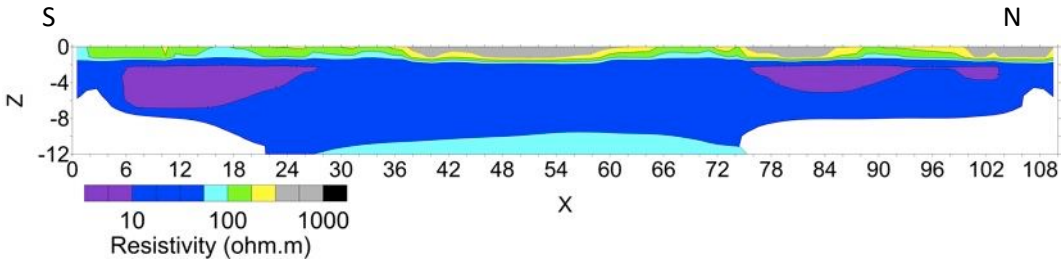


Figure 4-35: Final resistivity model for line 4.

Many of the models for line 4 show a slightly more resistive zone between 38 m and 60 m along the profile (from about 0 m to 2 m depth). The centre of the line coincides with the position of a *Searsia lancea* tree with shallow roots. The tree could potentially cause this.

In Figure 4-36 the interpreted chargeability section is shown. A spatially limited anomaly is seen in the IP models for the data collected on line 4. The fact that the anomaly does not extend to the maximum depth of the profile suggests that the anomaly is not caused by noise in the data. This is so for line 4 as well as the previous IP anomalies mentioned on line 2 and line 3. The source can only be in the subsurface.

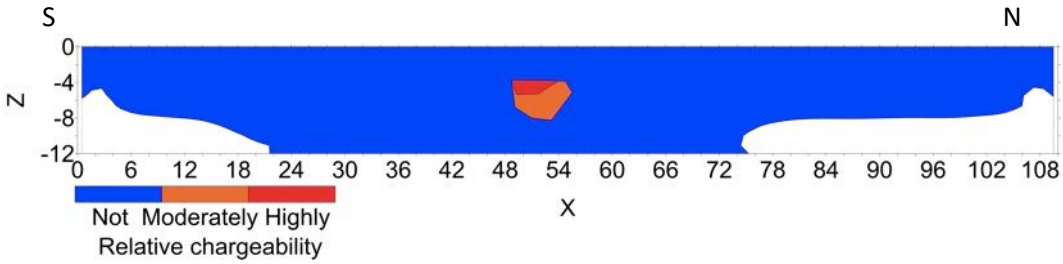


Figure 4-36: Final chargeability model for Line 4.

The interpretation and some of the surface features are shown in Figure 4-37 with the final resistivity model for line 4.

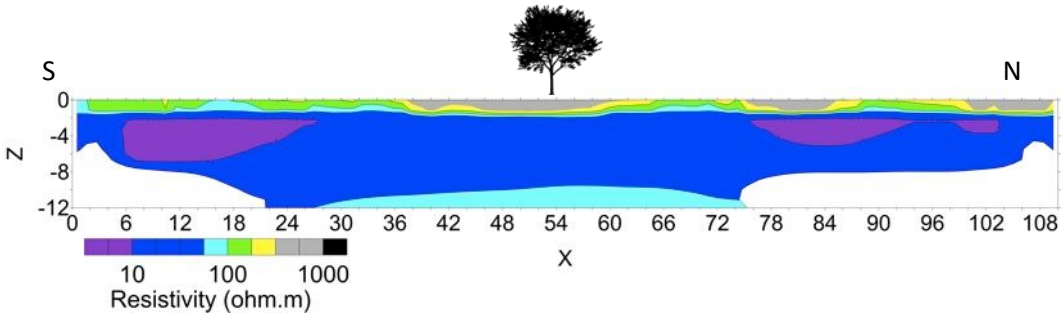


Figure 4-37: Final resistivity model for line 4 with surface features.

The interpretation and some of the surface features are shown in Figure 4-38 with the final chargeability model for line 4.

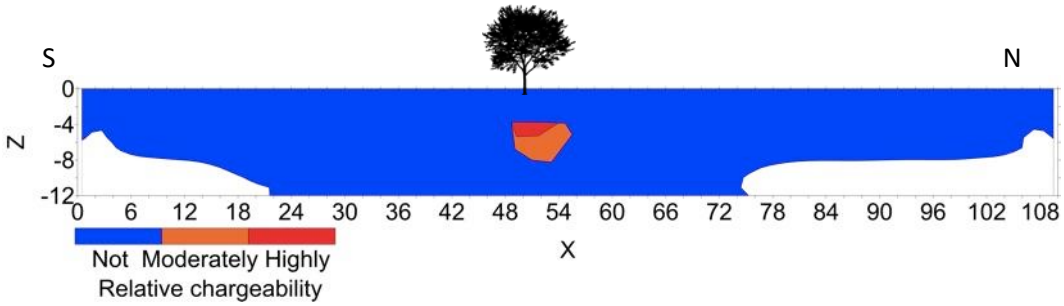


Figure 4-38: Final chargeability model for line 4 with surface features.

4.2 Electrical resistivity profile in the direction of the groundwater flow in the lavas

In this section the modelling and interpretation of the four lines acquired in the direction of the groundwater flow in and over the lavas are discussed. Only electrical resistivity data are available for these four lines. Three of the lines make a space lapse from in between the TSFs towards the Schoonspruit. A fourth line of data are presented that shows the resistivities of lava and lava derived soil where the groundwater is less contaminated than the other lines. Positioning of the four lines are shown in Figure 1-1 and Figure 3-3. Borehole data are plotted in a coloured contour map in Figure 3-3. The lines are presented consecutively from east to west. The numbering is a bit confusing, but Figure 1-1b should clear this up.

4.2.1 ER data along line 9

The data for line 9 are collected over dolomite (see Figure 1-1b for line position). The background resistivities (uncontaminated groundwater) for lines acquired of the dolomite are contained in the data for line 11 (Section 4.3).

4.2.1.1 Wenner Schlumberger ER data along line 9

The model obtained (Figure 4-39a) from the smoothness-constrained inversion (see Appendix A for the Res2DInv settings) of the Wenner Schlumberger data acquired on line 9 in (data in Figure D-15 in Appendix D) has a misfit of 4.5% after three iterations (see Appendix B: Figure A-8). The estimated data error is only 1.1%. The smoothness-

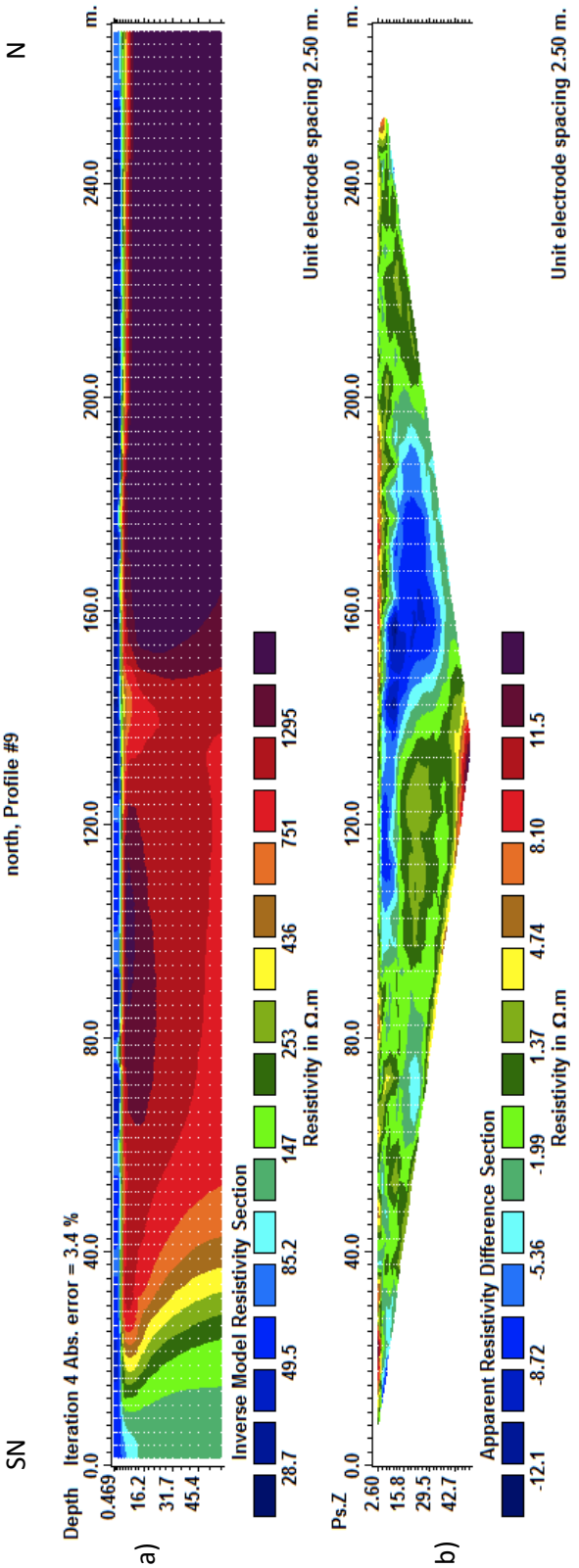


Figure 4-39: A model of resistivity (a) and a misfit in the apparent resistivity space (b) for the third iteration of the Wenner Schlumberger data acquired on line 9 (Res2dInv).

constrained inversion does not deliver a satisfactory model as the misfit pseudo section (Figure 4-39b) is not random and the difference between the error in the measured data and the misfit is large.

For line 9 alternative inversion parameters were used and the general trend in the misfit pseudo section is remarkably consistent. This may be because a section of the data is influenced by noise. The misfit pseudo sections that are not random cannot be caused by the choice of inversion parameters as many different inversion parameters gave spurious results. The relatively low apparent resistivities measured for the deepest layers in the middle of the pseudo section are the most likely explanation (Figure D-15 in Appendix D). This feature is also present in the dipole-dipole data (Figure D-16 in Appendix D). An alternative model is shown in Figure 4-40 where the L_2 norm is used with a different algorithm all together.

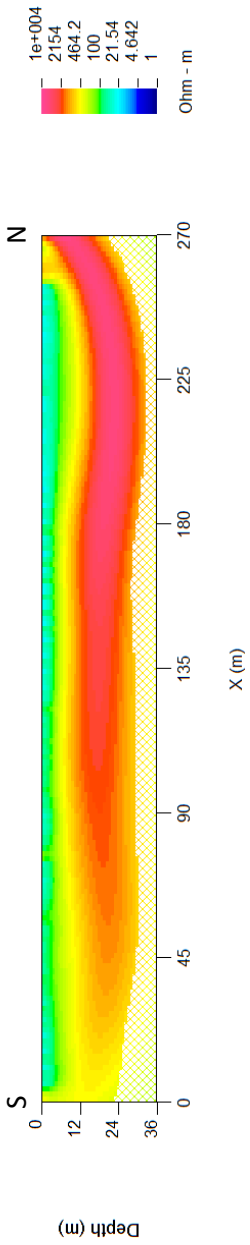


Figure 4-40: A model of the Wenner Schlumberger data from line 9, obtained using a different inversion algorithm (DCIP2D).

4.2.1.2 Dipole-dipole ER data along line 9

The model (Figure 4-41a) obtained from the smoothness-constrained inversion (see Appendix A for the Res2DInv settings) of the dipole-dipole data acquired on line 9 (same data as Figure D-16 in Appendix D) has a misfit of 4.7% after four iterations (see Appendix B: Figure A-9). The estimated data error is only 1.8%. The smoothness-constrained inversion does deliver a satisfactory model, as the misfit pseudo section (Figure 4-41b) is random. The.

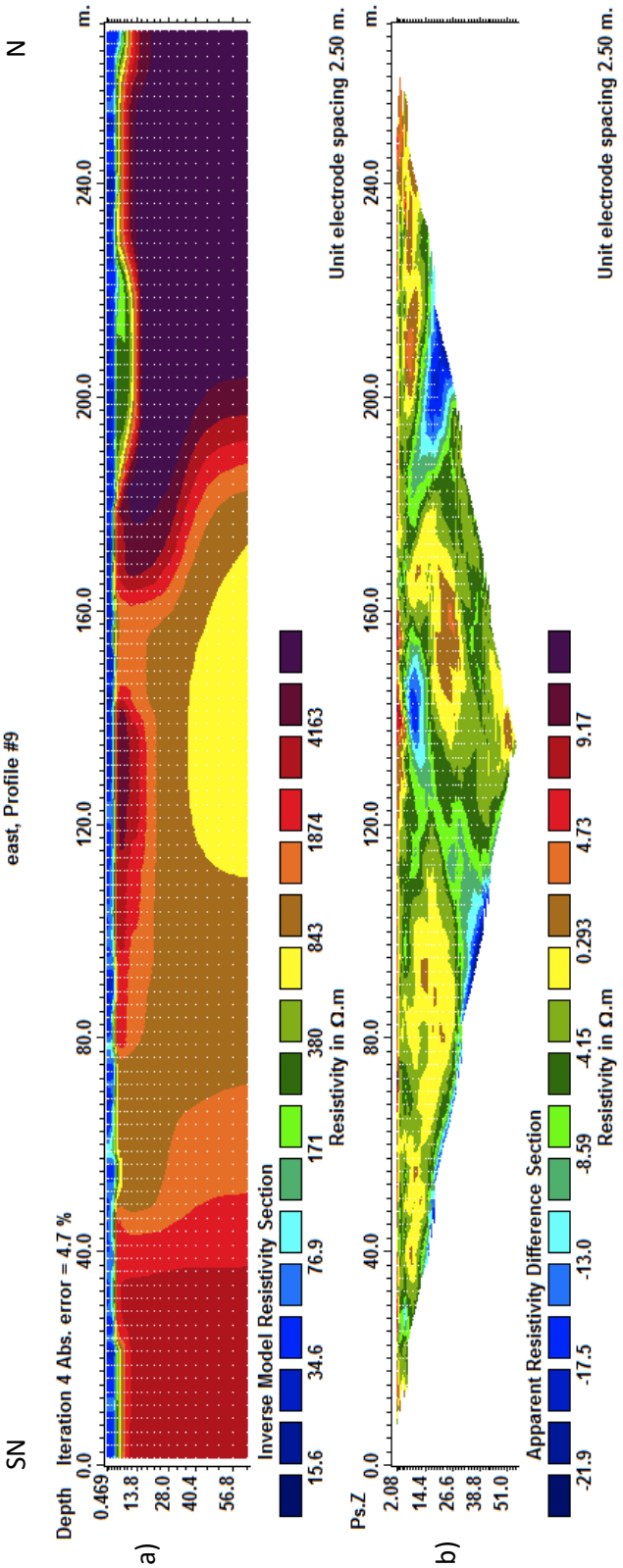


Figure 4-41: A model of resistivity (a) and a misfit in the apparent resistivity space (b) for the second iteration of the dipole-dipole data acquired along line 9 (Res2dInv).

model underinterprets the data as can be seen by the difference between the data error and the model misfit

The depth of investigation for the dipole-dipole arrays is shown in Figure 4-42. At shallow depths the two models used to calculate the DOI indices are very similar as can be seen at the DOI indices and density of contour lines in the depths shallower than 20 m. There are deeper depths where the compared models are similar up to depths of 80 m.

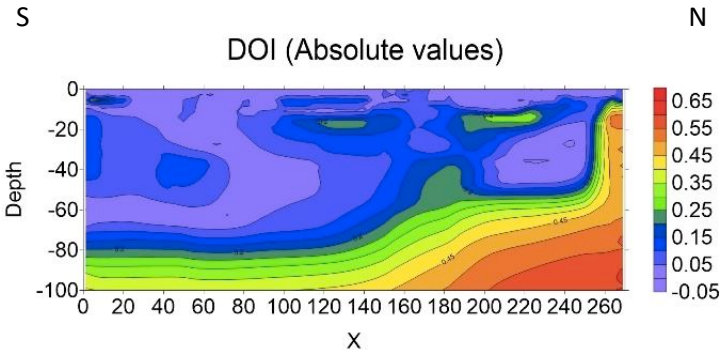


Figure 4-42: Different starting models produced similar model resistivities for the dipole-dipole data on line 9. The DOI index is shown.

4.2.1.3 Final model for line 9

In the models presented for the Wenner Sclumberger and dipole-dipole data, the first 5 m are the same. The final resistivity model is presented in Figure 4-43 (which is the Wenner Sclumberger model presented in Figure 4-40). The resistivities at greater depths cannot be reliably interpreted, as the models for the two arrays are different at these depths. The depth to bedrock for the data acquired on line 9 was not mapped to any degree of certainty and only the first layer is shown here. This layer is highly conductive compared to similar depths in the areas where profiles were done over the lavas (in the west of the site). This is likely due to a plume originating in the TSF propagating eastward. The low resistivities are also the cause for the low depth penetration. The first layer in this model has an *in situ* electrical resistivity of between 10 and 56 ohm.m.

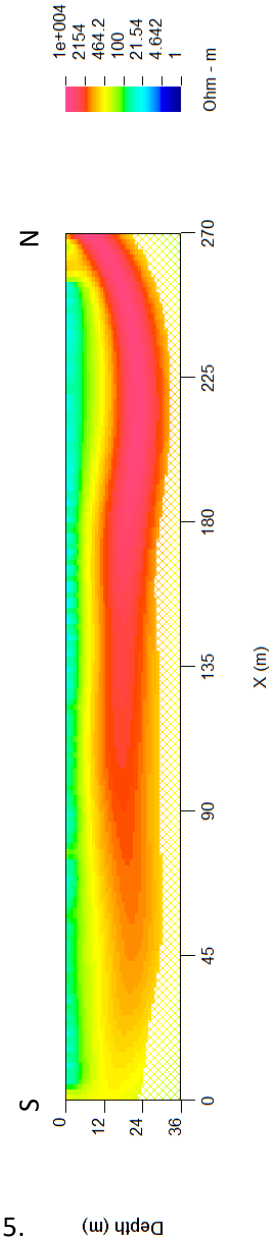


Figure 4-43: A model of the Wenner Schlumberger data (line 9) from line obtained using a different inversion algorithm (DCIP2D).

4.2.2 ER data along line 12

The data for line 12 are collected over lava (see Figure 1-1b for line position). The background resistivities (uncontaminated groundwater) for lines 5 and 6 (Subsection 4.2.3 and Subsection 4.2.4) are obtained from this line.

4.2.2.1 Wenner Schlumberger ER data along line 12

The model obtained (Figure 4-44a) from the smoothness-constrained inversion (see Appendix A for the Res2DInv settings) of the Wenner Schlumberger data acquired on line 12 (data in Figure D-17 in Appendix D) has a misfit of 3.5% after three iterations (see Appendix B: Figure A-10). The estimated data error is 6.0%. The misfit pseudo section (Figure 4-44b) is layered.

The data are remodelled and one alternative model (Figure 4-45a) was created with the following settings been changed from the ones listed in Appendix A: (i) the convergence limit for relative change in RMS error has been increased to 5%, (ii) the RMS convergence limit has been set to 1% and (iii) the model refinement has been set to "normal". The misfit pseudo section (Figure 4-45b) is more random than for the model obtained from the smoothness-constrained inversion.

From both the pseudo section and the two models presented here it is apparent that a simple layered geology is present underlying line 12. The DOI obtained from the smoothness-constrained inversion was calculated from models with misfit pseudo sections similar to the pseudo section in Figure 4-44 but, as the models in Figure 4-44 and 5-45 are so similar, it will not be presented here.

An alternative model is shown in Figure 4-46 where the L_2 norm is used with a different algorithm all together.

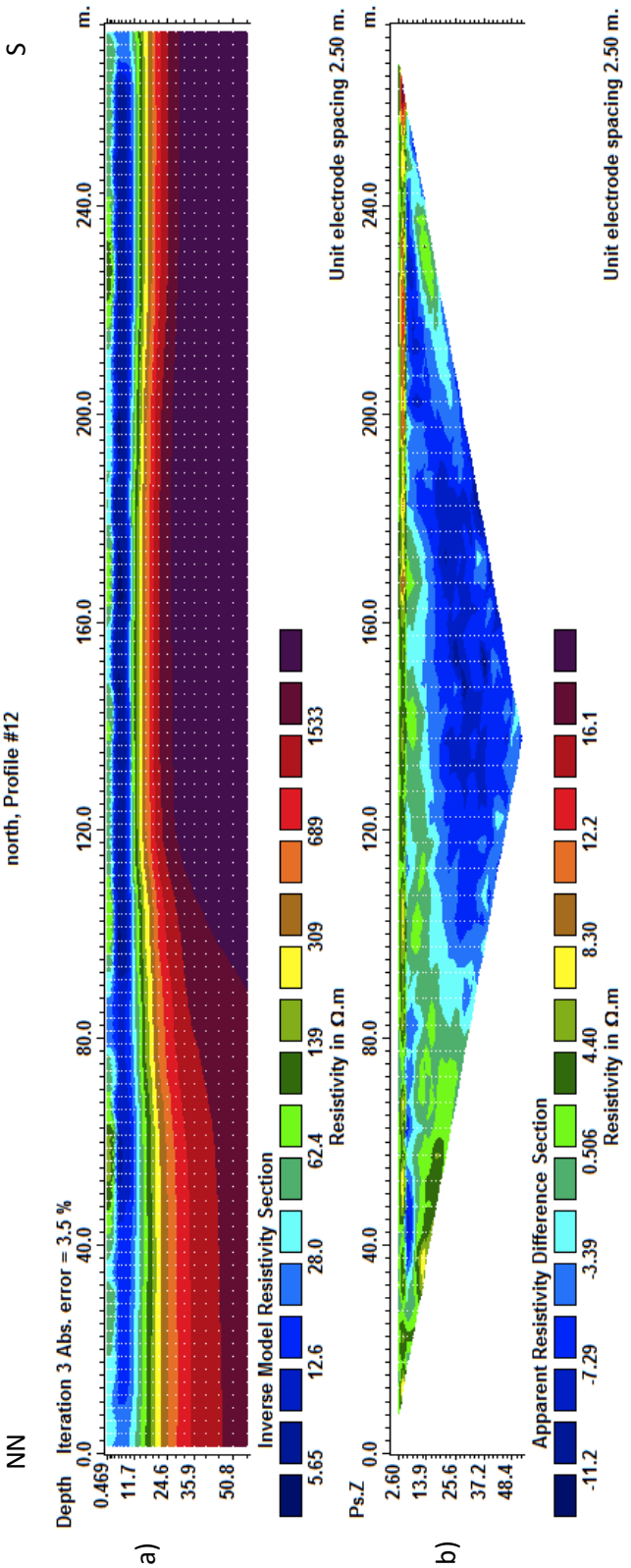


Figure 4-44: A model of resistivity (a) and the misfit in the apparent resistivity (b) for the third iteration of the Wenner Schlumberger data acquired along line 12 (Res2dInv).

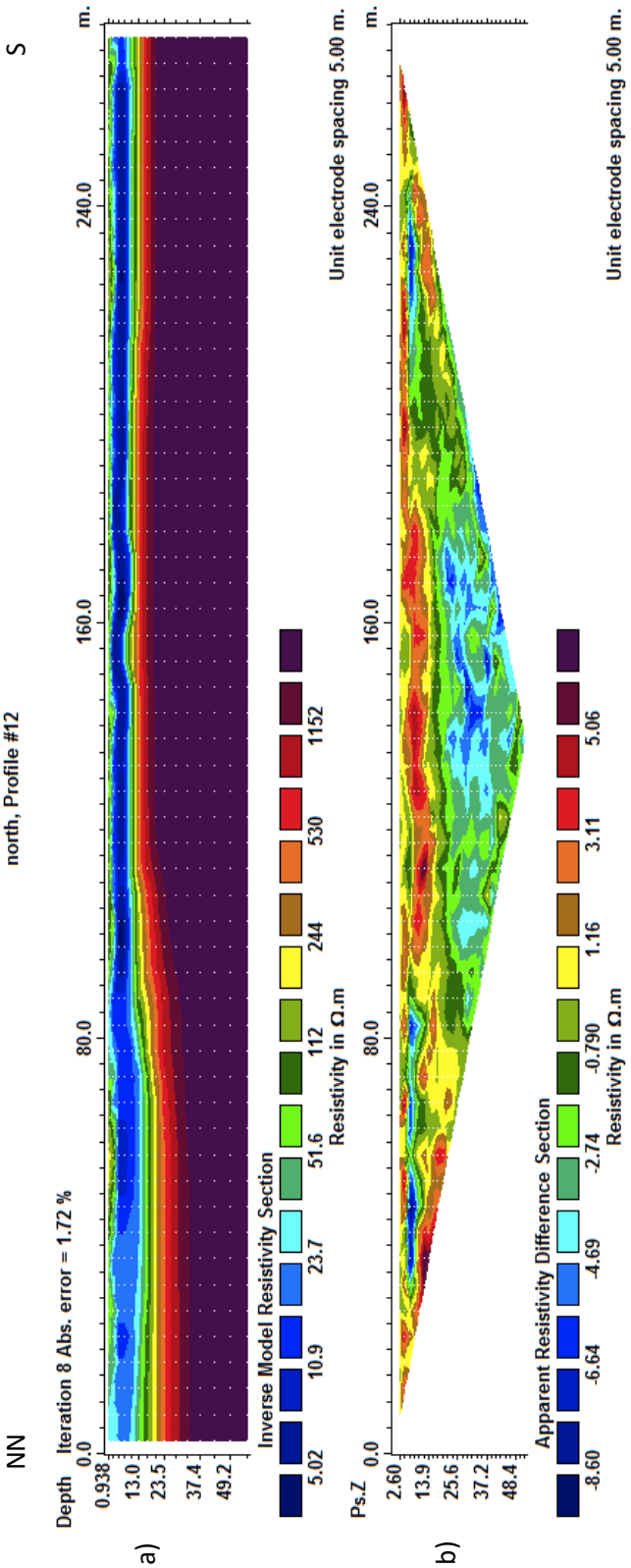


Figure 4-45: Alternative model for the Wenner Schlumberger data acquired on line 12 (Res2dInv).

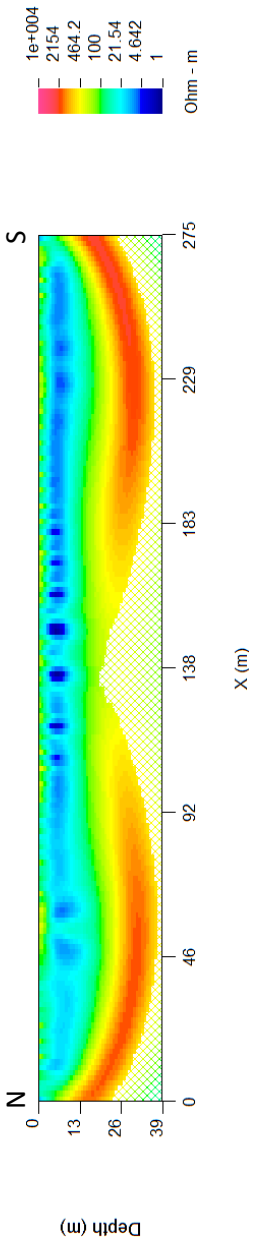


Figure 4-46: A model of the Wenner Schlumberger data from line 12 obtained using a different inversion algorithm (DCIP2D).

4.2.2.2 Dipole-dipole ER data along line 12

The model (Figure 4-47a) obtained from the smoothness-constrained inversion of the dipole-dipole data acquired on line 9 in (data in Figure D-18 in Appendix D) has a misfit of 3.4% after three iterations (see Appendix B: Figure A-11). The estimated data error is 40% due to the input current being low. The misfit pseudo section (Figure 4-47b) is random but if the data are inaccurate as this, the model over interprets the data.

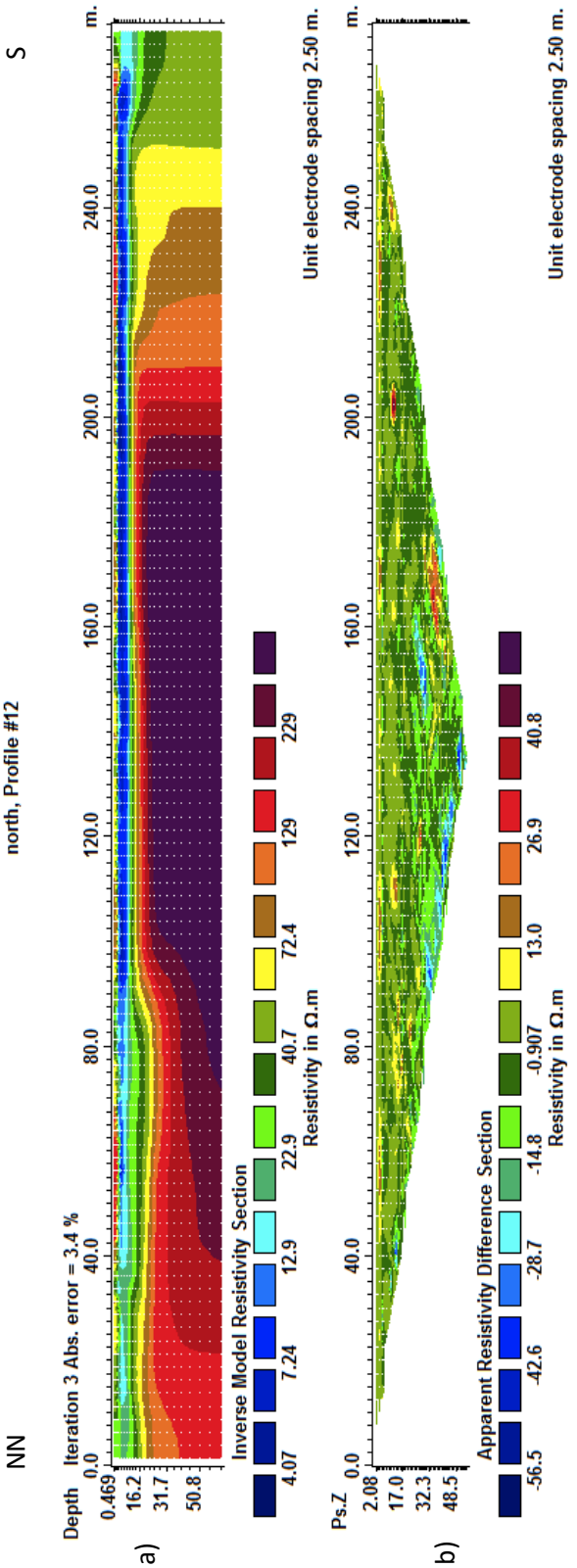


Figure 4-47: A model of resistivity (a) and the misfit in the apparent resistivity space (b) for the third iteration of the smoothness-constrained inversion of the dipole-dipole data on line 12 (Res2dInv).

DOI index for line 12 (Figure 4-48) shows the model (Figure 4-47) is sensitive to variations up to depths between 15 and 20 m.

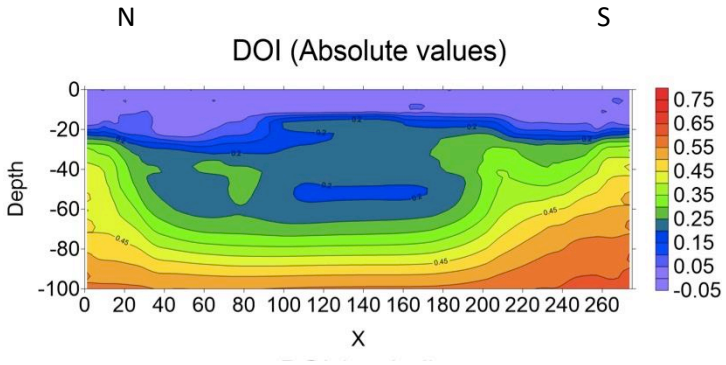


Figure 4-48: DOI indices for the resistivity data acquired with the dipole-dipole array on line 12.

4.2.2.3 Final model for line 12

In Figure 4-49 the final resistivity model is shown for the data acquired on line 12. This line is underlain by Ventersdorp lava and it is expected that the plume has not influenced the line. This can be seen from the relatively low SO_4 concentrations from the coloured contour map at the position of this line (between 2941 and 2951 ppm). The model provides three pieces of information. Firstly, it provides the background resistivity for the soils overlying the Ventersdorp lava that is 10 to approximately 56 ohm.m. This will be compared to the models for line 5 and line 6, which are expected to show influence by the AMD plume. Secondly, the depth to bedrock in the areas underlain by Ventersdorp lavas is apparent, and the rock is between 5 and 15 m below the surface. Thirdly, the resistivity of *in situ* Ventersdorp lava can be modelled and this is expected to be in excess of 100 ohm.m. This does not correlate well with the value that was obtained for the data acquired on line 1 (Section 5.1.1.2) of 1000 ohm.m. The model is expected to be smooth and this is the reason why the resistivity of the lava is underestimated in this model. The *in situ* electrical resistivity of the water-saturated soil is between 3 to 56 ohm.m.

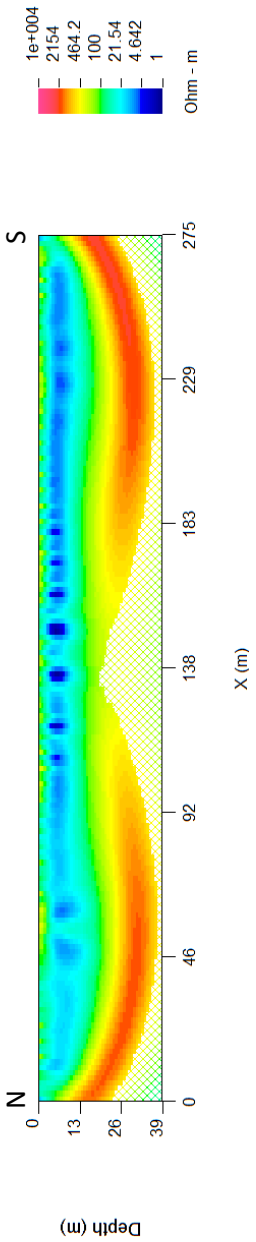


Figure 4-49: Final resistivity model for line 12, the Wenner Schlumberger model from Figure 4-46.

4.2.3 ER data along line 5

The data for line 5 are collected over lava (see Figure 1-1b for line position). The resistivities expected for the geological units containing contaminated groundwater are supposed to be much lower than for line 12 (as discussed in Chapter One).

4.2.3.1 Wenner Schlumberger ER data along line 5

The model (Figure 4-51a) obtained from the smoothness-constrained inversion (see Appendix A for the Res2DInv settings) of the Wenner Schlumberger data acquired on line 5 (data in Figure D-19 in Appendix D) has a misfit of 3.5% after three iterations (see Appendix B: Figure A-12). The estimated data error is only 2.6%. The misfit pseudo section (Figure 4-51b) has a trend and shows that the margins of the model space are not well defined. The hint of a dipping layer present in the data (and in the misfit pseudo section), results in a dip in the model as can also be seen in the model (Figure 4-51a).

The DOI section for the Wenner Schlumberger data on line 5 in Figure 4-50 must be considered before the model can be interpreted. At shallow depths the models are very similar as can be seen at the DOI indices and density of contour lines in the depths shallower than 20 m.

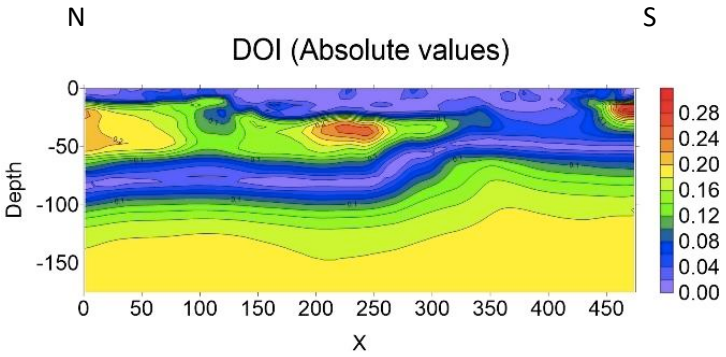


Figure 4-50: DOI indices for the resistivity data acquired with the Wenner Schlumberger array on line 5.

In Figure 4-52 an alternative model for the Wenner Schlumberger data is shown. The models are similar for the two algorithms. This confirms the model used for interpretation below.

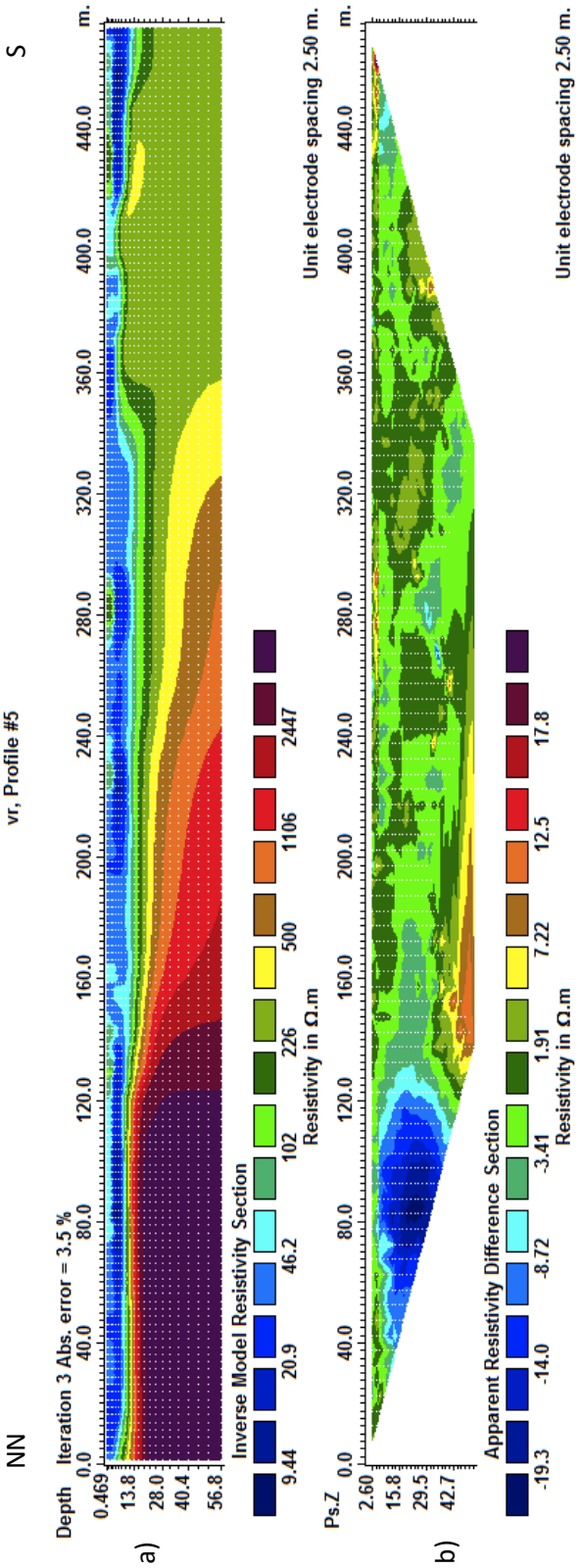


Figure 4-51: A model of resistivity (a) and the misfit in the apparent resistivity space (b) for the third iteration for the Wenner Schlumberger data from line 5 (Res2dInv).

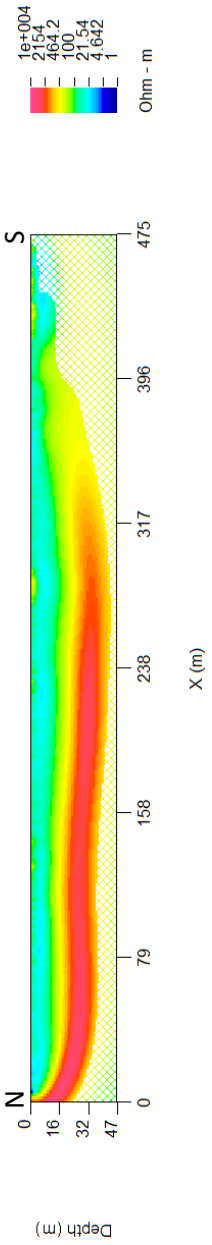


Figure 4-52: A model of the Wenner Schlumberger data from line 5 obtained using a different inversion algorithm (DCIP2D).

4.2.3.2 Dipole-dipole ER data along line 5

The model (Figure 4-53a) obtained from the smoothness-constrained inversion (see Appendix A for the Res2DInv settings) of the dipole-dipole data acquired on line 5 (data in Figure D-20 in Appendix D) has a misfit of 3.7% after three iterations (see Appendix B: Figure A-13). The estimated data error is 16.4%. The misfit pseudo section (Figure 4-53b) is random. The data only start 200 m along the profile of the Wenner Schlumberger data. The reason for this is the limited field time available.

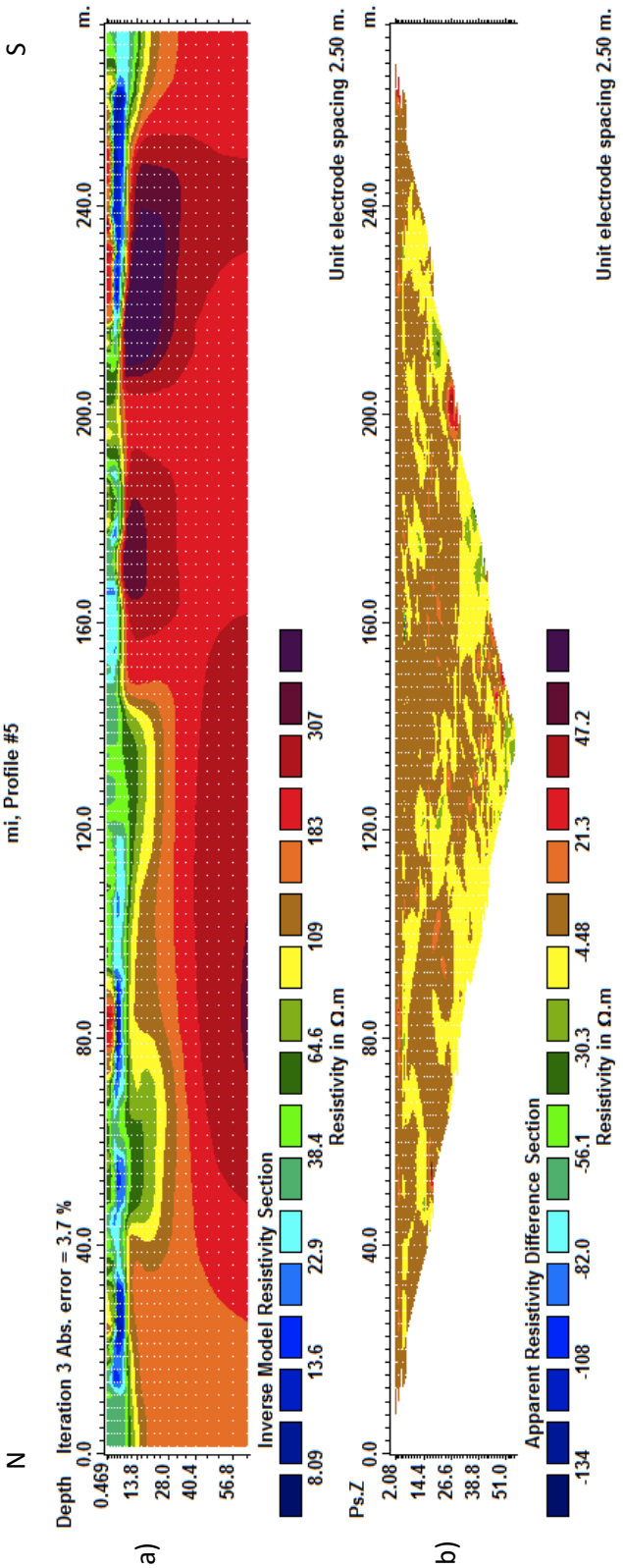


Figure 4-53: A model of resistivity (a), and a misfit in the apparent resistivity space (b) for the second iteration of the inversion of the dipole-dipole data along line 5 (Res2dInv).

The DOI for the dipole-dipole arrays (Figure 4-54a) shows that at shallow depths the models are very similar as can be seen at the DOI indices and density of contour lines in the depths shallower than 10 m. Most of the model space can reliably be interpreted up to 40 m.

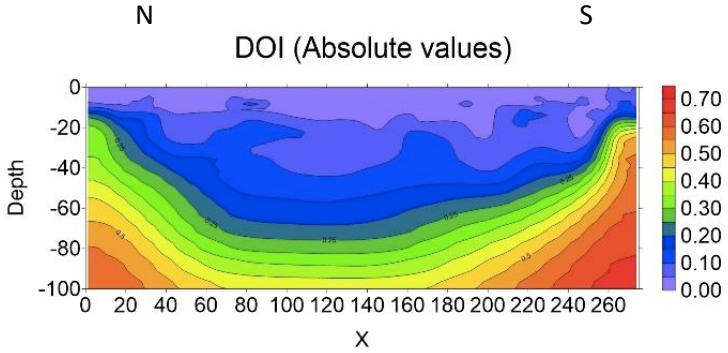


Figure 4-54: DOI indices for the resistivity data acquired with the dipole-dipole array on line 5.

The dipole-dipole models and the Wenner Schlumberger models differ quite dramatically. An alternative model for the dipole-dipole data (Figure 4-55) are similar to the models from the data acquired using the Wenner Schlumberger data but only for the most shallow data. The models presented for the data acquired on line 5 demonstrate a problem where many different models have been generated using similar inversion parameters. The models produced by the Wenner Schlumberger and by the dipole-dipole data on line 5 have little in common at depth. Either one (or both) have been corrupted by noise to such an extent that modelling is not possible. This is not true for shallow data and deeper depths are ignored for the purpose of interpretation.

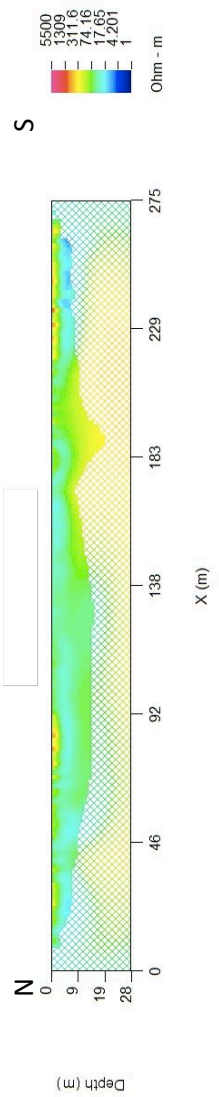


Figure 4-55: A model of the dipole-dipole data from line 5 obtained using a different inversion algorithm (DCIP2D).

4.2.3.3 Final model for line 5

In Figure 4-56 the final resistivity model is shown for the data acquired on line 5. This model shows simple geology. Although the depth to bedrock has been smeared by the smooth inversions, this is presented as the final model as the depth to bedrock was not well resolved in the robust (or sharp or blocky) inversion schemes. This line lies immediately adjacent to the TSF and the relatively high conductivity that is present in the first layer of the model is from the plume emanating from the western edge of the

TSF. The *in situ* electrical resistivity of the model (interpreted as water-saturated soil) is between 10 to 100 ohm.m. At depth (at 120 m along the profile) the resistivities are as high as 1000 ohm.m (and higher). This corresponds well with the resistivity found for the lavas from the data on line 1 (Section 5.1.1.2).

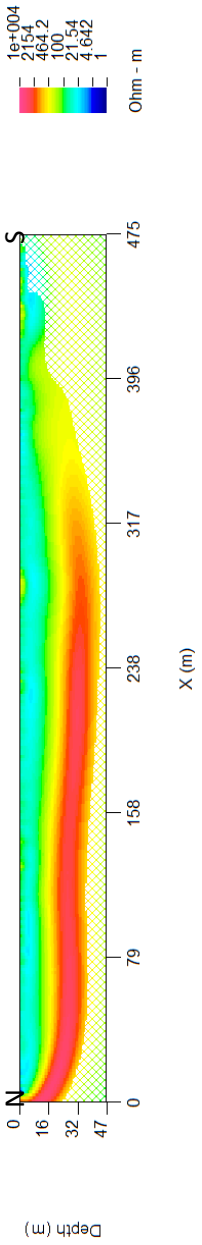


Figure 4-56: Final resistivity model for line 5, the Wenner Schlumberger model from Figure 4-52 (DCIP2D).

The conductivity of the first layer in the model is higher than the model for line 12 (Figure 4-52), where the groundwater is expected to have been affected by pollutants. The plume also affects the area around line 12. It is not possible to compare these

directly as the resistivities occur over a range in the first layer on these two lines with the resistivity for the first layer in line 5 having a upper and lower bound higher than the bounds for line 12. The upper bound for that model on line 5 (100 ohm.m) is higher than the upper bound for line 9 (56 ohm.m). The lower bound for these two lines is equal.

4.2.4 ER data along line 6

The data for line 6 are collected over lava (see Figure 1-1b for line position). The resistivities expected for the geological units containing contaminated groundwater are supposed to be much lower than for line 12 (as discussed in Chapter One) and if it is lower than for line 5, it will show that the resistivity increases with distance form the TSF. The resistivity is correlated with TDS and the assumption will then be that the TDS has decreased.

4.2.4.1 Wenner alpha ER data along line 6

The model (Figure 4-57a) obtained from the smoothness-constrained inversion (see Appendix A for the Res2DInv settings) of the Wenner alpha data acquired on line 6 (Figure D-23 in the appenix) has a misfit of 4.8% after three iterations (see Appendix B: Figure A-14). The estimated data error is only 1.2% and the model underinterprets the data. The misfit pseudo section (Figure 4-57) has a strong trend and is not suitable for interpretation. The data were acquired only on the last section of the profile line where the dipole-dipole data and Wenner Schlumberger data were acquired.

An alternative model (Figure 4-58a) obtained by using slightly different inversion parameters is used. This model is similar to Figure 4-57a with improvement in the misfit and a more random misfit pseudo section (Figure 4-58b). The following setting have been changed fro the ones listed in Appendix A: (i) the convergence limit for relative change in RMS error has been increased to 5%, (ii) the RMS convergence limit has been set to 1% and (iii) the model refinement has been set to “normal”. This inversion (delivering the sharp model in Figure 4-58a) corroborates the smooth model shown in Figure 4-57a.

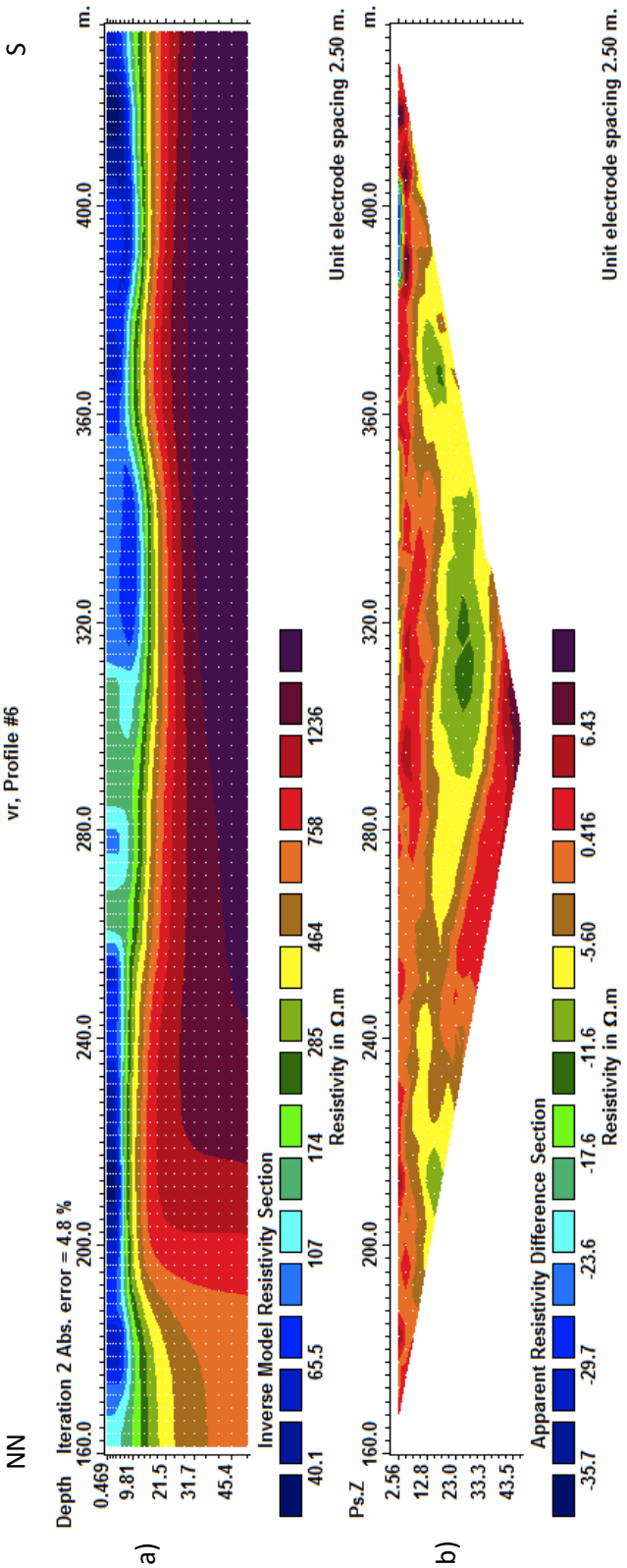


Figure 4-57: A model of resistivity (a) and the misfit in the apparent resistivity space (b) for the second iteration of the Wenner alpha data acquired on line 6 (Res2dInv).

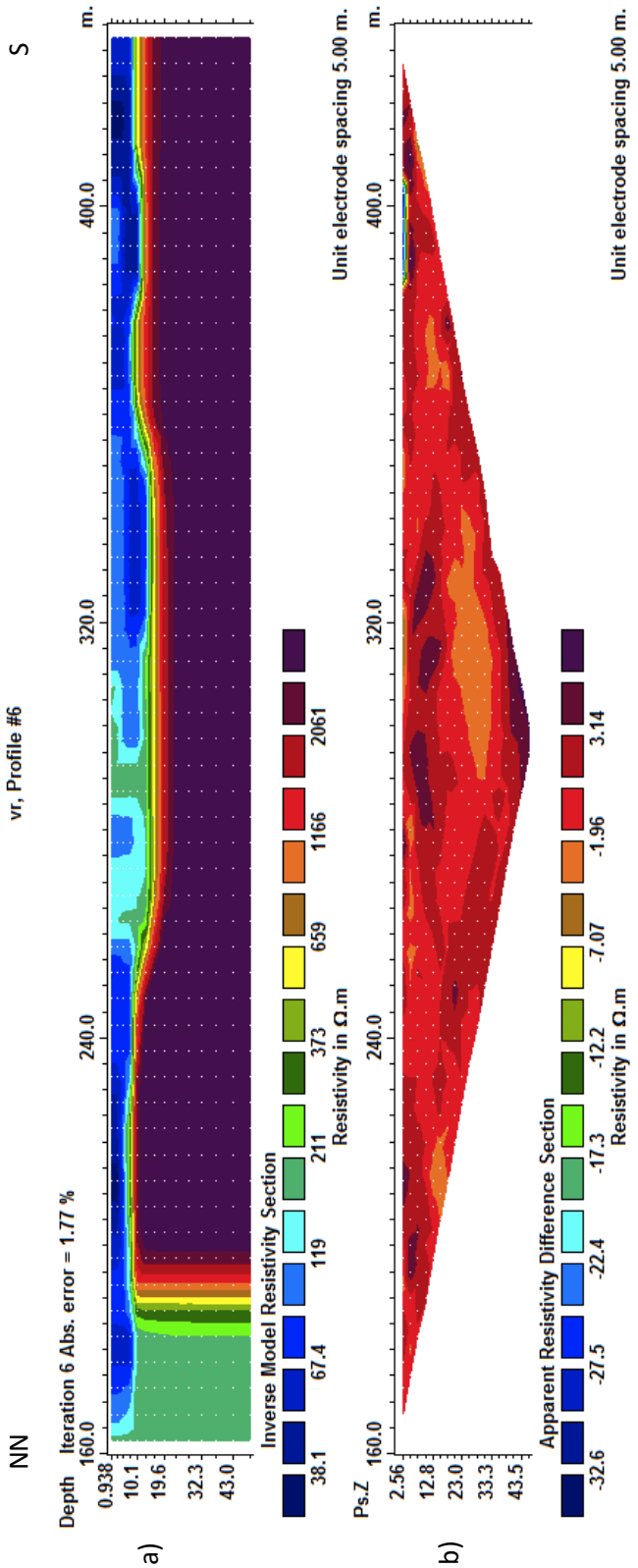


Figure 4-58: A model of resistivity (a) and the misfit in the apparent resistivity space (b) for the fourth iteration of Wenner alpha data acquired on line 6 (Res2dInv).

An alternative model for the Wenner alpha data (Figure 4-59) is similar for the two algorithms. This confirms the model used for interpretation below.

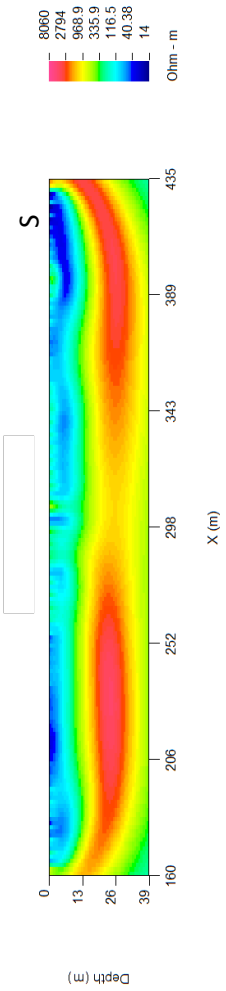


Figure 4-59: A model of the Wenner alpha data from line 6 obtained using a different inversion algorithm (DCIP2D).

4.2.4.2 Wenner Schlumberger ER data along line 6

The model obtained from the smoothness-constrained inversion (see Appendix A for the Res2DInv settings) of the Wenner Schlumberger data acquired on line 6 in Figure 4-60a (same data as Figure D-21 in Appendix D with some points removed) has a misfit of 2.9% after three iterations (see Appendix B: Figure A-15), shown in Figure 4-60b. The estimated data error is only 1.6% and the model underinterprets the data, but only slightly. The misfit pseudo section is shown in Figure 4-60c. The misfit pseudo section is random.

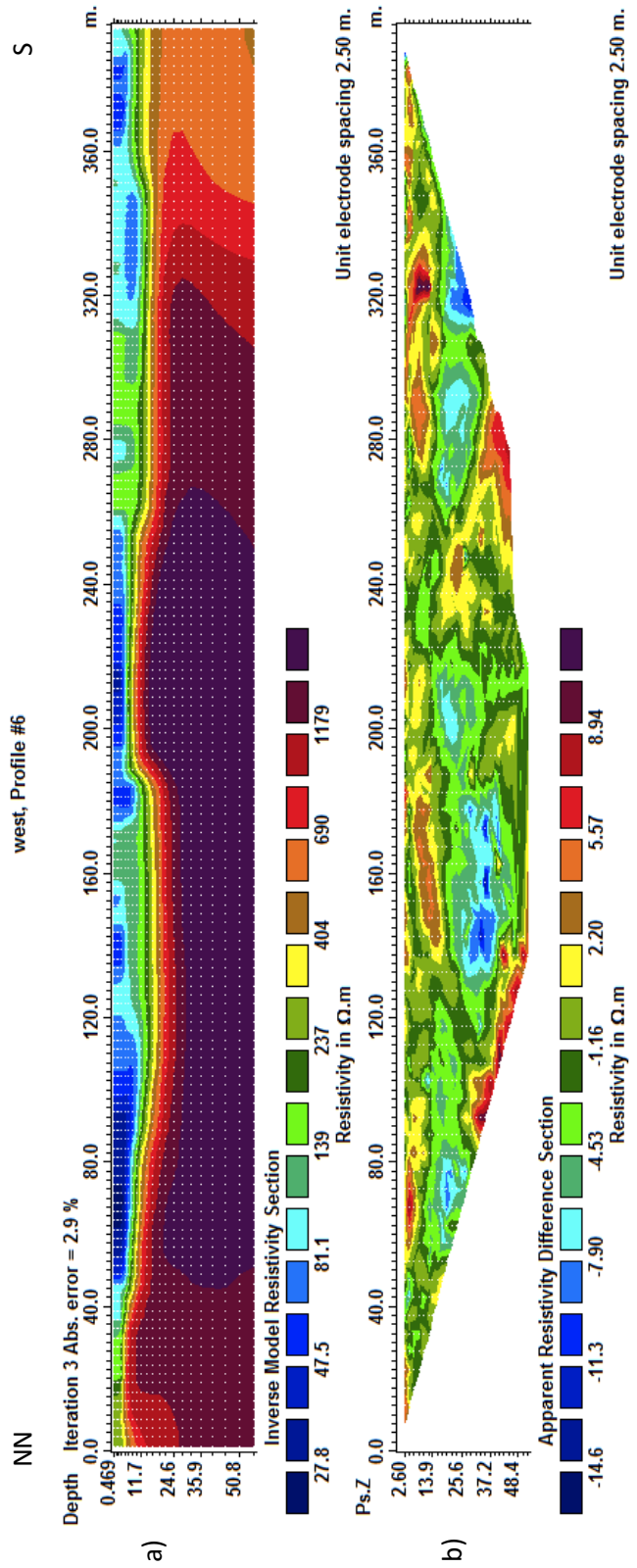


Figure 4-60: A model of resistivity (a) and the misfit in the apparent resistivity space (b) for the third iteration of the Wenner Schlumberger data of line 6 (Res2dInv).

The misfit sections shown here confirm the model presented in Figure 4-60b but a model is presented (Figure 4-61) obtained from the same data, using a different inversion scheme.

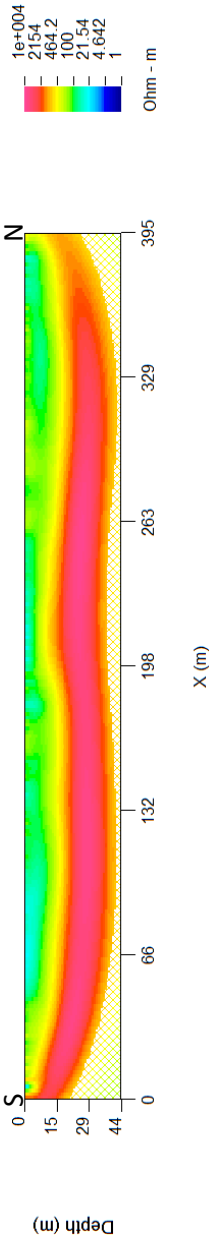


Figure 4-61: A model of the Wenner Schlumberger data from line 6, obtained using a different inversion algorithm (DCIP2D).

4.2.4.3 Dipole-dipole ER data along line 6

The model (Figure 4-62a) obtained from the smoothness-constrained inversion (see Appendix A for the Res2DInv settings) of the dipole-dipole data acquired on line (data in

Figure D-22 in Appendix D) has a misfit of 4.0% after four iterations (see Appendix B: Figure A-16). The estimated data error is only 9.1% and the model overinterprets the data. The misfit pseudo section (Figure 4-62b) has no trend, as for the Wenner Schlumberger data.

In Figure 4-63 the DOI is shown for the dipole-dipole data. At shallow depths the models (for similar inversion setting with large differences in initial model resistivity) are very similar as can be seen at the DOI indices and density of contour lines in the depths shallower than 10 m. At the centre of the spreads of resistivity data the depth investigated increases slightly to 20 m. The feature in the centre of the model space is due to chance. As was seen in some previous models the model is theoretically sensitive to changes here, although a cursory glance at the models for this region show that they are consistent in terms of their resistivities (Figure 4-62b and the models for the Wenner alpha and Wenner Schlumberger data in Figure 4-58a and Figure 4-60b). So, the survey would have mapped variations in this area quite well, but the variations do not seem to exist.

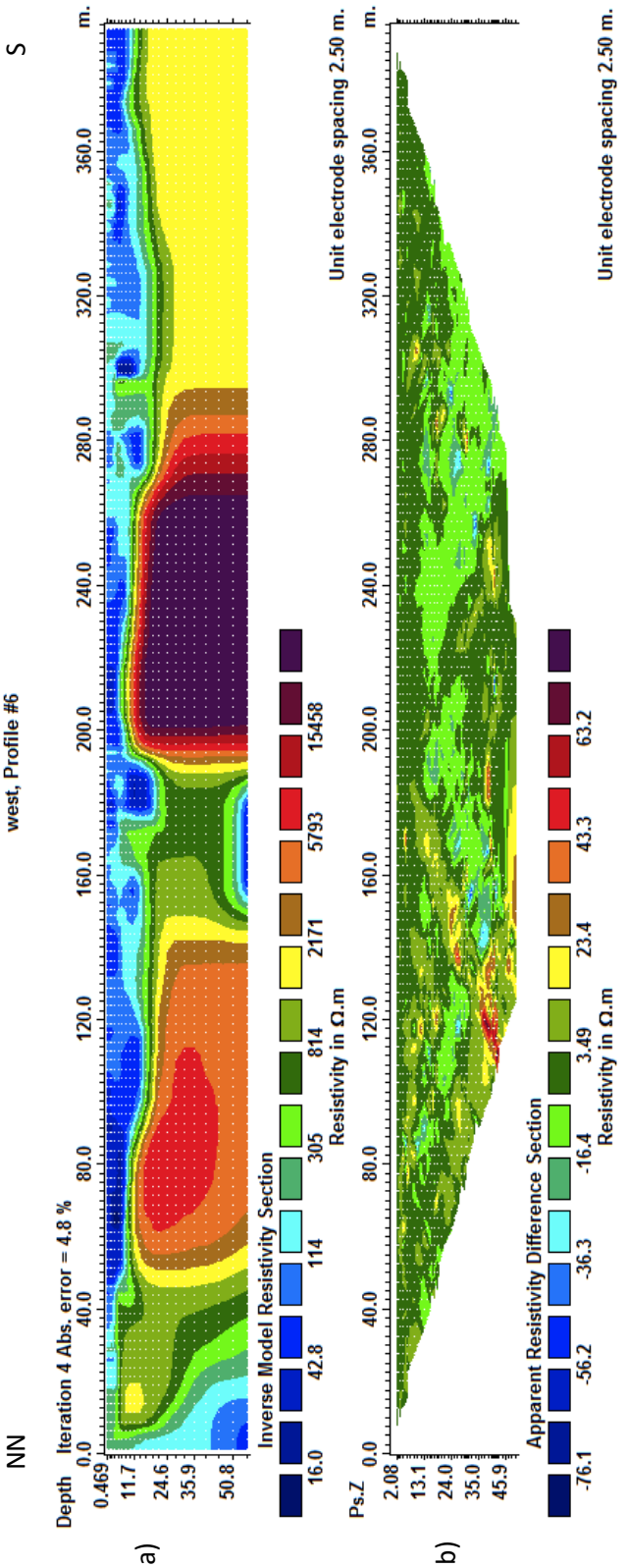


Figure 4-62: A model of resistivity (a) and the misfit in the apparent resistivity space (b) for the fourth iteration of the dipole-dipole data acquired on line 6 (Res2dInv).

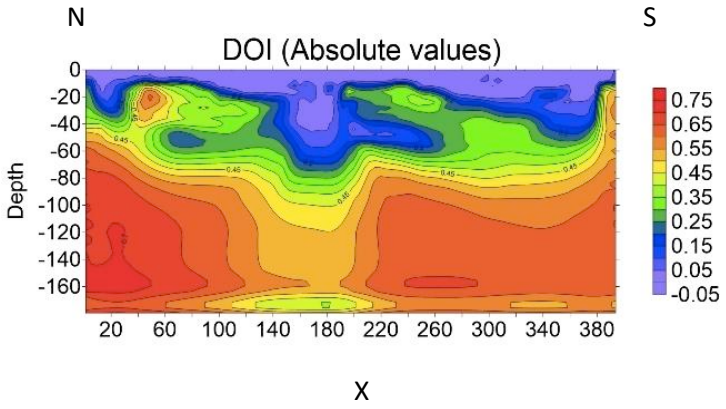


Figure 4-63: Different starting models produced similar model resistivities for the dipole-dipole data acquired on line 6 for depths up to 10 m with the DOI indices plotted.

4.2.4.4 Final model for line 6

In Figure 4-64 the final resistivity model is shown for the data acquired on line 6. The water in the first layer in Figure 4-64 is a combination of water coming from the TSF and seepage into the aquifer from the surface. This is because of the distance between the plume and the line; more rainwater fell between the plume and this line, than for any of the others, which creates the opportunity for the water to be mixed with fresh rainwater. The polluted water is flowing from the TSF towards the Schoonspruit and will flow through a zone where woodland tree species have been established. These trees were too young (in February 2014) to have impacted the polluted groundwater. The increase in resistivity, could alternatively be caused by the normal attenuation of the amount of pollutants in the groundwater away from the source of the plume, or from noise in the data (the line runs parallel to a railway line). Resistivity method is influenced by industrial installations such as powered train lines, but the influence is small e.g. Dahlin (1996).

The first layer (groundwater-saturated soil) has an *in situ* electrical resistivity of 10 to 177 ohm.m. The depth to bedrock have not been extensively mapped, and if the grey layer in Figure 4-63 is bedrock, it does not coincide well with the previous in situ resistivities of the lava of 1000 ohm. (i.e. it underestimates the resistivity).

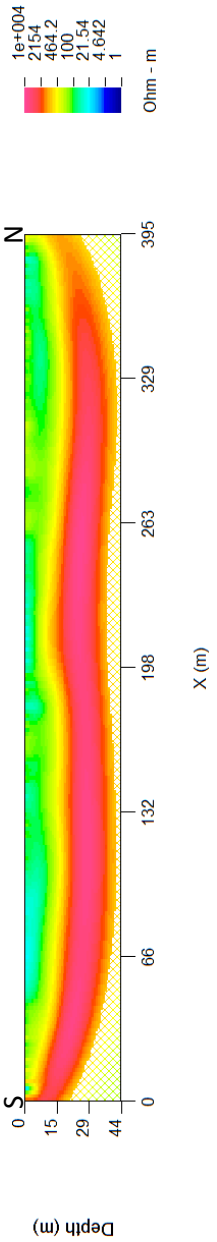


Figure 4-64: A model of the Wenner Schlumberger data from line 6 (DCIP2D).

4.3 Electrical resistivity profile in the direction of the groundwater flow in the dolomites

In this section the modelling and interpretation of the three lines acquired in the direction of the groundwater flow in and over the dolomite are discussed. Only electrical resistivity data are available for these three lines. These lines are acquired parallel to each other in (successively) uncontaminated, to contaminated to phytoremediated groundwater. Positioning of the four lines are shown in Figure 1-1 and Figure 3-4.

Borehole data are plotted in a coloured contour map in Figure 3-4 in addition to the position of a *Tamarix* woodland established by the Wits Woodlands Project. The lines are presented consecutively from north to south. The numbering is a bit confusing, but Figure 1-1b should clear this up.

4.3.1 ER data along line 11

The data for line 11 are collected over dolomite (see Figure 1-1b for line position). The background resistivities (uncontaminated groundwater) for lines acquired in Section 5.3 are contained in the data for this line.

4.3.1.1 Wenner Sclumberger ER data along line 11

The model (Figure 4-65a) obtained from the smoothness-constrained inversion (see Appendix A for the Res2DInv settings) of the Wenner Schlumberger data acquired on line 11 (data in Figure D-24 in Appendix D) has a misfit of 4.4% after three iterations (see Appendix B: Figure A-17). The estimated data error is only 1.3%. The misfit pseudo section shows a trend (Figure 4-65b). This is especially problematic in the area of the model (Figure 4-65a) where a conductor underlies the resistor. Many of the models generated from inversion (using either set of the inversion parameters that have been used) deliver this in the misfit. One alternative with different inversion parameters is shown in Figure 4-66a with the misfit shown in Figure 4-66b. The changed inversion parameters are that four nodes were used between adjacent electrodes (instead of 2). The misfit pseudo section is more random than before and this model is superior for this reason. The model in Figure 4-66a corroborates the model in Figure 4-65b as they are similar.

Another data set is available for line 11 and the DOI for the Wenner Schlumberger data is not shown because of this.

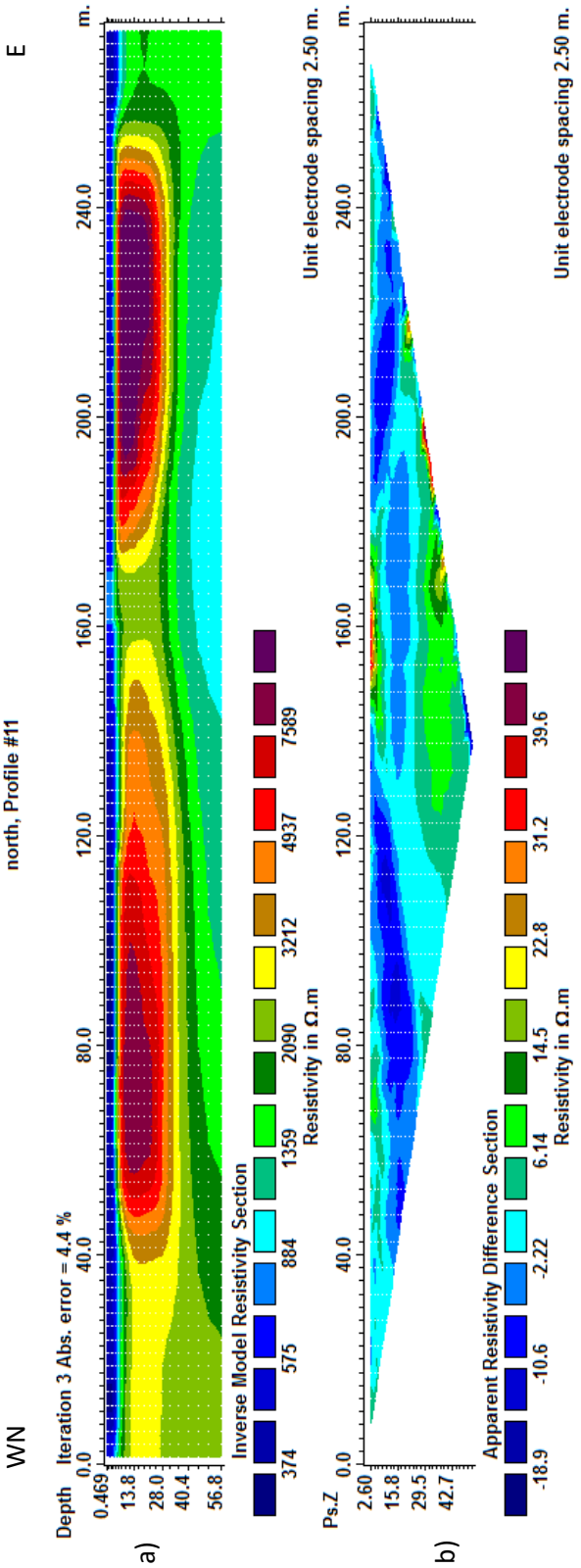


Figure 4-65: A model of resistivity (a) and the misfit in the apparent resistivity space (b) after the third iteration of the Wenner Sclumberger data acquired on line 11 (Res2dInv).

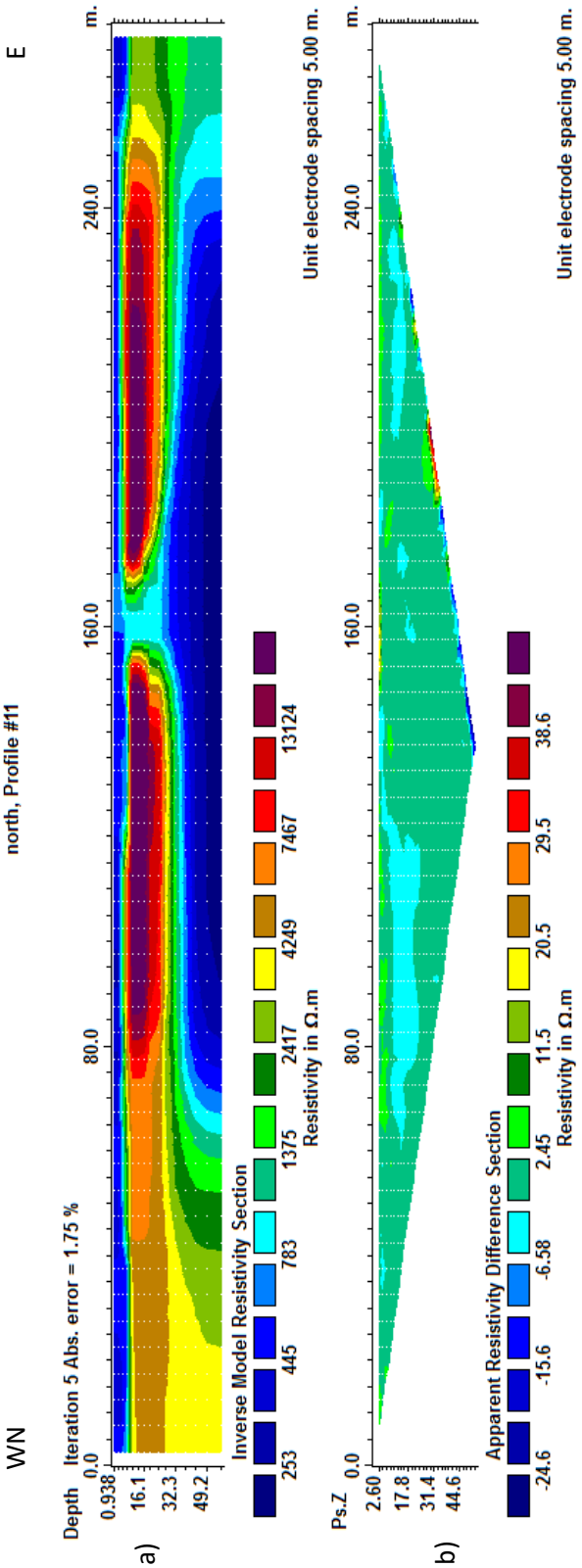


Figure 4-66: Alternative model for the Wenner Schlumberger data acquired on line 11 (a) with the misfit in apparent resistivity space (b) (Res2dInv).

4.3.1.2 Dipole-dipole ER data along line 11

The model (Figure 4-68a) obtained from the smoothness-constrained inversion (see Appendix A for the Res2DInv settings) of the dipole-dipole data acquired on line 11 (data in Figure D-25 in Appendix D) has a misfit of 3.6% after four iterations (see Appendix B: Figure A-18). The estimated data error is only 1.6%. The misfit pseudo section (Figure 4-68b) is random. The model shows the same trend as the Wenner-Schlumberger data.

In Figure 4-67 the DOI section for the dipole-dipole data on line 11 is shown. The model is sensitive to variations up to depths of 40 to 80 m and this reiterates that the models needed to explain the data from the inversions used are all similar.

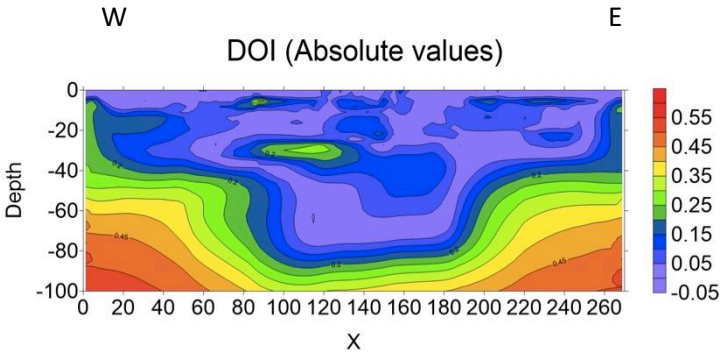


Figure 4-67: DOI indices for the resistivity data acquired with the dipole-dipole array on line 11.

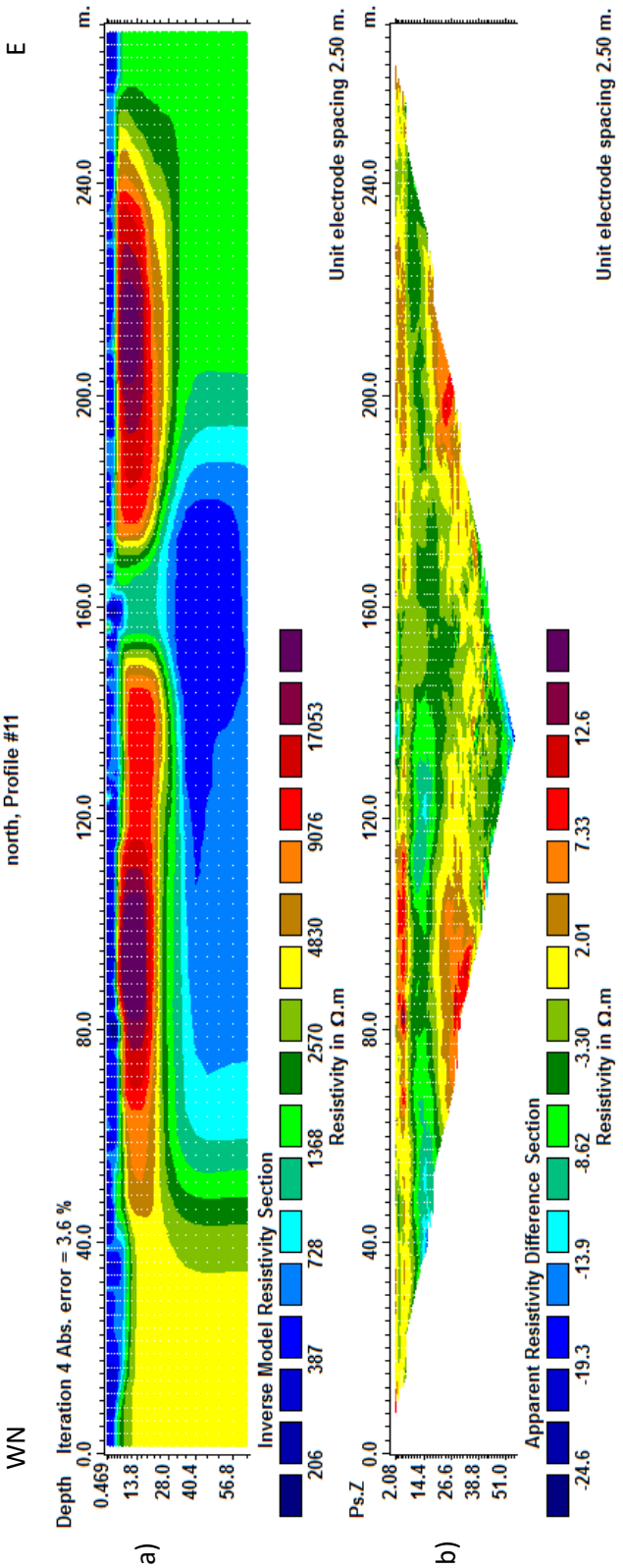


Figure 4-68: A model of resistivity (a) and the misfit in the apparent resistivity space (b) for the fourth iteration of the dipole-dipole data acquired along line 11 (Res2dInv).

4.3.1.3 Final model for line 11

In Figure 4-69 the final resistivity model is shown for the data acquired on line 11. The models presented here for line 11 are expected to show near-surface conditions of groundwater unaffected by the influence of contaminants from the TSF. The following two lines (discussed below in this section) show conditions where the groundwater is expected to have been influenced by the TSF plume and remediation efforts. At approximately 160 m along the profile of line 11 a possible fault structure is present in the resistivity model. The material with a resistivity above 1000 ohm.m is interpreted as bedrock (black in Figure 4-69). The material overlying the rock is interpreted as water saturated soils. This has an electrical resistivity of between 281 and 794 ohm.m.

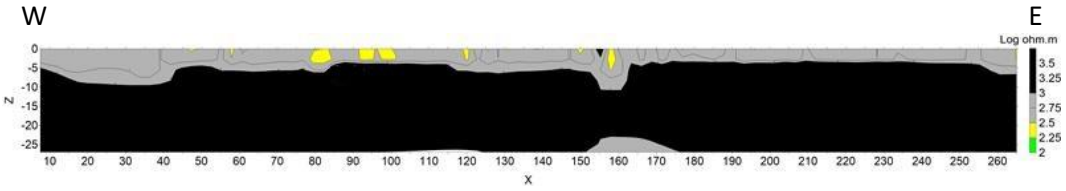


Figure 4-69: Final resistivity model for line 11.

The depth to bedrock has been smoothed out but lies between about 1 m and 8 m below the surface. Slightly more detail for line 11 is shown in Figure 4-70 with a different colour bar. In this model the black material is interpreted as the rock and the green material as the groundwater-saturated soil. The two shades of grey are either a weathered zone on the rock or the inversion process smoothed out the contact.

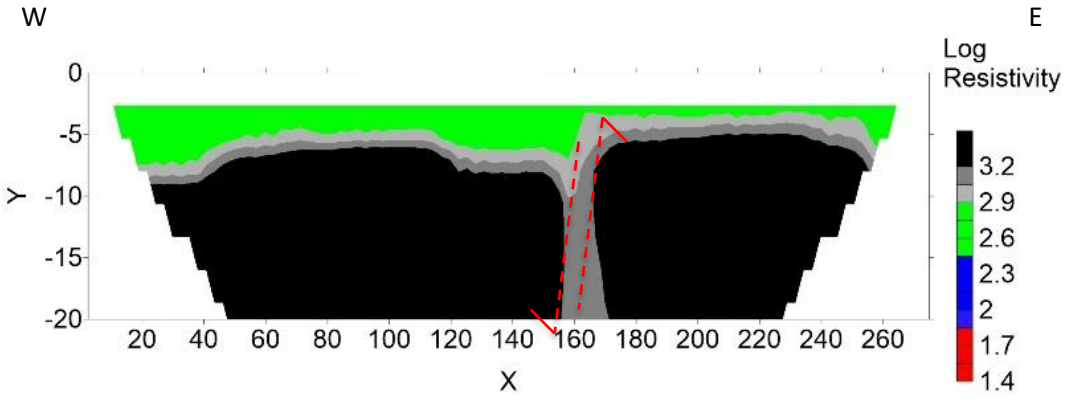


Figure 4-70: Final resistivity model for line 11 with the position and throw of the fault (the vertical scale has been increased).

4.3.2 ER data along line 8

The data for line 8 are collected over dolomite (see Figure 1-1b for line position). The groundwater that is expected to fill the pore spaces in the rock underneath this line, are expected to be highly contaminated and electrically conductive.

4.3.2.1 Wenner Sclumberger ER data along line 8

The model (Figure 4-71a) obtained from the smoothness-constrained inversion (see Appendix A for the Res2DInv settings) of the Wenner Schlumberger data acquired on line 8 (data in Figure D-26 in Appendix D) has a misfit of 3.0% after four iterations (see Appendix B: Figure A-19). The estimated data error is only 1.2%. The misfit pseudo section (Figure 4-71c) has a slight trend in the data in that it is layered with large positive misfit overlying a small positive misfit overlying a medium sized positive misfit. This existence of the trend renders the model uninterpretable.

An alternative model (Figure 4-72a) is created using different inversion parameters (the nodes between adjacent electrodes were doubled to 4). The misfit after six iterations is 2.3% but the misfit pseudo section (Figure 4-72b) is not random There is a separate data set available for this line and the models obtained from the dipole-dipole data will be used for interpretation of this section.

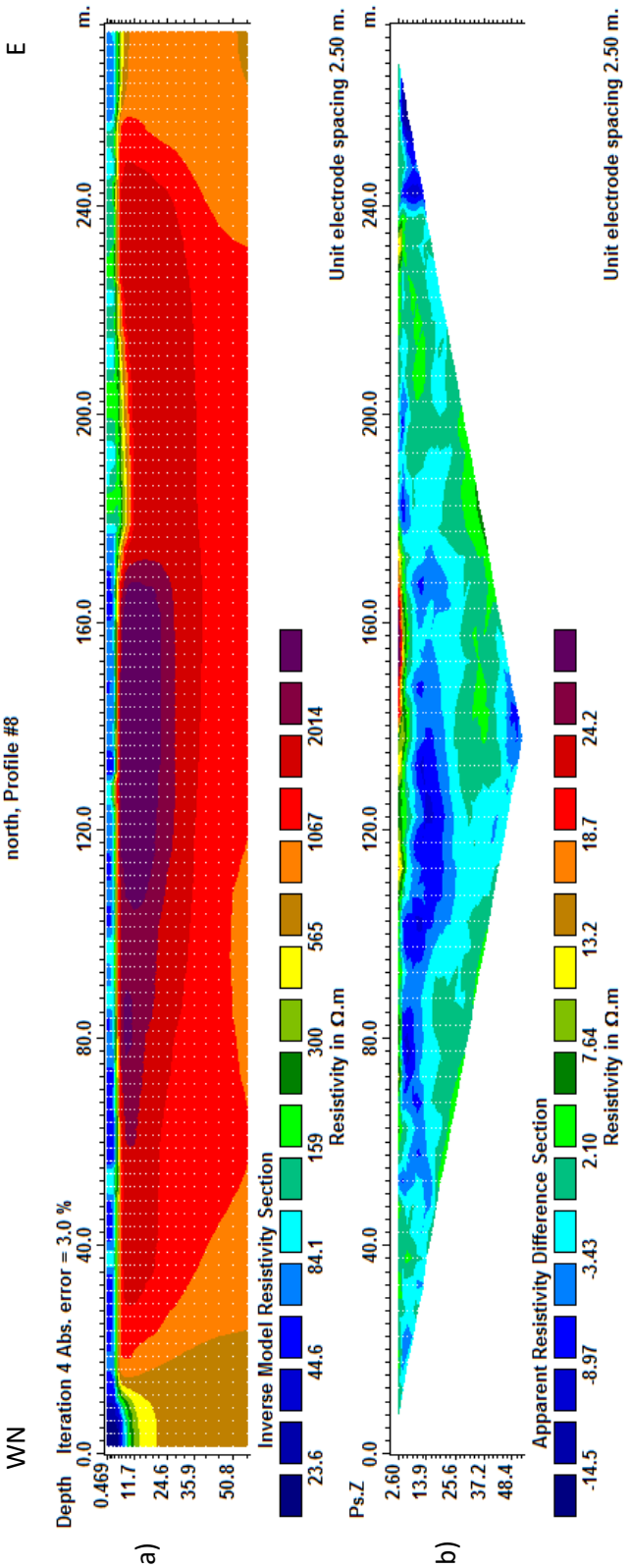


Figure 4-71: The model obtained after four iterations of running the inversion scheme on the Wenner Schlumberger data acquired on line 8. The figure shows a calculated model (a) and the difference between the observed and calucated apparent resisitiivity values (b).

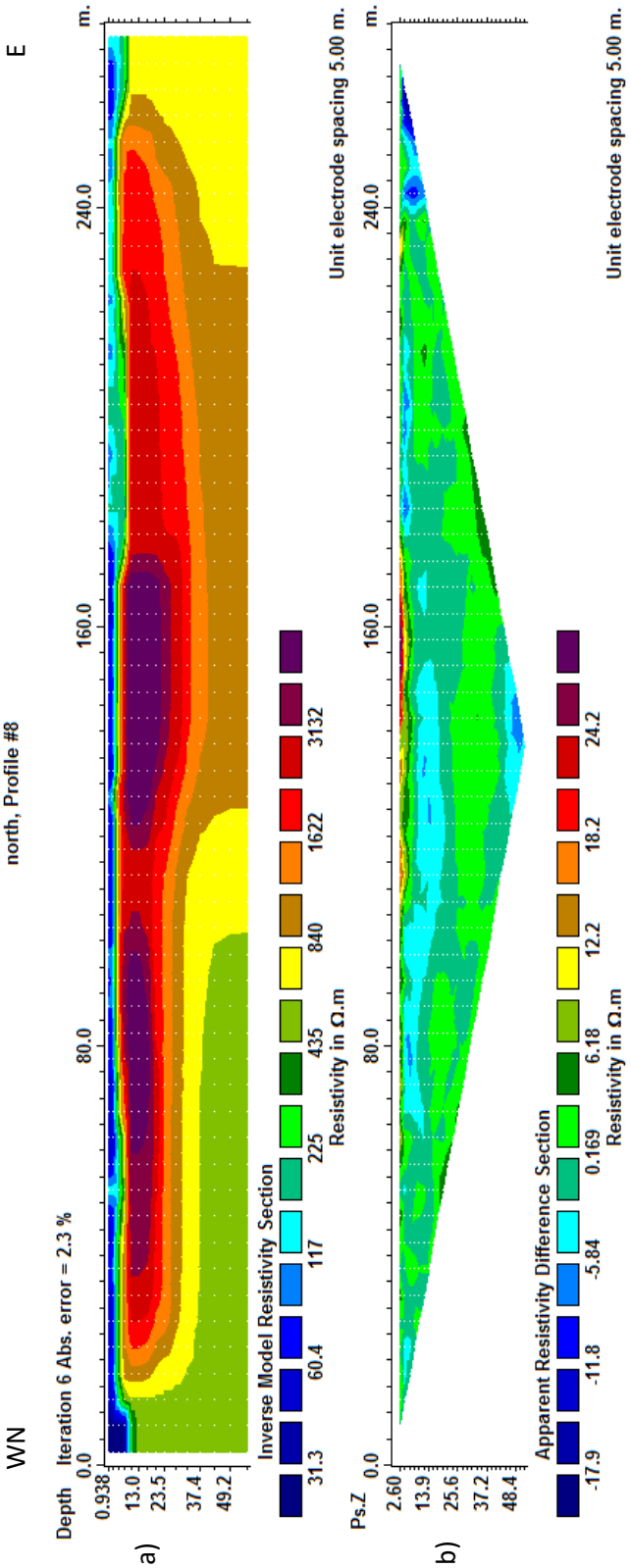


Figure 4-72: An alternative model for the Wenner Sclumberger data acquired in line 8 (a) with the resulting misfit pseudo section (b).

The DOI for the Wenner Schlumberger data is shown in Figure 4-73. This DOI is obtained from the smoothness-constrained inversion. Note that the reference models used for this method were a tenth the linear average and ten times the linear average, not the average of the logarithms. The DOI shown here does not constrain the depth of investigation. The models are sensitive (even using a DOI index cut-off of 0.1) for up to 60 m or more. This could be because only small variations in the resistivities at these depths are possible.

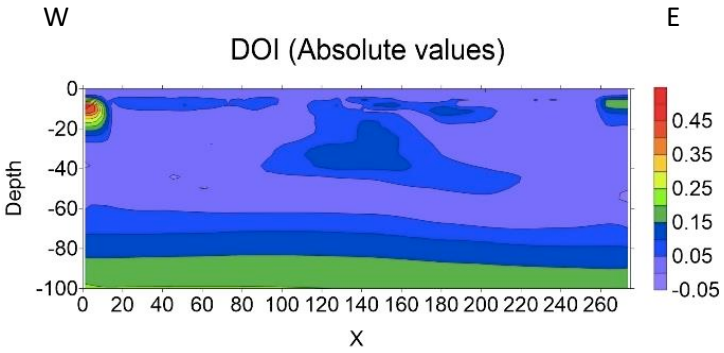


Figure 4-73: DOI for the Wenner Schlumberger data acquired along line 8.

4.3.2.2 Dipole-dipole ER data along line 8

The model (Figure 4-74a) obtained from the smoothness-constrained inversion (see Appendix A for the Res2DInv settings) of the dipole-dipole data acquired on line 8 (data in Figure D-27 in Appendix D) has a misfit of 5.4% after ten iterations (see Appendix B: Figure A-20). The estimated data error is only 1.5%. The misfit pseudo section (Figure 4-74c) is clearly not usable.

The smoothness constrained inversion delivered models that were a better fit to the data where the inversion used an initial model with resistivity different from the average (the other inversion parameters are as presented in Appendix A). Two such models are shown in Figure 4-75. The model presented in Figure 4-75a has RMS errors of 3.5 % and the model in Figure 4-75b 4.1 %. The models are qualitatively similar, particularly at depths of less than 5 m.

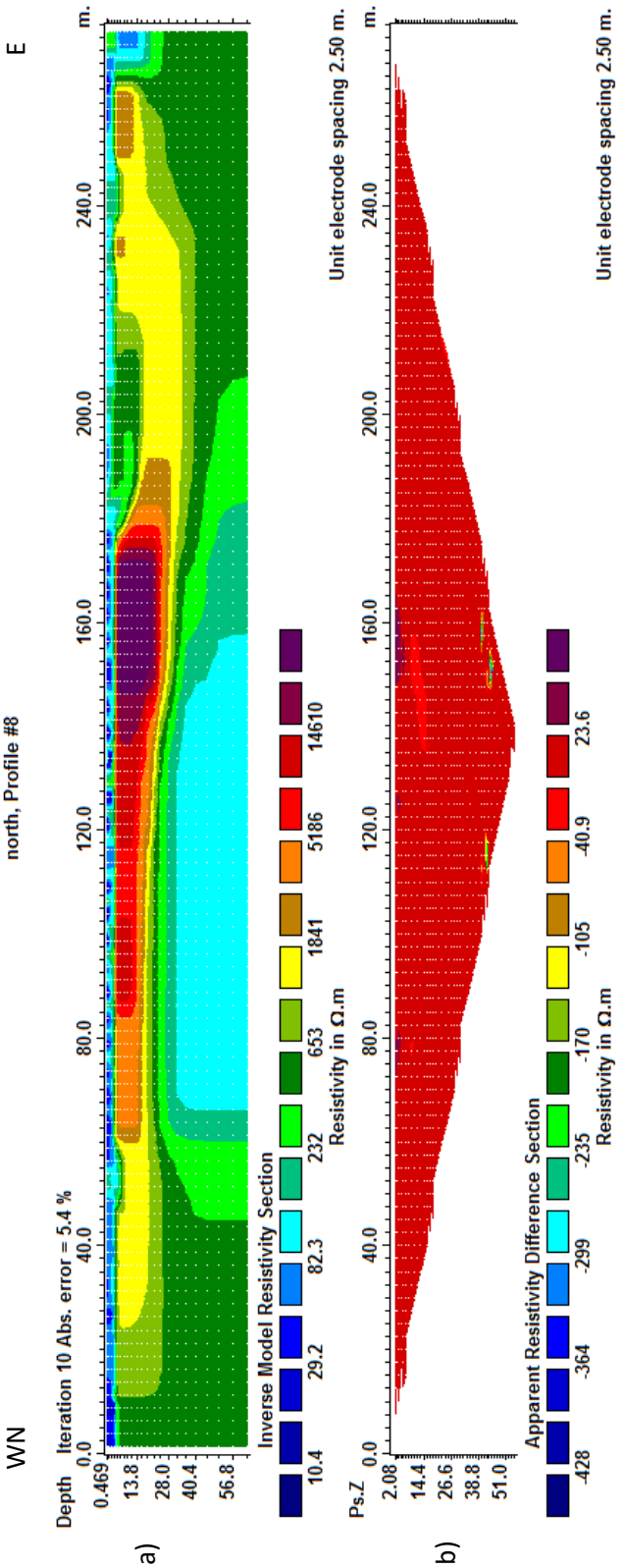


Figure 4-74: The model obtained after four iterations of running the inversion scheme on the dipole-dipole data acquired on line 8. The figure a calculated model (a) and the difference between the observed and calucated apparent resisitiivity values (b).

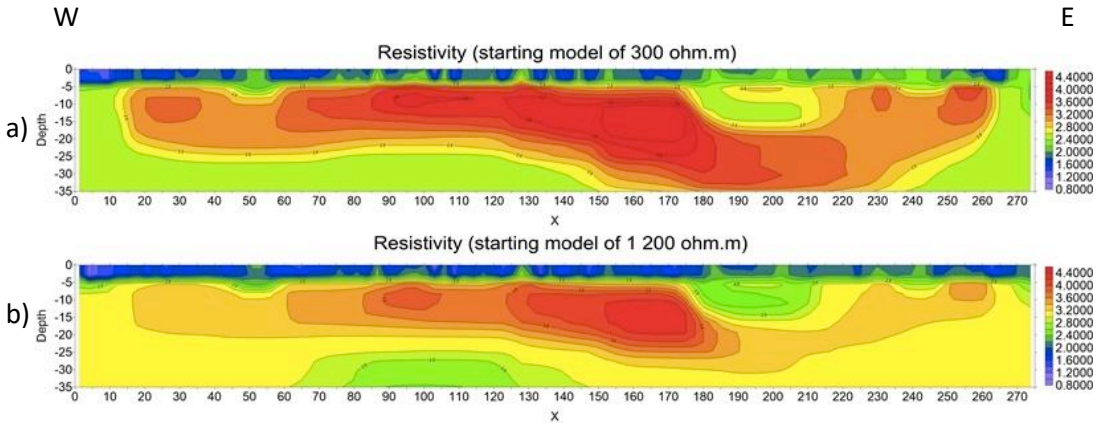


Figure 4-75: Alternative models for the dipole-dipole data collected on line 8 using smoothness constrained inversion with initial models of homogenous half-spaces with resistivities of 300 ohm.m (a) and 1200 ohm.m (b).

The similarity between the models in Figure 4-75 is emphasised by the DOI section shown in Figure 4-76. This (Figure 4-76) demonstrates that even up to 100 m in depth very similar models are obtained from smoothness constrained inversion.

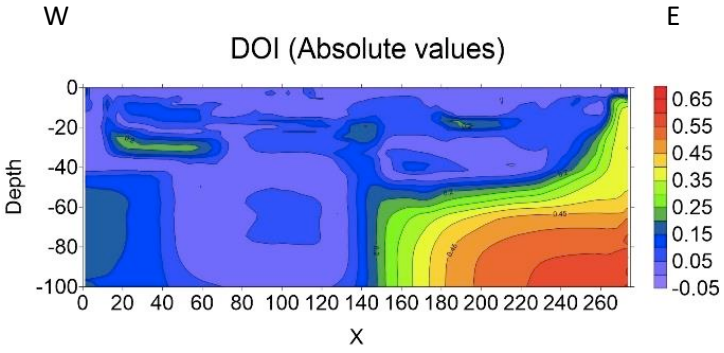


Figure 4-76: DOI indices for the dipole-dipole data acquired on line 8 for depths up to 100 m (a) and the scaled values (b).

4.3.2.3 Final model for line 8

In Figure 4-77 the final resistivity model is shown for the data acquired on line 8. In this section the conductivity has increased from line 11 and this section represents the second section in the space lap, from uncontaminated groundwater to highly contaminated water (which this line represents) to remediated groundwater. This may be caused by higher water content in the weathered material and the soil or by an increase in pore water conductivity or a combination of both.

The *in situ* electrical resistivity of the first layer is 70 to 281 ohm.m.

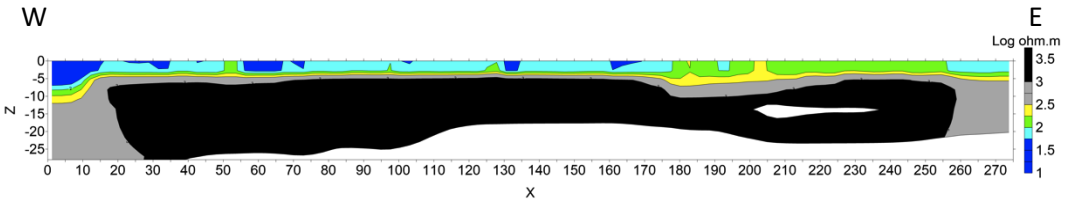


Figure 4-77: Final resistivity model for line 8.

In Figure 4-78 some more detail is shown for line 8. The soil and weathered material that hosts the superficial aquifer (interpreted as the blue and green zones in Figure 4-78) in the vicinity of both line 8 and line 11 suggests that the water content could not have drastically increased from the previous section to this one. The change in aquifer resistivity is due to a change in pore water conductivity. Taking into account the spatial change in SO_4 content of boreholes in this area (as shown in the colour contour map, Figure 3-4), it is likely that this is directly caused by an increase in contaminant content in the groundwater emanating from the TSF.

The bedrock has *in situ* electrical resistivity in excess of 1000 ohm.m (interpreted as the black in Figure 4-78)

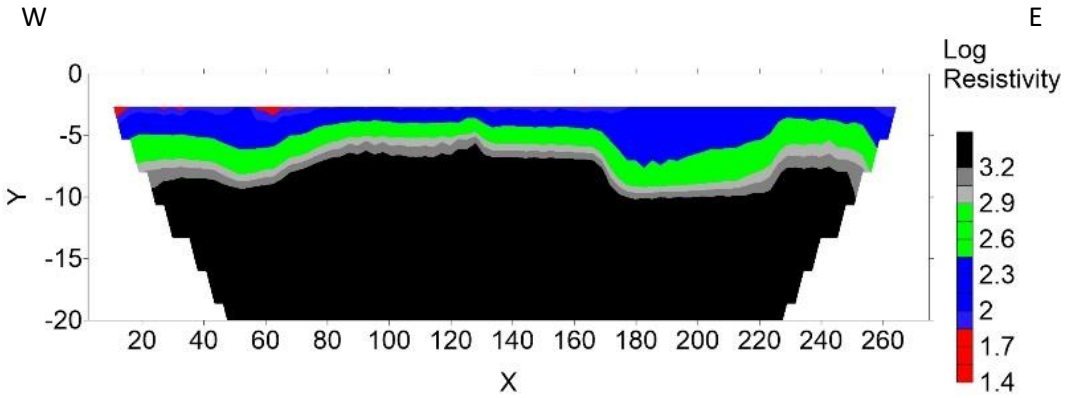


Figure 4-78: Final resistivity model for line 8 (the vertical scale has been increased).

4.3.3 ER data along line 10

The data for line 8 are collected over dolomite (see Figure 1-1b for line position). The groundwater that is expected to fill the pore spaces in the rock underneath this line, are expected to be affected by the phytoremediation.

4.3.3.1 Wenner Schlumberger ER data along line 10

The model (Figure 4-80) obtained from the smoothness-constrained inversion (see Appendix A for the Res2DInv settings) of the Wenner Schlumberger data acquired on line 10 (data in Figure D-28 in Appendix D) has a misfit of 3.0% after three iterations (see Appendix B: Figure A-21). The estimated data error is only 1.2%. The misfit pseudo section (Figure 4-80c) is random and will be used for interpretation along with the dipole-dipole data on this line.

The DOI index values for the Wenner Schlumberger data are shown in Figure 4-79. According to the DOI index calculations the data are sensitive to model changes in only the top 7 m.

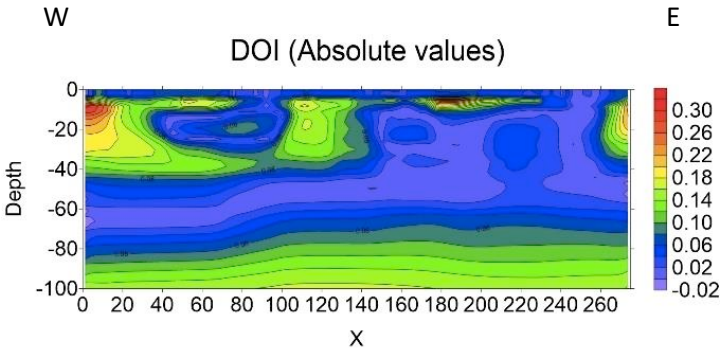


Figure 4-79: The DOI index for the Wenner Schlumberger data acquired on line 10.

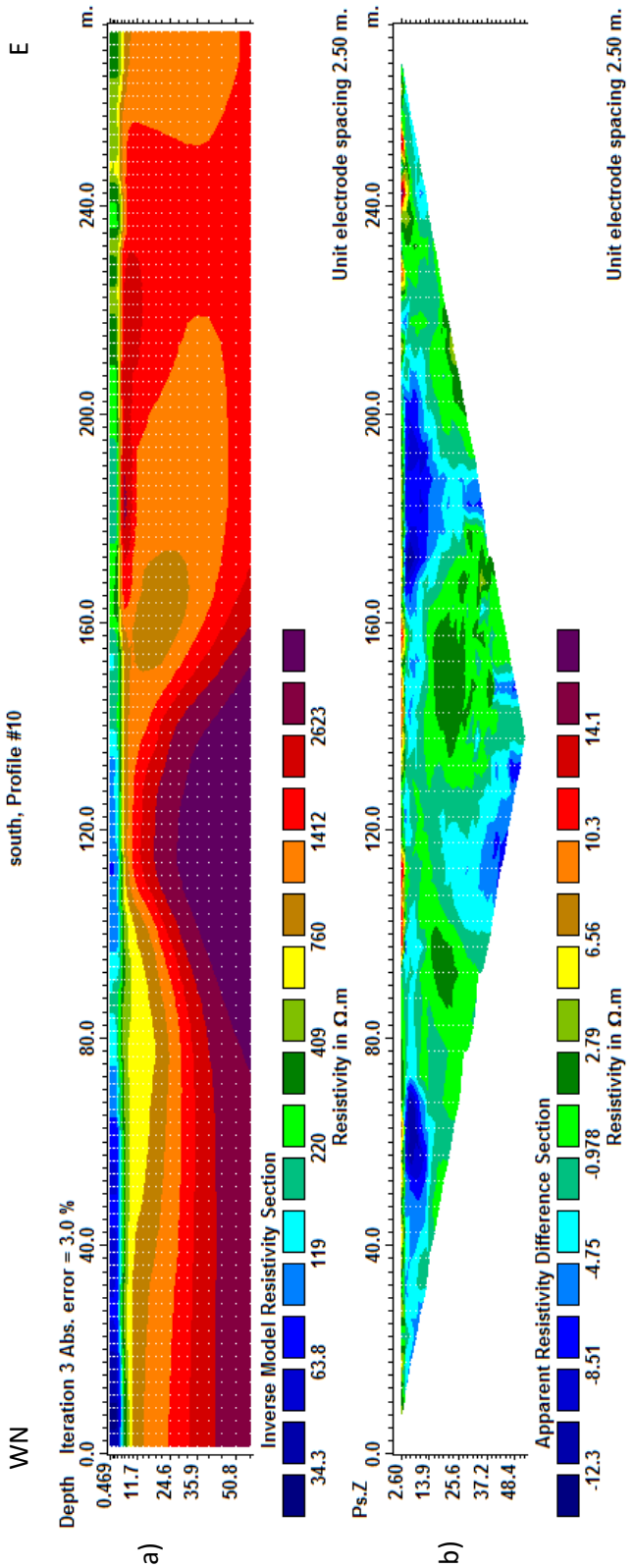


Figure 4-80: A model of resistivity (a) and the misfit in the apparent resistivity space (b) obtained after the third iteration of the smoothness-constrained inversion process for the Wenner Sclumberger data acquired on line 10 (Res2dInv).

4.3.3.2 Dipole-dipole ER data along line 10

The model (Figure 4-82a) obtained from the smoothness-constrained inversion (see Appendix A for the Res2DInv settings) of the dipole-dipole data acquired on line 10 (data in Figure D-29 in Appendix D) has a misfit of 3.0% after three iterations (see Appendix B: Figure A-22). The estimated data error is 2.4%. The misfit pseudo section (Figure 4-82b) is random.

The DOI indices of the dipole-dipole data are shown in Figure 4-81. The DOI section shows that the models for this section are similar even at depths of up to 80 m.

W E

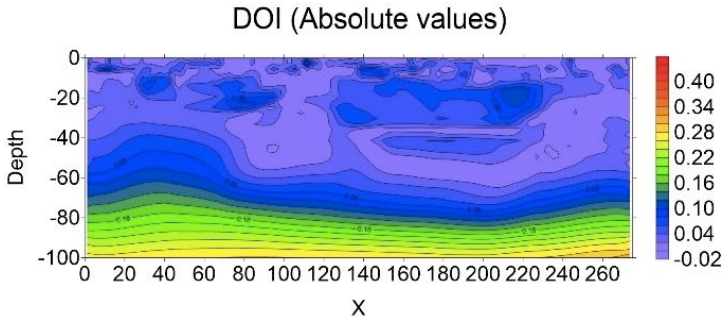


Figure 4-81: DOI for dipole-dipole data acquired on line 10 (a), and the scaled DOI indices for the same line (b).

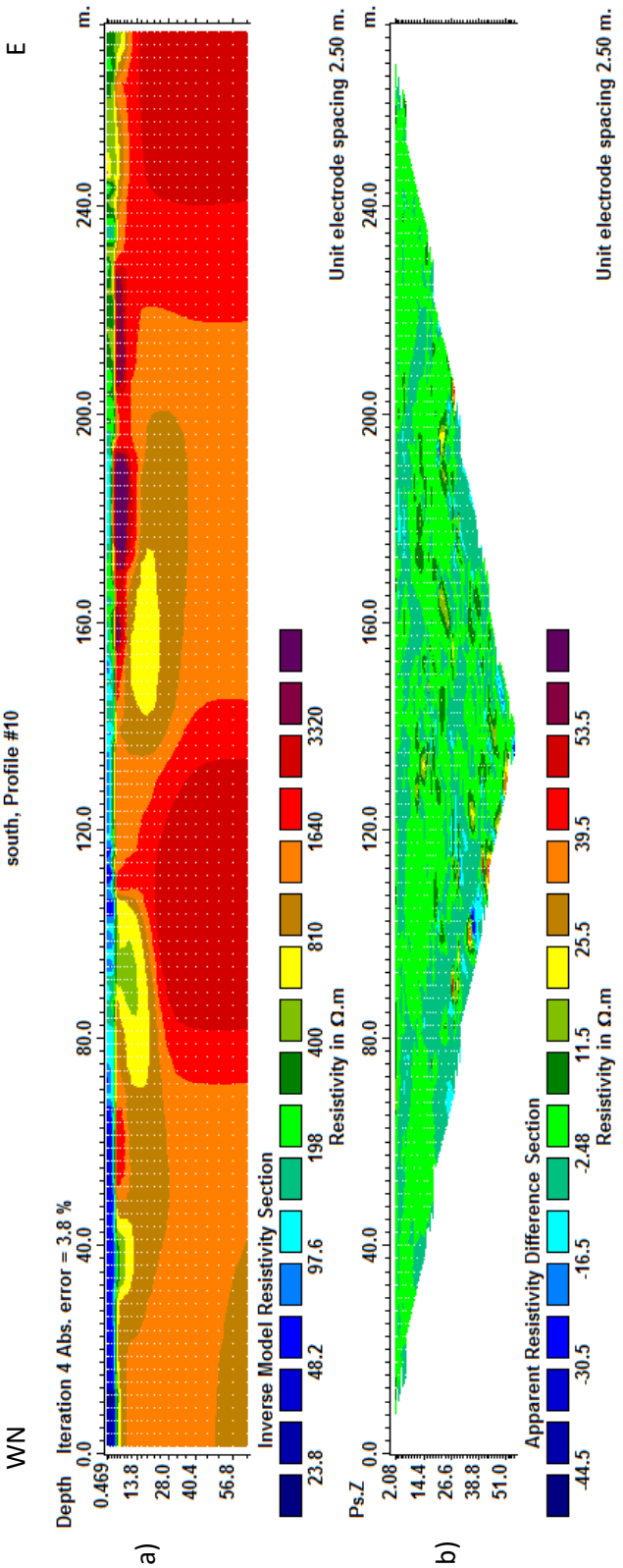


Figure 4-81: A model of resistivity (a) and the misfit in the apparent resistivity space (b) for the fourth iteration of the inversion of the dipole-dipole data acquired on line 10 (Res2dInv).

4.3.3.3 Final model for line 10

In Figure 4-83 the final resistivity model is shown for the data acquired on line 10. The surficial aquifer shows a decrease in conductivity from the model presented in Figure 4-77 for line 8.

Two things should be noted from this model. Firstly, the possible presence and existence of karst topography and underground caves or sinkholes. The largest problem caused by this is a change in the type of flow of groundwater. Where groundwater moves into areas where it flows relatively freely (such as karst environments) the associated contaminants also spread freely. The area suggested by the resistivity modelling should therefore influence the positioning of future woodlands. The second thing that can be seen in the resistivity section for line 10 is the decrease in conductivity for the surficial aquifer (*in situ* electrical resistivity of 70 to 562 ohm.m.). This may be caused by a decrease in pore water presence, or by a change in the composition of the soil. The change in groundwater chemistry recorded in nearby boreholes (Figure 3-4) suggests that the contaminant content in the water is less than on line 8. Contaminant content decreases as the groundwater flows south. This may be caused by one of two factors. Either the contaminants are stored in the ecosystem naturally and they decrease in content over distance, or contaminants were removed by some other mechanism.

The section running from west to east in the study site shows that the resistivity of the surficial aquifer does increase naturally but only slightly (see section 5.2 above). The only conclusion is then that the decrease is due to another mechanism removing contaminants from the groundwater. The most likely mechanism for this is the *Tamarix* Woodland that has been established.

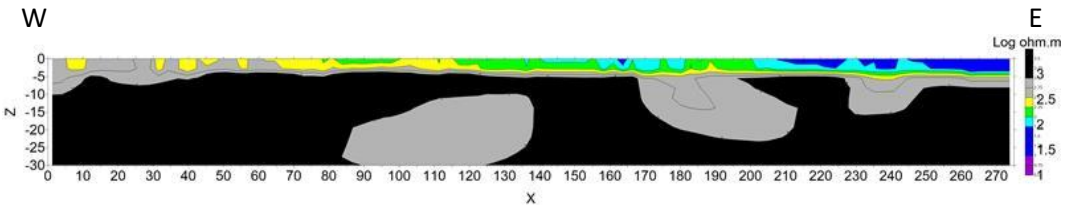


Figure 4-83: Final resistivity model for line 10.

A further motivation for this interpretation is the change in resistivity along the profile for line 8. This is shown in the more detailed model in Figure 4-84. The groundwater

influenced by the woodland has decreased conductivity while the water flowing eastwards to the east of the woodland has the same resistivity as the aquifer in the section along line 8.

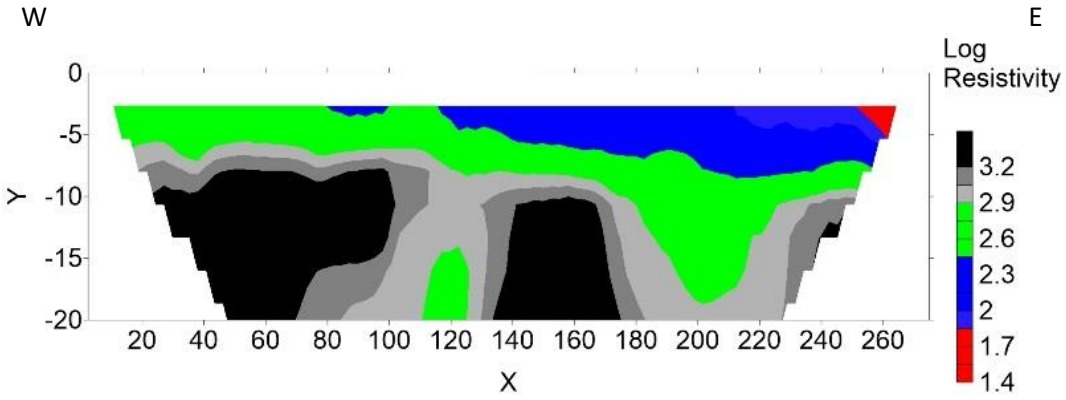


Figure 4-84: Final resistivity model for line 10 (vertical scale has been exaggerated).

4.4 Summary

In this chapter all the modelling for the electrical resistivity and induced polarisation data were discussed. This is the results section. Time was spent in showing different models and depth of investigation sections to allow the reader to understand the modellers logic in deciding on one best model for each section

Chapter 5 - Archie's law and hydraulic conductivity

In this chapter the relationships between SO_4 concentration and electrical resistivity are investigated with the aim of obtaining Archie's law's coefficients for the surficial aquifer. If Archie's law is valid the hydraulic conductivity of the unit can be obtained. Archie's law assumes that the relationship between pore water conductivity and rock conductivity is linear.

SO_4 point data and electrical conductivity data were gathered for the boreholes in the study area in 2010. SO_4 is used as an indicator of contaminant concentration because it is easy to measure, can be taken up by plants as it is soluble in water and it does not decay over time. The borehole locations and the contour maps of the SO_4 concentration distribution data are shown in Chapter Three and the borehole data, including gathered electrical conductivity data, is presented in Table 5-3. Plotting SO_4 data against first layer models of ER data contained in this chapter allows for investigation of the correlation between ER and SO_4 content.

The data used for the contour plots in Chapter Three and for extracting the data discussed in that chapter are presented in Table 5-1 and Table 5-2. Table 5-1 shows some of the borehole data for the boreholes installed in the dolomites. These data were used for the colour contour plots in Chapter Three where the borehole collars were shown as the SO_4 concentration readings.

Table 5-1: Borehole data showing the name, description and date measured for pH, electrical conductivity, SO_4 concentration, water level from the collar and coordinates in LO27 (WGS84 datum) for some boreholes installed in the dolomite (data provided by AGA without unit of measure).

Location	Description	Date	pH	EC	TDS	SO4	Water level (m)	X posiiton	Y position	Z position
VRM38	West of Ariston Gully @ Old Black Reef Treatment Plant	21-Jan-10	4,5	678	9051	4374	2,95	-31785,5	-2980071,95	1312,1
VRM57	West of Ariston Gully TSF	21-Jan-10	6,4	441	5697	2764	6,33	-32606,781	-2980007,832	1299,395
VR04	West of West Complex TSF along main Klerksdorp - Orkney road	15-Jan-10	6,9	351	4219	2164	7,01	-33131,624	-2980728,89	1329,518
VRM69	West of West Pay Dam near gravel road	15-Jan-10	5,9	557	5681	3508	1,22	-32596,799	-2980977,59	not given

The data for the boreholes installed in the lava are shown in Table 5-2.

Table 5-2: Borehole data showing the name, description and date measured for pH, electrical conductivity, SO_4 concentration, water level from the collar and coordinates in LO27 (WGS84 datum) for some boreholes installed in the lava (data provided by AGA without unit of measure).

Location	Description	Date	pH	EC	TDS	SO_4	Water level	X posiiton	Y position	Z position
VRM43S	Woodlands - West Complex Tailings (Shallow)	15-Jan-10	9,14	620	5827	3107	2	-30323,85	-2980178,68	1313,71
VRM24	Between West Complex and West Extention (old no NTBH4)	15-Jan-10	7	1500	16000	9395	3,06	-30063,1	-2980587,04	1312,85
VRM25	East of West Complex (old no.WPBH5)	15-Jan-10	6,9	714	6082	3837	3,51	-30336,17	-2981934,64	1311,25

The values for the SO_4 concentration (in ppm) and *in situ* ER are presented in Table 5-3 below. The highest and lowest SO_4 concentration values are shown for each line (for which it was available, see Chapter Three). These are tabulated with the maximum and minimum values of the *in situ* electrical resistivity for that line (see Sections 5.1, 5.2 and 5.3).

Table 5-3: The high and low values of the SO_4 concentration (in ppm) distribution extracted from the SO_4 contour maps and the *in situ* ER (in ohm.m) read from the final models.

	ER (ohm.m)	SO_4 (ppm)	Rock type
Line 1 min	10	3173	Lava
Line 1 max	56	3251	Lava
Line 2 min	3	4420	Lava
Line 2 max	56	4431	Lava
Line 4 min	5,6	3482	Lava
Line 4 max	56	3486	Lava
Line 5 min	10	3450	Dolomite
Line 5 max	100	3452	Dolomite
Line 6 min	10	2898	Lava
Line 6 max	177	3054	Lava
Line 8 min	70	4041	Lava
Line 8 max	281	9294	Lava
Line 9 min	10	3847	Dolomite
Line 9 max	56	3944	Dolomite
Line 10 min	70	4137	Dolomite
Line 10 max	562	9380	Dolomite
Line 12 min	3	2941	Dolomite
Line 12 max	56	2951	Dolomite

The data contained in this table are plotted (with error bars) in Figure 5-1. The lava and the dolomite data are plotted separately. There is a correlation between the SO_4 data

and the ER data. A natural logarithmic trend line is fitted to the data to demonstrate this. The relationships are as follows:

For the lava and the lava derived soils:

$$SO_4 \text{ content in dolomite} = 1145 \ln(\text{Unit ER}) - 430{,}25 \quad (5.1)$$

as are shown in Figure 4.83a and for the dolomite and the dolomite derived soils:

$$SO_4 \text{ content in dolomite} = 1487{,}3 \ln(\text{Unit ER}) - 1926 \quad (5.2)$$

as are shown in Figure 4.83b.

The ER for the water sampled in the boreholes can be obtained from the conductivity. In Figure 5-2 the data are plotted (separately for the dolomite and lava data). The correlation for these lines between the SO_4 content and the ER of the water in the boreholes exists and fitting a trend line with a power function to the data explains demonstrate this. The relationships are as follows:

For the lava and the lava derived soils (Figure 4-86a):

$$SO_4 \text{ content in water in lava} = 6583{,}6 (\text{Water ER})^{-1{,}063} \quad (5.3)$$

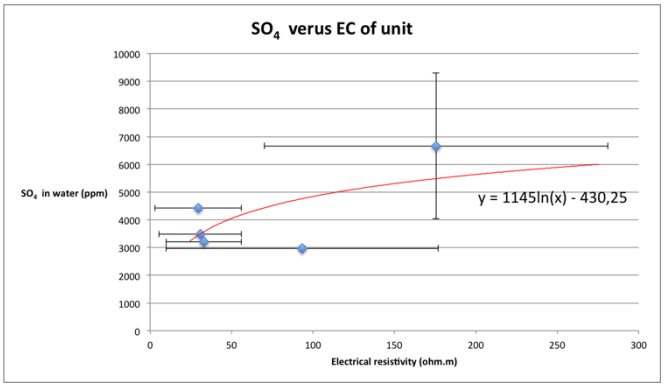
And for the dolomite and the dolomite derived soils (Figure 5-2b):

$$SO_4 \text{ content in dolomite} = 4597{,}2 (\text{Water ER})^{-0{,}74} \quad (5.4)$$

Combining equations 5.1 and 5.3 the following is obtained:

$$1145 \ln(\text{Unit ER}) - 430{,}25 = 6583{,}6 (\text{Water ER})^{-1{,}063} \quad (5.5)$$

a)



b)

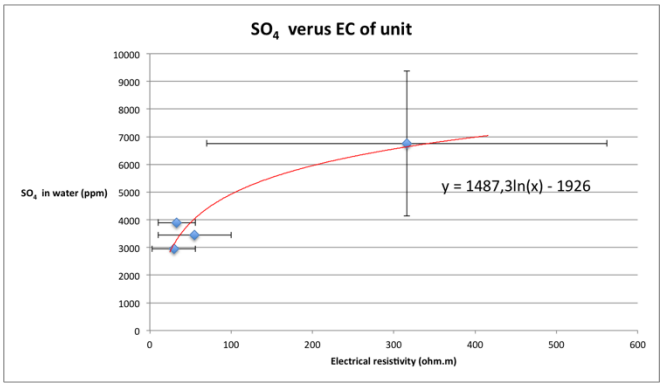
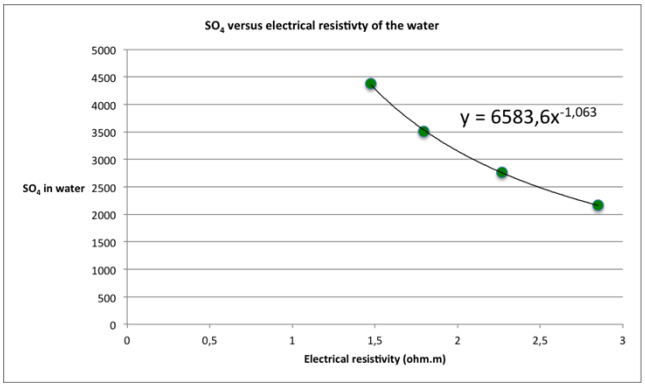


Figure 5-1: Logarithmic correlation between ER of the layer and SO_4 content in boreholes surrounding the resistivity sections for data in areas underlain by lava (a) and dolomite (b).

Comparing this to Archie's law (equation 2.1) shows that there is no linear relationship between the ER of the rock unit and the resistivity of the pore water (a similar result is obtained by combining equations 5.2 and 5.4). Archie's law is used to obtain the formation factor of aquifers, which is used to calculate hydraulic conductivity (see for example Glover, 2016) and is given by:

$$R_{rock} = \tau p^{-c} Sat^{Sat_{exp}} R_{water} \quad (2.1)$$

a)



b)

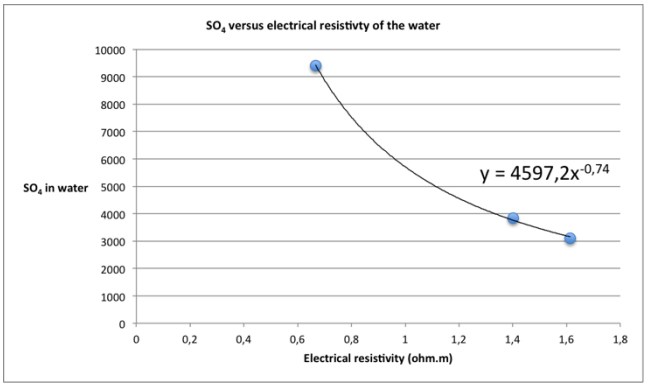


Figure 5-2: Correlation between ER of the water and SO_4 content in boreholes surrounding the resistivity sections for data in areas underlain by lava (a) and dolomite (b).

with each parameter as it was defined in Chapter Two. Schõn (1996) proposed a method to determine the surface conductivity of the grains in the aquifer in which the pore water occurs, which is also dependant on a linear relationship between the pore fluid conductivity and aquifer conductivity. As there is no linear relationship between the conductivities the model from Schõn (1996) cannot be used.

Chapter 6 - Summary of results

In this study, an investigation of AMD was conducted at a representative tailings storage facility (TSF) site on the Witwatersrand gold fields near the town of Orkney in the North West Province of South Africa. The study site has an AMD plume emanating from the east and the west of the TSF, which has been modelled for its future growth by De Sousa *et al*. (2006, who used numerical modelling to predict the contaminant transport) and Grindley (2014, who used MIKE SHE hydrological modelling to model the effect of phytoremediation on contaminant transport) using boreholes drilled on the site to monitor the plume propagation (and provide lithological information).

Bimodal lavas of the Platberg Group are located on the west of the site. This is unconformably overlain by the Black Reef Formation that strikes roughly north-south in the centre of the site. The dolomites of the Chuniespoort Group are located on the east of the site and overlies the Black Reef Formation (Figure 1-1). The available borehole data did not distinguish between weathered and fresh bedrock in the quartzites of the Black Reef Formation. In the dolomite, an altered transition zone of 6 m can exist between fresh bedrock and the soil. In addition to this a zone where karst sinkholes, often filled with magnesium oxide (wad), can be present between the weathered and fresh dolomite (AngloGold Ashanti, 2003). In the lavas, the rock can be as much as 5 m deep (from one data point, Dressel, 2005) although the lava outcrops to the west of the study site (De Sousa *et al*., 2006). The soils are derived from the underlying geology and can be described as clayey and/or silty sand with additional pieces (gravel or cobble sized) of the underlying bedrock and are typically less than 2 m thick (AngloGold Ashanti, 2003).

There are few known faults or lineaments in the area and the geology dips towards to the east. The presence of both the Transvaal and Ventersdorp Supergroups allows for the study of the two units independently. The simplicity of the geology, and the presence of a phytoremediation program by the Mine Woodlands Project, on the site allows for the study of the effects of the phytoremediation on AMD.

The Mine Woodlands Project has established woodlands of different tree species in different areas around the TSF over several years, partly to test the efficacy of the trees types on AMD rehabilitation. *Searsia lancea* (karee) woodlands have been established in

the west of the site and a *Tamarix usneoides* (wild tamarisk) woodland in the east. A lane of *Eucalyptus* trees, not part of the project, occurs in the west and there are also naturally occurring *Searsia lancea* trees to be found scattered around the site.

Large, mature root systems are important for trees to effectively remediate contaminated water. The western *Searsia lancea* woodland is too young to have influenced the AMD plume yet at the time of this study (Grindley, 2014). The older, more mature *Eucalyptus* lane, *Tamarix usneoides* woodland and naturally occurring *Searsia lancea* are suitable for studying the effects of phytoremediation.

Acid mine water is expected to have a conductivity much higher than the conductivity of uncontaminated or remediated groundwater, and geophysical techniques appropriate to mapping this change measure the conductivity (or its reciprocal) the resistivity of the subsurface.

The current study was conducted using electrical resistivity (ER) measurements, as depth of penetration (which is relatively low compared to other electromagnetic techniques) and resolution (higher than most other electromagnetic techniques, except for GPR) were considered. Additionally, induced polarisation (IP) data were collected to establish whether contaminants remain in and around the root systems of the trees and whether it is possible to map this. The GPR method was unable to provide sufficient depth information for meaningful interpretation.

The electrical resistivity method is sensitive to changes in pore water content, mineralogy and pore water make-up. AMD contamination will change the pore water make up and decrease the resistivity of the material it is found in. Phytoremediation will either decrease the water content or change the make-up of the water and by doing this it will increase the resistivity of the material is found in. In some cases, phytoremediation will store contaminants in the rhizosphere of a plant and the subsequent change in mineral content will also influence the resistivity (decrease and increase dependant on the stored and host material).

The change from a dry soil to water saturated soil (or dry weathered rock to water saturated weathered rock) is between 1.5 and 11.8 m below ground level (De Sousa *et*

al., 2006). The contact between fresh and weathered rock is also usually expected to have a large resistivity contrast, although this boundary is most often gradational.

Parallel profiles of electrical resistivity data acquired in the direction of groundwater flow in the lava shows a clear decrease in conductivity in the first layer with distance from contaminant source. This is as expected. A combination of dilution from rainwater infiltration and possible reaction of the acidic water with andesitic lava reduces the acidity of the water. This leads to a decrease in the water's ability to carry contaminants, which decreases the total dissolved solids in the groundwater. This leads to an increase in electrical resistivity.

Further parallel profiles of electrical resistivity data acquired in the direction of groundwater flow in the dolomite show a clear decrease in first layer conductivity which could be associated with the *Tamarix usneoides* woodland in the east of the study site. These data tend to confirm the effectiveness of the phytoremediation, as the woodland removes contaminants from the groundwater and the groundwater is more resistive due to a decrease in total dissolved solids. This is quite specifically only the *Tamarix usneoides* trees as (as discussed below) the other tree species do not necessarily remove contaminant from the soil.

Electrical resistivity profile lines centred around the *Eucalyptus* and *Searsia lancea* trees not associated with the Mine Woodlands Project show a decrease in electrical resistivity around the roots. These effects are deeper for *Eucalyptus* trees than for *Searsia lancea*, which suggests different effects by deep and shallow root systems. The *Eucalyptus* trees extract large amounts of water from deeper depths, while the *Searsia lancea* may be removing contaminants from the soil while extracting nutrients at shallower depths.

Induced polarisation data were used to establish whether the contaminants potentially stored in the rhizosphere could be mapped directly and whether contaminated and remediated water could be distinguished from one another.

A low power source (the ARES system is battery powered) was available and the data precision is consequently low (as the input currents and measured potentials are low). The inversion models tend to show a large chargeability anomaly coincident with the expected position of the tree roots and the rhizosphere.

Electrical resistivity has been shown in this study to be useful for monitoring phytoremediation and AMD plume propagation. However, a relationship between resistivity values and the TDS of the contaminant plume could only be defined qualitatively as the relationship between whole unit resistivity and groundwater resistivity was not linear. IP gave results that are worth investigating further for directly mapping contaminant storage in the rhizosphere.

6.1 Discussion of electrical resistivity results

Eleven profile lines of ER data were acquired over three site features: (1) Four profiles to assess the *Searsia lancia* and *Eucalyptus* trees and their effects on resistivity; (2) Four profiles over the lavas from the TSF to the Schoonspruit river; and (3) Three profiles over the dolomite to the south of the TSF.

Both algorithm used employs the smoothness constrained least-squares equation and inverts the data using the Gauss-Newton formulation (with the Marquardt–Levenberg and additional weighting matrix modification). The target misfit is chosen directly as a percentage for the one algorithm (Res2dInv), while the size of the objective function for the second algorithm used (DCIP2D) is influenced by the choice of a value which trades off the smoothness of the model against the difference between the predicted and calculated resistivity values. One way to choose the correct size of this trade-off value is by varying it and constructing of a Tikhonov Curve where the value of the misfit is plotted against the value of the model norm. The L-bend in the resulting curve should be used as this is the optimal compromise between the size of the norm and the size of the misfit.

The interpreted responses from the effect of the *Eucalyptus* trees (Figure 6-1) show an increase of 46 to 112% in electrical resistivity (from approximately 30 or 44 ohm.m to 64 ohm.m) along the profile and that the aquifer can be dried out by this species of tree. The trees are removing water carrying contaminants from the aquifer towards the surface water source, and reducing the flow of AMD into the Schoonspruit. This effect is observed where the resistivity line crosses a lane of *Eucalyptus* trees and not with an individual tree.

The planting of these species of trees in controversial, but they can clearly help in protecting surface water sources from infiltration from contaminated groundwater. These trees are also used commercially in mines, plastic manufacturing and elsewhere and it can help the remediation strategy if the trees deliver a useful product over time.

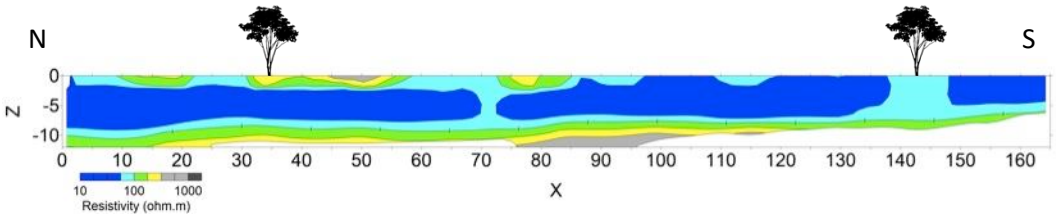


Figure 6-1: Final resistivity model with tree locations for Wenner Schlumberger data acquired line 1 (reproduced from Figure 5-6).

The *Searsia lancea* trees do not show effects on the aquifer to depth, as the *Eucalyptus* trees do, but only on the shallow subsurface (Figure 6-2). The soil in the first 2 m immediately surrounding the tree has a decreased resistivity, which is interpreted here as dried out soil. It could be that the tree is removing conductive metals or water from the soil. If this is the case, this does not have the effect of inhibiting the flow of AMD.

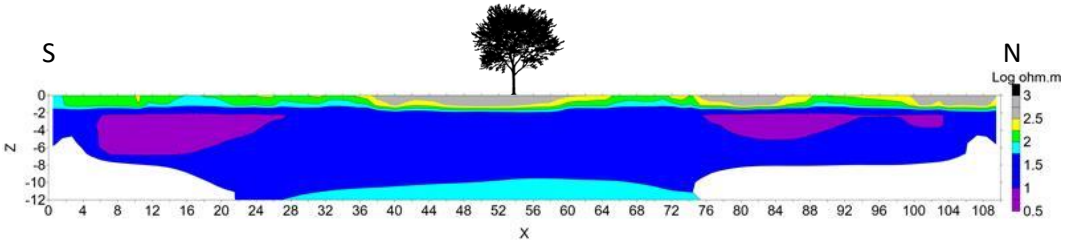


Figure 6-2: Final ER resistivity model of the dipole-dipole data for line 4 with tree (reproduced from Figure 5-39).

These first four ER profile lines also give information as to the depth of the water table and the resistivity of the material directly beneath the surface. The water table depths are variable, between 2 and 4 m deep. This is a useful parameter for future studies of the site, as it will constrain the minimum depth to which the hydrogeology and the AMD plume should be mapped. The implication is that airborne data is not useful, unless a drone can fly at about 2 to 4 m above the surface. In addition time-domain EM data is likely not to be useful in mapping AMD at a Witwatersrand goldmine either as the method is not sensitive to electrical conductivity variations at such a shallow depth.

The conceptual model for the effect of various processes on AMD is reproduced here (from Figure 2-3, Figure 6-3). The vector AI (the neutralisation by wetland) is similar to the effect on water when contaminants are stored in the biomass or rhizosphere of the plants. A vector in the vicinity of the vectors AH and AI will be similar to the effect of water reacting with felsic lavas. Mixing with rainwater is the same as mixing with surface water (vector AB). Further contamination with extra acid mine water will have the opposite effect as vector AB.

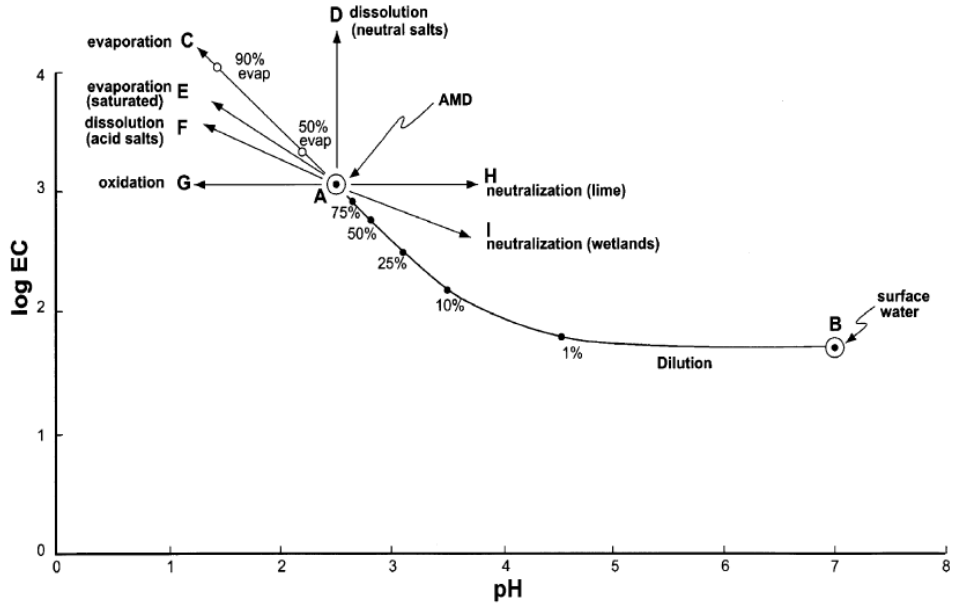


Figure 6-3: Schematic diagram showing how electrical conductivity (in log S/m) and pH of acidic water change when they are subject to different processes. Point A represents acid mine water (from Tutu *et al*., 2008).

The final models for the three lines obtained for the parallel lines in the direction of the groundwater flow in the lavas (Figure 6-4) are discussed next. Line 9 does not extend over the lavas as the TSF forms an obstruction (Figure 3-3) and line 12 can be used to see what the resistivity would be like in an area where the groundwater has been less effected by contamination.

To compare the lines, the layer in the model with the lowest average resistivity will be isolated and the median value of the resistivities for that layer will be used to compare with the other lines. The median resistivity of the model cells at 0.4 m depth on line 9 is 45.0 ohm.m and at 5.4 m depth on line 12 is 9.5 ohm.m. The median resistivity of the model cells at 4.6 m depth on line 5 is 29.9 ohm.m and at 1.2 m depth on line 6 is 89.1

ohm.m. From line 5 to six (moving westward) a 200 % reduction in the resistivity is found.

The increase in resistivity coincides with the decrease in contaminant over distance from the contaminant source (the TSF) in the lava. This is well documented in previous studies and confirmed in these models. Possible causes of this decrease are reaction with silicate minerals in the felsic lava or the opportunity for rain water to interact with and dilute the contaminated groundwater over the distance from the TSF. This does not happen with the parallel lines over the dolomite as the distance between the contaminant source (the TSF) and the profile line is much smaller and the opportunity for water to fall and infiltrate the ground is correspondingly less.

The fact that the resistivity data along line 12 has a very low resistivity (on average 9.5 ohm.m at 5.4 m depth) is problematic. Either the derived resistivity model is confined to a localized more clayey, conductive locality and thus not representative of weathered Ventersdorp derived soil in the vicinity (more ERT traverses could prove this) or the derivation of the average resistivities for the top layer was performed incorrectly. The first suggestion is probably correct as the SO_4 concentration near line 12 is not suspiciously high. There is also no mechanism for the pore water content to be much higher in this area. Looking at the models in Figure 6-4 the choice of resistivity for the line is not incorrect. Therefore unwittingly the ERT line was placed in a locality that has a naturally lower conductivity than the surrounding area.

These models have mapped the resistivity deep enough to provide some information on the underlying geology. The depth to bedrock is discussed below. The maximum and minimum resistivities obtained from smoothness constrained least squares inversion is smaller (for the maximum) and larger (the minimum) than the actual geology. For this reason the *in situ* resistivity of the lava is at least 1000 ohm.m.

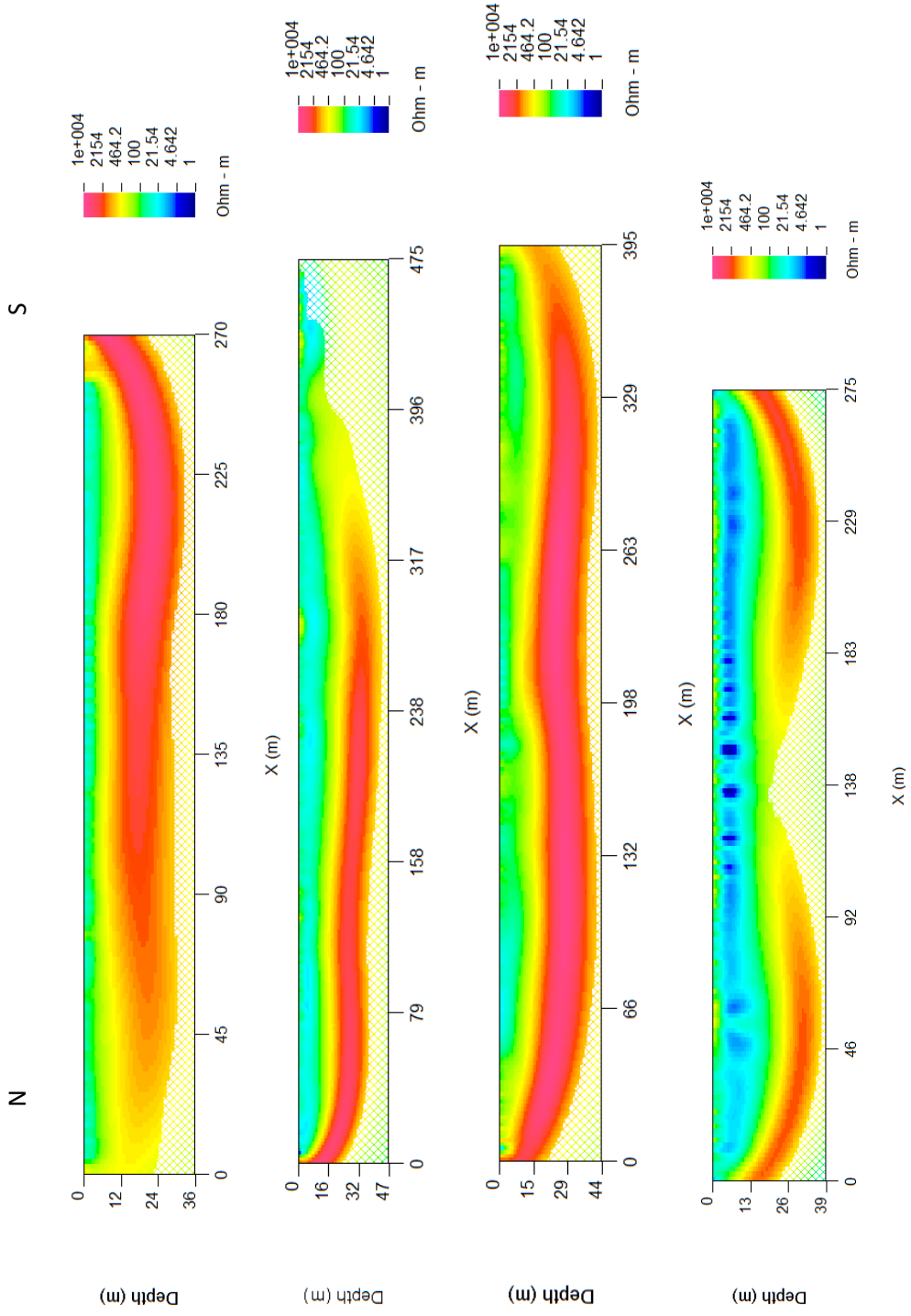


Figure 6-4; Parallel line ER models form the Wenner Schlumberger in the direction of the groundwater flow in the lavas. The final resistivity model for line 9 (reproduced from Figure 5-44a), final resistivity model for line 5 (reproduced from Figure 5-56b), the final resistivity model for line 6 (reproduced from Figure 5-62c) the final model for line 12 (DCIP2D).

The final models for the three lines obtained for the parallel lines in the direction of the groundwater flow in the dolomite are shown in Figure 6-5. The models confirm the

change in contaminant concentration in the boreholes. The resistivity in the surficial aquifer in Figure 6-5a is relatively high and this decreases in the model in Figure 6-5b. The resistivities for the surficial aquifer in the third model are are significantly higher in the western part of the line than in the eastern part. This is attributed to the change to the groundwater by the *Tamarix usneoides* woodland. The interpretation of the model shows that the *Tamarix usenoides* woodland has the effect of removing contaminants from AMD contaminated water and increasing the resistivity of the water saturated soil.

The models have mapped the resistivity deep enough to provide some information on the underlying geology. A fracture zone is interpreted from the model for line 11 (Figure 6-5a). Karst topography is interpreted from the model for line 10 in Figure 6-5c. Groundwater flows from the surficial aquifer to underlying aquifers in karst and fracture zones, which allows a larger spread of AMD than if the water was contained in a surficial aquifer. Remediation efforts should therefore focus on preventing contaminated water from reaching these deeper aquifers.

The third model demonstrates the advantage of continuous data obtainable using geophysical methods. The change in resistivity over a short profile can be mapped by the ER method to show the effects of the phytoremediation on the AMD plume. This is not possible with borehole data, unless the boreholes drilled on a very small grid.

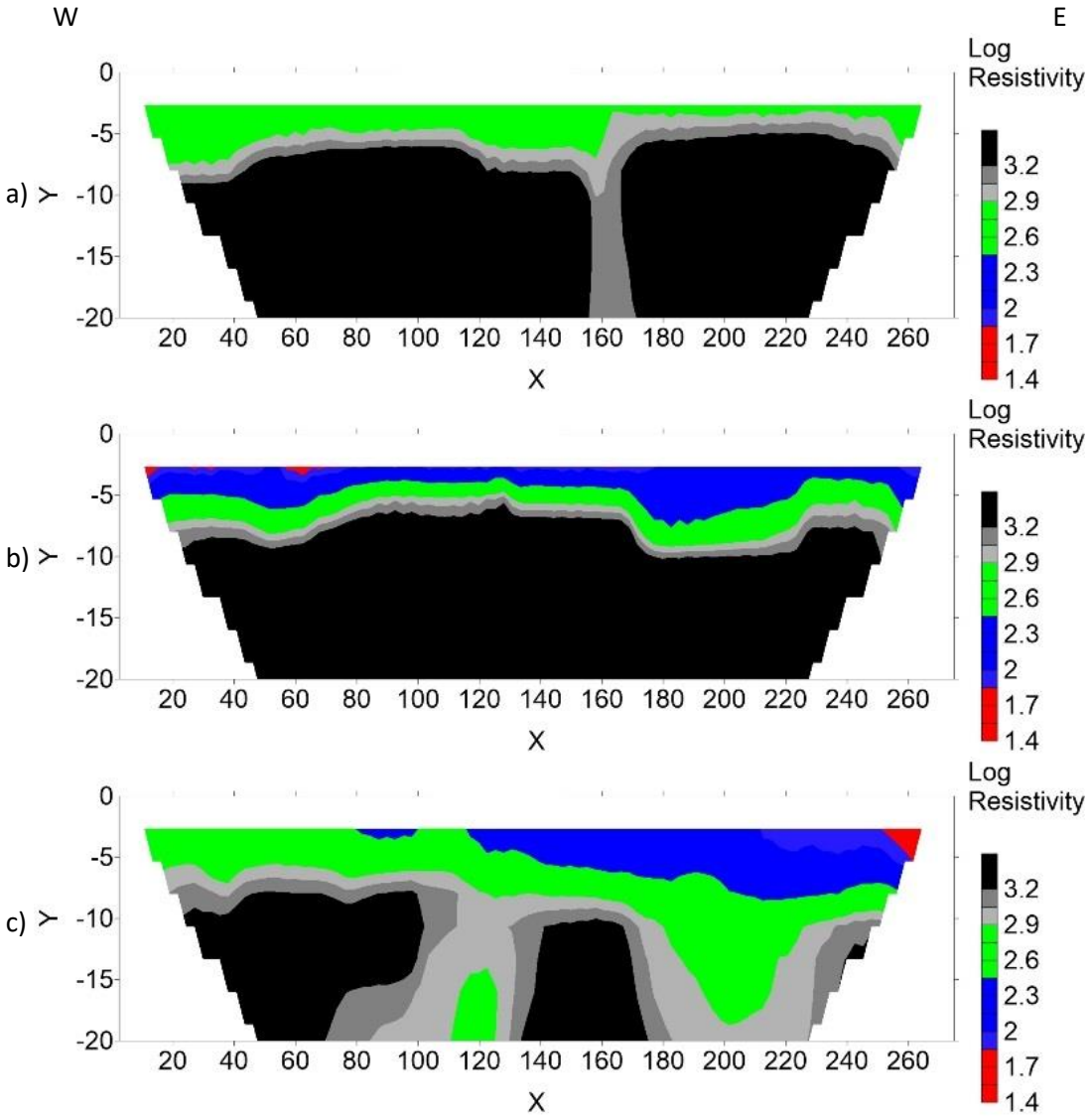


Figure 6-5: Parallel line ER models from the Wenner Schlumberger in the direction of the groundwater flow in the dolomites. The final resistivity model for line 11 (reproduced from Figure 5-68a), the final resistivity model for line 8 (reproduced from Figure 5-76b) and the final resistivity model for line 10 (reproduced from Figure 5-82c. The vertical scale has been exaggerated for this figure).

These models are best viewed relative to the Wild Tamarisk woodland (Figure 6-6). The woodland is on the left of the image and only affects the water flowing towards the reader on the one side of the final profile.

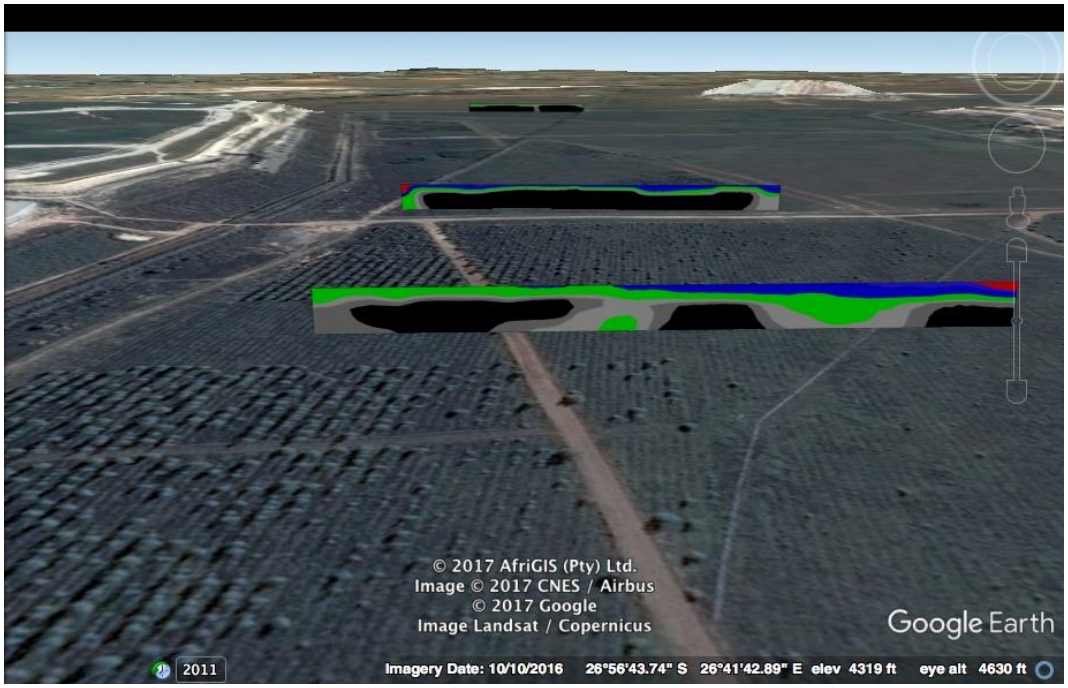


Figure 6-6: Parallel line ER models from the Wenner Schlumberger in the direction of the groundwater flow in the dolomites (Google Earth, 26°56'43.74" S 26°41'42.89" E, 2017).

6.2 Discussion of induced polarization results

Both the AMD and the tree roots show a response in time-domain IP data. The soil saturated by contaminated groundwater may be slightly chargeable while the area where the tree roots are expected to occur shows a stronger IP response (Figure 6-7). This probably indicates that sulphides or other chargeable materials are stored in and around the root system of the *Eucalyptus* tree. This tends to confirm the effectiveness of the phytoremediation efforts to stall the flow of AMD by storing the contaminants in the rhizosphere, and preventing them from flowing into the Schoonspruit.

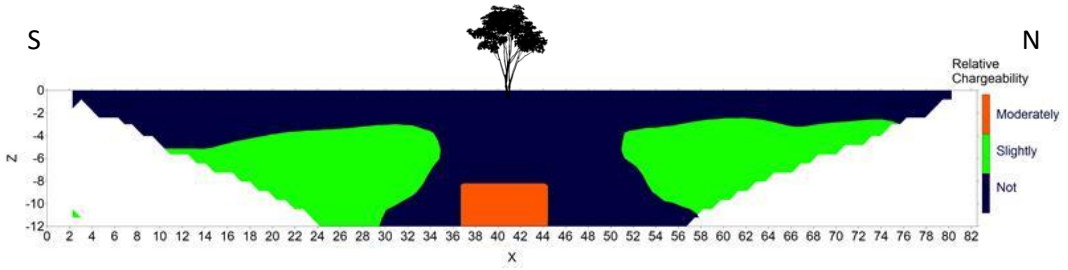


Figure 6-7: Final chargeability model for line 2 with surface features (reproduced from Figure 5-20).

In Figure 6-7 the groundwater-saturated soil at a distance of about ten meters from the tree roots of the *Eucalyptus* tree shows a small IP response. This is not the case in the

groundwater near the *Searsia lancea* trees shown in Figure 6-8 and Figure 6-9. The areas where the *Searsia lancea* tree roots are expected to be (less then 3 m north and south of the tree base) show a similar IP response to the response for the *Eucalyptus* tree (Figure 6-7). This is true for the tree with deep roots (Figure 6-8) and for the tree with shallow roots (Figure 6-9). It is apparent from the ER models that the *Searsia lancea* trees do not dry out the aquifer. The IP data show that they do remove contaminants from the groundwater and store them in the rhizosphere, achieving remediation of the water with the advantage of not inhibiting the flow of the water.

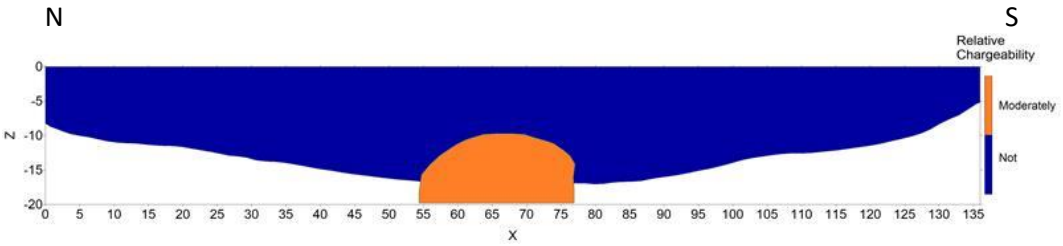


Figure 6-8: Final chargeability model for line 3 with surface features (reproduced from Figure 5-29).

The *Searsia lancea* tree with shallow roots shows the same features as the *Searsia lancea* tree with deep roots. The only difference is the size of the contaminant reservoir around the roots. The older tree with deeper roots stores a larger reservoir than the younger tree with shallower roots.

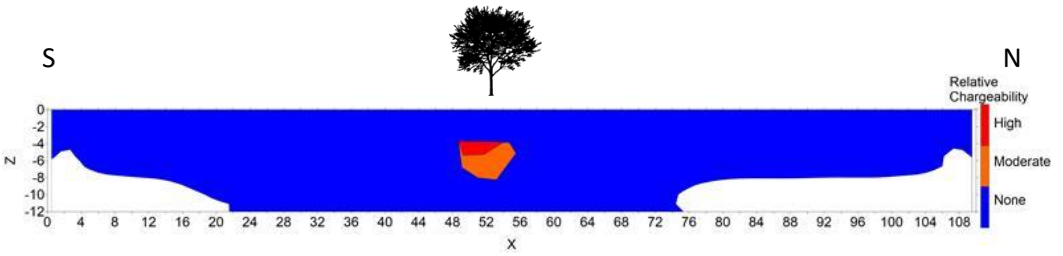


Figure 6-9: Final chargeability model for line 4 with surface features (reproduced from Figure 5-40).

The IP models are not well constrained because the data are inaccurate due to the low power source available for the study. The spatial relationship between the anomalies in the final models and the expected positions of the tree roots should be investigated further. The trees on the study site are planted because they survive in salty environments and they extract either large amounts of water (*Eucalyptus*) or they extract water and store the contaminants in the rhizosphere (*Searsia lancea*). Sulphides

stored in and around the root systems of these trees have given an IP response, showing this method to be useful for mapping the effectiveness of phytoremediation and its effects on AMD.

6.3 Interpretation

It is clear from the data acquired around the tree roots that the effects of the specific trees are visible in electrical resistivity data. This study presents evidence that a lane of *Eucalyptus* trees increases evapotranspiration to such an extent that the decrease in pore water content in weathered bedrock (specifically weathered andesitic lava) can change the resistivity in the unit to a measurable degree. A lane of trees of the species *Searsia lancea* does not have this same effect on the aquifer.

The electrical resistivity of the aquifer is unaffected at depth by the two mature *Searsia lancea* trees that were studied. The soil surrounding the tree roots had a decreased resistivity. This can have two possible explanations. It is either drier, or contains less conductive material than the areas where the tree does not act on the soil. Drier soil may be caused by the *Searsia lancea* extracting moisture with its shallow roots, or by the increased biological activity around the tree trunk, which may lead to greater water infiltration in the subsurface. The alternative is that the shallow roots remove conductive elements form the topsoil as it is removing nutrients.

The primary aim of this project was to map the AMD plume. The ER method is too slow to deliver the scale of spatial data required for mapping the entire plume. Ground penetrating radar (GPR) data were acquired with the aim of supplementing the ER data to map the AMD plume. There was, however, no change in the depth of penetration of the 40 MHz radar pulses and the data could not be used to map deeper than a few centimetres anywhere on the site. Three observations can be made from the sets of parallel lines obtained for this study.

Firstly, with increasing distance from the source of the contaminated water, the first layer electrical resistivity increases in the soil. Weathered material derived from the lavas are expected to be (at least partially) felsic, because the lavas of the Platberg Group are bimodal. Either the water mixes with rain water and the TDS is decreased along with the electrical conductivity (following vector AB in Figure 6-3), or the water

reacts with the weathered felsic lavas and the consequent decrease in resistivity means the water's carrying potential of heavier metals is decreased and the extra material is dumped. This should be found somewhere between vector AI and vector AH in Figure 6-3.

Secondly, with increasing distance from an area where uncontaminated water is expected (Figure 6-5a) to an area where an increase in water contamination is expected (Figure 6-5b, movement along vector AF in Figure 6-3) to an area where water has been partially remediated (Figure 6-5c, movement along vector AI) large karst features are expected to be present. The size and extent of karst topography in dolomite mean that groundwater can flow much greater distances in less time in this type of aquifer than in crystalline aquifers found in rocks like lavas. It is crucial to the success of the entire system that acid water not be allowed to enter karst topography as the spread of contamination could be significantly accelerated.

Thirdly, the effect of the *Tamarix* woodland on the electrical resistivity data is very encouraging. It is expected that the *Tamarix* trees are not as thirsty as the *Eucalyptus* and that the decrease in conductivity is not due to the drying up of the aquifer, but due to the removal of contaminants (vector AI in Figure 6-3).

IP data were collected on the four profiles, which show IP anomalies where the roots of some of the plant species are expected to be found, and IP offers a novel method of mapping the contaminant storage in and around the root systems of these plants. Direct sampling of the roots immediately after measuring the IP response, preferably with a high power electrical current source, will allow future work to measure the size of contaminant reservoirs in and around tree roots. This will provide further information as to the effectiveness of different species and the impact of tree age and size on phytoremediation.

The part of the IP data that is especially encouraging is that the older tree has a larger (spatial) anomaly associated with it. This is what is expected of plants that accumulate contaminants in and around tree roots, as the soil becomes saturated with salts and the trees will eventually no longer have the desired effects on the AMD plume.

Chapter 7 - Conclusions and further studies

Together ER and IP demonstrate a quantifiable reduction of TDS in the water below the trees.

The electrical resistivity can map AMD plume propagation and the effects of phytoremediation at gold mine dumps in the Witwatersrand basin. This can be done by using electrical resistivity data and correlating it to the SO_4 concentration in boreholes. The number of boreholes can be decreased if geophysical data is used to extrapolate over an area.

For this study, bedrock was mapped at between 5 and 11 m depth. Considering that the water table in the area is as little as 1.5 m below surface (from the borehole data) any monitoring of the plume needs to occur between 1.5 and 11 m deep to map the entire surficial aquifer. The extent of a plume cannot be mapped by the electrical resistivity method if the data are not collected on a very large scale, which will be costly. The reason for this is that the method is relatively slow. GPR is much faster but the data were not interpretable. Time-domain EM will not be able to map the shallowest occurrence of water (less than 2 m). The last available option is to use frequency-domain EM data. More than one loop configuration and offset can be used at the same time and this will allow for mapping of the deeper and more shallow aquifers. Combining this data empirically with borehole SO_4 concentration, would allow for mapping of the plume, most efficiently.

Trees that increase evapotranspiration have measurable effects on the electrical resistivity of the aquifer. Trees that store contaminants in the rhizosphere can be monitored directly using induced polarisation data. Trees that accumulate contaminants in their own biomasses can have a measurable effect on the electrical resistivity of the surficial aquifer downstream from the source of the contaminants in a TSF. This needs to be studied further as the data (and the resulting models) were of poor quality.

The IP anomalies need to be tested by either using an auger drill sampling the stored contaminants directly or by using a high power (one ampere or more) source or (preferably) both. An opportunity exists for doing frequency-domain EM and correlating the data with groundwater data from the boreholes at the same time. This will allow

calibration of the measurements and produce a map of SO_4 concentration that other scientists and engineers can work with. Understanding the relationship between water conductivity and the measured conductivity in metamorphosed rocks would be extremely useful as Archie's law is not helpful in such environments.

References

Abiye, T.A. Mengistu, H. and Demlie, M.B. (2011) Groundwater resources in the crystalline rocks of the Johannesburg area, South Africa, *Journal of Water Resource and Protection*, vol. 3, pp. 199-212.

Akcil, A. and Koldas, S. (2006) Acid Mine Drainage (AMD): causes, treatment and case studies, *Journal of Cleaner Production*, vol. 14, pp. 1139-1145.

Alexandre, P. Andreoli, M.A.G. Jamison, A. and Gibson, R.L. (2006) 40Ar/39Ar age constraints on low-grade metamorphism and cleavage development in the Transvaal Supergroup (central Kaapvaal Craton, South Africa): implications for the tectonic setting of the Bushveld Igneous Complex. *South African Journal of Geology*, vol. 109, pp. 393–410.

Anderson, L.A. and Keller, G.V. (1964) A study in induced polarization, *Geophysics*, vol. 29, iss. 5, pp. 848-864.

AngloGold Ashanti. (2003) AngloGold Vaal River and West Wits Operations – Development of monitoring boreholes for the Wits AngloGold Woodlands Project, AGES – Africa Geo- Environmental Services, *Technical Report: AS/R/04/09/14*, Pretoria.

Anjum, N.A. Pereira, M.E. Ahmad, I. Duarte, A.C. Umar, S. and Khan, N. A. eds. (2012) *Phytotechnologies: Remediation of Environmental Contaminants* Florida, CRC Press.

Barnard, H.C. (1999) *Hydrogeological Map of Johannesburg 2526, 1:500 000*, Pretoria: Department of Water Affairs and Forestry.

Barnard, H.C. (2000) *An Explanation for the 1:500 000 Hydrogeological Map of Johannesburg 2526,* Pretoria: Department of Water Affairs and Forestry.

Blaylock, M.J. and Huang, J.W. (2000) Phytoextraction of metals, In: Raskin, I. and Ensley, B.D. eds. *Phytoremediation of toxic metals. Using plants to clean up the environment*. New York: John Wiley & Sons, Inc. pp. 53-70.

Bridge, C.F. Bizzell, K.R. and Ramachandran, K. (2015) Mapping Acid Mine Drainage at an abandoned mine site in Ottawa County, Oklahoma using 3D electrical resistivity tomography, *Symposium on the Application of Geophysics to Engineering and Environmental Problems*, Society of Exploration Geophysicists and Environment and Engineering Geophysical Society, pp. 287-291.

Burke, K. Kidd, W.S.F. and Kusky, T. (1985) Is the Venterdorp Rift System of Southern Africa related to a continental collision between the Kaapvaal and Zimbabwe cratons at 2.64 Ga Ago? *Tectonophysics*, vol. 115, pp. 1-24.

Camden-Smith, B. Johnson, R. Richardson, R. Billing, D. and Tutu, H. (2013) Investigating the potential impact of efflorescent mineral crusts on water quality: complementing analytical techniques with geochemical modelling, *Reliable Minewater Technology, IMWA 2013*, pp. 281-287.

Campbell, D.L. and Fitterman, D.V. (2000) Geoelectrical methods for investigating mine dumps, *Proceedings of the Fifth International Conference on Acid Rock Drainage, SME,* Littleton, Colorado, pp.1513-1524.

Campbell, D.L. Horton, R.J. Bisdorf, R.J. Fey, D.L. Powers, M.H. and Fitterman, D.V. (1999) Some geophysical methods for tailings/mine waste work, *Tailings and Mine Waste '99, Proceedings of the Sixth International Conference*, Colorado, pp. 35-43.

Crow, C. and Condie, K.C. (1988) Geochemistry and origin of late Archean volcanics from the Ventersdorp supergroup, South Africa, *Precambrian Research*, vol. 42, no.1–2, pp. 19-37.

Dahlin, T. (1996). 2D resistivity surveying for environmental and engineering applications, *First Break*, vol. 14 no. 7, pp. 275-283. DOI: 10.3997/1365-2397.1996014.

De Sousa, E. Marais, A. and Prinsloo, M. (2006) *AngloGold Ashanti Emergency Dam Construction Project: Hydrogeological Study*, South Africa: GCS (Pty) Ltd (Unpublished).

Dressel, M. (2005) *AngloGold Ashanti Vaal River Operations Proposed Storm Water Dam Seepage Analysis*, South Africa: GCS (Pty) Ltd (Unpublished).

Durand, J.F. (2012) The impact of gold mining on the Witwatersrand on the rivers and karst system of Gauteng and North West Province, South Africa, Journal of African Earth Sciences vol. 68, pp. 24–43.

Dye, P.J. and Weiersbye, I.M., 2010. The Mine Woodlands Project in the Witwatersrand Basin gold fields of South Africa: strategy and progress. *Mine Water and Innovative Thinking, Sydney, Nova Scotia*.

Ebraheem, A.M. Hamburger, M.W. Bayless, E.R. and Krothe, N.C. (1990) A study of acid mine drainage using earth resisitivity measurements, *Groundwater*, vol. 28, no. 3, pp. 361-368.

Edwards, L.S. (1977) A modified pseudosection for resistivity and induced-polarization, *Geophysics*, vol. 42, pp. 1020-1036.

Egiebor, N.O. and Oni, B. (2007) Acid rock drainage formation and treatment: a review, *Asia-Pacific Journal of Chemical Engineering*, vol. 2, iss. 1, pp. 47-62.

Ellis, R.G. and Oldenburg D.W. (1994) Applied geophysical inversion. *Geophysical Journal International*, vol. 116, pp. 5–11.

Eriksson, P.G. Condie, K.C. Tirsgaard, H. Mueller, W.U. Altermann, W. Miall, A.D. Aspler, L.B. Catuneanu, O. and Chiarenzelli, J.R. (1998) Precambrian clastic sedimentation systems, *Sedimentary Geology*, vol. 120, pp. 5–53.

Eriksson, P.G. Altermann, W. and Hartzer, F.J. (2006) The Transvaal Supergroup and its Precursors, In: Johnson, M.R. Anhaeusser, C.R. and Thomas, R.J. eds. *The Geology of South Africa*. Johannesburg: Geological Society of South Africa, pp.187-208.

Ewart, T.I. (2011) *Acid mine drainage in the Gauteng province of South Africa - a phenomenological study on the degree of alignment between stakeholders concerning a sustainable solution to acid mine drainage*, M.Phil thesis, University of Stellenbosch (Unpublished).

Fiandaca, G. Auken, E. Christiansen, A.V. and Gazoty, A. (2012) Time-domain-induced polarization: full-decay forward modeling and 1D laterally constrained inversion of Cole-Cole parameters. *Geophysics* vol. 77, pp. E213 –E225.

Franke, O.L. Reilly, T.E. Haefner, R.J. and Simmons, D.L. (1990) *Study guide for a beginning course in groundwater hydrology*, Reston, Virginia, US Geological Survey, pp. 184.

Fraser, W.W. and Robertson, J.D. (1994) Subaqueous disposal of reactive mine waste: an overview and update of case studies-MEND/Canada, *International Land Reclamation and Mine Drainage Conference*, Pittsburgh, PA, pp. 250-259.

Frimmel, H.E. (1994) Metamorphism of Witwatersrand gold, *Exploration Mining Geology*, vol. 3, pp. 357–370.

Fripp, J. Ziemkiewicz, D.F. and Charkavorki, H. (2000) Acid Mine Drainage Treatment, *EMRRP Technical Notes Collection (ERDC TN-EMRRP- SR-14)*, U.S. Army Engineer Research and Development Center, Vicksburg, MS.

Garcia, C. Moreno, D.A. Ballester, A. Blazquez, M.L. and Gonzalez, F. (2001) Bioremediation of an industrial acid mine water by metal-tolerant sulphate-reducing bacteria, *Minerals Engineering*, vol. 14, iss. 9, pp. 997-1008.

Gazea, B. Adam, K. and Kontopoulos, A. (1996) A review of passive systems for the treatment of acid mine drainage, *Minerals engineering*, vol. 9, iss. 1, pp. 23-42.

Glover, P.W.J. (2016) Archie's law – a reappraisal, *Solid Earth*, vol. 7, pp. 1157-1169.

Google Earth V. 7.1.5.1557. (11 March 2017) Orkney, North West, South Africa, 35J, 467539.65 m E, 7020910.03 m S, elev 1306 m, eye alt 1.90 km, CNES/Astrium 2016, available from*: http://code.google.com/apis/earth/*

Grindley, S. (2014) *Modelling the effects of trees on a contaminated groundwater plume from a gold tailings storage facility in the Orkney district*, MSc thesis, University of the Witwatersrand (Unpublished).

Gudjurgis, P.J. Katsube, T.J. and Gingerich. J. (1997) Complex resistivity characteristics of pyrite and clays altered by acid-mine-drainage contaminants: implications for monitoring of advancing contamination fronts. *Expanded Abstracts with Biographies, Society of Exploration Geophysicists International Exposition and Sixty-Seventh Annual Meeting*, Dallas Texas, vol.1, pp.344-347.

Guy, B.M. Beukes, N.J. and Gutzmer, J. (2010) Paleoenvironmental controls on the texture and chemical composition of pyrite from non-conglomeratic sedimentary rocks of the Mesoarchean Witwatersrand Supergroup, South Africa, *South African Journal of Geology*, vol. 113, pp. 195–228.

Hawkins, J.W. (1994) Assessment of contaminant load changes caused by remining abandoned coal mines, *International Land Reclamation and Mine Drainage Conference*, Pittsburgh, PA, pp. 20-29.

Hedlin, R. S. and Watzlaf, G. R. (1994) The effects of anoxic limestone drains on mine water chemistry, *3rd International Conference on the Abatement of Acidic Drainage*, Pittsburgh, PA, pp. 185-194.

Hong, M.S. Farmayan, W. F. Dortch, I. J. and Chiang, C. Y. (2001) Phytoremediation of MTBE from a Groundwater Plume, *Environ Sci Technol*, vol. 35, no. 6, pp 1231–1239.

Huang, J.W. Chen, J. Berti, W.R. and Cunningham, S.D. (1997) Phytoremediation of lead-contaminated soils: role of synthetic chelates in lead phytoextraction, *Environmental Science & Technology*, vol. 31, no.3, pp. 800-805.

Hupfer, S. Martin, T. Weller, A. Gunther, T. Kuhn, K. Ngninjio, V.D.N. and Noell, U. (2015) *Journal of Applied Geophysics*, vol. 135, pp. 456–46.

Hustwit, C.C. Ackman, T.E. and Erickson, P.E. (1992) The role of oxygen transfer in acid mine drainage (AMD) treatment, *Water Environment Research*, vol. 64, no. 6, pp. 817-823.

Johnson, D.B. and Hallberg, K.B. (2005) Acid mine drainage remediation options: a review, *Science of the Total Environment,* vol. 338, pp. 3–14.

Kirsch, R. ed. (2009) *Groundwater geophysics: a tool for hydrogeology, 2nd Ed*. Berlin: Springer-Verlag.

Kumar, P.B.A.N. Dushenkov, V. Motto, H. and Raskin, I. (1995) Phytoextraction: the use of plants to remove heavy metals from soils, *Environmental Science and Technology*, vol. 29, pp. 1232 – 1238.

Li, Y. and Oldenburg, D.W. (1994) Inversion of 3-D DC resistivity data using an approximate inverse mapping, *Geophysical Journal International*, vol. 116, pp. 527–537.

Loke, M. (2004) *Tutorial: 2-D and 3-D electrical imaging surveys*. Copyright M.H. Loke, available from*:* www.geoelectrical.com.

McCarthy, T.S. (2006) The Witwatersrand Supergroup, In: Johnson, M.R. Anhaeusser, C.R. and Thomas, R.J. eds. *The Geology of South Africa*. Johannesburg: Geological Society of South Africa, pp. 155-186.

McCarthy, T.S. (2011) The impact of acid mine drainage in South Africa, *South African Journal of Science*, vol. 107, no. 5, article no. 712, pp. 7.

McCleskey, R.B. Nordstrom, D.K. Ryan, J.N. and Ball, J.W. (2012) A new method of calculating electrical conductivity with applications to natural waters, *Geochimica et Cosmochimica Acta*, vol. 77, pp. 369–382.

Mcgleorth, B. (2014) personal communication: February.

Mendez, M.O. and Maier, R.M. (2008) Phytoremediation of mine tailing in temperate and arid environments, *Reviews in Environmental Science and Biotechnology*, vol. 7, pp. 47–59.

Merkel, R. H. (1972) The use of resistivity techniques to delineate acid mine drainage in groundwater, *Groundwater*, vol. 10, pp. 38-42.

Naicker, K. Cukrowska, E. and McCarthy, T.S. (2003) Acid mine drainage arising from gold mining activity in Johannesburg, South Africa and environs, *Environmental Pollution*, vol. 122, pp. 29-40.

Naidoo, B. (2009) Acid mine drainage single most significant threat to South Africa's environment, *Mining weekly*, available from: http://www.miningwe ekly.com/article/in-the-midst-of-a-disaster-2009-05-08 [Accessed on 8 September 2013].

Nordstrom, D. K. (1979) Aqueous pyrite oxidation and the consequent formation of secondary iron minerals, In: *Acid Sulfate Weathering. Soil Science Society of America Special Publication No. 10*, pp. 37-56.

Nyquist, J.E. and Corry, C.E. (2002) Self-potential: The ugly duckling of environmental geophysics, *The Leading Edge*, vol. 21, iss. 5, pp. 446-451.

Oldenburg, D.W. and Li, Y. (1994) Inversion of induced polarization data, *Geophysics*, vol. 59, pp. 1327–1341.

Oldenburg, D.W. and Li, Y. (1999) Estimating depth of investigation in DC resistivity and IP surveys, *Geophysics*, vol. 64, no. 2, pp. 403-416.

Olenchenko, V.V. Kucher, D.O. Bortnikova, S.B. Gas'kova, O.L. Edelev, A.V. and Gora, M.P. (2016) Vertical and lateral spreading of highly mineralized acid drainage solutions (Ur dump, Salair): electrical resistivity tomography and hydrogeochemical data, *Russian Geology and Geophysics*, vol. 57, no. 4, pp. 617-628.

Oristaglio, M. and Spies, B. (1999) *Three-dimensional Electromagnetics*. Society of Exploration Geophysicists.

Paterson, N. Robertson, D. Hearst, R. Stanton-Gray, R. Miller, E. and Silverthorn, S. (1994) Application of remote sensing and geophysics to the detection and monitoring of acid mine drainage: *MEND Project #4.6.3*, Ottawa, Ontario: CANMET Library, pp. 116.

Perren, L. (2005) *Investigating the Performance of Electrical Resistivity Arrays*, MSc thesis, Virginia Polytechnic Institute and State University, (Unpublished).

Rabhi M. Karray-Bouraoui, N. Medini, R. Attia, H. Athar, H. Lachaâl, M. Abdelly, C. and Smaoui, A. (2010a): Seasonal variations in the capacities of phytodesalination of a salt-affected soil in two perennial halophytes in their natural biotope, *J. Biol. Res*, vol. 14, pp. 181-189.

Revil, A. and Glover, P.W.J. (1998) Nature of surface electrical conductivity in natural sands, sandstones, and clays, *Geophysical Research Letters*, vol. 25, no. 5, pp. 691-694.

Robb, L.J. and Robb, V.M. (1998) Gold in the Witwatersrand basin, In Wilson, M.G.C. and Anhaeusser, C.R. eds. *The Mineral Resources of South Africa*, *Handbook*, Pretoria: Council for Geosciences, vol. 16, pp. 294-349.

Rösner, T. (1999) The environmental impact of seepage from gold mine tailing dams near Johannesburg, South Africa, PhD Thesis, University of Pretoria (Unpublished).

Rösner, T. and Van Schalkwyk, A. (2000) The environmental impact of gold mine tailings footprints in the Johannesburg region, South Africa, Bulletin of Engineering Geology and the Environment, vol. 59, pp. 137–148.

Rucker, D.F. Glaser, D.R. Osborne, T. and Maehl, W.C. (2009) Electrical resistivity characterization of a reclaimed gold mine to delineate acid rock drainage pathways, *Mine Water and the Environment* vol. 28, pp. 146–157.

Rucker, D.F. (2010) Moisture estimation within a mine heap: an application of cokriging with assay data and electrical resistivity, Geophysics, vol. 75, no. 1, pp. B11-B23.

SACS (South African Committee for Stratigraphy, 1980). Stratigraphy of South Africa. Part 1 (Compiled by L.E. Kent). *Lithostratigraphy of the Republic of South Africa, South West Africa/Namibia, and the republics of Bophuthatswana, Transkei and Venda.* Handbook 8, Geological Survey, South Africa, pp. 690a

Schõn, J.H. (1996) *Physical properties of Rocks: Fundamentals and Principles of Petrophysics*, Oxford: Elsevier Science Publishers.

Seigel, H.O. (1959) Mathematical formulation and type curves for induced polarization, *Geophysics*, vol. 24, pp. 547–565.

Sherlock, E.J. Lawrence, R.W. and Poulin, R. (1995) On the neutralization of acid rock drainage by carbonate and silicate minerals, *Environmental Geology*, vol. 25, pp. 43-54.

Soininen, H. (1984) The behavior of the apparent resistivity phase spectrum in the case of a polarizable prism in an unpolarizable half-space, *Geophysics*, vol. 49, no. 9, pp. 1534-1540.

Sridhar, S. Victor, F.M. and Steven, C.M.C. (2002) Phytoremediation: An ecological solution to organic chemical contamination, *Ecological Engineering*, vol 18, pp. 647–658.

Sumner, J.S. (1976) *Principles of Induced Polarization for Geophysical Exploration* Elsevier: Amsterdam.

Telford, W.M. Geldart, L.P. and Sheriff, R.E. (1990) *Applied Geophysics 2nd Ed*. Cambridge: Cambridge University Press.

Tutu, H. McCarthy, H.S. and Cukrowska E. (2008) The chemical characteristics of acid mine drainage with particular reference to sources, distribution and remediation: The Witwatersrand Basin, South Africa as a case study, *Applied Geochemistry*, vol. 23, pp. 3666–3684.

Unsworth, M.J. Soyer, W. Tuncer, V. Wagner, A. Barnes, D. (2007) Hydrogeologic assessment of the Amchitka Island nuclear test site (Alaska) with magnetotellurics, *Geophysics*, vol. 72, no. 3, pp. B47-B57.

Van der Westhuizen, W.A. De Bruiyn, H. and Meintjes, P.G. (1991) The Ventersdorp Supergroup: an overview, *Journal of African Earth Sciences (and the Middle East)*, vol. 13, no. 1, pp. 83-105.

Van der Westhuizen, W.A. De Bruiyn, H. and Meintjies, P.G. (2006) The Ventersdorp Supergroup, In: Johnson, M.R. Anhaeusser, C.R. and Thomas, R.J. eds. *The Geology of South Africa*. Pretoria: Geological Society of South Africa, pp. 187-208.

Van Schoor, M. Mare, L.P. and Fourie, C.J.S. (2009) Comparison between time- and frequency-domain induced polarisation parametres, *11th SAGA Biennial Technical Meeting and Exhibition*, pp. 259-263.

Wardlaw, S. and Wagner, R. (1994) Development of waste rock sampling protocol using induced polarization: Final Report, CANMET-MSL Div. LR, 777-071, Natural Resources Canada: Ottawa.

Weiersbye, M. (2007) Global review and cost comparison of conventional and phyto-technologies for mine closure, In Fourie, A.B. Tibbett, M. and Wiertz, J. eds. *Mine Closure 2007, Proceedings of the 2nd international Seminar on Mine closure*, Santiago, pp 13—29.

Wolke, R. and Schwetlick, H. (1988) Iteratively reweighted least squares algorithms, convergence analysis, and numerical comparisons, *SIAM Journal of Scientific and Statistical Computations*, vol. 9, pp. 907-921.

Wright, E.P. and Burgess, W.G. eds. (1992) The Hydrogeology of Crystalline Basement Aquifers in Africa, *Geological Society Special Publication,* no. 66, pp. 1-27.

Yuval, D. and Oldenburg, W. (1996) DC resistivity and IP methods in acid mine drainage problems: results from the Copper Cliff mine tailings impoundments, *Journal of Applied Geophysics*, vol. 34, pp. 187-198.

Appendices

Appendix A: Setting used for smoothness constrained inversion in Res2dInv

Inversion settings

Initial damping factor 0.15

Minimum damping factor 0.02

Line search option Always

Convergence limit for relative change in RMS error in percent 0.1

Minimum change in RMS error for line search in percent 0.5

Number of iterations 10

Vertical to horizontal flatness filter ratio 1

Model for increase in thickness of layers User defined

Number of nodes between adjacent electrodes 2

Flatness filter type, Include smoothing of model resistivity Directly on model

Type of Jacobian matrix calculation Gauss-Newton

Increase of damping factor with depth 1.05

Robust data constrain? Yes

Cutoff factor for data constrain 0.05

Robust model constrain? Yes

Cutoff factor for model constrain 0.005

Allow number of model parameters to exceed datum points? Yes

Use extended model? Yes

Reduce effect of side blocks? Slight

Type of mesh Normal

Optimise damping factor? Yes

Thickness of first layer 0.375

Factor to increase thickness layer with depth 1.1

USE FINITE ELEMENT METHOD No

WIDTH OF BLOCKS Normal width

MAKE SURE BLOCKS HAVE THE SAME WIDTH Yes

RMS CONVERGENCE LIMIT 5%

USE LOGARITHM OF APPARENT RESISTIVITY Yes

TYPE OF IP INVERSION METHOD Concurrent

PROCEED AUTOMATICALLY FOR SEQUENTIAL METHOD No

IP DAMPING FACTOR 0.25

USE AUTOMATIC IP DAMPING FACTOR No

LIMIT RESISTIVITY VALUES No

Upper limit factor 50

Lower limit factor 0.02

Type of reference resistivity Average

Model refinement Half-width cells

Combined Combined Marquardt and Occam inversion Not used

Type of optimisation method Gauss-Newton

Use reference model in inversion Yes

Damping factor for reference model 0.01

Use fast method to calculate Jacobian matrix. Yes

Use higher damping for first layer? Yes

Extra damping factor for first layer 5

Type of finite-element method Trapezoidal elements

Factor to increase model depth range 1.05

Optimize Jacobian matrix calculation No

Automatically switch electrodes for negative geometric factor Yes

Force resistance value to be consistant with the geometric factor No

Shift the electrodes to round up positions of electrodes No

Use active constraint balancing No

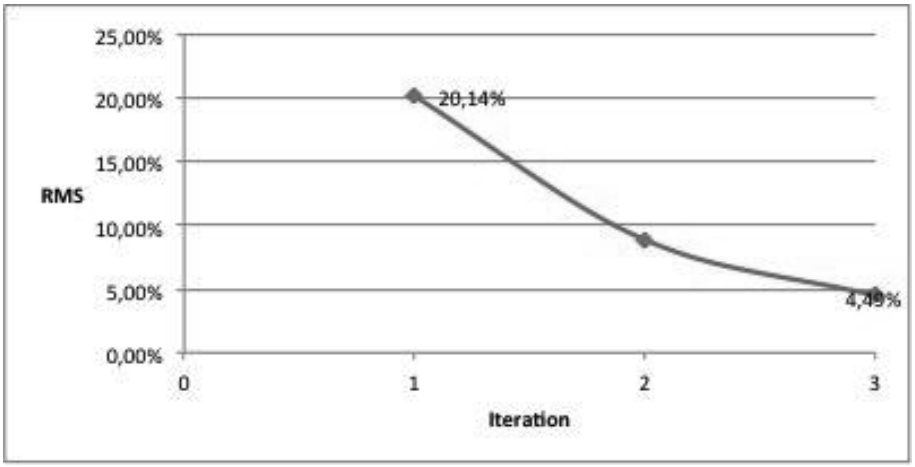
Type of active constraints Normal

Lower damping factor limit for active constraints 0.4

Upper damping factor limit for active constraints 2.5

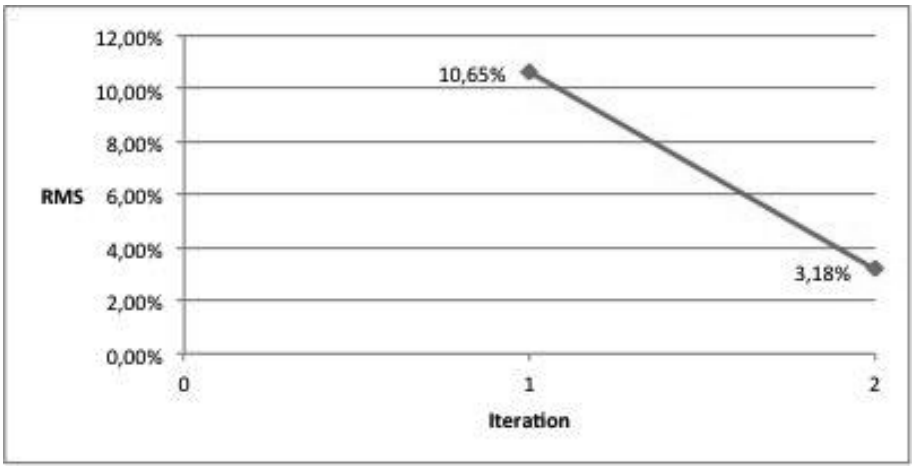
Appendix B: Select convergence curves for resistivity inversion

The convergence of smoothness constrained inversion for the Wenner Schlumberger data acquired along line 1 is shown in Figue B-1.



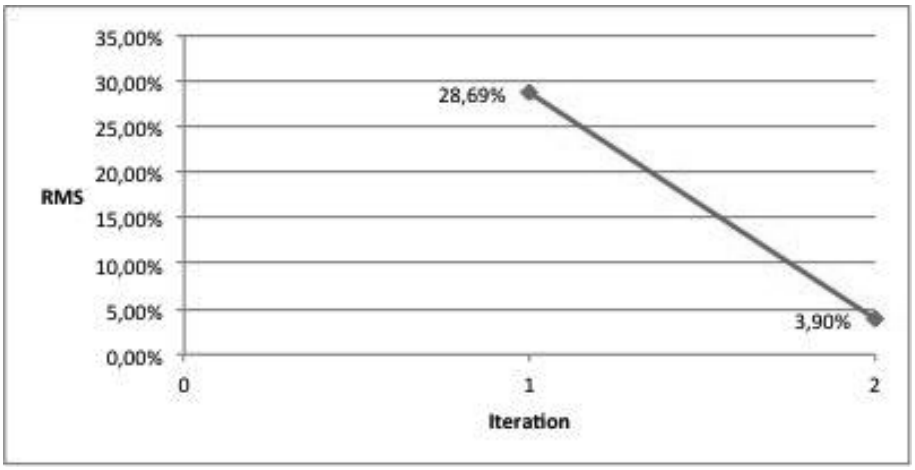
Figue B-1: Data misfit in percent root mean squared versus number of iterations (Wenner Schlumberger data line 1).

The convergence of smoothness constrained inversion for the Wenner alpha data acquired along line 2 is shown in Figue B-2.



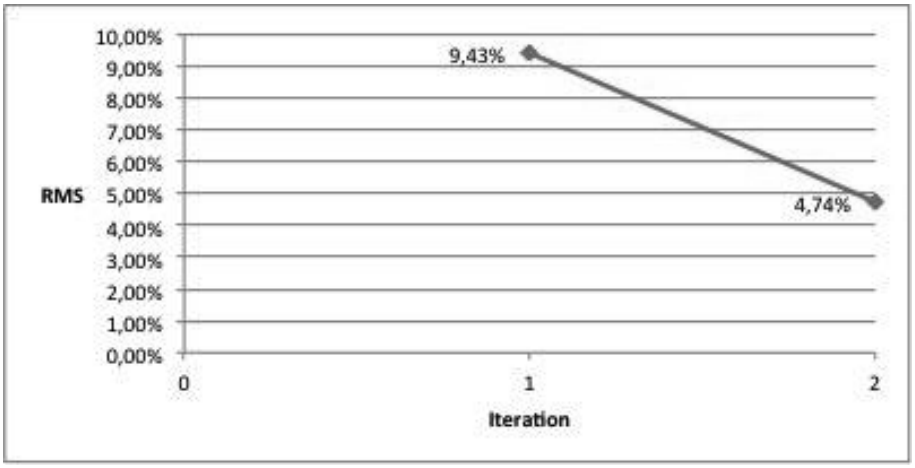
Figue B-2: Data misfit in percent root mean squared versus number of iterations (Wenner alpha data line 2).

The convergence of smoothness constrained inversion for the dipole-dipole data acquired along line 2 is shown in Figue B-3.



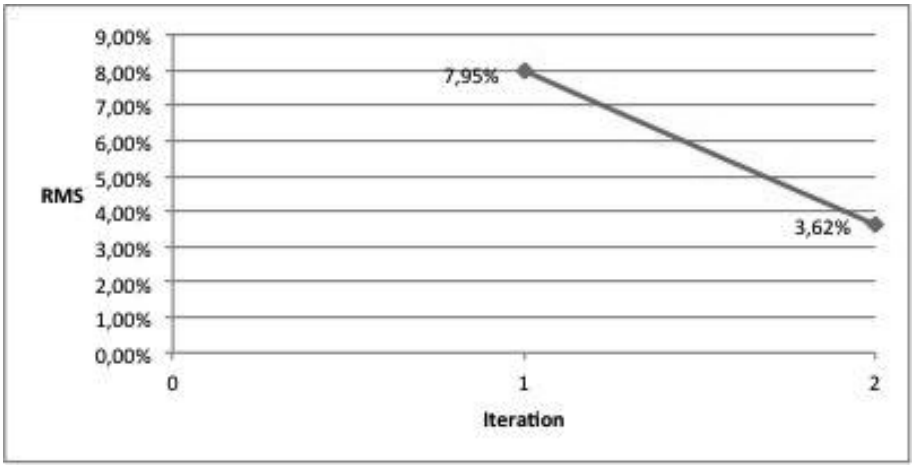
Figue B-3: Data misfit in percent root mean squared versus number of iterations (dipole-dipole data line 2).

The convergence of smoothness constrained inversion for the Wenner alpha data acquired along line 3 is shown in Figue B-4.



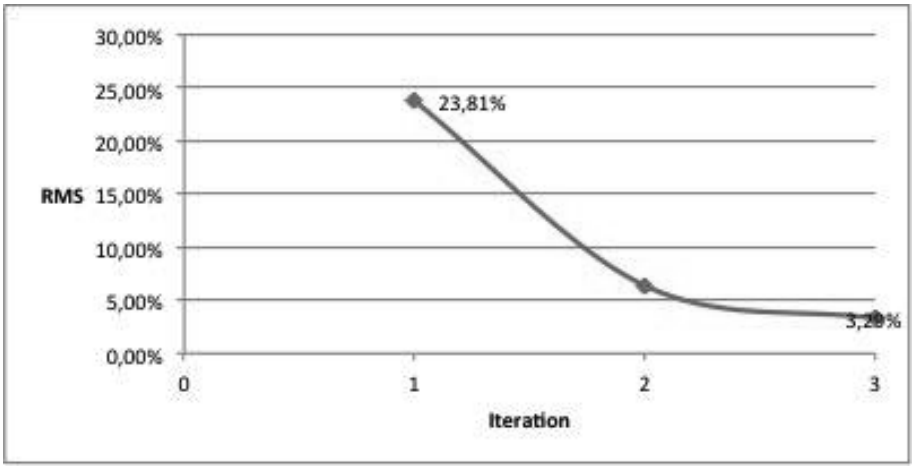
Figue B-4: Data misfit in percent root mean squared versus number of iterations (Wenner alpha data line 3).

The convergence of smoothness constrained inversion for the dipole-dipole data acquired along line 3 is shown in Figue B-5.



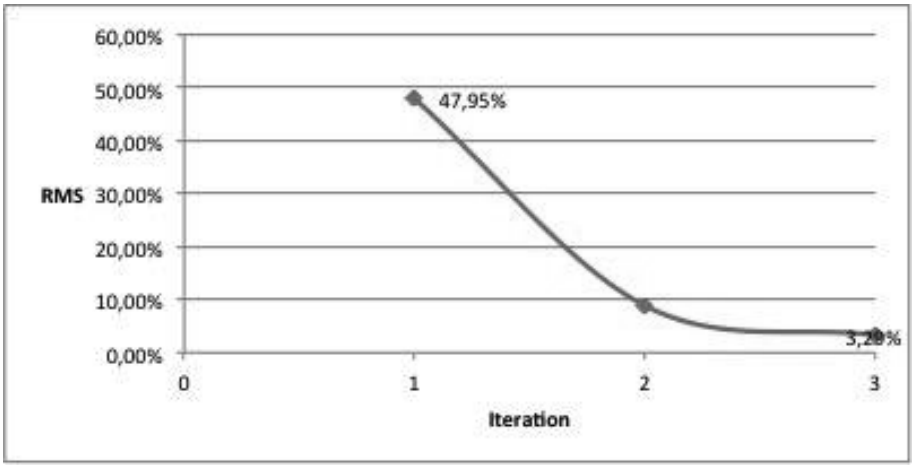
Figue B-5: Data misfit in percent root mean squared versus number of iterations (dipole-dipole data line 3).

The convergence of smoothness constrained inversion for the Wenner alpha data acquired along line 4 is shown in Figue B-6.



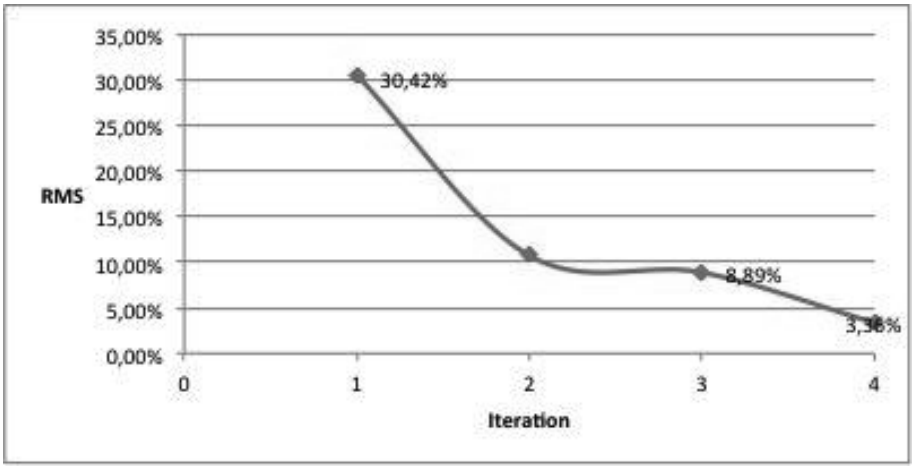
Figue B-6: Data misfit in percent root mean squared versus number of iterations (Wenner alpha data line 4).

The convergence of smoothness constrained inversion for the Wenner beta data acquired along line 4 is shown in Figue B-7.



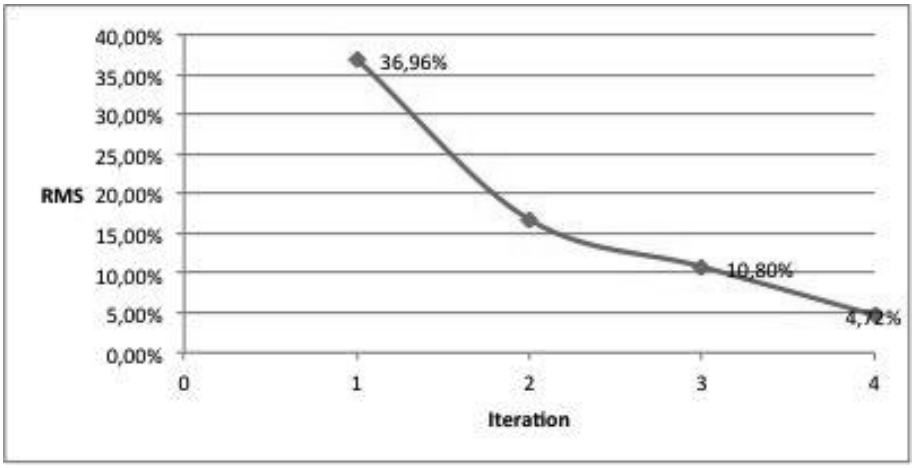
Figue B-7: Data misfit in percent root mean squared versus number of iterations (Wenner beta data line 4).

The convergence of the smoothness constrained inversion for Wenner Schlumberger data acquired along line 9 is shown in Figue B-8.



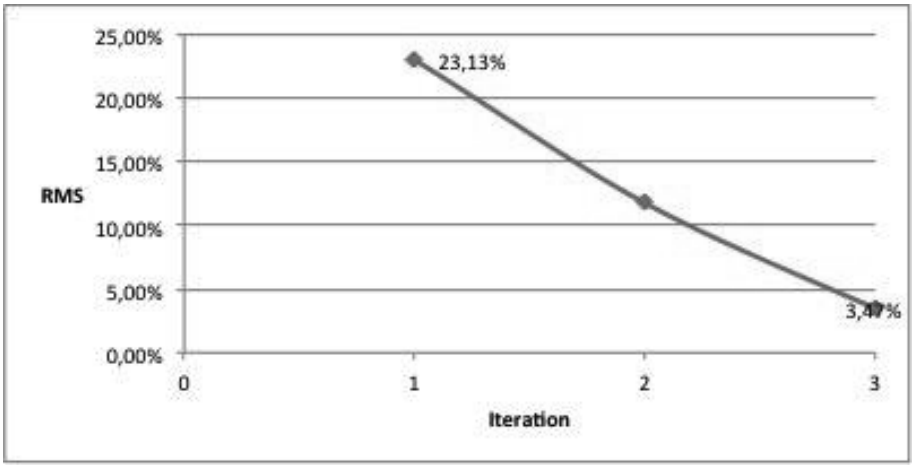
Figue B-8: Data misfit in percent root mean squared versus number of iterations (Wenner Schlumberger data line 9).

The convergence of smoothness constrained inversion for the dipole-dipole data acquired along line 9 is shown in Figue B-9.



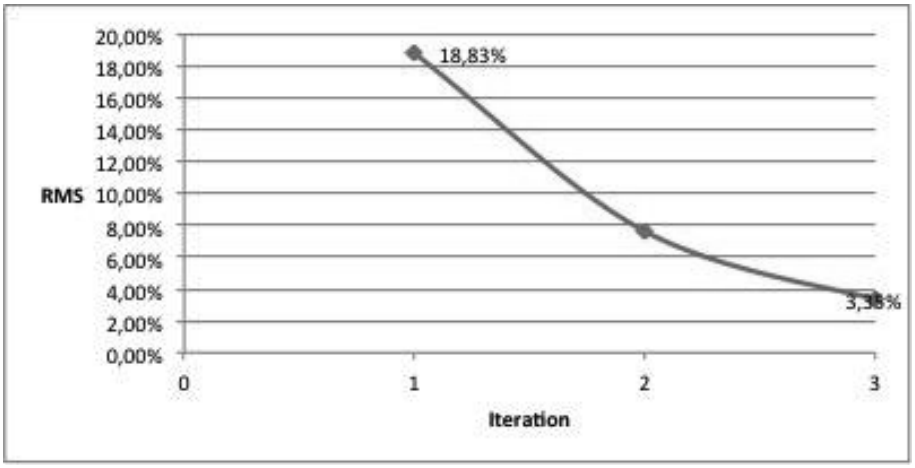
Figue B-9: Data misfit in percent root mean squared versus number of iterations (dipole-dipole data line 9).

The convergence of smoothness constrained inversion for the Wenner Schlumberger data acquired along line 12 is shown in Figue B-10.



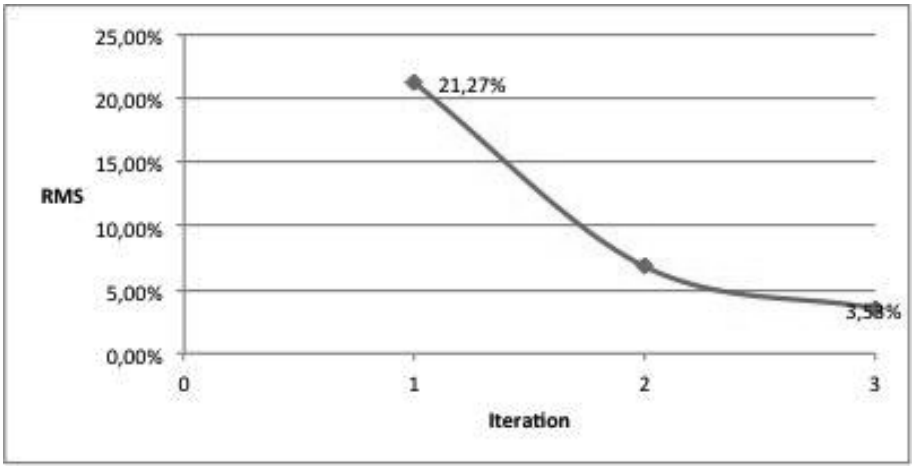
Figue B-10: Data misfit in percent root mean squared versus number of iterations (Wenner Schlumberger data line 12).

The convergence of smoothness constrained inversion for the dipole-dipole data acquired on line 12 is shown in Figue B-11.



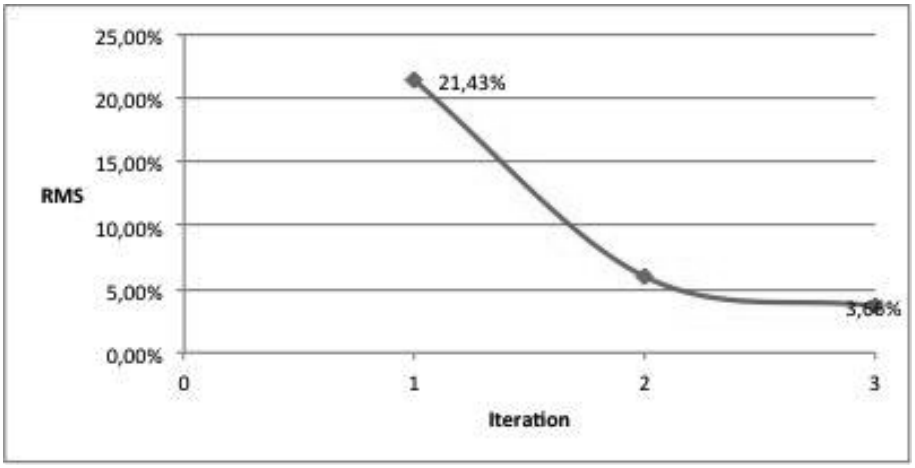
Figue B-11: Data misfit in percent root mean squared versus number of iterations (dipole-dipole data line 12).

The convergence of smoothness constrained inversion for the Wenner Sclumberger data acquired along line 5 is shown in Figue B-12.



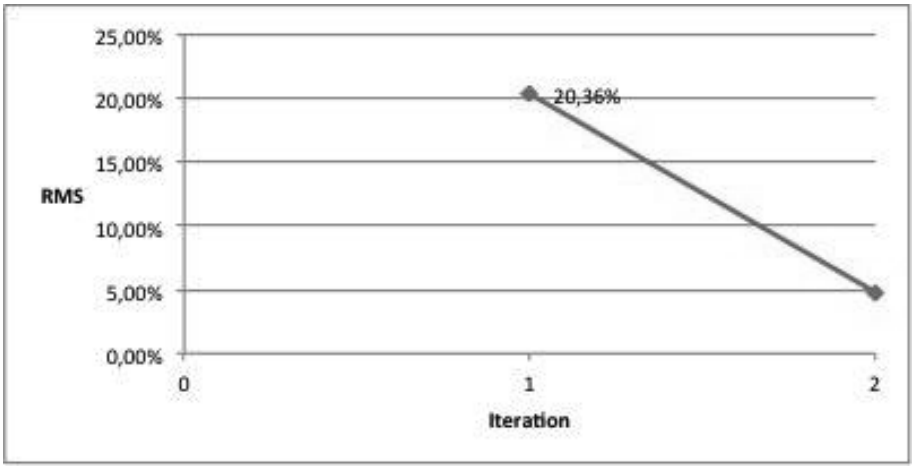
Figue B-12: Data misfit in percent root mean squared versus number of iterations (Wenner Schlumberger data line 5).

The convergence of smoothness constrained inversion for the dipole-dipole data acquired along line 5 is shown in Figue B-13.



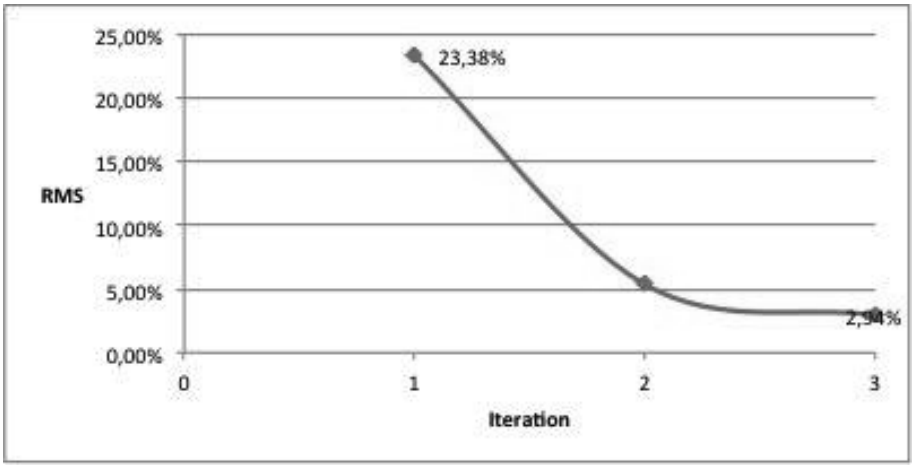
Figue B-13: Data misfit in percent root mean squared versus number of iterations (dipole-dipole data line 5).

The convergence of smoothness constrained inversion for the Wenner alpha data acquired along line 6 is shown in Figue B-14.



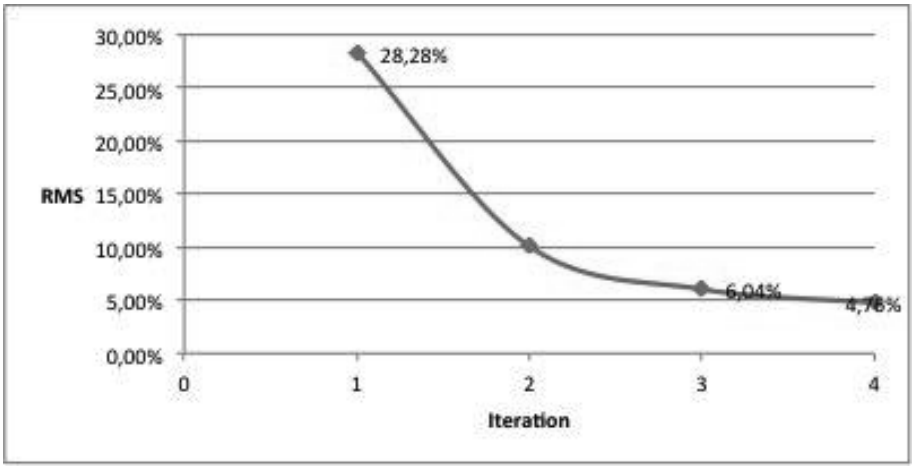
Figue B-14: Data misfit in percent root mean squared versus number of iterations (Wenner alpha data line 6).

The convergence of smoothness constrained inversion for the Wenner Sclumberger data acquired along line 6 is shown in Figue B-15.



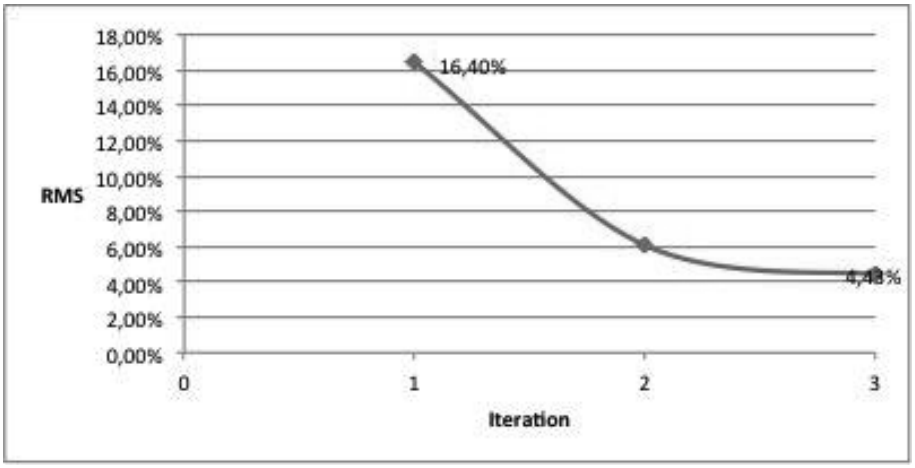
Figue B-15: Data misfit in percent root mean squared versus number of iterations (Wenner Schlumberger data line 6).

The convergence of smoothness constrained inversion for the dipole-dipole data acquired along line 6 is shown in Figue B-16.



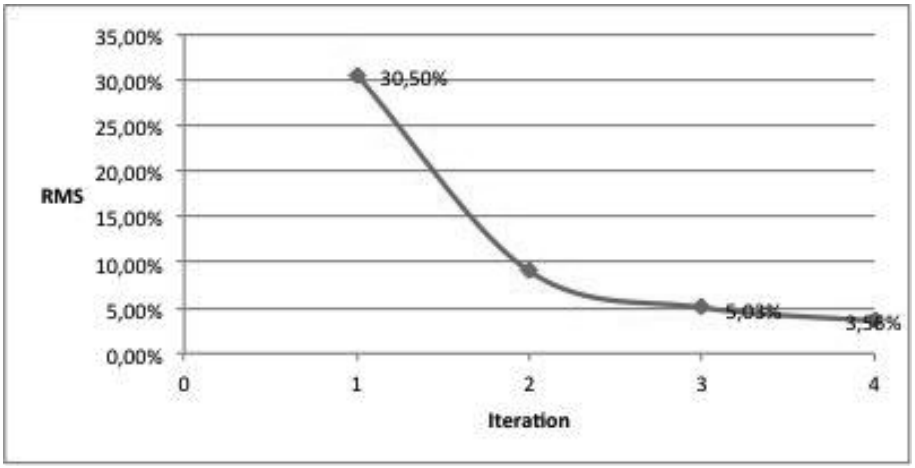
Figue B-16: Data misfit in percent root mean squared versus number of iterations (dipole-dipole data line 6).

The convergence of smoothness constrained inversion for the Wenner Schlumberger data acquired along line 11 is shown in Figue B-17.



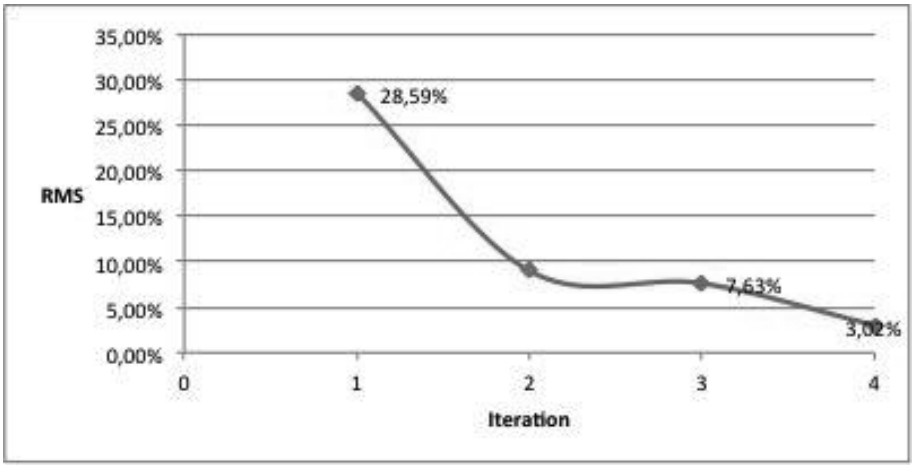
Figue B-17: Data misfit in percent root mean squared versus number of iterations (Wenner Schlumberger data line 11).

The convergence of smoothness constrained inversion for the dipole-dipole data acquired along line 11 is shown in Figue B-18.



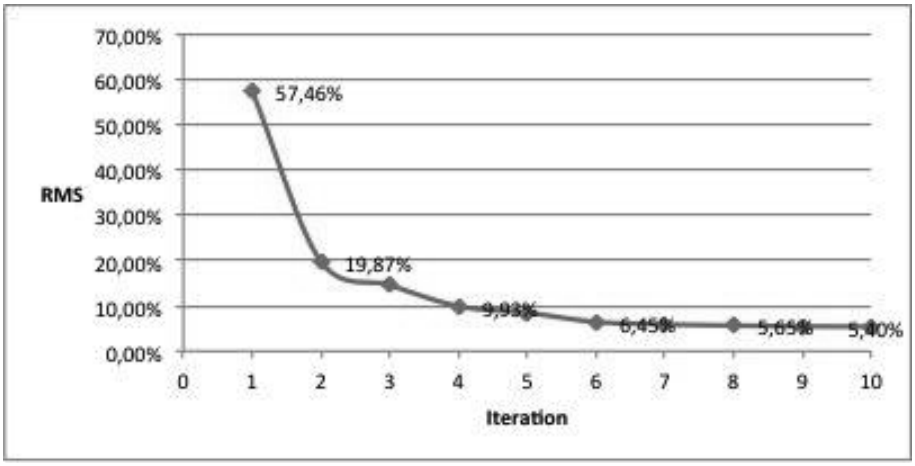
Figue B-18: Data misfit in percent root mean squared versus number of iterations (dipole-dipole data line 11).

The convergence of smoothness constrained inversion for the Wenner Schlumberger data acquired along line 8 is shown in Figue B-19.



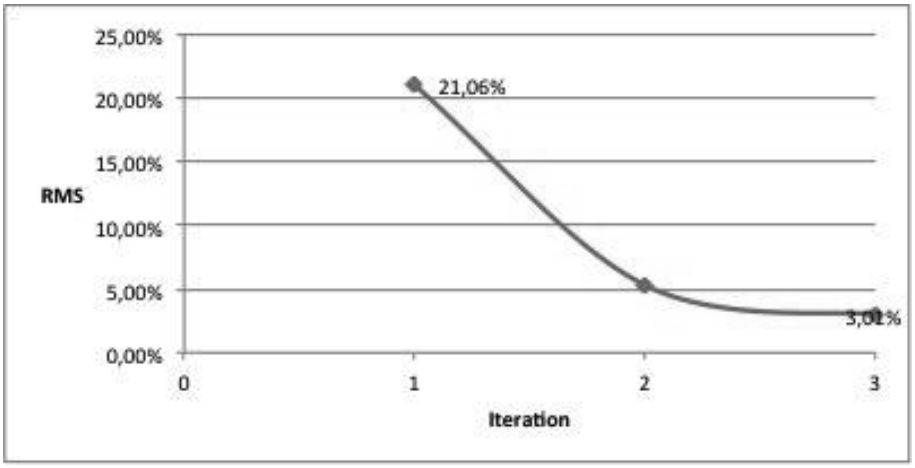
Figue B-19: Data misfit in percent root mean squared versus number of iterations (Wenner Schlumberger line 8).

The convergence of smoothness constrained inversion for the dipole-dipole data acquired along line 8 is shown in Figue B-20.



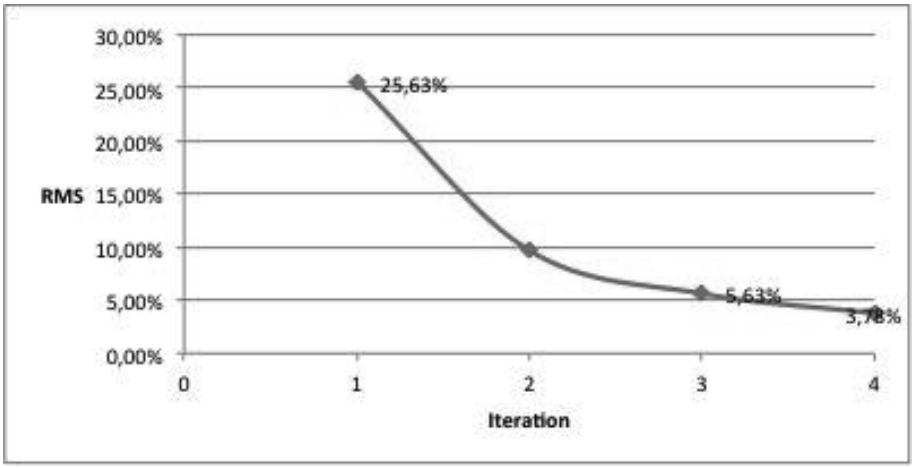
Figue B-20: Data misfit in percent root mean squared versus number of iterations (dipole-dipole data line 8).

The convergence of smoothness constrained inversion for the Wenner Schlumberger data acquired along line 10 is shown in Figue B-21.



Figue B-21: Data misfit in percent root mean squared versus number of iterations (Wenner Schlumberger line 10).

The convergence of smoothness constrained inversion for the dipole-dipole data acquired along line 10 is shown in Figue B-22.



Figue B-22: Data misfit in percent root mean squared versus number of iterations (dipole-dipole data line 10).

Appendix C: Matlab code used for resistivity processing

The code in this section was used to display the IP data in the thesis. The first script's (called "Pseudo section script") results are shown in Chapter 4.

Pseudo section script:

```
% Read the IP data from a file
IPdata=load('l1WS_ip_.dat');

% Read the pulse length from a file
TIMEdata=load('l2dipMatlab_pulse.dat');

% Get the size of the read files
[r,c]=size(IPdata);
[rr,cc]=size(TIMEdata);

% Extract the time data from the file
toriginal=TIMEdata(1,1:11);

% Assigne the size of the read data to a new varialbe
tuse=toriginal;

% Change the first window to a zero
tuse(1,1)=0;

% Calculate the actual start and end points for each measuremnt window
for countt=2:11,
   tuse(1,countt)=tuse(1,countt-1)+toriginal(1,countt);
end

% Assign the IP depth and posiiton along the profile to variables fro
% plotting
sizeofdots=ones(r,1);
xlength=IPdata(:,1);
zdepth=IPdata(:,3);

% Cycle through the ten IP windows
for thiscounter=1:10;

   % Assign the IP alue of each window
   IP=10.*IPdata(:,(thiscounter*2)+4);

   % Clear the figure
   figure(thiscounter); clf;

% Plot the data
   scatter(xlength,zdepth,sizeofdots.*50,IP,'filled');

   % Change the properties of the plots
```

```
   axis equal;
   axis tight;
   daspect([5 1 1]);
   xlabel('X (m)');
   ylabel('Depth (layer)');
   set(gca,'yDir','rev');
   title(['IP decay: window from ',num2str(tuse(1,thiscounter)),' sec to
',num2str(tuse(1,thiscounter+1)),' sec']);
end
```

The code in this section was used to display the IP data in the thesis. The second script's (called "Decay curve script") results are not shown but were used to test if the IP response for each electrode pair decays, after the data was processed using a spreadsheet.

Decay curve script

```
% Read the IP data from a file
IPdata=load('l1WS_ip_only.dat');

% Read the pulse and windows length from a file
TIMEdata=load('l1WSMatlab_pulse.dat');

% Store the size of the loaded data
[r,c]=size(IPdata);
[rr,cc]=size(TIMEdata);

% Store the pulse and sampling window length
xoriginal=TIMEdata(1,1:11);
lastwin=xoriginal(1,11);

% Set the start time for the first measurement window to the automatic value
x(1,1)=0.02;
xoriginal(1,1)=0.02;

% Assign a place holder variable a zero
xbegin=0;

% Cycle through the measuremnet windows
for count=2:cc

   %Set the start of the measuremnt window
   xbegin=xbegin+xoriginal(1,count-1);

   % Calcualte the midpoints of the window
   x(1,count)=(xoriginal(1,count-1)+xoriginal(1,count))/2;

end

%Assign the midpoints of the windows to a new variable
X=x(1,2:10);
```

```
% Cycle htrough all the IP data by datum
for count=1:r
   % Extract the four electrode posiitons
   a=IPdata(count,1);
   b=IPdata(count,2);
   m=IPdata(count,3);
   n=IPdata(count,4);

   % Extract the last IP window data
   lastwindow=10*IPdata(count,28);

   % Extract the IP readings fro the different windows

y=[IPdata(count,10),IPdata(count,12),IPdata(count,14),IPdata(count,16),IPdata(count,18),IP
data(count,20),IPdata(count,22),IPdata(count,24),IPdata(count,26)];

   % Times all the values by ten
   y=10*y;

   % Decide which subplot to be used
   whichsub=mod(count,6);

   % Decide which figure to use
   figure(ceil(count/6));

   if whichsub==0
      usesub=6;
   else
      usesub=whichsub;
   end

   % Plot the data
   subplot(3,2,usesub,'replace'),plot(X,y)

   % Change some of the plot features
   axis tight;
   xlabel('Time after switch off (s)');
   ylabel('Chargeabillity msec');
   title(['IP decay: last window signal is ',num2str(lastwindow),' msec over
',num2str(lastwin),' s']);
   height=ylim;
   text(0.1,(height(1,2)*0.75),['Current electodes at ',num2str(a),' and ',num2str(b)]);
   text(0.1,(height(1,2)*0.5),['Potential electodes at ',num2str(m),' and ',num2str(n)]);

end
```

Appendix D: Acquired data

For the pseudo sections presented here pseudo depths are exported directly from Res2dInv and plotted using Surfer 10. The pseudo depths are obtained by Res2dInv using the effective depth method from Edwards (1977). The effective depth is the depth in the Earth above which 50 percent of the current would flow if the Earth was homogenous. Each resistivity measurement is in fact a response of the whole Earth. Highly conductive bodies much deeper than the effective depth can influence readings although they cannot be modelled. The horizontal positions are taken as the centre of the four electrodes used. The horizontal positions are shown in metres along the profile. The data are presented as measured. “Bad-points” have not been removed, as advised by Loke (2004), as the method of doing this is subjective and the modelling (Chapter 5) should allow for noise in the data.

D.1 Electrical methods along the tree roots

The data from the lines acquired along the trees are presented first.

D.1.1 Resistivity data

The apparent resistivity data acquired on line 1 (Figure 3-1) with the Wenner Sclumberger array are shown in Figure D-1. The apparent resistivity increases gradually with depth. There is also some lateral variation in the near subsurface. Three zones of higher resistivity (c. 100 ohm.m) are present at approximately 35 m, 75 m and 145 m along the profile in the near subsurface.

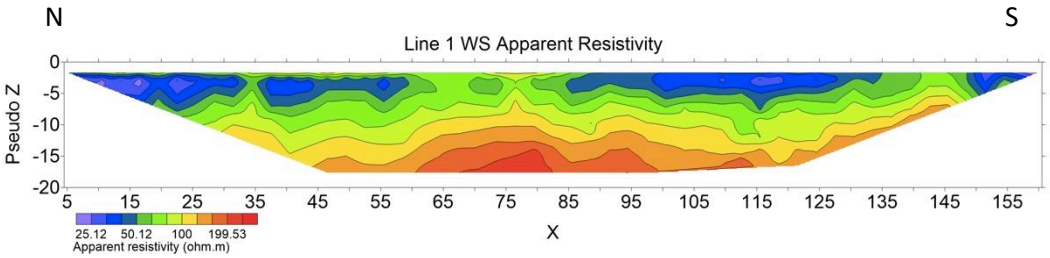


Figure D-1: Wenner Schlumberger apparent resistivity data for line 1. See Figure 3-1 for line position.

Twenty four-points were acquired with both the 2.5 s and 1 s transmitter pulses. This allows a measure of the precision of the data. The average difference between the two measurements for these points is 0.8%. The maximum difference of these points is 4.1%. This is less than the average error (precision) of the data set-obtained from the standard deviation (SD) readings and the constraint of a minimum 0.001 V error at the receiver. The data are more precise than the error constraint calculates (for the precision). If this were to be used as the error estimate of the data, the error estimate would not allow for systematic errors (e.g. misplacement of electrodes, cross talk between cables, problems with the uncalibrated measuring device). For this reason, and to be conservative in terms of over utilising the data, a data error of 5% will be assumed and all the data will be inverted to the point where the misfit between the calculated and measured apparent resistivities falls under this threshold.

At 39 m along the profile a large Eucalyptus tree was present. Between 60 and 85 m along the profile no change in surface features were noted. A line of *Eucalyptus* trees cross cut the profile at 145 m along the profile.

No other data were acquired on this line due to time constraints.

The apparent resistivity data for line 2 (Figure 3-1) are shown in Figure D-2 and Figure D-3. The Wenner alpha data in Figure D-2 show a simple resistive layer overlying a slightly more conductive layer, overlying a resistive layer with the top layer extending slightly deeper at about 35 m along the profile.

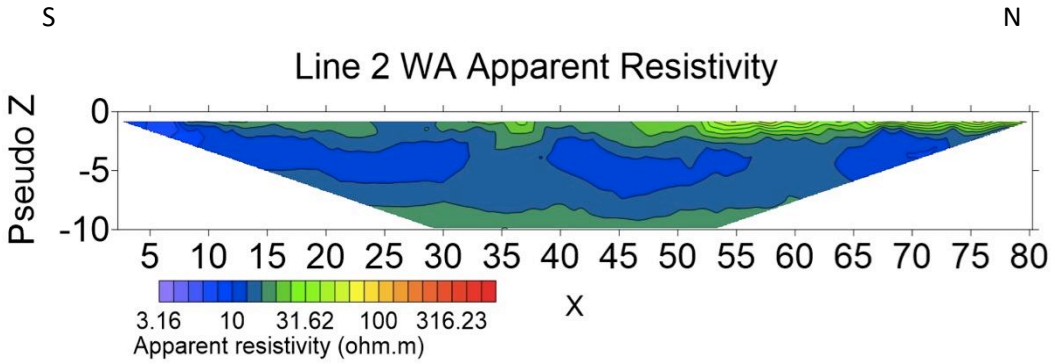


Figure D-2: Wenner alpha apparent resistivity data for line 2. See Figure 3-1 for line position.

The dipole-dipole data in Figure D-3 show a similar trend to the data in Figure D-2 but this data set is noisier and the anomalous resistivity high at 35 m in Figure D-2 is not visible at all.

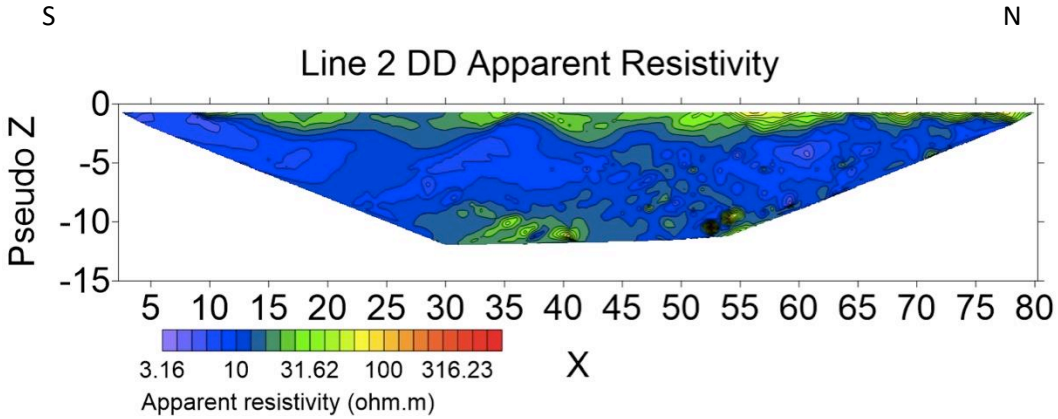


Figure D-3: Dipole-dipole apparent resistivity data for line 2. See Figure 3-1 for line position.

At 41 m along the profile another large tree was present. Between 60 and 85 m along the profile no change in surface features was noted. A line of *Eucalyptus* trees cross-cut the profile at 145 m along the profile.

The apparent resistivity data for line 3 (Figure 3-1) are shown in Figure D-4 and Figure D-5. The Wenner alpha data shown in Figure D-4 show a resistive layer overlain by more conductive material with some of the readings in the shallowest subsurface showing an elevated resistivity as compared to the conductive zone.

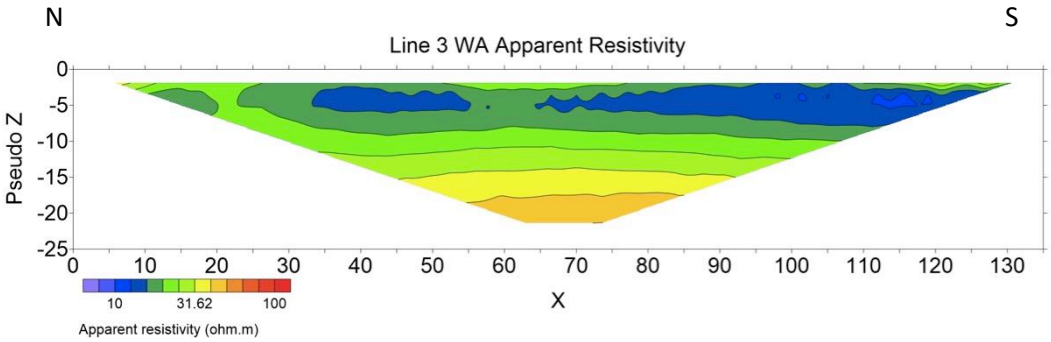


Figure D-4: Wenner alpha apparent resistivity data for line 3. See Figure 3-1 for line position.

The dipole-dipole data shown in Figure D-5 show the same general trend as the Wenner alpha data in Figure D-4, with a resistive layer overlain by more conductive material overlain by a thin layer of more resistive material. The data are much more noisy than the readings shown in Figure D-4. At the ends of the pseudo section it can be seen that data were not acquired for the whole profile. The reason for this was limited field time.

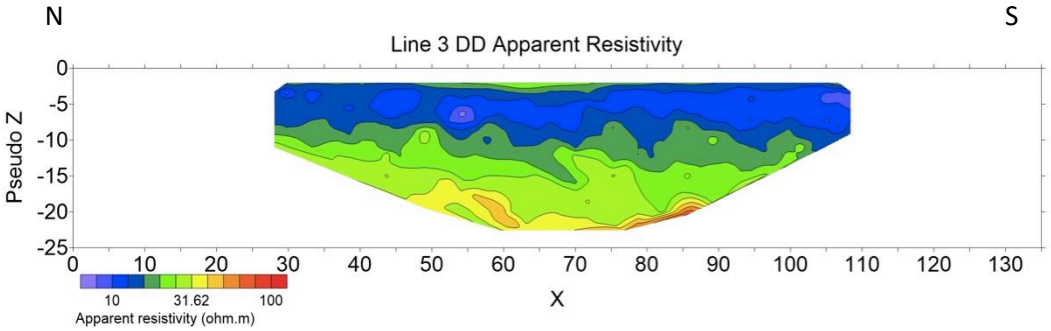


Figure D-5: Dipole-dipole apparent resistivity data for line 3. See Figure 3-1 for line position.

The apparent resistivity data for line 4 (Figure 3-1) are shown in Figure D-6 and Figure D-7. The Wenner alpha data shown in Figure D-6 show two lenses of more conductive material (10 to 20 ohm.m) lying between two more resistive layers (40 -70 ohm.m). One of these layers is at the surface and the other at depth.

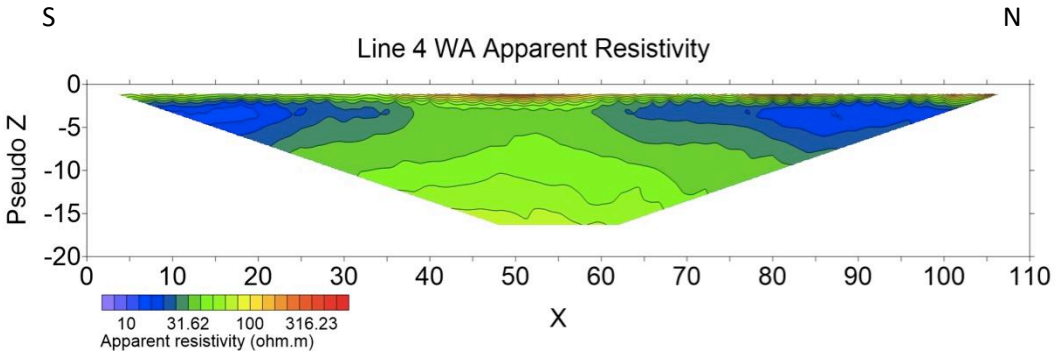


Figure D-6: Wenner alpha apparent resistivity data for line 4. See Figure 3-1 for line position.

The Wenner beta data shown in Figure D-7 show a slightly resistive layer overlaying two lenses of more conductive material. The data are similar in trend in apparent resistivity readings to the Wenner alpha data, but they contain more noise.

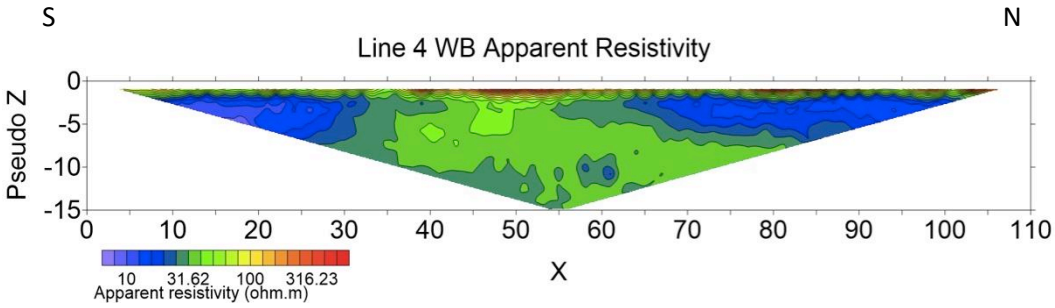


Figure D-7: Wenner beta apparent resistivity data for line 4. See Figure 3-1 for line position.

D.1.2 IP data

In this subsection the IP data are presented in pseudo plots. The contoured images for these data are not readable and the plots, as presented here, are slightly better. The depths given are effective depths and the x-axis on all the plots is in meters along the profile. The ARES system measures the potential after current switch off by integrating the potential difference readings over pre-determined time-windows.

The data are (manually) subjected to a constraint that the measured integral potential decay curve for each pair of electrodes (each data point over successive windows) has to be decreasing for the full measurement cycle. This is to ensure that points that have been affected by noise have been removed. The noise can be telluric, or from eddy current introduced by the source or from electrode polarisation. The telluric current will influence readings at different times over the survey and especially so when the input

current is low. Eddy current introduced by the source is expected to only influence data in the early windows. Electrode polarisation occurs when sufficient time has not been allowed for the electrode to lose polarisation before a measurement is taken again using the electrode as a potential electrode.

The IP data acquired on line 1 (presented as a pseudo plot in Figure D-8) were few points. The window showed here is the summed data for windows 5 to 8 (after 0.24 s for 0.96 s). No other data were acquired on this line due to time constraints.

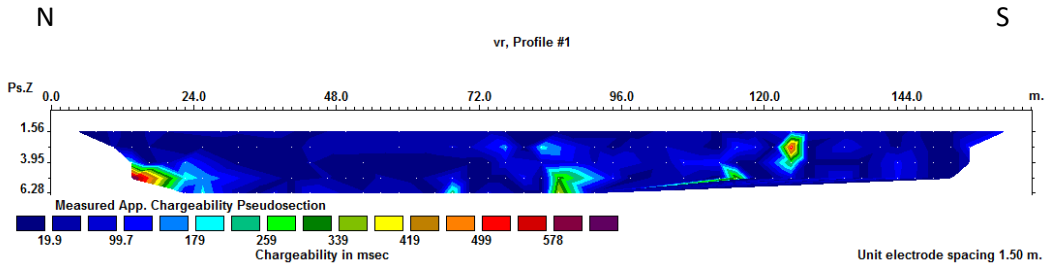


Figure D-8: Wenner Schlumberger IP data for line 1. Windows 5 to 8 are shown. See Figure 3-1 for line position (Res2dInv).

The data are fairly noisy and there is not a significant amount of IP signal observed. The separate decay windows (not shown) for each electrode pair show that only fourteen pairs have a decaying curve. The other points shown in the pseudo section have a value of zero. This is caused by noise (telluric or from polarisation of the stainless steel electrodes), which renders the data unhelpful, and these data will not be discussed further.

The IP data for line 2 (Figure 3-1) are presented as pseudo sections (Figure D-9 and Figure D-10). The data are noisy, but it is not clear how bad the situation is. There is a slight increase of chargeability with depth on the Wenner alpha data with some random points having a higher reading than the rest. This may be noise.

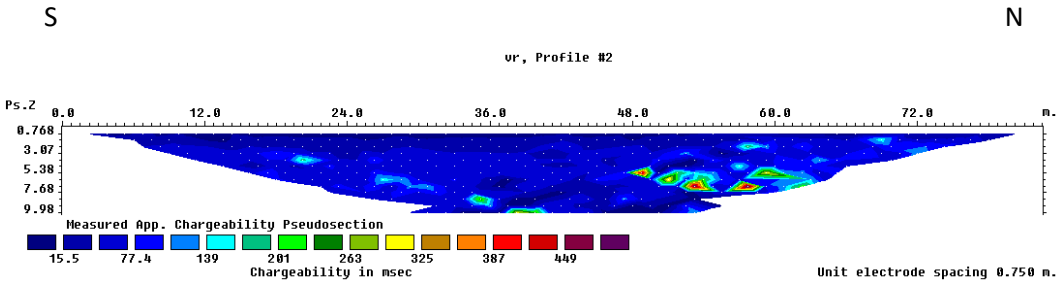


Figure D-9: Wenner alpha IP data for line 2. Integral windows 2 to 6 are summed and the delay after the pulse is 0.04 s for only 0.26 s See Figure 3-1 for line position (Res2dInv).

Dipole-diploe data have also been acquired on this line. Many of the data points, especially at intermediate pseudo depths, have been left out due to the constraint that the entire decay curve must be decreasing for each point. Dipole-dipole data suffer more from noise than the Wenner alpha array and this is evident by comparing Figure D-9 to Figure D-10 and seeing the number of points available for modelling. The data are very noisy.

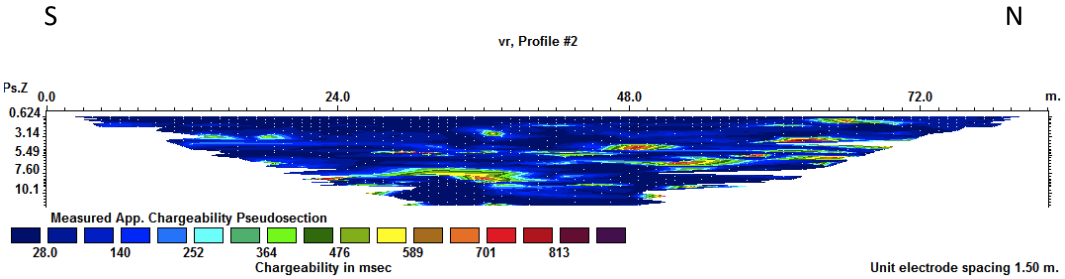


Figure D-10: Dipole-dipole IP data for line 2. Integral windows 6 to 10 are summed and the delay after the pulse is 0.22 s for 1.04 s. See Figure 3-1 for line position (Res2dInv).

The IP data for line 3 (Figure 3-1) are presented as pseudo sections (Figure D-11 and Figure D-12). For the Wenner alpha data on line 3 (Figure D-11) the smallest electrode separations (shallower pseudo depths) do not appear to show many anomalous readings and higher chargeabilities are recorded for greater pseudo depths.

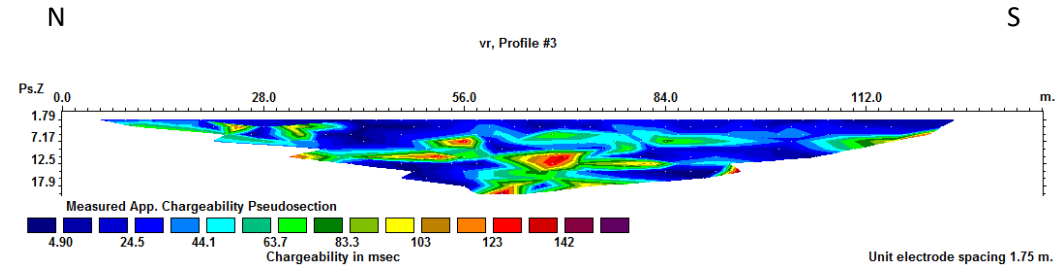


Figure D-11: Wenner alpha IP data for line 3. Integral windows 6 to 10 are summed and the delay after the pulse is 0.22 s for 1.04 s. See Figure 3-1 for line position (Res2dInv).

The dipole-dipole data acquired on line 3 (Figure D-12) show slightly elevated readings (c. 250 to 450 ms) for intermediate electrode spacings (corresponding to effective depths of approximately 6 to 14 m) and then only in the first three windows. The data acquired using the Wenner alpha array also show a negligible response at shallow apparent depths, but this is the only similarity between the datasets. Many of the dipole-dipole data points have been removed through the decay constraint method.

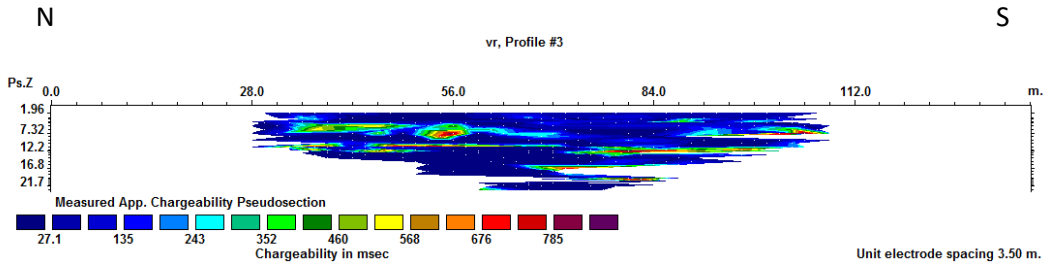


Figure D-12: Dipole-dipole IP data for line 3. Integral windows 6 to 10 are summed and the delay after the pulse is 0.1 s for 0.52 s. See Figure 3-1 for line position (Res2dInv).

The IP data for line 4 (Figure 3-1) are presented as pseudo section (Figure D-13 and Figure D-14). The pseudo sections for the Wenner beta (Figure D-13) data show slightly higher readings at pseudo depths of 10 m to 16 m approximately 50 m to 70 m along the profile for all decay windows.

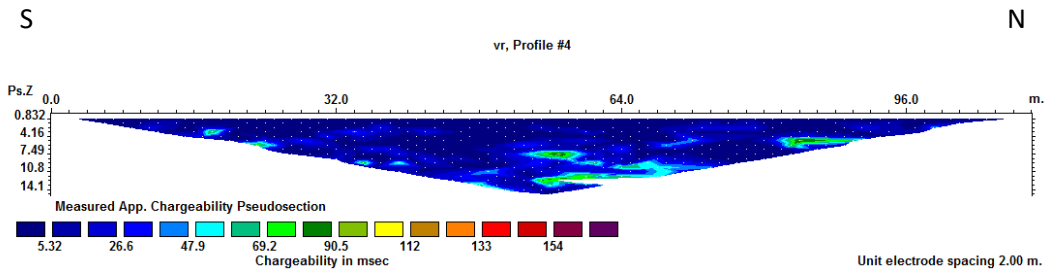


Figure D-13: Wenner beta IP data for line 4. Integral windows 6 to 10 are summed and the delay after the pulse is 0.1 s for 0.52 s. See Figure 3-1 for line position (Res2dInv).

In Figure D-14 the relatively higher values that are visible in Figure D-13 are not visible and, except for some discrete points at large electrode spacings, the data do not show any anomalous features. The pseudo sections of the two different arrays measured on line 4 do not correlate. This is either because of noise in the data (and the data should

not be used or considered) or it is due to the differences in the subsurface response to the two arrays. The inverted data (in Chapter 5) will shed light on this.

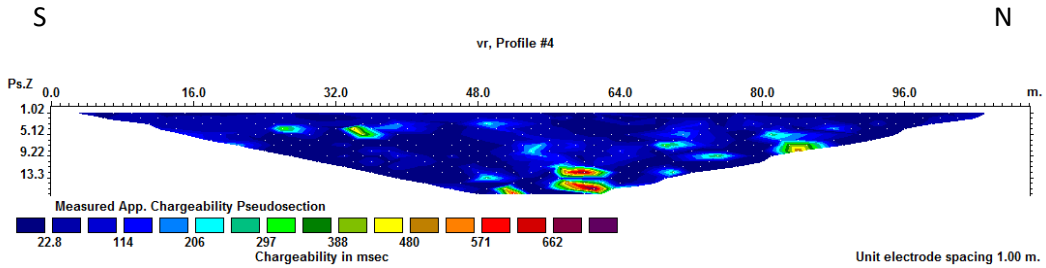


Figure D-14: Wenner alpha IP data for line 4. Integral windows 6 to 10 are summed and the delay after the pulse is 0.06 s for 0.4 s. See Figure 3-1 for line position (Res2dInv).

D.2 Electrical resistivity profile in the direction of the groundwater flow in the lavas

The parallel profiles data acquired from between to two tailings storage facilities down to the Schoonspruit are presented here. The data along line 9 were acquired over the dolomite. Line 5 and 6 were acquired over the lava. These three lines make out a profile from east to west along the flow direction of the groundwater in the lava. Line 12 is in an area where the groundwater is expected to be less influenced by the TSF than line 5 and 6.

The apparent resistivity data for line 9 (Figure 1-1) are shown in Figure D-15 and Figure D-16.

The Wenner Schlumberger data for line 9 shown in Figure D-15 show an increase in resistivity with depth. There are four spikes in the data at approximately 60, 80, 125 and 180 metres along the profile line (at an effective depth of approximately 7 m). These may be due to noise. Three bulbous features occur at greater pseudo depth.

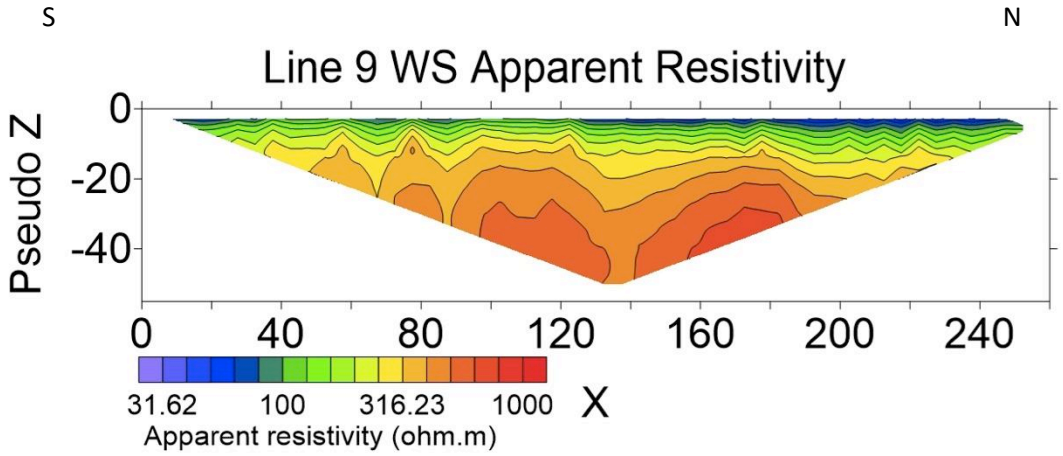


Figure D-15: Wenner Schlumberger apparent resistivity data for line 9. See Figure 1-1 for line position.

The dipole-dipole data for line 9 shown in Figure D-16 data have a high frequency component that the Wenner Schlumberger data do not have. The spikes seen in Figure D-15 are not visible, but the bulbous features at greater pseudo depth are. In general the data are more noisy than the Wenner Schlumberger data.

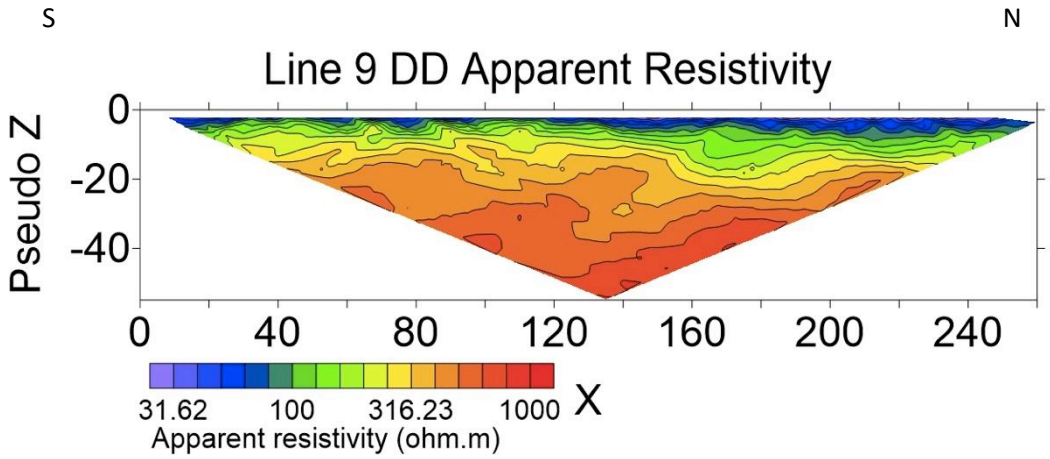


Figure D-16: Dipole-dipole apparent resistivity data for line 9. See Figure 1-1 for line position.

The apparent resistivity data for line 12 (Figure 1-1) are shown in Figure D-17 and Figure D-18.

The Wenner Schlumberger data for line 12, shown in Figure D-17 show a simple layered resistivity with the apparent resistivity values increasing with greater pseudo depth.

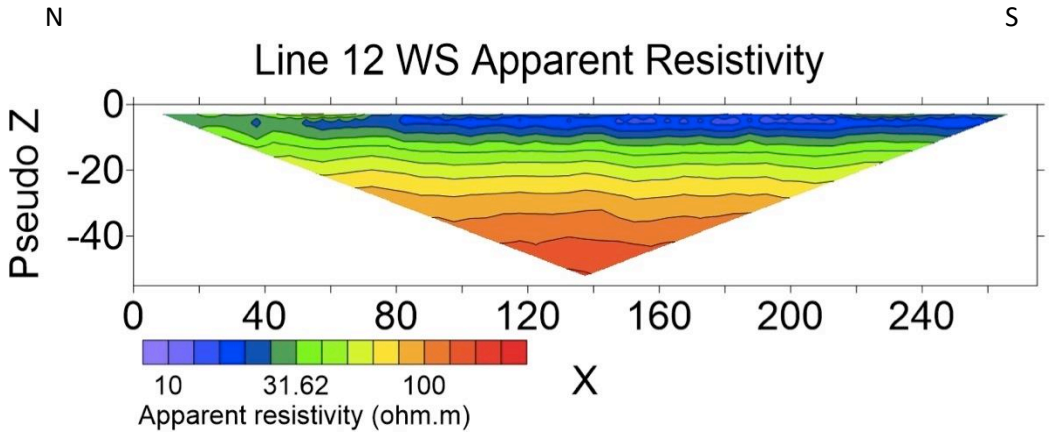


Figure D-17: Wenner Schlumberger apparent resistivity data for line 12. See Figure 1-1 for line position.

The apparent resistivity data in the dipole-dipole pseudo section for line 12 shown in Figure D-18 are similar to the Wenner Schlumberger data but more influenced by high frequency variations that are likely noise.

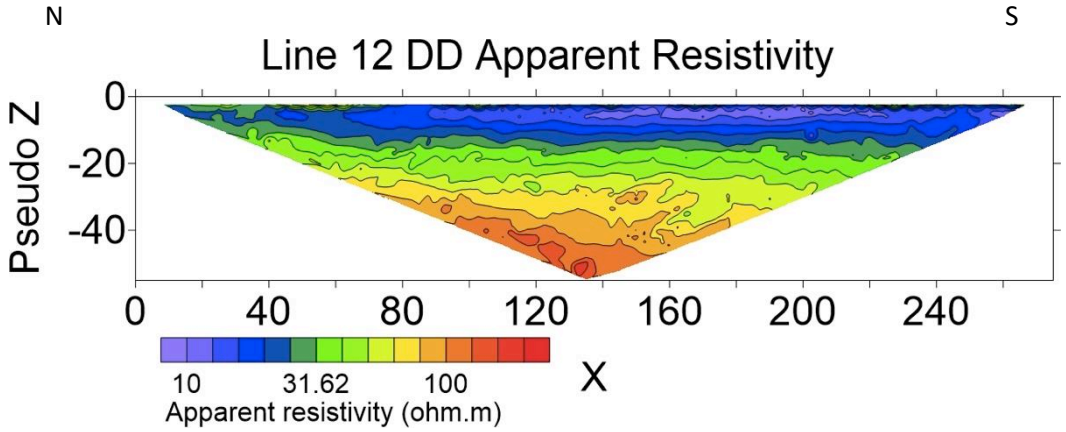


Figure D-18: Dipole-dipole apparent resistivity data for line 12. See Figure 1-1 for line position.

The apparent resistivity data for line 5 (Figure 1-1) are shown in Figure D-19 and Figure D-20.

The data for line 5 acquired with the Wenner Schlumberger array shown in Figure D-19 shows a sub horizontal layering with the resistivity increasing with pseudo depth. Some spiky features are visible on the pseudo section and this may be from noise.

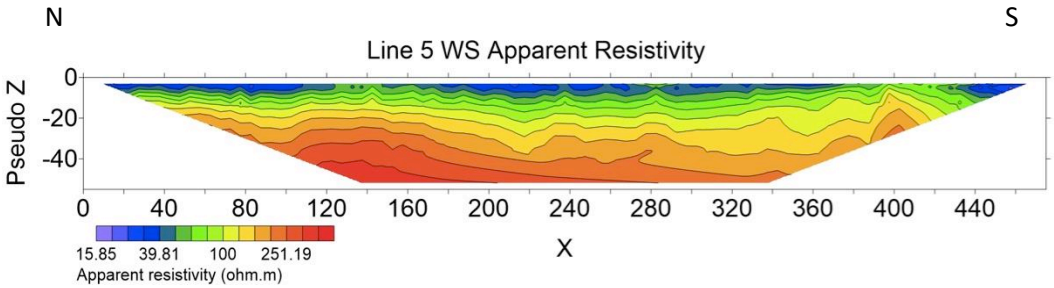


Figure D-19: Wenner Schlumberger apparent resistivity data for line 5. See Figure 1-1 for line position.

The dipole-dipole data acquired on line 5 shown in Figure D-20 were on a section that corresponds with the last overlay of the Wenner Sclumberger data shown in Figure D-19. This was due to a limited amount of field time available for the specific area. The variation of the apparent resistivity over this short section is small, from 10 ohm.m to 200 ohm.m.

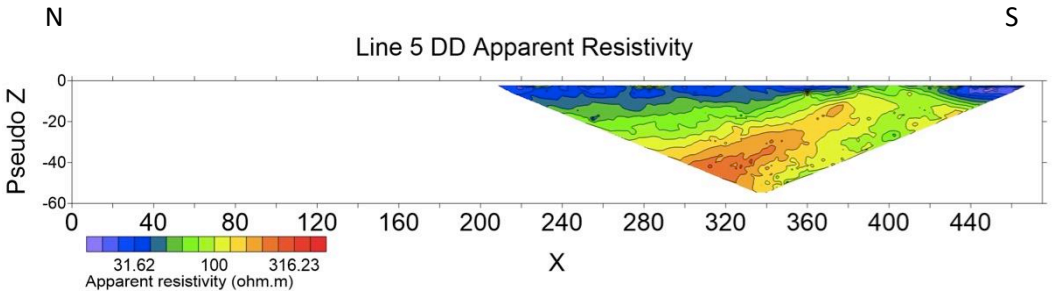


Figure D-20: Dipole-dipole apparent resistivity data for line 5. See Figure 1-1 for line position.

The apparent resistivity data for line 6 (Figure 3-2) are shown in Figure D-21, Figure D-22 and Figure D-23.

The Wenner Sclumberger data for line 6 shown in Figure D-21 show a gradational increase with pseudo depth. A slightly lower resistivity zone at pseudo depths between 20 and 40 m occurs between 50 and 100 m along the profile line.

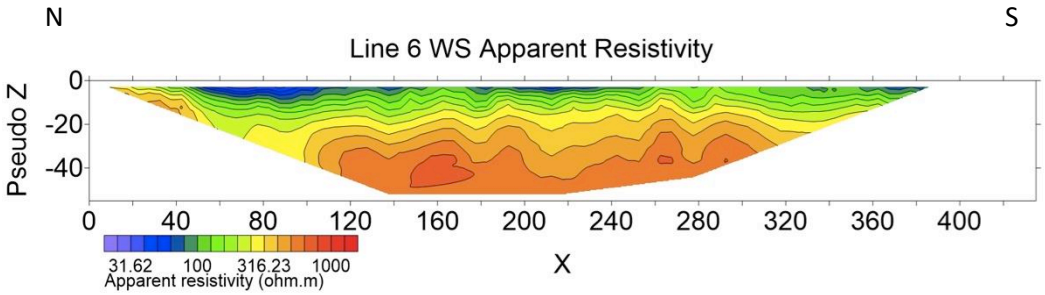


Figure D-21: Wenner Schlumberger apparent resistivity data for line 6. See Figure 1-1 for line position.

The dipole-dipole data for line 6 shown in Figure D-22 show a gradational increase with pseudo depth with a zone of slightly lower resistivity at pseudo depths between 20 and 40 m occurring between 110 and 190 m along the profile line. The feature does not correlate well with the WS data as the more conductive area visible in these data is not seen in Figure D-21. The data also have a higher frequency component, and this could be because the data have been influenced by noise. The modelling in Chapter 5 might shed light on to this as the two arrays are sensitive to slightly different areas of the subsurface.

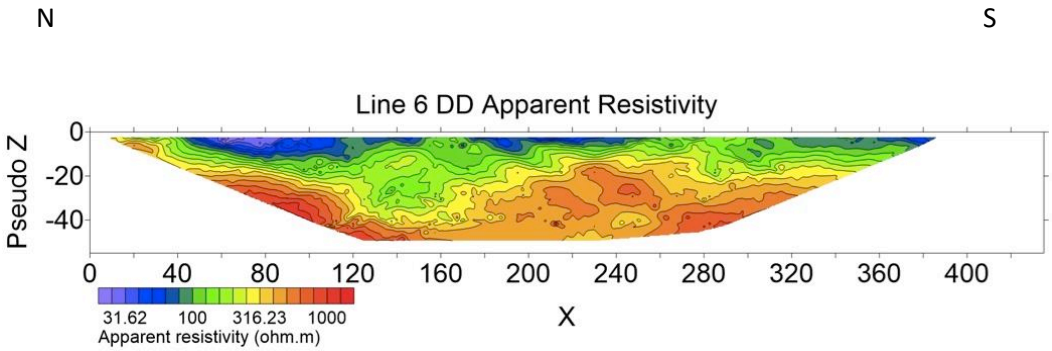


Figure D-22: Dipole-dipole apparent resistivity data for line 6. See Figure 1-1 for line position.

The Wenner alpha data for line 6 shown in Figure D-23 show a gradational increase with pseudo depth. Only the last overlay of the field setup for the Wenner Schlumberger and dipole-dipole data were acquired with this array due to time constraints.

The three data sets for the section where the Wenner alpha (WA) data are available are similar, with the WA data the smoothest and the dipole-dipole data the most influenced by a high frequency component.

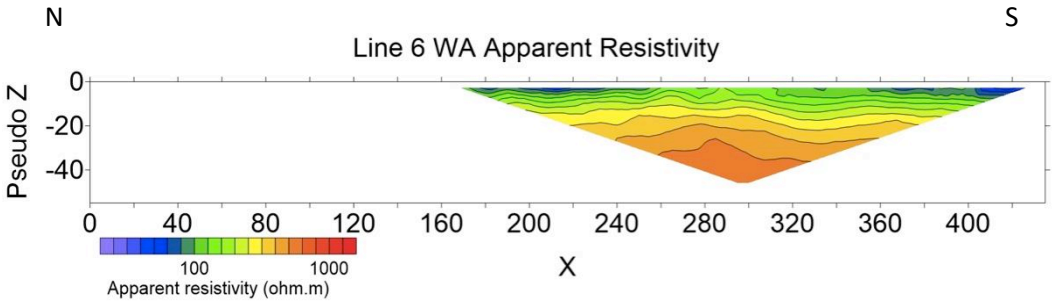


Figure D-23: Wenner alpha apparent resistivity data for line 6. See Figure 1-1 for line position.

D.3 Electrical resistivity profile in the direction of the groundwater flow in the dolomites

The parallel lines acquired over an area of unaffected to affected to remediated groundwater are presented here. All three lines are acquired over the dolomite and they are acquired in the direction the groundwater flows in this unit (from north to south). The data along line 11 were acquired to give background values for the Earth resistivity where the groundwater is unaffected by AMD. Line 8 should show the lowest resistivity in the surficial aquifer, as the groundwater here should have been affected by AMD. Line 10 was surveyed in an area where the groundwater is expected to have been remediated by a *Tamarix* woodland.

The apparent resistivity data for line 11 (Figure 1-1) are shown in Figure D-24 and Figure D-25.

Figure D-24 shows that a conductive layer overlies a highly resistive layer with circular features with apparent resistivity much higher than 1000 ohm.m.

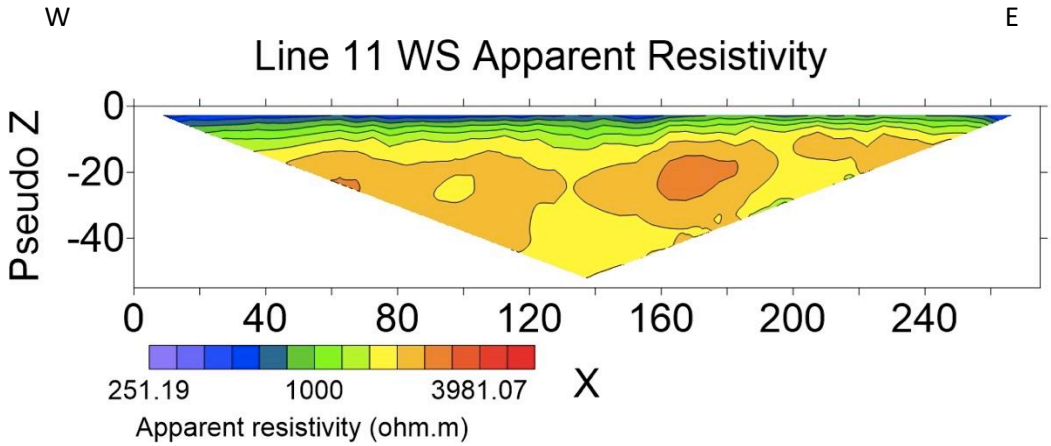


Figure D-24: Wenner Schlumberger apparent resistivity data for line 11. See Figure 1-1 for line position.

Figure D-25 looks quite different from Figure D-24 although both show apparent resistivity pseudo sections for the same line. A conductive layer overlies a resistive layer with some features with apparent resistivities as high as 4000 ohm.m. In both sections, between 70 and 120 m (between 14 and 40 m pseudo depth), a resistor of this magnitude is present. The sections are also similar between 190 m and 240 m (at all pseudo depths).

These two sections show a good example of how little can be learnt from the pseudo section itself.

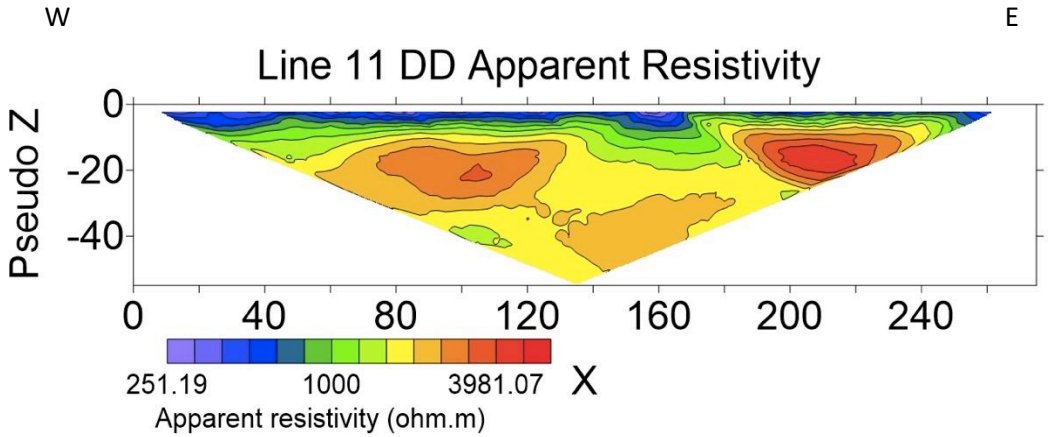


Figure D-25: Dipole-dipole apparent resistivity data for line 11. See Figure 1-1 for line position.

The apparent resistivity data for line 8 (Figure 1-1) are shown in Figure D-26 and Figure D-27.

In Figure D-26 a relatively conductive layer overlies a resistive layer with some spikes in the data present at regular intervals from 40 m to 240 m along the profile. These spikes could be due to noise in the data.

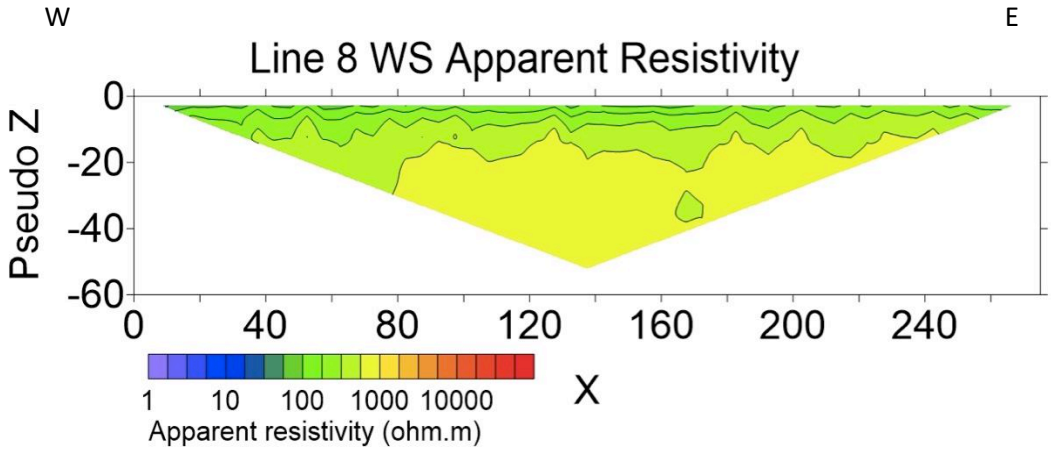


Figure D-26: Wenner Schlumberger apparent resistivity data for line 8. See Figure 1-1 for line position.

In Figure D-27 some abnormally high readings were recorded with large dipole separation (at greater pseudo depth). The effect of these noisy readings on the pseudo section smears the data scale and makes even an elementary interpretation impossible.

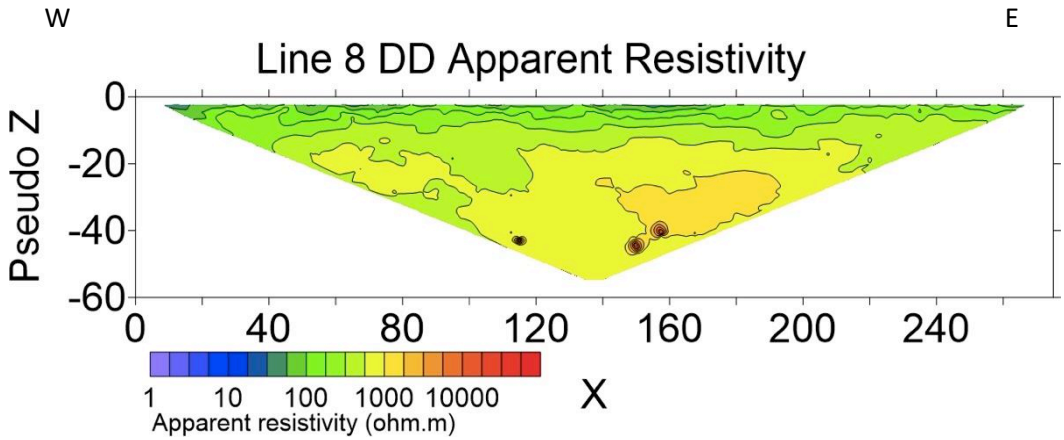


Figure D-27: Dipole-dipole apparent resistivity data for line 8. See Figure 1-1 for line position.

The apparent resistivity data for line 10 (Figure 1-1) are shown in Figure D-28 and Figure D-29.

In Figure D-28 the pseudo sections for line 10 show a dipping resistor and the resistivity increasing with depth. Shallow spikes are present as previously and this could be from noise.

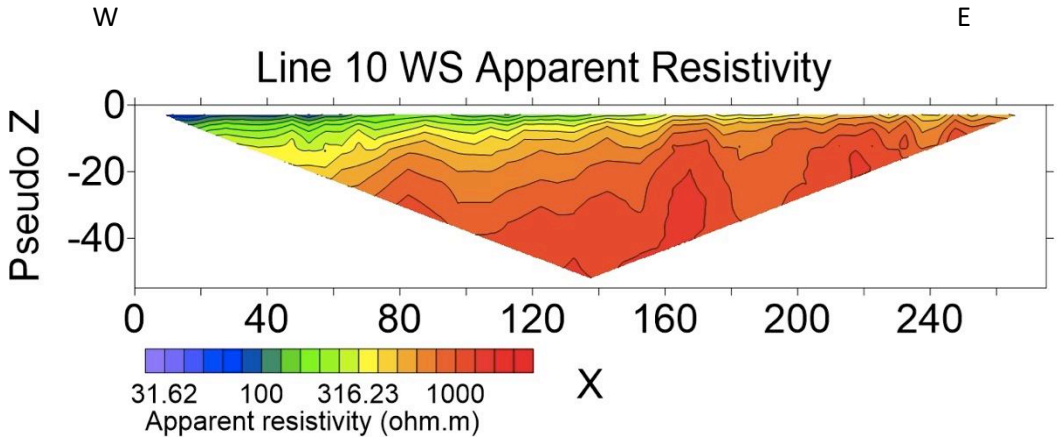


Figure D-28: Wenner Schlumberger apparent resistivity data for line 10. See Figure 1-1 for line position.

The dipole-dipole data shown in Figure D-29 are noisier than the Wenner Schlumberger data as can be seen from the high frequency details at depth, but the overall trend of resistivity increasing with pseudo depth over a dipping resistor is present in both the dipole-dipole and the Wenner Schlumberger data.

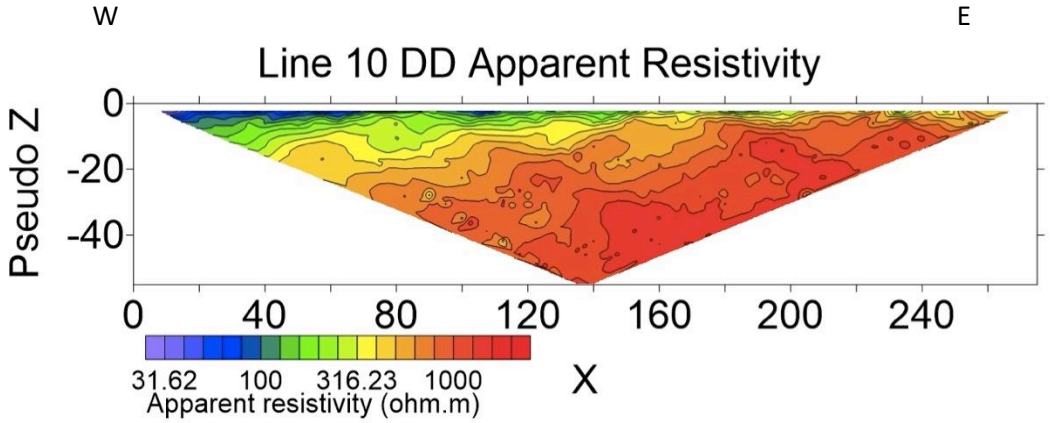


Figure D-29: Dipole-dipole apparent resistivity data for line 10. See Figure 1-1 for line position.

D.4 GPR data

The GPR data did not show the deeper penetration and a representative sample of (distance-normalised) data is shown in Figure D-30.

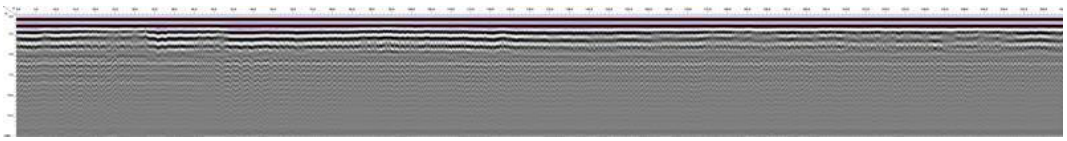


Figure D-30: Representative sample of distance normalised raw GPR data.

The rest of the GPR data are not presented as no evidence of increased depth of penetration (directly related to soil conductivity) was observed. These data will not be considered any further.